Universidade Estadual de Campinas
Instituto de Física "Gleb Wataghin"

Andres Alejandro Navarro Alsina

Efeitos da modelagem da PSF em estimativas cosmológicas usando lentes gravitacionais fracas

Effects of PSF modeling in cosmological estimates using weak gravitational lensing

Campinas
2020

Andres Alejandro Navarro Alsina

Effects of PSF modeling in cosmological estimates using weak gravitational lensing

Efeitos da modelagem da PSF em estimativas cosmológicas usando lentes gravitacionais fracas

Dissertation presented to the "Gleb Wataghin" Physics Institute of the University of Campinas in partial fulfillment of the requirements for the degree of Master in Physics, in the area of physics.

Dissertação apresentada ao Instituto de Física "Gleb Wataghin" da Universidade Estadual de Campinas como parte dos requisitos exigidos para a obtenção do título de Mestre em Física, na área de Física.

Supervisor/Orientadora: Prof. Dr. Flávia Sobreira

Este exemplar corresponde à versão final da dissertação defendida pelo aluno Andres Alejandro Navarro Alsina, e orientado pela Prof. Dra. Flávia Sobreira.

Campinas
2019

Ficha catalográfica
Universidade Estadual de Campinas
Biblioteca do Instituto de Física Gleb Wataghin
Lucimeire de Oliveira Silva da Rocha - CRB 8/9174

Navarro Alsina, Andres Alejandro, 1993-
N228e Effects of PSF modeling in cosmological estimates using weak gravitational lensing / Andres Alejandro Navarro Alsina. – Campinas, SP : [s.n.], 2019.

Orientador: Flávia Sobreira.
Dissertação (mestrado) – Universidade Estadual de Campinas, Instituto de Física Gleb Wataghin.

1. Cosmologia. 2. Lentes gravitacionais. 3. Estruturas em larga escala (Astronomia). I. Sobreira, Flávia, 1982-. II. Universidade Estadual de Campinas. Instituto de Física Gleb Wataghin. III. Título.

Informações para Biblioteca Digital

Título em outro idioma: Efeitos da modelagem da PSF em estimativas cosmológicas usando lentes gravitacionais fracas
Palavras-chave em inglês:
Cosmology
Gravitational lenses
Large scale structure (Astronomy)
Área de concentração: Física
Titulação: Mestre em Física
Banca examinadora:
Flávia Sobreira [Orientador]
Márcio José Menon
Eduardo Serra Cypriano
Data de defesa: 10-12-2019
Programa de Pós-Graduação: Física

Identificação e informações acadêmicas do(a) aluno(a)
- ORCID do autor: https://orcid.org/0000-0002-3173-2592
- Currículo Lattes do autor: http://lattes.cnpq.br/7725320092753327

MEMBROS DA COMISSÃO JULGADORA DA DISSERTAÇÃO DE MESTRADO DE **ANDRES ALEJANDRO NAVARRO ALSINA – RA 209786** APRESENTADA E APROVADA AO INSTITUTO DE FÍSICA "GLEB WATAGHIN", DA UNIVERSIDADE ESTADUAL DE CAMPINAS, EM 10 / 12 / 2019.

COMISSÃO JULGADORA:

- Profa. Dra. Flávia Sobreira – Orientadora – DRCC/IFGW/UNICAMP
- Prof. Dr. Marcio José Menon – DRCC/IFGW/UNICAMP
- Prof. Dr. Eduardo Serra Cypriano – IF/USP

OBS.: Ata da defesa com as respectivas assinaturas dos membros encontra-se no SIGA/Sistema de Fluxo de Dissertação/Tese e na Secretaria do Programa da Unidade

CAMPINAS
2019

Dedicado a Aguasclaras

Agradeço.

Em especial à professora Flávia Sobreira, pela orientação, paciência e todo apoio necessário para realização deste trabalho.

To the weak lensing working group of DES. I want to express my most sincere gratitude with Mike Jarvis, Niall MacCrann Lucas Secco and Marco Gatti, the core of this work come from your ideas and discussion. Also I want to thank Alex Amon and Daniel Gruen, your coordination work make this work progress significantly.

À Unicamp e ao IFGW pela ótima estrutura que oferecem aos estudantes e pesquisadores.

À CNPq pela oportunidade dada através da bolsa de mestrado concedida.

À todos os funcionários do IFGW, principalmente ao CCJDR pelo excelente suporte.

Ao Laboratório Interinstitucional de e-Astronomia (LIneA) pela coordenação da participação brasileira no DES.

Aos familiares e amigos, sejam presentes ou distantes, que sempre me apoiaram em cada passo.

Resumo

O cisalhamento cósmico representa uma técnica promissora para estudar o universo e contrastar modelos cosmológicos com dados. No presente trabalho, apresentamos uma introdução da cosmologia padrão, lentes fracas desde os catálogos ate observáveis, e realizamos testes essenciais no processo de validação dos catálogos do Y3 produzidos pela colaboração DES. Em particular, essas análises envolveram validar a PSF implementada. Realizamos modelagem de quão significativa a sistemática de PSF poderia adicionar na função de correlação de cisalhamento de dois pontos. Utilizando correlações de diagnóstico foi determinado no espaço real o viés tomográfico produzido pela PSF. Observamos que esses erros sistemáticos se tornam mais significativos em grandes escalas. No entanto, em comparação com a função fiducial, o viés era duas ordens de grandeza menor. Realizamos uma série de análises de previsões, propagando o viés da PSF obtido na função de cisalhamento e estimando parâmetros cosmológicos, na cosmologia padrão. Observa-se que os parâmetros cosmológicos estimados não foram afetados pela contaminação do PSF. Isso indica que os erros sistemáticos da PSF não estão influenciando nossas estimativas cosmológicas.

Palavras-chave: Cosmologia, Lenseamento Fraco, Função de Disperção de um ponto, PSF, medidas de forma, sistematicas, DES

Abstract

Cosmic shear represents a promising technique to study the universe and contrast cosmological models with data. In the present work, we give an introduction of standard cosmology, weak lensing from catalogs to observables, and we performed essential tests in the process of validation of the Y3 shear catalogs produced by the DES collaboration. In particular, these analyses involved the evaluation of the goodness of the implemented PSF modeling. We performed modeling of how significant PSF systematic errors could add in the shear two-point correlation function. Using diagnostic two-point correlations it was determined in real space the total tomographic PSF bias. We observed that PSF systematic errors become more significant at large scales. However, in comparison with the fiducial shear two-point correlation function, it was two orders of magnitude smaller. We performed a series of forecasts, propagating the obtained PSF bias in a fiducial shear two-point function, and estimating cosmological parameters of standard cosmology. The estimated cosmological parameters were no affected by PSF contamination. This indicates that PSF additive systematic errors are not biasing our cosmological estimates.

Keywords: Cosmology, Weak gravitational lensing, Point Spread Function ,PSF, shape measurements, systematics, DES

List of Figures

List of Tables

Contents

Chapter 1

Introduction

Motivation

In the last decades, experimental cosmology has reached an incredible growth. Never before humankind had been able to explore the universe as now. Maps of tens of billions of galaxies covering tens of thousands of square degrees of the sky will be a reality in the near future [1]. Besides, this growth has been reached with extraordinary precision of measurements [2, 3], allowing for a better understanding of how to improve and lead our cosmological models.

The current paradigm in cosmology is known as the standard cosmological model, ΛCDM. It explains a wide variety of phenomena, from the origin and evolution of large scale structures to the current epoch of accelerated expansion. This model is supported so far by the general theory of relativity. However, two exotic components are dominant: dark matter and energy. To study these and other cosmological observables many facilities around the world have been combining different probes. CMB (Cosmic Microwave Background), type IA supernovae, galaxy lensing, and galaxy clustering might be the most widely used. For this work, the interest will be focused on *weak lensing*, since this technique have recently acquired an important progress, specially because improvements on CCD cameras technology have allowed larger surveys, letting in this way to have the required statistics to carry out accurate measurements, which had not been possible before due to the low statistics.

Weak gravitational lensing

When photons are emitted by a source far away from us, like a galaxy or other luminous object, they propagate through several inhomogeneities in the universe. In consequence, photon's paths consecutively bend until they reach our telescopes. This fact distorts the intrinsic information about the source, and these distortions are very useful because they can reveal how the inhomogeneities are, i.e., the matter density variation along the line

of sight.

All the process of distortion of images produced by the large scale structure of the universe, is known as *cosmic shear* and the deviation of a photon's paths because the tidal force is known as *gravitational lensing*. Depending on the level of distortion, lens effects classify in micro, weak, and strong. Weak gravitational lensing is the deflection of light by matter distribution that produces around 1% distortion level of images of galaxies, or, in rough terms, any small modification but not visually striking as multiple images or arcs[4]. But, how can we distinguish if we are observing a galaxy that has suffered such a small distortion or not? The truth is that it will be impossible to know if we were analyzing only one galaxy. However, when we observe many of them, we see privileged orientations of their ellipticities, which, as we will see, it is related to the gravitational potential along the line of sight.

Any probe that uses weak lensing as an analysis tool must start with two basics assumptions. First, that in the absence of lensing, galaxies are randomly oriented, and second, that under the same conditions, on average, galaxies would appear with a circular shape. In other words, galaxies should not have a privileged orientation or ellipticity because the universe is homogeneous and isotropic. Hence, if it is bare in mind the lensing effect, nearby structures will appear with their shapes and orientations correlated. This correlation has an amplitude and scale dependence, useful to determine the statistical distribution of matter (both baryonic and dark), unlike angular or redshifts surveys that measure galaxies distribution. Consequently, with this distribution of matter, it is also possible to study the evolution of the cosmic structure and properties of dark energy. This last statement and the no assumption about the dynamical state of the matter converts weak lensing in one of the most sensitive and promissory probes to constrain cosmological parameters. [5]

Some applications of weak lensing

1. Determine the Structure of dark matter Halos. (Mass maps)
2. Measure the expansion rate of the universe (H_0).
3. Distinguish different cosmological models (modified gravity and dark energy) for explaining the acceleration of the universe. (Tomography)
4. Study the global geometry of the universe.

Chapter 2

Introduction to the standard cosmology

Modern cosmology starts at the beginning of the nineteen century. In that time, the paradigm about the nature of the universe laid into two currents of thought: the steady-state universe and the Big Bang universe. The *steady state* or stationary universe is based on *the perfect cosmological principle*. According to this principle, there are not favored time, either direction or position in the universe, space, and time are infinite, and there are no worries about the existence of an origin. On the other hand, Big Bang theory only assumes *cosmological principle*, i.e, the homogeneity and isotropy of the space Time can be perfectly in-homogeneous. According to this theory, the universe does have an origin, the Big Bang, and immediately after that tremendous explosion, the universe started a process of expansion.

The race between these two models came to its end with the observations of Hubble and Lemaitre around 1930. They found that the further some stars were, the faster they were recessing, leading to the conclusion that the universe was in expansion. This represented a severe problem for the steady-state model since, from this perspective, a universe in expansion should be creating mass constantly; otherwise, density and energy would not conserve. However, this hypothetical spontaneous mass creation would not be more than a violation of energy conservation. It is to say, with the observations of Hubble and Lemaitre, the steady-state model had to accept that there were periods with lower and higher density, violating the time homogeneity embedded in the model.

Another significant milestone in the construction of modern cosmology was the discovery of the CMB (Cosmic Microwave Background) by Penzias and Wilsons in 1965. CMB spectrum is the best black-body spectrum (T= 2.7 K) we have ever measured. We observe the same kind of spectrum in any direction in the sky. Besides, the astonishing fact that we are receiving radiation that comes from the early universe. CMB is a remarkable proof of the isotropy of the universe.

The cosmological principle and Einstein's theory of relativity are the starting blocks to build a model of the universe and to study its dynamics. We also need to include its con-

stituents and their interaction. With the development of the standard model of particles during the 70s and 80s, significant contributions were made in this direction. However, in 30s Zwicky observed a tension between measurement of mass in Coma cluster[6] using dispersion velocity of galaxies and luminous density. Further works by Babcock [7], Rubin and Ford[8] and Roberts and Whitehurst[9], studying rotational curves of galaxies prove that the lack of Keplerian drop-off was a necessary condition of non-luminous mass halos in spiral galaxies. Later discussions[10] about gravitational stability in this system convince most of astronomer that the missing mass was true and might have cosmological impact.

The missing non-luminous mass was called *dark matter*. However, it is unclear its nature. Eighties discussion was about if it was hot: relativistic neutrinos, or cold: dwarfs stars, black holes. After several works [11–13] using lensing, X-ray observations, Bullet cluster, and other probes, hot dark matter and compact cold dark matter were downplayed, and current speculation favor non-compact cold dark matter candidates[14, 15].

In the transition to the twenty one century, observing type Ia supernova, Perlmutterm[16] and Riess[17], discovered that the universe was not only expanding but also that this expansion was accelerating.[1] There is not an accepted theory to explain the phenomena. The best we have done up to now is to build models based on Einstein's equation, the cosmological principle, and perturbation theory. Our more successful model today, we call it ΛCDM (Λ Cold Dark Matter), and it can explain most of the observations we got from different cosmological probes. In the context of this model, the cosmological constant Λ or anti-gravity is responsible for this accelerated expansion. The cosmological constant is also interpreted as the energy of the vacuum. However, when compared with theoretical calculations of quantum field theory, we have a tremendous difference by a factor of 10^{-120}[18], probably our worst theoretical prediction.

The nature of dark matter and dark energy is the most prominent paradigm of cosmology nowadays. In the following chapter, we give a summary of the more essential concepts associated with the standard model of cosmology ΛCDM. We start presenting the smooth universe, described by Friedman equations; then, we discuss the way how we measure some observable in the universe and the way how we link measurements with parameters of this smooth universe. And finally, we present a brief discussion about perturbation theory and more elaborated observable as the matter power spectrum.

2.1 Models of universe

A vast majority of the modern cosmological models are based on the assumption that the universe is homogeneous and isotropic, at least on large scales. This principle is known

[1] To be more specific, with this acceleration we mean $\ddot{a} > 0$ since the Newtonian acceleration is already present since Hubble's law

as the *cosmological principle*, together with a theory of gravity, represent the base stone for building models of the universe. Informally talking, homogeneity means that there are not privileged locations and isotropy that there are not privileged directions[19]. In more formal terms, these principles state that measurements on large scales should be invariant under translations or rotations of the universe. According to the principle of invariance of physical laws, it is equivalent to say, that it is independent of how we translate or rotate the observer. As a consequence of the cosmological principle, measurements on large scales of the universe should look the same, statistically speaking. A universe with the mentioned properties is known as the *smooth universe*, and his scale factor and geometry characterize it. The *scale factor* is a parameter used to link our physical frame of reference to a comoving frame, where coordinates are moving together with the expansion of the universe. We relate the *proper distance* $\overrightarrow{d_p}$ with the *comoving distance* $\overrightarrow{x}$, through

$$\overrightarrow{r} = a\overrightarrow{d_p}, \tag{2.1}$$

where a is the scale factor, and the comoving distance is time-independent. On the other hand, universe geometry refers to the way how we define the size and the curvature in the universe. Observations have led to the conclusion that our universe is flat, i.e., it has no curvature, although this data is might be compatible with other shapes [20–22]. Generally speaking, we can think in a *flat universe*, as one where the path of parallel particles remain parallel. While *closed universes* paths converge, and *open universes* paths diverge. Below we will see that the type of curvature and the way how the scale factor involves depend mainly on the energy density. Our observations about the size of the universe are less conclusive. However, whether or not it is finite or infinite, we study it mathematically as a differentiable manifold without boundaries.

2.1.1 Perfect fluid and no interacting components

To get a first intuitive idea of how a smooth model of the universe is, let's include two additional assumptions, besides the cosmological principle. First, the universe has three *no interacting components*: radiation, matter, and the cosmological constant. Second, the universe is a *perfect fluid*. i.e. it can not conduct heat, does not have viscosity or shear stress. Under those assumptions, a set of 4 equations: Friedman equations, the equation of energy conservation and the state equation of the fluid, determine the cosmic dynamic.

Friedman equations

In appendix A we present a detailed deduction of the Friedman's equations,

$$\left(\frac{\dot{a}}{a}\right)^2 + \frac{kc^2}{a^2} = \frac{8}{3}\pi G\rho \tag{2.2}$$

$$2\frac{\ddot{a}}{a} + \left(\frac{\dot{a}}{a}\right)^2 + \frac{kc^2}{a^2} = -\frac{8\pi G}{c^2}p \tag{2.3}$$

which are a set of differential equations, relating the scale factor a and the curvature k with the density ρ and pressure p of an ideal fluid which represents the components of the universe.

Energy conservation

Using the equation of conservation of the moment-energy tensor (see appendix B), we can deduce the equation of conservation of the energy

$$\boxed{\dot{\epsilon} + 3H(\epsilon + p) = 0,} \tag{2.4}$$

some books prefer to call this equation, the *continuity equation* or the *the fluid equation.*

Equation of state

Finally, it only remains the equation of state; this is essentially an equation that relates two or more state variables. In our case, those variables are the pressure and the internal energy density of the fluid. Though we are looking for an equation of the form

$$P = P(\epsilon). \tag{2.5}$$

In general, this could be a complicated equation. However, we are considering the universe as a perfect fluid. Moreover, it is approximately a *dilute gas*; then the previous equation can be written in the form

$$\boxed{p = w\epsilon,} \tag{2.6}$$

with w a dimensionless number. Because we are working with no interacting components, our perfect fluid can be thought as a mixture of three independent dilute gasses, so that the previous equations are valid for each component of the universe. With

$$\begin{cases} w = 0 & \text{for no relativistic matter} \\ w = \frac{1}{3} & \text{for relativistic matter} \\ w = -1 & \text{for cosmological constant.} \end{cases} \tag{2.7}$$

From classical statistical mechanics, we can deduce the values for the constant w in the cases of relativistic and no relativistic matter. To justify why $w = -1$ for the cosmological constant, let's see what happens when you replace in eq. (2.4) the energy density of the cosmological constant. Given that the energy density of the vacuum does not change with expansion, eq. (2.4) becomes $3H(\epsilon + p) = 0$, that can only be true only if $p = -\epsilon$.

If we substitute the temporal Friedman equation in the spatial equation, we get another important equation the *acceleration equation*

$$\frac{\ddot{a}}{a} = -\frac{4\pi G}{3c^2}(\epsilon + 3p). \tag{2.8}$$

It is relevant since it does not depends on the curvature and we can have an idea of under what circumstance of pressure and density the universe will have accelerated expansion or compression. We call *dark energy* to any component able to produce accelerate expansion $\ddot{a} > 0$, which is only possible if $p < -\frac{\epsilon}{3}$. i.e when $w < -\frac{1}{3}$. Since the cosmological constant satisfies this condition, we will say that it is a candidate for dark energy.

Dynamic equations

Although all the physical information of interest is contained in the previous equation, it worth to play with them a little be more, to get more intuitive expressions and become familiar with the notation. If we replace the equation of state in the equation of energy conservation, we get a differential equation for the energy density, whose solution is

$$\epsilon_i(a) = \epsilon_{i,0} a^{-3(1+w_i)}. \tag{2.9}$$

Where $\epsilon_{i,0}$ is the energy density of the ith component observed today. We can see that the energy density will decrease as a power law, respect to the scale factor. Then, if the universe continues in accelerated expansion, the energy density of photons will decrease faster (fourth power) than matter (third power). While the energy density associated with a cosmological constant will remain constant. It results convenient to write the previous equation in terms of dimensionless quantities. Therefore we will divide it by the *critical energy density*, which we will define as the energy density of all the component of the universe in the absence of curvature. Hence, from the temporal Friedman equation, eq. (2.2) we have

$$\epsilon_c(t) = \frac{3H^2c^2}{8\pi G}. \tag{2.10}$$

Moreover, we will define the *density parameter* as

$$\Omega(t) = \frac{\epsilon(t)}{\epsilon_c(t)} = \frac{\rho(t)}{\rho_c(t)}. \tag{2.11}$$

Bearing this definitions in mind, the total energy density in the universe can be written as

$$\frac{\epsilon(a)}{\epsilon_{c,0}} = \sum_i \Omega_{i,0} a^{-3(1+w_i)} = \Omega_{m,0}a^{-3} + \Omega_{r,0}a^{-4} + \Omega_{\Lambda,0}. \tag{2.12}$$

Defining a density parameter for the curvature

$$\rho_k = -\frac{3kc^2}{8\pi G}, \tag{2.13}$$

temporal Friedman equation becomes

$$H^2 = H_0^2 \left(\Omega_{m,0} a^{-3} + \Omega_{r,0} a^{-4} + \Omega_\Lambda + \Omega_k a^{-2}\right). \tag{2.14}$$

Using the convention that the scalar factor today is equal to one. We have the constrain

$$\Omega_{m,0} + \Omega_{r,0} + \Omega_\Lambda + \Omega_k = 1, \tag{2.15}$$

which we can be introduced in the previous equation to avoid an explicit dependency with the curvature. Leading to the expression

$$\boxed{H^2 = H_0^2 \left(\Omega_{r,0} a^{-4} + \Omega_{m,0} a^{-3} + \left(1 - \Omega_{m,0} - \Omega_{r,0} - \Omega_\Lambda\right) a^{-2} + \Omega_\Lambda\right)}. \tag{2.16}$$

To simplify notation, we will define a function $E(a)$, that depends on the scale factor and the density parameters

$$H^2 = H_0^2 E^2(a). \tag{2.17}$$

2.2 Physical quantities to probe cosmological models

To test cosmological models, it is needed to define how to measure the physical quantities. This is not a trivial decision since different models of the universe could change our intuitive conception of the physical quantity. For instance, the rate of expansion of the universe depends on the content of its components, and different models can have various components and densities. As a consequence, the time a light beam lasts (and the distance it travels) to arrive at our detectors depends on the amount of matter, radiation, and the cosmological constant (or another exotic component your model could have). It is to say, measurements of physical quantities depend on the model.

The reader might ask, how can we test a cosmological model if the measurement of the physical quantities will depend on the model itself and its parameters. Well, the solution to this apparent paradox is to measure those physical quantities using different probes and compare all the results. If our measurement is not in good *concordance* with our model, then we should discard it[2].

Let us see the definition of some physical quantities that we will use throughout this work and the dependency of some of them with the cosmological parameters of the ΛCDM

[2]Actually we can use only one probe to test cosmology. The measurement can depend on the model. But some parameters of the model will do a best fit than other

model.

2.2.1 Time interval and distance measures

Mathematically speaking the way how we determine the distance between two points in a non-euclidean space is given by the metric. The metric of a homogeneous and isotropic universe is known as the *The Friedman-Robertson-Walker* metric,

$$\boxed{ds^2 = -c^2dt^2 + a^2(t)\left[d\chi^2 + S_k^2(\chi)d\Omega^2\right],} \tag{2.18}$$

where ds is the space-time interval, t is the cosmic time, a the scale factor, χ the comoving radial distance, $d\Omega$ is the differential comoving angular coordinates that satisfies $d\Omega = d\theta^2 + \sin^2\theta d\Phi^2$ and

$$S_k(\chi) = \begin{cases} R_0 \sin\left(\frac{\chi}{R_0}\right) & (\kappa = +1) \\ \chi & (\kappa = 0) \\ R_0 \sinh\left(\frac{\chi}{R_0}\right) & (\kappa = -1). \end{cases} \tag{2.19}$$

Using this metric, the dynamics of the universe is determined by the Friedman equations. In the case of a universe formed by no interacting components and described as a perfect fluid, it is eq. (2.16).

To define distances and time intervals, we will define two independent events, first the emission of a photon from a distant source (t_2), and second the arrival of that photon to our frame of reference in Earth (t_1). For all the definitions of distance, we will assume null radial geodesics.

It is important to remember that the observable quantity in practice is the redshift and not the time or the distance. However, if we neglect peculiar velocities, we can link the redshift of galaxies with the scale factor, this last is associated with a particular time of the evolution history. The expression

$$\boxed{1 + z = \frac{1}{a}} \tag{2.20}$$

allow us to do this association.

Proper time interval

Lets introduce our first physical quantity the proper time, some time also call *cosmic time*. This is the time that an observer travelling with the photon would measure between the two events. From equation eq. (2.17) it is easy to see that the time interval can be written

in terms of the scale factor and the cosmological parameters as

$$dt = \frac{da}{aH_0E(a)} \tag{2.21}$$

$$\Delta t = \frac{1}{H_0}\int_{a_2}^{a_1} \frac{da}{aE(a)}, \tag{2.22}$$

where a_1 and a_2 are the scales factors at the times t_1 and t_2 respectively.

Co-moving distance

We are observing an universe with space-time in accelerated expansion, it results convenient to define a distance in the system of coordinates that grows together with this "Hubble flow", this distance is known as the comoving distance. Since photons travel along null geodesics, with $ds = 0$, from the metric eq. (2.18) we have

$$0 = -c^2dt^2 + a^2(t)d\chi^2 \rightarrow \boxed{d\chi = c\frac{dt}{a(t)}} \rightarrow d\chi = \frac{c}{H_0}\frac{da}{a^2E(a)}, \tag{2.23}$$

where in the last step we used eq. (2.21). Integrating between the two events, we get

$$\chi = \frac{c}{H_0}\int_{a_2}^{a1} \frac{da}{a^2E(a)}. \tag{2.24}$$

Proper distance

The proper distance is the physical distance between the two events measured by an hypothetical observer, for which both events happened simultaneously, i.e , the spatial geodesic at a fixed time, then from the metric eq. (2.18) we have

$$ds^2 = a(t)^2d\chi^2 \rightarrow \boxed{ds = a(t)d\chi}. \tag{2.25}$$

where we have neglected the angular part since the angle remain constant. It follows

$$d_p(t) = a(t)\int_0^{\chi} d\chi' = a(t)\chi, \tag{2.26}$$

which is in fact the definition of the scale factor. Using the radial parametrization[3] presented in appendix Awe have,

$$d_p(t) = a(t)\int_0^{r} \frac{dr'}{\sqrt{1-kr'^2}} \tag{2.27}$$

[3]This is $d\chi' = \frac{dr'}{\sqrt{1-kr'^2}}$

with the following solutions depending on the curvature

$$d_p(t) = a(t) \begin{cases} R_0 \sin^{-1}\left(\frac{r}{R_0}\right) & (\kappa = +1) \\ r & (\kappa = 0) \\ R_0 \sinh^{-1}\left(\frac{r}{R_0}\right) & (\kappa = -1). \end{cases} \tag{2.28}$$

However, we are interested in to find a relation between the proper distance and the cosmological parameters, so that we replace eq. (2.23) in eq. (2.25)

$$d_p = c \int_{t_2}^{t_1} dt = c\Delta t. \tag{2.29}$$

Therefore, as it is expected, the proper distance it is essentially the cosmic time interval times the speed of light. Then using eq. (2.22) we get an expression for the proper distance as a function of cosmological parameters

$$d_p = \frac{c}{H_0} \int_{a_2}^{a_1} \frac{da}{aE(a)}. \tag{2.30}$$

Angular diameter distance

Previous definitions are essentially relations between cosmological models and what we could believe it is measurable. We have already emphasized that our measurements will be model dependent. However, we have not explained how we are going to measure the proper distance. Well, the truth is that this is not possible to measure; we do know where the observer who sees those two events as simultaneous is. We also highlighted the importance of having different probes to test our cosmological models. Therefore, it is necessary to have more than one technique to measure distances. The solution to all these interrogatives is to look for intrinsic properties of sources and study variations of that property per unit of depth. Our best guess is to extrapolate physical quantities from a euclidean universe to one in accelerated expansion.

One of those intrinsic property could be for instance the size of the object. Lets suppose by the moment we have a *standard ruler* with a well known proper length l , if the ruler is aligned respect our line of sight we can use the small angle approximation to calculate the distance

$$d_A = \frac{l}{\theta}, \tag{2.31}$$

from the metric eq. (2.18) we can deduce that the arch length between the ends of the ruler at the time of emission t_2 is

$$l = a(t_2) S_k(\chi) \theta. \tag{2.32}$$

Then, we can extrapolate the euclidean conception of distance and define the angular diameter distance as

$$\boxed{d_A(z_1, z_2) = a(z_2) S_k\left(\chi(z_1, z_2)\right).} \tag{2.33}$$

In analogy to the radial distance defined before, this particular result suggest us to define S_k as the *comoving angular diameter distance*.

Luminosity distance

Another intrinsic property of an object that is of particular interest is the luminosity. If we know the luminosity L of an object and we measure its flux f, the position d_L of the source is given by the expression

$$f = \frac{L}{4\pi d_L^2}. \tag{2.34}$$

Lets introduce the effect that an expanding universe have over the measured flux. It is intuitive that we will measure a flux f_0, smaller than the emitted flux f_e, the relation between those fluxes is

$$f_0 = a^2(z_2) f_e, \tag{2.35}$$

where one factor a appears because the energy of the photons are reduced by the expansion, since $E_0 = aE_e$. And the other factor a is a consequence of the time delay between photons detentions, i. e. $\delta t_0 = \frac{\delta t_e}{a}$. Additionally, we need to generalize the concept of proper area of the sphere used to determine the flux. This is

$$A_p(z_1) = 4\pi S_k^2\left(\chi(z1, z2)\right), \tag{2.36}$$

Bearing these considerations in mind, we can extrapolate the euclidean conception of distance[4] and define the *luminosity distance* as

$$f = \frac{La^2(z_2)}{4\pi S_k^2\left(\chi(z1, z2)\right)} \rightarrow \boxed{d_L(z_1, z_2) = (1 + z_2) S_k\big(\chi(z1, z2)\big)} \tag{2.37}$$

from direct comparison of eq. (2.37) and eq. (2.33) we find the following relation between the angular diameter distance and luminosity distance

$$d_L(z_1, z_2) = (1 + z_2)^2 d_A(z_1, z_2), \tag{2.38}$$

simply, we can interpret this as objects are further away than what they should. Because of the redshift effect in the luminosity, it worth highlighting some additional points. First and most important, we are not assuming a specific geometry of the universe, we are relating the euclidean idea of distance with a more general conception related to our

[4] Being more accurate, this is the distance at the time of emission.

cosmological model. In other words, the fact that the dynamics of the universe can be described by a geometry further than the euclidean does not prevent us from measuring it with euclidean geometry, as it is usually done in any field of physics.

Second, notice that the additive property of the comoving radial distance is not valid, neither for the angular diameter distance, nor for the luminosity distances, i .e

$$\chi(z_1, z_2) = \chi(0, z_2) - \chi(0, z_1) = \chi(z_2) - \chi(z_1) \tag{2.39}$$

$$d_A(z_1, z_2) \neq d_A(z_2) - d_A(z_1) \tag{2.40}$$

$$d_L(z_1, z_2) \neq d_L(z_2) - d_L(z_1) \tag{2.41}$$

If the universe were flat, this linear property of the distance would be valid. Moreover, the angular and proper distance would be the same. There is another point here that we have not mentioned. It is that we do know the intrinsic luminosity of many objects. Although there are objects, as Cepheid and type IA supernovae, that can relate their luminosity with other periodic properties. Not all the objects have this property. Then, how can we get the distance of these objects? Well, in this case, we need to use the concept of magnitudes. By convention the apparent m and the absolute M magnitude of an object are

$$m = -2.5 \log_{10}(f/f_x) \qquad M = -2.5 \log_{10}(L/L_x), \tag{2.42}$$

where f is the bolometric flux, L the luminosity, $f_x = 2.53 \times 10^{-8}$ [watt $\times$ m^{-2}] and $L_x = 3.014 \times 10^{28}$ [watt]. It is important to emphasize the minus sign in both definitions, since they imply lower magnitudes for brighter objects, and higher for fainter. Now, in principle, we can measure both magnitudes. The next step is to relate both with the luminosity distance. This is done through eq. (2.34) and substracting both magnitudes. Usually, this difference is known as the *distance modulus*

$$m - M = 5 \log_{10}(d_L/1Mpc) + 25. \tag{2.43}$$

We can think the r.h.s is our model vector, while the l.h.s our data vector. Therefore this last expression represents a common expression to test cosmological models. Particularly, using probes as type IA supernovae.

2.3 Structure growth

When we observe the universe around our neighborhood, we do not see a homogeneous and isotropic universe at all. Instead, multiple regions with over-densities are observed.

Planets, solar systems, galaxies, and other forms of clustering are prevalent. This type of structure does not represent most of the constitutes of baryonic matter. Around 85% of the matter is in the form of intergalactic dust. However, it is interesting to try to figure out how has been the evolution of these structures. And try to find an explanation of these inhomogeneities. Since in large scales, the universe seems isotropic and homogeneous.

Observations of the CMB[5] obtained by surveys as Cobe, WMAP, and Planck. Showed that the temperature was homogeneous and isotropic in all the Celeste sphere, even for regions with angular separation larger than the last scattering surface separation[6], i.e., regions that were not in causal contact in the radiation era. So, how was it possible that two regions with no causal connection have the same temperature. Without going into the details, the solution to this problem is a period when space-time grew tremendously fast, which is known as the inflation period, so in this way, those regions at some point were causally connected, even though later they will not.

Additionally, in the CMB spectrum, there is temperature fluctuation ($\frac{\delta T}{T}$) around the fifth decimal point, two main reasons cause this. First, acoustics oscillation in the primordial plasma inside the horizon, Second temperature fluctuations outside the horizon, which were generated during the inflation. These small fluctuations are significant because they are the origin of the growth of the structure we see today. Actually, during the inflation, those perturbations inside the horizon did not grow because they were shielded by the expansion[7], and in the radiation era they were shielded by the radiation pressure[8]. Therefore, fluctuations that origin the structures come from those modes that were outside the horizon, before the last scattering. They later enter in the horizon and began to grow by gravitational instability (see appendix C).

2.3.1 Linear perturbation theory

Although we have been working with a uniform and isotropic universe, the truth is that in small scales, there are many inhomogeneities. Some practical examples of these inhomogeneities are you in comparison with the air surrounding, planets in the solar system, galaxies in the local group, and so on.

Unfortunately, no theory can predict in which region there will be more or less matter, instead, we treat this problem statistically, then we are interested into find a probability function that describe the distribution of matter. For this porpoise, it is convenient to define the over-density field

$$\delta(\overrightarrow{x},t)=\frac{\rho_m(\overrightarrow{x},t)-\bar{\rho}_m(t)}{\bar{\rho}_m(t)}. \tag{2.44}$$

[5]This corresponds to the best black body ever measured.
[6]this corresponds today to angular separation higher than around one degree
[7]Mathematically speaking, the power spectrum was of Harrison Zeldovich
[8]This includes a transfer function

This definition is telling us that where there are denser regions in comparison with the mean (structures), $\delta(\overrightarrow{x}, t)$ is positive. And when there is a lack of matter (voids) $\delta(\overrightarrow{x}, t)$ is negative. If we model the universe as a fluid, and we include small perturbation, we find the following differential equation for the over-density

$$\ddot{\delta} + 2H\dot{\delta} - 4\pi G\bar{\rho_m}\delta = c_s^2\nabla^2\delta + \sigma\nabla^2\delta S \tag{2.45}$$

one interesting property in this differential equation if perturbations are adiabatic, is that there are not spatial derivative, neither coefficients that depends on the position explicitly, meaning that the over-density is stationary in the comoving frame. This property suggests that we can define a function to propagate from primordial over-densities to other particular time as a independent and involving function. This particular function is known as the *linear Grow factor*

$$\delta(\chi, a) = D(a)\delta_p(\chi). \tag{2.46}$$

The statistical properties of the over-density are fully determined by the *matter power spectrum* $P_\delta(k)$, defined as (see appendix F)

$$(2\pi)^3\delta_D^3(\overrightarrow{k} - \overrightarrow{k}')P_\delta(k) = \langle\delta_{\mathbf{k}}\delta_{\mathbf{k}'}\rangle, \tag{2.47}$$

where each $\delta_{\mathbf{k}}$ is a Fourier mode of the over-density field, i.e are the coefficients of the expansion of the over-density field in the Fourier base,

$$\delta(\mathbf{x}, t) = \sum \delta_{\mathbf{k}}(t)e^{i\mathbf{k}\cdot\mathbf{r}} \tag{2.48}$$

$$\delta_{\mathbf{k}}(t) = \frac{1}{(2\pi)^{3/2}}\int \delta(\mathbf{x}, t)e^{-i\mathbf{k}\cdot\mathbf{r}}d^3x \tag{2.49}$$

It is out of the scope of the present work to prove that the matter Power spectrum right after the epoch of inflation was proportional to the wave vector, $P_{\delta,p}(k) = A_s k$. In general we can extend this and go from the power spectrum after inflation to the Power spectrum in other moment using the *transfer function* T(k,z)

$$P_\delta(z, k) = A_s k^{n_s}T^2(k, z), \tag{2.50}$$

where n_s is another cosmological parameter, known as the spectral index. The transfer function can be split in two parts to include the redshift dependence, the first of this parts is the growth factor and the second the *scale function*

$$T(k, z) = \frac{D(z)}{D(z = 0)}a(z)T(k). \tag{2.51}$$

However, equation eq. (2.50) does not describe the power spectrum fully. In appendix C we have considered only linearised equation, then to include no linear effects and additional term should be included.

Chapter 3

Weak lensing formalism

In general terms, we want to study the problem of dispersion of a light beam passing nearby a distribution of mass. Unlike, scattering theory, here we will not be interested in changes of energy that the light beam can suffer. Instead, the interest is on how are the changes in the shape of background galaxies. To study this problem, we will discuss first the deflection angle, which initially represents our first guess of one observable. The deflection angle contents all the information about the gravitational potential generated by the lens. Later we will see that in spite of not being observed, the deflection angle connects through the lens equation and the lensing potential, with more realistic observables, the shear, and the convergence, which are estimated in a statistical sense. Finally, it is presented the shear two-point correlation function, which will be the fundamental function containing all the cosmological information, and from which the present work would be based on.

3.1 The deflection angle

In the eighteen century, Cavendish did a calculation for the deflection of a light corpuscle, passing by a point particle with mass M. Its calculation lead to the the expression

$$\delta\theta_{class} = \frac{2MG}{bc^2}, \tag{3.1}$$

where G is the Newton's constant, b the impact parameter and c the speed of light. Almost two centuries later, Einstein's calculation using general relativity, led to a modification in the deflection of a point source by a factor of two (see section D.5).

$$\delta\theta = \frac{4MG}{bc^2} \tag{3.2}$$

The previous equation can be generalized when we have a spherical distribution of mass, in appendix D, we prove that under this assumption, the deflection angle can be written

as:

$$\boxed{\overrightarrow{\delta\theta} = \frac{2}{c^2}\int_C \nabla_\perp \Phi ds.} \tag{3.3}$$

In other words, the deflection angle is the integral along photon's trajectory, of the variation of the Newtonian potential Φ in the perpendicular direction of the path. Given that scalar potentials also satisfy the superposition principle. We conclude that the total deflection angle is the vectorial sum of each deflection angle produced by a spherically distributed mass. By the moment we will not worry about the distribution of lens, we will treat this problem in a further section.

3.2 The lens equation

We are interested in extracting physical information of the lens from measuring distortions in the source. In the previous section, we saw that the deflection angle is related to the Newtonian potential of the lens. Thus, somehow, we could estimate the mass of the lens if we were able to measure the deflection angle. Let's suppose by the moment that astronomers were able to figure out how to measure the actual and apparent position of a source. We are interested in finding a relation between these two observables with the deflection angle.

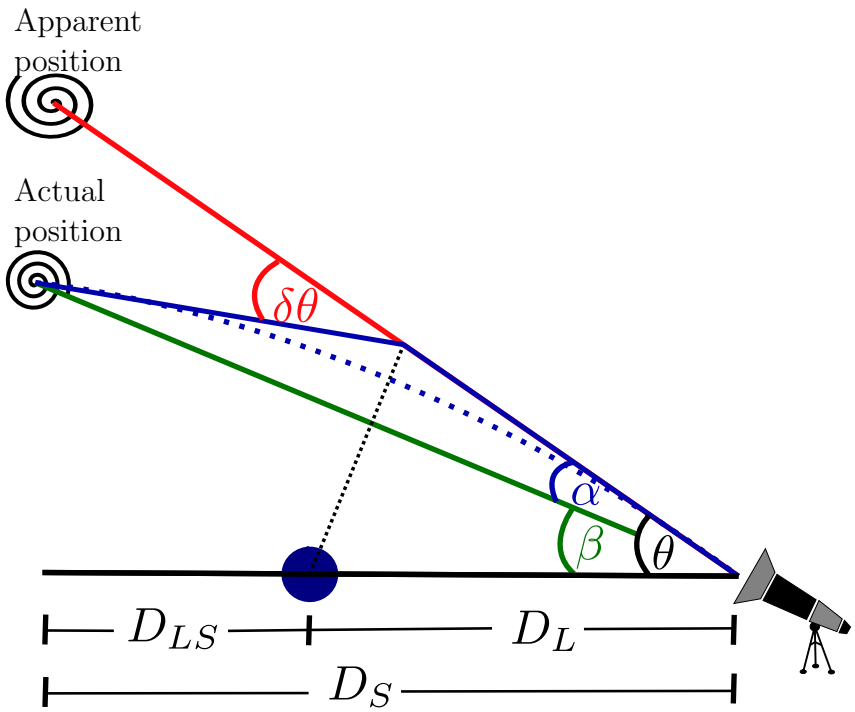

Figure 3.1: *Diagram of the deflection of a light beam traveling from a galaxy located at β, but observer at θ, because of a lens located at a distance D_L from the observer deflect its trajectory (blue dashed line)*

We can treat this problem using Euclidean geometry, and the effect of an expanding universe will be included in the dependence of the distances with cosmological parameters involved in our problem, as we will see later. From fig. 3.1 we can deduce the apparently simple relation

$$\boxed{\vec{\beta} = \vec{\theta} - \vec{\alpha}(\vec{\theta}).} \tag{3.4}$$

This equation is known as the *lens equation*. Where $\vec{\beta}$ is the actual angular position of the source, $\vec{\theta}$ is the apparent angular position and $\vec{\alpha}$ is the reduced deflection angle. By looking at fig. 3.1, it seems unnecessary defining vectors in the lens equation. If we have only one lens, the apparent actual positions of the source will be in the same plane as the observer; more than one angular parametrization for only one plane would seem excessive. In practice, this is not always true because the path of the photons can be deflected by more than one lens. Thus, the angles represent different polar parameterization of different planes. For instance, $\hat{\beta}$ represents the polar unitary vector of the plane joining the observer the lens and the actual position of the source, $\hat{\theta}$ the polar unitary vector of the plane joining the observer the lens and the apparent position of the source, And $\hat{\alpha}$ the polar unitary vector of the plane joining the observer and the real and apparent position of the source. Thus, although the magnitudes of these vectors are angular separations, they can not bee added as scalars because objects can be in different planes.

The eq. (3.4), despite the simple form, it contents a lot of information. First, notice that this is not a linear equation since the reduced deflection angle depends on θ. How

large will be the tilt depends on how so close the photons passes by the lens, i.e., $D_L\theta$. Additionally, there could be multiple solutions, i.e, for each actual angular position of the source $\overrightarrow{\beta}$, multiple values of the apparent angular position $\overrightarrow{\theta}$ satisfy eq. (3.4). Therefore, this equation describes lensing in general, including multiple images.

In the deduction of the deflection angle, we have not included $\delta\theta$, which is the variable that carries out the physical information of the lens. Hence, we need to relate it with the reduced deflection angle $\overrightarrow{\alpha}$. To find this relation we need first to clarify, that fig. 3.1 is an exaggerated diagram, all angles involved in the problem are very small, and the distance travelled by the light to the point of maximum approach can be approximated to D_{LS}. In other words, the triangle formed by the lens, the point of maximum approach and the observer is approximately rectangle, bearing this consideration in mind we have the following approximation:

$$\overrightarrow{\theta}\, D_s = \overrightarrow{\delta\theta} D_{LS} + \overrightarrow{\beta}\, D_s \tag{3.5}$$

$$\overrightarrow{\theta} = \overrightarrow{\delta\theta}\frac{D_{LS}}{D_s} + \overrightarrow{\beta} \tag{3.6}$$

Finally comparing with eq. (3.4) we find:

$$\boxed{\overrightarrow{\alpha} = \overrightarrow{\delta\theta}\frac{D_{LS}}{D_s}} \tag{3.7}$$

3.3 Some useful approximations

In the deflection angle eq. (3.3), there is a dependency on the photon's path and the separation between the photon and the lens. The full problem would demand to have a parametrization for the path and an additional strategy to determine the separation between the lens and the photon. To avoid these complications, we will do some approximations in eq. (3.3) and particularly in the Newtonian potential.

The Born's approximation

To illustrate our first approximation, let's call briefly a more general system, where unlike our system of one lens, we will have a set of lenses distributed along the photon's path. In fig. 3.2, we depict how it would be the trajectory of the photon produced by this system. The *Born's approximation* assumes that the path in the line integral of the potential is approximately equal to the unperturbed path, which corresponds to the line of sight. [1]

[1] This corresponds to the first order used in the iterative relation of the perturbed wave function, used in atomic and nuclear physics, where the zero-order is the wave function of a free particle. This is the original meaning of Born's approximation. But now, instead of talking of the wave function, we use the classical idea of the trajectory of the photon.

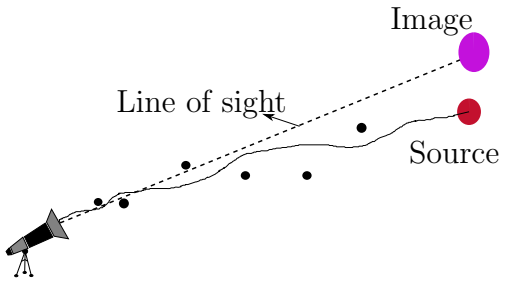

Figure 3.2: *Diagram of the Born's approximation, where we assume that the path that photon travel (jagged curve) is equal to the line of sight*

Consequently, eq. (3.3) becomes

$$\boxed{\overrightarrow{\delta\theta} = \frac{2}{c^2}\int_{s(z=0)}^{s(z_{\mathrm{OBS}})} \nabla_{\perp}\Phi ds.} \tag{3.8}$$

where s is a coordinate along the line of sight.

Thin lens approximation

Although Born's approximation simplifies a lot our problem, the deflection angle (see eq. (3.8)) still depends on the perpendicular direction to the line of sight and the separation from the lens to the photon $\left|\overrightarrow{r} - \overrightarrow{r}'\right|$. We are interested in finding a relation between these dependencies and θ since it is directly related to measurements. In this sense, we need to introduce the thin lens approximation, i.e., we will assume that our Newtonian potential acts mainly in the neighborhood of the mass; hence, contributions in other regions will be negligible. This approximation is reasonable given that the size of a lens is much smaller than the distance light has to travel to reach us. Keeping this in mind, we now can write the separation from the lens to the photon as

$$\boxed{\overrightarrow{r} - \overrightarrow{r}' \approx D_L\,\overrightarrow{\theta}\,.} \tag{3.9}$$

In fig. 3.3 is presented a diagram to illustrate this, we have used the variable θ to determine the position of the photon. Note this θ is different from the one that describes the apparent position of the source, but in this thin lens regime, those two variables are essentially the same. Furthermore, notice that the arguments we used to find eq. (3.7) are necessarily the same that those in this approximation, so we have already used it without making it explicit. Additionally, we can rewrite the gradient in the perpendicular direction $\nabla_{\perp}$ in terms of the gradient in the direction of the angular position ∇_{θ}. From curvilinear coordinates theory we know,

$$\nabla = \hat{x}\partial_x + \hat{y}\partial_y + \hat{z}\partial_z = \frac{\hat{q}_j}{h_j}\partial_{q_j} = \frac{\hat{\theta}}{h_\theta}\partial_\theta + \frac{\hat{y}}{h_y}\partial_y + \frac{\hat{z}}{h_z}\partial_z, \tag{3.10}$$

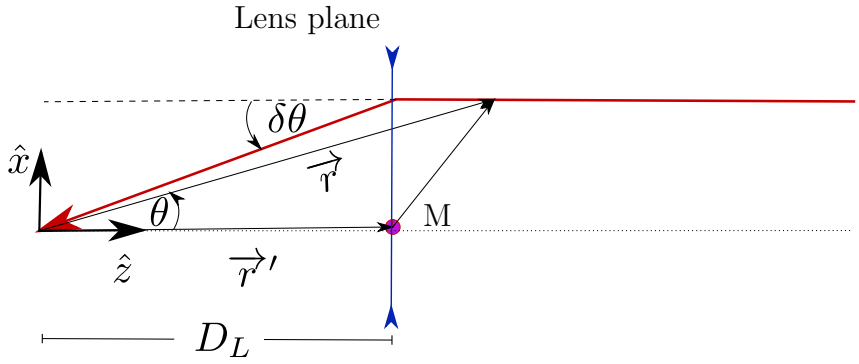

Figure 3.3: *Diagram of the thin lens approximation.*

where $\hat{q}_j$ are the unitary vectors of the curvilinear coordinates and $h_j = \left|\partial\vec{r}/\partial q_j\right|$. In our case, we want to change only one coordinate, so our equation of transformation

$$x = D_L\theta \quad , \quad y = y \quad , \quad z = z \tag{3.11}$$

lead to

$$h_\theta = D_L \quad , \quad h_y = 1 \quad , \quad h_z = 1 \tag{3.12}$$

and

$$\boxed{\nabla_\perp = \hat{x}\partial_x = \frac{\hat{\theta}}{D_L}\partial_\theta = \frac{1}{D_L}\nabla_\theta.} \tag{3.13}$$

Finally, the deflection angle using Born's and thin lens approximation, is

$$\boxed{\vec{\delta\theta} = \frac{2}{c^2 D_L}\int_{s(z=0)}^{s(z_{\rm OBS})} \nabla_\theta\Phi(D_L\theta, s)ds.} \tag{3.14}$$

3.4 The lensing potential

Now, we are interested in quantifying the capability to produce lensing of a structure of the universe ("optical system"), using certain characteristic properties, as the location of the source and lens on the line of sight. To do this, we first write the reduced deflection angle, eq. (3.7), using all the approximations presented in the previous section, and summarized in eq. (3.14)

$$\vec{\alpha} = \frac{D_{LS}}{D_S}\vec{\delta\theta} = \frac{2D_{LS}}{c^2 D_S D_L}\int \nabla_\theta\Phi(D_L\theta, s)ds. \tag{3.15}$$

inverting the order of the gradient and the integral,

$$\vec{\alpha} = \nabla_\theta\left[\frac{2D_{LS}}{c^2 D_L D_S}\int \Phi(D_L\theta, s)ds\right]. \tag{3.16}$$

The form of the previous equation is analogous to the second Newton's law, with the difference that instead of a Cartesian gradient, we have an angular gradient. This similarity suggests to define a characteristic potential for our problem, which we will call the *lensing potential*, although other authors prefer to call it the *deflection potential* or *shapiro potential* [23]

$$\boxed{\overrightarrow{\alpha} = \nabla_\theta \psi.} \tag{3.17}$$

From eq. (3.16) and eq. (3.17) we get

$$\boxed{\psi = 2\frac{D_{LS}}{c^2 D_S D_L}\int \Phi(D_L\theta, s)ds}, \tag{3.18}$$

this expression is valid for any single thin lens. The next step in our development is to write this potential in terms of the density, so that, it is convenient to study the Laplacian of the lensing potential, because Poisson's equation $\nabla^2\phi = 4\pi G\rho$ will allow us to introduce the density. In a similar way as described in section D.4, we can decompose the Laplacian as

$$\nabla^2 = \nabla_\parallel^2 + \nabla_\perp^2 = \nabla_\parallel^2 + \frac{1}{D_L^2}\nabla_\theta^2 = \partial_s^2 + \frac{1}{D_L^2}\nabla_\theta^2, \tag{3.19}$$

where ∂_s^2 is the laplacian along the line of sight. Then

$$\nabla_\theta^2 = D_L^2[\nabla^2 - \partial_s^2]. \tag{3.20}$$

Applying this operator to the lensing potential we have

$$\nabla_\theta^2\psi = 2\frac{D_{LS}D_L}{D_S c^2}\left[\int \nabla^2\Phi(D_L\theta, s)ds - \partial_s\Phi(D_L\theta, s)\mid_{\text{boundaries}}\right] \tag{3.21}$$

The r.h.s of the integral can be neglected, because the variation of the potential along the line of sight, far from the boundaries of an isolated lens is very small, in a good way this is a consequence of the thin lens approximation. Keeping this in mind and introducing Poisson's equation, the previous equation simplifies to

$$\nabla_\theta^2\psi = 2\times 4\pi G\frac{D_{LS}D_L}{D_S c^2}\left[\int \rho ds\right], \tag{3.22}$$

where the term in the brackets is defined as the *surface density*,

$$\boxed{\Sigma(\overrightarrow{\theta}) = \int \rho(\overrightarrow{\theta}, s)ds.} \tag{3.23}$$

The surface density is a physical quantity used typically in atmospheric physics. To have a physical intuition of its meaning, we can think in it as the projection of the mass of one object in a plane. Let's suppose, that the object is the Pisa's tower if we assume it has

uniform density and is not tilted, the projection in the plane perpendicular to the tower, will show a circle uniformly filled, meaning that the amount of mass contented is the same. On the other hand, if our object is the Pyramid of Giza, the projection in a plane parallel to the ground will be a square[2] not uniformly filled where the center will have larger values than the corners, meaning that most of the mass is located in the central column of the pyramid. For this reason, other authors prefer to call it *column density* since we can imagine the object as a set of columns whose height is proportional to his mass.

It is important to highlight that the surface density store all the information about the mass of the object. However, we lose information about the depth and the way how that mass is distributed[3]. For instance, if we divide the pyramid in two slices and we move one slice along the line of the projection, then the surface density will remain equal, unlike if we move the slice in another direction.

Additionally, we define the *critical surfaces density* as

$$\boxed{\Sigma_c = \frac{c^2 D_S}{4\pi G D_{LS} D_L},} \tag{3.24}$$

this constant is related to the regimes of weak and strong lensing. But, we will discuss it later, by the moment assume it is a constant, introduced to simplify the form of eq. (3.22). This constant is smaller when the source is closer to us (small D_S) and when the lens is not too far from the observer nor the source (not too large D_{LS} and D_L). In other words, the critical density gets its smallest value when the lens is halfway in between the source and the observer. Given these two definitions eq. (3.23) and eq. (3.24) of the surface densities, eq. (3.22) that relates the density with the lensing potential, now becomes into a Poisson's equation

$$\nabla^2_{\theta}\psi = 2\frac{\Sigma(\overrightarrow{\theta})}{\Sigma_c}. \tag{3.25}$$

Defining the ratio between surface densities as a new variable κ, which we will call *convergence*,

$$\boxed{\kappa(\overrightarrow{\theta}) = \frac{\Sigma(\overrightarrow{\theta})}{\Sigma_c},} \tag{3.26}$$

then the lens Poisson's equation becomes

$$\nabla^2_{\theta}\psi = 2\kappa(\overrightarrow{\theta}). \tag{3.27}$$

[2]Assuming that the base of the pyramid is a square

[3]This discussion is relevant in applications like mass maps

The solution to this Poisson's equation is

$$\boxed{\psi(\overrightarrow{\theta}) = \frac{1}{\pi}\int d^2\theta' \kappa(\overrightarrow{\theta}')ln\left|\overrightarrow{\theta} - \overrightarrow{\theta}'\right|.} \tag{3.28}$$

Every structure in the universe has a potential similar to eq. (3.28). To give a qualitative meaning to this potential, let's suppose the surface density is constant, in this case, the convergence becomes in a pre-factor of the integral, then we will have the maximum impact when $\kappa >> 1$ or $\Sigma_c << \Sigma(\overrightarrow{\theta})$, which from now we will distinguish as the *strong lensing condition*. The strongest effect happens when the lens is in the halfway between the observer and the source. Of course something similar can be said about the case $\kappa << 1$, i.e, the impact of the lens system is very small when $\Sigma_c >> \Sigma(\overrightarrow{\theta})$ and this is considered the *weak lensing condition*.

3.5 The distortion tensor and weak lensing observables

Only in very particular cases, where distances and dimensions of the lens are very well known, it is possible to measure the deflection angle. However, in most of the cases, we are interested in sources which could suffer multiple deviations, and it is technically impossible to measure such kind of physical quantity. Instead, it is needed to define another observable, which, as you can expect, would have a statistical foundation. These quantities are the *shear*, the *convergence* and the *magnification*. And it will be defined in this section. In the previous section, we have already given an introductory definition of the convergence as the density analogous of the Poisson equation, but instead of gravitational potential, we have now the lensing potential. We saw that the convergence is not only considered a *direct* measurement of the mass projected along the line of sight. But also it carries information of the cosmological model efficiency, since it depends directly on the angular diameter distances, which depends on cosmological parameters. Below we will give an geometrical interpretation for the convergence, and the weak lensing observables.

In practice, we observe a distorted image, and we want to know how was it originally before the light travels through the large scale structure. Mathematically, we can study the deformation of this image due to the tidal force as a mapping, i.e., our problem is a vectorial function

$$A : \Theta \subseteq \mathbb{R}^2 \to \mathbb{B} \subseteq \mathbb{R}^2, \tag{3.29}$$

where Θ represents the domain of the transformation and $\mathbb{B}$ the range. The coordinates θ_1 and θ_2 of the vectors in Θ represents the apparent position of the perturbed image. And the coordinates β_1 and β_2 of the vectors in $\mathbb{B}$ represent the actual position of the

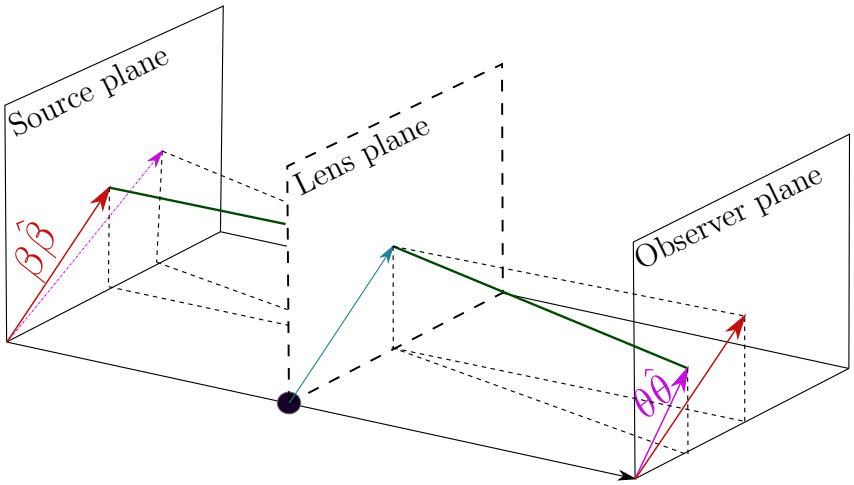

Figure 3.4: *Diagram of the transformation of one point in on the source plane, to one point in in the observer plane. Using curvilinear coordinates for each plane.*

unperturbed image. In fig. 3.4 is depicted how a particular lens can change the positions of two points that seem located at different positions in the source plane and the observer plane. The transformation given by eq. (3.29) is not valid in general. For instance, in the strong lensing regime, a particular vector in Θ could have assigned more than one vector in $\mathbb{B}$, this kind of mapping are not functions. However, in the weak lensing regime, we can apply this transformation, since the Liouville's theorem[4] guarantees that the surface brightness will be conserved, and processes of absorption, scattering by particles or pair creation are negligible, since most of the photon would travel essentially through the vacuum, i.e., we have

$$S^{\mathrm{OBS}}(\theta_i) = S^{\mathrm{SOURCE}}(\beta_i), \tag{3.30}$$

and this allows for to use eq. (3.29), which in components can also be written as

$$\beta_i = A_{ij}\theta_j \quad \text{where} \quad A_{ij} = \frac{\partial \beta_i}{\partial \theta_j}. \tag{3.31}$$

We are now interested in writing our *matrix of transformation* A, in terms of common quantities that reflect the deflecting power. From our discussion before, we can predict that this quantity is the lensing potential. Then to do this, we use eq. (3.4) and eq. (3.17),

$$A_{ij} = \frac{\partial}{\partial \theta_j}(\theta_i - \alpha_i) = \delta ij - \frac{\partial \alpha_i}{\partial \theta_j}, \tag{3.32}$$

$$\boxed{A_{ij} = \delta_{ij} - \frac{\partial^2 \psi}{\partial \theta_i \partial \theta_j}.} \tag{3.33}$$

As we can expect the δ_{ij} term will keep unaltered the coordinates of the mapping, so basically all the significant effects are in the second term, which we will call *the distortion*

[4]The number of particles per unit of volume is the phase space is constant in time

matrix

$$\Psi_{ij} = \frac{\partial^2 \psi}{\partial\theta_i \partial\theta_j} = \frac{\partial \alpha_i}{\partial\theta_j}, \tag{3.34}$$

since we are working with mapping from a plane to another plane, two coordinates will describe fully the position of any point in a particular plane. Then our distortion matrix can be written explicitly using a 2×2 matrix

$$\Psi = \begin{bmatrix} \kappa + \gamma_1 & \gamma_2 \\ \gamma_2 & \kappa - \gamma_1 \end{bmatrix}, \tag{3.35}$$

where we have used the definition of the convergence given by eq. (3.26) that can also be written as

$$\boxed{\kappa = \frac{1}{2}\left(\partial^2_{\theta_1}\psi + \partial^2_{\theta_2}\psi\right),} \tag{3.36}$$

and we define the *shear* as

$$\boxed{\gamma_1 = \frac{1}{2}\left(\partial^2_{\theta_1}\psi - \partial^2_{\theta_2}\psi\right),} \tag{3.37}$$

$$\boxed{\gamma_2 = \partial_{\theta_1}\partial_{\theta_2}\psi.} \tag{3.38}$$

As a consequence, in matrix representation the total transformation is

$$\boxed{A = \begin{bmatrix} 1 - \kappa - \gamma_1 & -\gamma_2 \\ -\gamma_2 & 1 - \kappa + \gamma_1 \end{bmatrix}.} \tag{3.39}$$

Before giving an interpretation to this *observable* let's introduce the *magnification*. We define the magnification as the unlensed and observed images fluxes ratio, in term of the surface brightness it is

$$\mu = \frac{S^{\text{OBS}}(\overrightarrow{\theta})dA(\overrightarrow{\theta})}{S^{\text{Source}}(\overrightarrow{\beta})dA(\overrightarrow{\beta})}, \tag{3.40}$$

using the conservation of the surface brightness eq. (3.30) we have

$$\mu = \left|\frac{dA(\overrightarrow{\theta})}{dA(\overrightarrow{\beta})}\right| = \left|\frac{\partial\overrightarrow{\theta}}{\partial\overrightarrow{\beta}}\right| = \left|A^{-1}\right|, \tag{3.41}$$

i.e, the magnification is the Jacobian of the transformation from the source plane to the image plane. However, our transformation is determined by eq. (3.33), so we can relate all the observable calculating the determinant of the matrix of transformation A. Consequently,

$$\boxed{\mu = \frac{1}{det(A)} = \left[(1-\kappa)^2 - \gamma^2\right]^{-1}} \tag{3.42}$$

Now, let's do some brief calculations to give an interpretation to all these observables.

Let's assume there is not shear in a lensed image, i.e, $\gamma_1 = \gamma_2 = 0$. Under these assumption eq. (3.33) becomes

$$\frac{\partial \beta_i}{\partial \theta_j} = \begin{bmatrix} 1-\kappa & 0 \\ 0 & 1-\kappa \end{bmatrix}, \tag{3.43}$$

which is clearly a linear equation whose solution with the contour condition $\vec{\beta}(\vec{0}) = \vec{0}$ is

$$\vec{\beta} = (1-\kappa)\vec{\theta}. \tag{3.44}$$

Keeping this result in mind, we can interpret geometrically the convergence with the help of fig. 3.5. There, it is depicted the case of a round source delimited by the black continuous circle, and the consequences of a positive and negative convergence, supposing the observed image would not be shifted from the center. In the case of positive convergence $\left|\vec{\theta}\right| > \left|\vec{\beta}\right|$ the image will seem bigger, while in the case of negative convergence $\left|\vec{\theta}\right| < \left|\vec{\beta}\right|$ it will seem smaller.

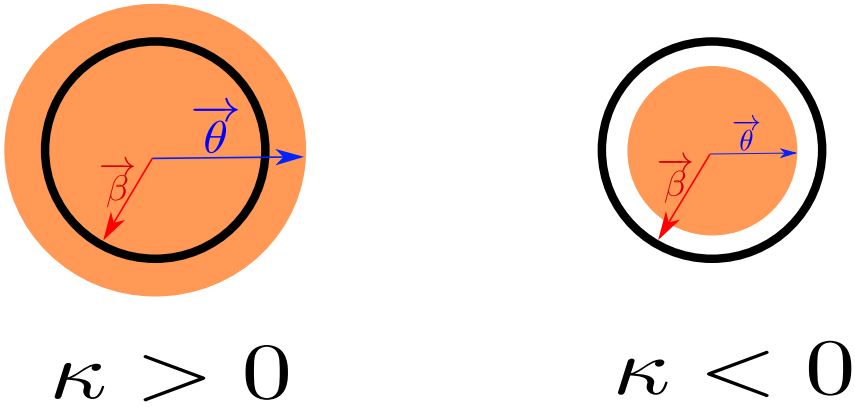

Figure 3.5: *Diagram of the convergence. In the absence of shear a round image keep round, however if the convergence is positive then the source will seem bigger (the l.h.s) or with larger radius. While if the convergence is negative the observed image is smaller.*

Next, we interpret the shear component. Let's suppose this time we do not have convergence either second component of shear, i.e., $\kappa = 0$ and $\gamma_2 = 0$, under this assumption the transformation matrix eq. (3.33) lead to

$$\frac{\partial \beta_i}{\partial \theta_j} = \begin{bmatrix} 1-\gamma_1 & 0 \\ 0 & 1+\gamma_1 \end{bmatrix}, \tag{3.45}$$

which is clearly a set of linear equations whose solution with the contour condition $\vec{\beta}(\vec{0}) = \vec{0}$ are

$$\beta_1 = (1-\gamma_1)\theta_1 \qquad \beta_2 = (1+\gamma_1)\theta_2. \tag{3.46}$$

If we consider the same case than before, where the source image is round, then we have the constrain $\beta_1^2 + \beta_2^2 = \beta^2 = \text{cte}$. It follows then that the observed shape satisfies the

equation

$$(1-\gamma_1)^2\theta_1^2 + (1+\gamma_1)^2\theta_2^2 = \beta^2, \tag{3.47}$$

which is clearly the equation of the ellipse. Reorganizing, to the traditional way we have

$$\left(\frac{\theta_1}{\beta(1-\gamma_1)^{-1}}\right)^2 + \left(\frac{\theta_2}{\beta(1+\gamma_1)^{-1}}\right)^2 = 1, \tag{3.48}$$

where we can see that the semi-minor and semi-major axis are $a = \left|\beta(1-\gamma_1)^{-1}\right|$ and $b = \left|\beta(1+\gamma_1)^{-1}\right|$. Then the sign of γ_1 determine if the semi-major is over θ_1 axis or θ_2. This result is depicted in fig. 3.6.

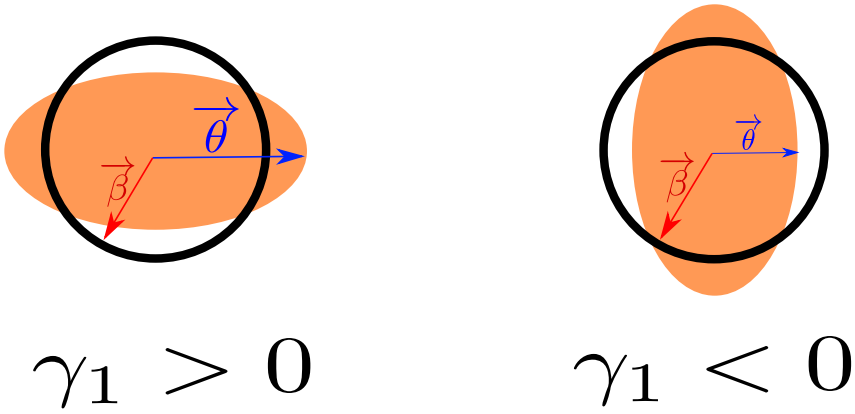

Figure 3.6: *Diagram of the first shear component. In the absence of γ_2 and κ, a round image does not keep round, it becomes elliptical and the semi-major axis depends on the sign of γ_1. If γ_1 is positive then the source will seem elliptical with semi-major axis over the θ_1 axis. While if γ_1 is negative the observed elliptical image has semi-major axis over θ_2 axis .*

The following quantity it worths to observe is the eccentricity of the ellipse. It somehow quantifies the stretching produced by lensing. By definition we have

$$\text{eccentricity} = \sqrt{1-\frac{b^2}{a^2}} = \sqrt{1-\left(\frac{1-\gamma_1}{1+\gamma_1}\right)^2} = \frac{2\sqrt{|\gamma_1|}}{|1+\gamma_1|}. \tag{3.49}$$

Then we can conclude that the stretching is maximum when $\gamma_1 = 1$ and we recover the round shape when $\gamma_1 = 0$, as expected. Besides, if $-1 < \gamma_1 < 1$, we always will observe an ellipse and no other conical section.

Let's now see the geometrical meaning of the second component of the shear γ_2, similarly to the previous cases we set $\gamma_1 = 0$, and $\kappa = 0$, the matrix of transformation is

$$\frac{\partial\beta_i}{\partial\theta_j} = \begin{bmatrix} 1 & -\gamma_2 \\ -\gamma_2 & 1 \end{bmatrix}, \tag{3.50}$$

and we end up with the following linear system of equations,

$$\frac{\partial\beta_1}{\partial\theta_1} = 1 \quad \frac{\partial\beta_1}{\partial\theta_2} = -\gamma_2 \quad \frac{\partial\beta_2}{\partial\theta_2} = 1 \quad \frac{\partial\beta_2}{\partial\theta_1} = -\gamma_2. \tag{3.51}$$

It is easy to see the solution using the Anzatz $\beta_i = A_i\theta_1 + B_i\theta_2$, then using the contour condition $\overrightarrow{\beta}(\overrightarrow{0}) = \overrightarrow{0}$ we have

$$\beta_1 = \theta_1 - \gamma_2\theta_2 \quad \beta_2 = \theta_2 - \gamma_2\theta_1, \tag{3.52}$$

follows immediately another ellipse equation,

$$\beta^2 = (\theta_1 - \gamma_2\theta_2)^2 + (\theta_2 - \gamma_2\theta_1)^2. \tag{3.53}$$

However, this one in particular is a rotated one, then it result more convenient to write it in the form of eq. (E.2).

$$\beta^2 = (1+\gamma_2^2)\theta_1^2 - 4\gamma_2\theta_1\theta_2 + (1+\gamma_2^2)\theta_2^2 \tag{3.54}$$

Comparing with eq. (E.8) we have

$$\begin{cases} b^2\cos^2\phi + a^2\sin^2\phi & = (1+\gamma_2^2) \\ \sin(2\phi)(b^2-a^2) & = -4\gamma_2 \\ b^2\sin^2\phi + a^2\cos^2\phi & = (1+\gamma_2^2) \\ a^2b^2 = \beta^2. \end{cases} \tag{3.55}$$

where ϕ is the rotation angle measure from θ_1 to θ_1', and a and b are the semi-minor and semi-major axis. From the first and the third equation in eq. (3.55) we get

$$a^2(\cos 2\phi) = b^2(\cos 2\phi), \tag{3.56}$$

if $\cos 2\phi$ is not null, then we have $a = b$ and from the second equation $\gamma_2 = 0$, which is not more than the trivial solution where our source image keep round. We are interested in the not trivial solution, it occurs when $\cos 2\phi = 0$, i.e.,

$$\phi = \pm\frac{\pi}{4}, \pm\frac{3\pi}{4}. \tag{3.57}$$

Given these possible solutions let's see the possible orientation of the observed ellipse, when we have different γ_2 sings. In the case $\gamma_2 > 0$, if $b > a$ the second equation signs impose $\sin(2\phi) < 0$, i.e., $\phi = -\frac{\pi}{4}, \frac{3\pi}{4}$. If $a > b$, then $\sin(2\phi) > 0$, i.e, $\phi = \frac{\pi}{4}, -\frac{3\pi}{4}$. All the previous cases correspond to rotations of $\frac{\pi}{4}$ of the coordinate systems, but since ellipse are invariant under π radian rotations the other two rotations correspond to relabelling the semi-major and semi-minor axis. Actually the observed image keeps unaltered, it is an ellipse with his semi-major axis oriented $\frac{\pi}{4}$ respect to θ_1 axis. As depicted in fig. 3.7, a similar analysis can be done in the case of $\gamma_2 < 0$, and can be deducted that the observed

ellipse will have the semi-major axis rotated $-\frac{\pi}{4}$ respect to θ_1 axis.

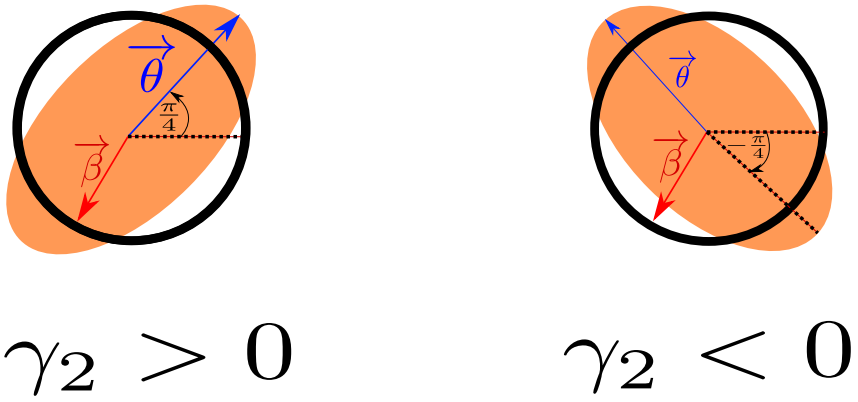

Figure 3.7: *Diagram of the second shear component. In the absence of γ_1 and κ, a round image does not keep round, it becomes elliptical and the major axis orientation depends on the sign of γ_2. If γ_2 is positive then the source will seem elliptical with semi-major axis rotated $\frac{\pi}{4}$ over the θ_1 axis. While if γ_2 is negative the observed elliptical image has semi-major axis rotated $-\frac{\pi}{4}$ over the θ_1 axis*

To calculate the eccentricity, let's replace the solutions of ϕ eq. (3.57) in eq. (3.55) to obtain

$$\begin{cases} b^2 + a^2 & = 2(1+\gamma_2^2) \\ b^2 - a^2 & = \mp 4\gamma_2 \\ a^2 b^2 = \beta^2. \end{cases} \tag{3.58}$$

solving for b^2 and a^2 we have

$$\begin{cases} b^2 & = (1 \mp \gamma_2)^2 \\ a^2 & = (1 \pm \gamma_2)^2, \end{cases} \tag{3.59}$$

where independently of the label we can conclude that the semi-major axis is $|1+\gamma_2|$ and semi-minor is $|1-\gamma_2|$. On the other hand, the eccentricity is

$$\text{eccentricity} = \sqrt{1 - \frac{(1\mp\gamma_2)^2}{(1\pm\gamma_2)^2}} = \sqrt{1 - \frac{(1\mp\gamma_2)^2}{(1\pm\gamma_2)^2}} = \sqrt{\frac{\pm 2\gamma_2}{(1\pm\gamma_2)^2}} = \frac{2\sqrt{|\gamma_2|}}{|1+\gamma_2|}. \tag{3.60}$$

Then, we can conclude that the stretching is maximum when $\gamma_2 = 1$, and we recover the round shape when $\gamma_2 = 0$ as expected. Besides, if $-1 < \gamma_2 < 1$ we always will observe an ellipse and no other conical section. In appendix E we present a deduction for the general case when both component of the shear are present.

To sum up, our starting point in this section was that lensing keeps unchanged the surface brightness[5]. However, not necessarily the shape of the image will keep the same. In the weak lensing regime, we can define a linear transformation to model this change in the shape of the galaxy. Then using the lens equation and the lensing potential,

[5] if you think in terms of points rather than energy, the surface brightness can be understood as surface density i.e. the number of points per area

we can determine the matrix of transformation. Which is entirely determined by two observable the convergence and the shear. We can think in the convergence as stretching or compression of the image in the radial direction (proportional scaling). And the shear takes round images and becomes them in ellipses, with only two components of the shear we have all the possible ellipses. Finally, the magnification represents a measure of the change in the area of the lensed image, since the surface brightness is conserved. It is important to notice that the shear γ is not easily related to the distribution of matter in the universe. On the other hand, the convergence κ is directly related to the mass distributions, moreover measuring the convergence can be more challenging than the shear. However, we will show that the two-point statistics of these two observable are the same, and we will be able to connect it with the matter power spectrum.

It is widespread to find variations of these fundamental observable in the literature [23–25]. We briefly present two of these variations. Firstly, it is common to define the *reduced shear* as

$$\boxed{g_i = \frac{\gamma_i}{1-\kappa}.} \tag{3.61}$$

This definition is convenient since we can separate the transformation matrix as

$$A = (1-\kappa)\begin{bmatrix} 1-g_1 & -g_2 \\ -g_2 & 1+g_1 \end{bmatrix}, \tag{3.62}$$

and additionally, as we will see later the reduced shear is intrinsically related with the concept of ellipticity and second moments of the surface brightness.

Secondly, it is the definition of the cross and tangential shear, eq. (E.20) in appendix E suggests us to use complex number notation and define the shear as

$$\boxed{\gamma = \gamma_1 + i\gamma_2 = |\gamma|\, e^{2i\phi}.} \tag{3.63}$$

Notice, that despite being using complex notation, we are still using a Cartesian frame of reference centered in the ellipse and with ϕ the rotation angle respect to the x-axis (or equivalently θ_1-axis). In application such as cluster lensing results convenient to rotate the frame of reference since we are measuring respect to the centre of the cluster. Let's characterize this rotation with the angle φ. As it is depicted in fig. 3.8 the rotation from the frame $(\hat{i}, \hat{j})$ to the frame $(\hat{i}_+, \hat{i}_\times)$ reference will be and angle $-(\frac{\pi}{2} - \varphi)$ respect to $\hat{i}$, however rotate the frame of reference clockwise is mathematically equivalent to rotate the galaxy counterclockwise, i.e, we can think that this change of frame of reference as an additional rotation in an angle of $\frac{\pi}{2} - \varphi$ of the galaxy. Therefore the complex shear can be written as

$$\boxed{\gamma_+ + i\gamma_\times = |\gamma|\, e^{2i(\phi+\frac{\pi}{2}-\varphi)} = -(\gamma_1 + i\gamma_2)e^{-2i\varphi},} \tag{3.64}$$

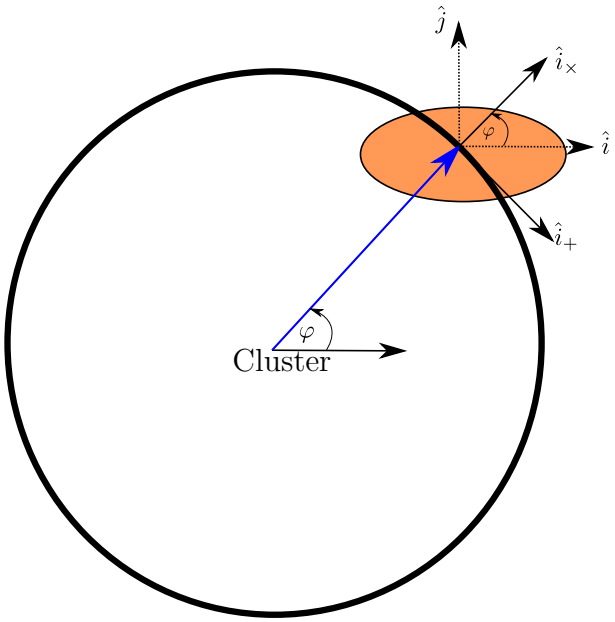

Figure 3.8: *Diagram to illustrate the change of coordinates respect to the cross and tangential frame of reference. Basically the change of coordinates can be thought as an additional rotation of* $\frac{\pi}{2} - \varphi$ *of the galaxy*

or explicitly in components as

$$\gamma_+ = -(\gamma_1 \cos 2\varphi + \gamma_2 \sin 2\varphi) \qquad \gamma_\times = -(\gamma_2 \cos 2\varphi - \gamma_1 \sin 2\varphi). \tag{3.65}$$

In fig. 3.9 is presented a set of examples of how change the values of the shear components depending on the orientation and the galaxy position. It is presented the comparison between the cross and the Cartesian frame of reference. Then we can see how in the case of $\varphi = \frac{\pi}{2}$ the two frame of reference are coincident, when $\varphi = 0$ the axis the sign is inverted, i.e $\gamma_+ = -\gamma_1$ and $\gamma_\times = -\gamma_2$. And in the case of $\varphi = \frac{\pi}{4}$, $\gamma_+ = -\gamma_2$ and $\gamma_\times = -\gamma_1$.

3.6 Extension to a lens distribution

We are now interested in extending our definitions to the case where we have more than one lens, i.e., there is a distribution of lenses along the line of sight. This is the whole goal of Cosmic shear analysis; by definition, it is the weak lensing effect by the large scale structure of the universe. Since the superposition principle is valid for the gravitational potential, from eq. (3.3), we can see that this property will also hold for the deflection angle, and also in the thin lens approximation for the reduced deflection angle. Besides eq. (3.17) also guarantees the lensing potential satisfies the superposition principle, and as a consequence, so do all the weak lensing observables. In fig. 3.10, we present an illustration of how we model the problem of a lens distribution as a set of thin lenses, where we have one set of angular vector for each lens where the lens equation keeps

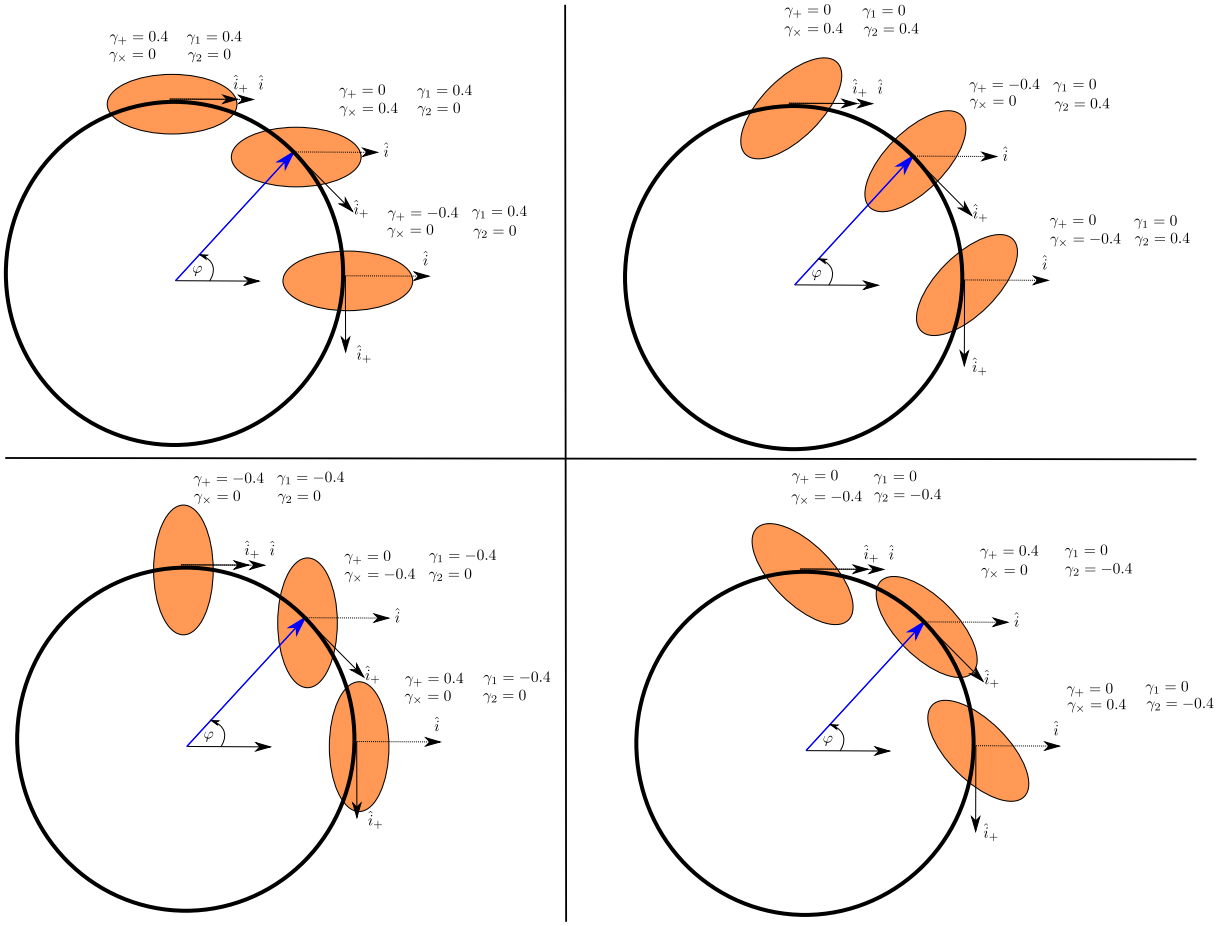

Figure 3.9: *Diagram to illustrate the different values of the shear components using the cross and Cartesian frame of reference*

true. The overall system satisfies the superposition principle. As a consequence, we can expect that the distribution of lenses can be replaced by only one lens representing the overall system; this is similar to the optical plane of a classical optical system. Therefore,

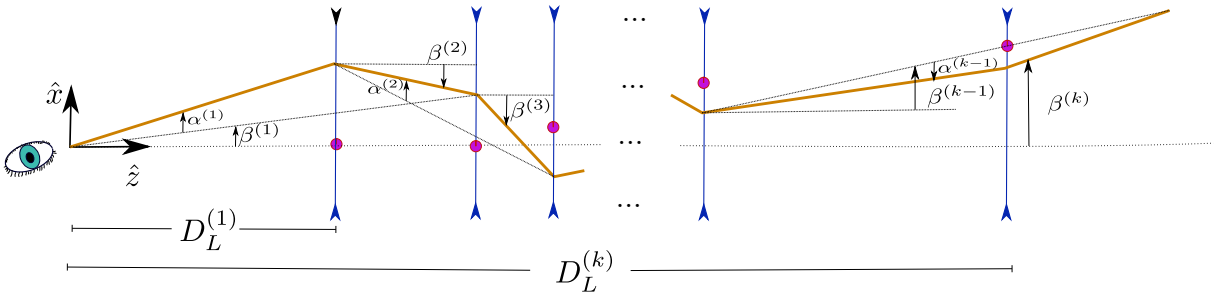

Figure 3.10: *Diagram to illustrate how we treat the problem of a lens distribution along the line of sight*

our general problem with more than one lens can be described by the quantities we have defined before. However, there is missing a last consideration, the substitution of Euclidean distances by comoving distances. This is a crucial step, because is here where we start to introduce our particular cosmological model. Let's start using the substitution

$$\frac{D_{LS}}{D_S D_L} \rightarrow \frac{S_K(\chi_s - \chi)}{S_K(\chi) S_K(\chi_s)}, \tag{3.66}$$

in eq. (3.18). We find the following expression for the called *effective lensing potential*

$$\boxed{\psi_{\text{eff}}(\chi_s) = \frac{2}{c^2} \int_0^{\chi_s} \frac{S_K(\chi_s - \chi)}{S_K(\chi_s) S_K(\chi)} \Phi d\chi.} \tag{3.67}$$

Where we return the prefactor inside the integral since it depends on the new integration variable. Consequently, from eq. (3.22) and eq. (3.27), we define the called *effective convergence* as

$$\kappa_{\text{eff}}(\theta, \chi) = \frac{4\pi G}{c^2} \int_0^{\chi_s} \frac{S_K(\chi_s - \chi) S_K(\chi)}{S_K(\chi_s)} a^2 \rho(S_K(\chi)\theta, \chi) d\chi. \tag{3.68}$$

We now want to write this expression in terms of the over-density field instead of the density. Using the critical density today eq. (2.10), we can deduce the equation

$$\bar{\rho} = \bar{\rho}_0 a^{-3} = \rho_{c0} \Omega_{m0} a^{-3} = \frac{3H_0^2}{8\pi G} \Omega_{m0} a^{-3}. \tag{3.69}$$

Ordering eq. (2.44) we came up with

$$\rho = (1 + \delta)\bar{\rho} = (1 + \delta) \frac{3H_0^2}{8\pi G} \Omega_{m0} a^{-3}. \tag{3.70}$$

Substituting in eq. (3.68) and simplifying we finally obtain

$$\boxed{\kappa_{\text{eff}}(\theta, \chi_s) = \frac{3H_0^2 \Omega_{m0}}{2c^2} \int_0^{\chi_s} \frac{S_K(\chi_s - \chi) S_K(\chi)}{S_K(\chi_s)} \left[1 + \delta(S_K(\chi)\theta, \chi)\right] \frac{1}{a(\chi)} d\chi.} \tag{3.71}$$

This is an extension of our initial definition of the convergence, with the difference that now we are using the comoving coordinates, which is more interesting from a cosmological perspective, and the over-density field instead of the density since it will be easier to link with the matter power spectrum. This previous expression considers only one source at comoving distance χ_s. A final consideration we need to do is to make a pondering considering all the sources at different redshift bins. Then, we need to introduce the redshift distribution of galaxies observed $p(z_s)$ along the line of sight [26]. It is in this step where we somehow are "projecting" all the different lenses to a plane. We define *the mean effective convergence* as

$$\boxed{\bar{\kappa}_{\text{eff}}(\theta, \chi) = \int_{\chi}^{\chi_H} \kappa_{\text{eff}}(\theta, \chi_s) p(\chi_s) d\chi_s,} \tag{3.72}$$

where χ is the comoving distance of a particular thin lens plane and χ_H is the comoving

horizon, i.e, the mean convergence at the position (θ, χ) is the projection of all the previous lenses the photons have passed by until reach the particular position. Therefore, the mean effective convergence in a particular direction θ on the sky is the projection until our location, i.e, $\chi = 0$ in eq. (3.72). Substituting eq. (3.71) in eq. (3.72) and changing the order of integration and the associated new limits we have

$$\bar{\kappa}_{\rm eff}(\theta) = \frac{3H_0^2\Omega_{m0}}{2c^2}\int_0^{\chi_H}\int_{\chi}^{\chi_H}\frac{S_K(\chi_s-\chi)S_K(\chi)}{S_K(\chi_s)}(1+\delta)\frac{1}{a}p(\chi_s)d\chi_s d\chi. \tag{3.73}$$

Defining the *lensing efficiency* $g(\chi)$ as

$$\boxed{g(\chi) = \frac{3H_0^2\Omega_{m0}}{2c^2a(\chi)}\int_{\chi}^{\chi_H}\frac{S_K(\chi_s-\chi)S_K(\chi)}{S_K}p(\chi_s)d\chi_s}, \tag{3.74}$$

the mean effective convergence can be written in the form

$$\boxed{\bar{\kappa}_{\rm eff}(\theta) = \int_0^{\chi_H} g(\chi)\left[1+\delta(S_K(\chi)\theta,\chi)\right]d\chi} \tag{3.75}$$

It is in terms of this mean effective convergence, that we will write what is known as the convergence power spectra, which is a second order statistics containing all the physical information of cosmic shear, and it is relevant since can be easily connected with the matter power spectra as we will see below.

3.7 Relation between Matter Power spectra and convergence

We have presented the definitions to introduce what might be is the most crucial relation in cosmic shear, to estimate cosmological parameters, *the convergence two-point correlation function*. This function is the link between weak lensing observables and a particular cosmology we are interested in testing. As we see in chapter 2, the matter power spectrum is a summary statistic that contents physical information of the evolution of the matter distribution in all the scales. If we somehow were able to model matter power spectra and also estimate it from data, we would be able to calculate the parameters of our particular cosmology. In the following section, we will see that the convergence two-point correlation function is directly related to the matter power spectra. Making cosmic shear one of the cleanest probes, since besides measuring straight pure gravitational information, we do not request another modeling, for instance, the ratio dark matter baryonic matter that is common in other cosmological probes. In fact from eq. (3.75) we can already see this connection between the convergence $\bar{\kappa}_{\rm eff}(\theta)$ and the over-density field $\delta(\chi)$

In appendix F, we present a full deduction of eq. (F.22), which is an equation relating

the power spectrum of a three-dimensional random field to his two-dimensional projection. We can see that eq. (3.75) is one particular example of a two-dimensional projection of the random field. Comparing with the procedure presented in eq. (F.22), the only difference with the labels used there is that in our case of interest, our random field is $1+\delta(S_K(\chi)\theta,\chi)$ and not $\delta(S_K(\chi)\theta,\chi)$. However, it is easy to see that both random fields have the same power spectrum and correlation function, since by definition $\left\langle \delta(S_K(\chi)\theta,\chi)\right\rangle = 0$. As a consequence, the eq. (F.22) is the one we are looking for

$$\boxed{P^{ij}_{\kappa\kappa}(l) = \int_0^{\chi_H} d\chi \frac{g_i(\chi)g_j(\chi)}{S_K^2(\chi)} P_\delta\left(k_\perp = \frac{l}{S_K(\chi)}, \chi\right)}. \tag{3.76}$$

It is important to recall two things. First our convergence power spectrum is actually using the mean effective convergence. Second, in the deduction of this equation was used the Limber's approximation, which basically establish that the weighting functions g_i and $S_K(\chi)$ do not vary much when the radial separation is smaller than a coherence distance which characterizes the scales where the matter power spectrum is null. And as a consequence only perpendicular modes of the matter power spectrum survive. This is a good approximation for small scales, but significant inaccuracies can appear at large scales.

3.8 Convergence and shear Power spectra

Continuing our theoretical construction, we now want to prove the equivalence between the convergence power spectrum and the *shear power spectrum*. We will see that these two functions correspond to the same statistical entity. This equivalence is fundamental since the convergence is not easily estimated while the shear is. Then in practice in cosmic shear, we use the shear power spectrum to do cosmological parameter estimation.

Let's start by finding an equation linking the shear and the convergence, and eliminating the lensing potential from eq. (3.68), eq. (3.37) and eq. (3.38). First we want to substitute eq. (3.28) in eq. (3.37) and eq. (3.38), before doing that, it is convenient to calculate all partial derivatives of the lensing potential.

$$\partial_{\theta_1}\psi = \frac{1}{\pi}\int d^2\theta' \kappa(\overrightarrow{\theta}') \frac{\theta_1 - \theta_1'}{\left|\overrightarrow{\theta} - \overrightarrow{\theta}'\right|^2} \tag{3.77}$$

$$\partial^2_{\theta_1}\psi = \frac{1}{\pi}\int d^2\theta' \kappa(\overrightarrow{\theta}') \frac{\left|\overrightarrow{\theta} - \overrightarrow{\theta}'\right|^2 - 2(\theta_1 - \theta_1')^2}{\left|\overrightarrow{\theta} - \overrightarrow{\theta}'\right|^4} \tag{3.78}$$

$$\partial^2_{\theta_2}\psi = \frac{1}{\pi}\int d^2\theta' \kappa(\overrightarrow{\theta}')\frac{\left|\overrightarrow{\theta} - \overrightarrow{\theta}'\right|^2 - 2(\theta_2 - \theta_2')^2}{\left|\overrightarrow{\theta} - \overrightarrow{\theta}'\right|^4} \tag{3.79}$$

$$\partial_{\theta_1}\partial_{\theta_2}\psi = -\frac{1}{\pi}\int d^2\theta' \kappa(\overrightarrow{\theta}')\frac{2(\theta_1 - \theta_1')(\theta_2 - \theta_2')}{\left|\overrightarrow{\theta} - \overrightarrow{\theta}'\right|^4} \tag{3.80}$$

Now, substituting in eq. (3.37) and eq. (3.38) we obtain

$$\gamma_1 = \frac{1}{\pi}\int d^2\theta' \kappa(\overrightarrow{\theta}')\frac{(\theta_2 - \theta_2')^2 - (\theta_1 - \theta_1')^2}{\left|\overrightarrow{\theta} - \overrightarrow{\theta}'\right|^4} \tag{3.81}$$

$$\gamma_2 = -\frac{1}{\pi}\int d^2\theta' \kappa(\overrightarrow{\theta}')\frac{2(\theta_1 - \theta_1')(\theta_2 - \theta_2')}{\left|\overrightarrow{\theta} - \overrightarrow{\theta}'\right|^4}, \tag{3.82}$$

this set of equation in complex notation are

$$\boxed{\boldsymbol{\gamma}(\overrightarrow{\theta}) = \frac{1}{\pi}\int d^2\theta' \kappa(\overrightarrow{\theta}')\boldsymbol{D}(\overrightarrow{\theta} - \overrightarrow{\theta}') \quad where \quad \boldsymbol{D}(\overrightarrow{\theta}) = \frac{\theta_2^2 - \theta_1^2 - 2i\theta_1\theta_2}{\left|\overrightarrow{\theta}\right|^4}.} \tag{3.83}$$

where we can notice that the shear is the convolution of the convergence with a kernel function **D**. The next step in our analysis is to write the shear power spectra using this link between convergence and shear. However, we need first to find the Fourier transform version, by definition of the Fourier transform of $\boldsymbol{\gamma}(\overrightarrow{\theta})$ is

$$\tilde{\gamma}(\overrightarrow{l}) = \int d^2\theta \gamma(\overrightarrow{\theta})e^{i\overrightarrow{\theta}.\overrightarrow{l}}. \tag{3.84}$$

Substituting eq. (3.83) we obtain

$$\tilde{\gamma}(\overrightarrow{l}) = \frac{1}{\pi}\int d^2\theta \int d^2\theta' \kappa(\overrightarrow{\theta}')\boldsymbol{D}(\overrightarrow{\theta} - \overrightarrow{\theta}')e^{i\overrightarrow{\theta}.\overrightarrow{l}}, \tag{3.85}$$

inverting the order of integration and using the substitution $\overrightarrow{\beta} = \overrightarrow{\theta} - \overrightarrow{\theta}'$

$$\tilde{\gamma}(\overrightarrow{l}) = \frac{1}{\pi}\int d^2\theta' \kappa(\overrightarrow{\theta}')e^{i\overrightarrow{\theta'}.\overrightarrow{l}} \int d^2\beta \boldsymbol{D}(\overrightarrow{\beta})e^{i\overrightarrow{\beta}.\overrightarrow{l}}, \tag{3.86}$$

hence the Fourier version of eq. (3.83) is

$$\tilde{\gamma}(\overrightarrow{l}) = \frac{1}{\pi}\tilde{\kappa}(\overrightarrow{l})\tilde{\boldsymbol{D}}(\overrightarrow{l}) \quad where \quad \tilde{\boldsymbol{D}}(\overrightarrow{l}) = \pi\frac{l_1^2 - l_2^2 + 2il_1l_2}{l^2} \tag{3.87}$$

which is expected given it is a convolution equation. Now, given eq. (F.8) we can write

the shear power spectrum $P_{\gamma\gamma}(\overrightarrow{l})$ as a function of its correlation function

$$(2\pi)^2\delta_D^2(\overrightarrow{l}-\overrightarrow{l}')P_{\gamma\gamma}(\overrightarrow{l})=\left\langle\tilde{\gamma}(\overrightarrow{l})\tilde{\gamma}^*(\overrightarrow{l}')\right\rangle, \tag{3.88}$$

inserting eq. (3.87) we have

$$(2\pi)^2\delta_D^2(\overrightarrow{l}-\overrightarrow{l}')P_{\gamma\gamma}(\overrightarrow{l})=\left\langle\tilde{\kappa}(\overrightarrow{l})\tilde{\kappa}^*(\overrightarrow{l}')T(\overrightarrow{l},\overrightarrow{l}')\right\rangle, \tag{3.89}$$

with

$$T(\overrightarrow{l},\overrightarrow{l}')=\frac{1}{l^2}\frac{1}{l'^2}\left[(l_1^2-l_2^2)(l_1'^2-l_2'^2)+4l_1l_1'l_2l_2'+2il_1'l_2'(l_1^2-l_2^2)-2il_1l_2(l_1'^2-l_2'^2)\right] \tag{3.90}$$

If we force $\overrightarrow{l}=\overrightarrow{l}'$, we have $T(\overrightarrow{l},\overrightarrow{l}')=1$, then the delta structure of eq. (3.89) impose

$$(2\pi)^2\delta_D^2(\overrightarrow{l}-\overrightarrow{l}')P_{\gamma\gamma}(\overrightarrow{l})=\left\langle\tilde{\kappa}(\overrightarrow{l})\tilde{\kappa}^*(\overrightarrow{l}')\right\rangle, \tag{3.91}$$

which is not other thing that the fundamental relation between the two point correlation function and the power spectrum. Finally we came up with

$$\boxed{P_{\gamma\gamma}(\overrightarrow{l})=P_{\kappa\kappa}(\overrightarrow{l}),} \tag{3.92}$$

which is one of the fundamental equations in cosmic shear. The shear power spectrum and the convergence power spectrum are the same. This is remarkable since we are now worried about only determining either the shear or the convergence. As we will later, usually, we choose the shear, given it is related to the ellipticities of the galaxies.

Notice that we use the simple convergence instead of the mean effective convergence, which is the real convergence we employ in the linking with the matter power spectrum. However, it can be demonstrated that eq. (3.83) holds for the mean effective versions of the convergence and shear.

Given that we have presented all the required tools, we finish this section giving what is known as the *Kaiser-Squires inversion*. Essentially, this method allows for to get the convergence from the shear; this is the inverse process of what we did to get eq. (3.83). Kaiser-Squires inversion has been relevant in weak lensing since this was one of the first ways to get the mass projection using weak lensing. So it is in the foundation of applications such as mass maps creation. Nowadays, this method is considered too noisy, but it worth to present it.

If we multiply eq. (3.87) by the complex conjugated of the convolution kernel $\tilde{\boldsymbol{D}}^*(\overrightarrow{l})$

and considering $\tilde{\boldsymbol{D}}^*(\overrightarrow{l})\tilde{\boldsymbol{D}}(\overrightarrow{l}) = \pi^2$ we obtain the inverse relation

$$\tilde{\kappa}(\overrightarrow{l}) = \frac{1}{\pi}\tilde{\gamma}(\overrightarrow{l})\tilde{\boldsymbol{D}}^*(\overrightarrow{l}) \tag{3.93}$$

using again the convolution theorem we can find a useful expression in real space

$$\boxed{\kappa(\overrightarrow{\theta}) = \kappa_0 + \frac{1}{\pi}\int d^2\theta' \tilde{\boldsymbol{D}}^*(\overrightarrow{\theta} - \overrightarrow{\theta}')\gamma(\overrightarrow{\theta}'))} \tag{3.94}$$

where κ_0 is a emerging constant of integration that reflects the fact that in the absence of shear we can have a constant surface density.

3.9 Cosmic Shear

The cosmic shear analysis is usually done on second-order statistical measurements of the distortion field, such as the shear Two point correlation function (2PCF). Since it is an observable that can be estimated by multiplying the ellipticities of galaxies pairs and averaging, the shear 2PCF is a useful tool to estimate the cosmological parameters. The shear 2PCF is defined by considering pairs of position ϑ and $\vartheta + \theta$. First, we define the tangential and cross-component of the shear $\gamma = \gamma_1 + i\gamma_2$ at position ϑ for this pair as

$$\gamma_t = -\Re(\gamma e^{-2i\phi}); \qquad \gamma_\times = -\Im(\gamma e^{-2i\phi}), \tag{3.95}$$

where ϕ is the polar angle of the separation θ. Then, we define the two shear correlation functions as

$$\xi_\pm(\theta) = \langle\gamma_t\gamma_t\rangle(\theta) \pm \langle\gamma_\times\gamma_\times\rangle(\theta) = \frac{1}{2\pi}\int_0^\infty d\ell\,\ell\,P_\kappa(\ell)\,J_{0,4}(\ell\theta), \tag{3.96}$$

where $J_{0,4}$ are the Bessel function related to the '+'('-') correlation function, P_κ is the power spectrum of the projected density field given by eq. (3.76), which depends on the cosmological parameters. And angle brackets will denote an average over all pairs separated by a distance $\boldsymbol{r}$, i.e.,

$$\big\langle a(\mathbf{x}+\mathbf{r})b(\mathbf{x})\big\rangle = \langle ab\rangle = \frac{1}{N_{\text{pairs}}}\sum_{N_{\text{pairs}}} a(\mathbf{x}+\mathbf{r})b(\mathbf{x}) \tag{3.97}$$

It is also important to say that the cross correlation we expect to vanish

$$\xi_\times(\theta) = \langle\gamma_t\gamma_\times\rangle \to 0 \tag{3.98}$$

This is because it is associated to B-modes, although parity arguments can be used as well.

On the other hand, we can also get the 2PCF from a shear catalog according to the estimator

$$\hat{\xi}_{\pm}(\theta) = \frac{\sum_{ij} w_i w_j (\epsilon_{t,i}\epsilon_{t,j} \pm \epsilon_{\times,i}\epsilon_{\times,j})}{\sum_{ij} w_i w_j}, \tag{3.99}$$

where the sum extends over pairs of galaxies (i,j) separated by a angular distance θ. Each galaxy has a measured ellipticity ϵ_i, and a weight w_i related to the measured uncertainty.

This is the most used estimator thanks to the approximation $\epsilon_i = \epsilon_i^s + \gamma(\theta_i)$ then the expectation values of ellipticities and shears are the same:

$$\langle \epsilon_{ti}\epsilon_{tj} \rangle = \Big\langle (\epsilon_i^s + \gamma_t(\theta_i)(\epsilon_j^s + \gamma_t(\theta_j) \Big\rangle = \langle \gamma_t \gamma_t \rangle \tag{3.100}$$

$$\langle \epsilon_{\times i}\epsilon_{\times j} \rangle = \Big\langle (\epsilon_{\times i}^s + \gamma_\times(\theta_i)(\epsilon_{\times j}^s + \gamma_\times(\theta_j) \Big\rangle = \langle \gamma_\times \gamma_\times \rangle \,. \tag{3.101}$$

In the absence of intrinsic alignment is expect no correlation between the intrinsic ellipticity and the shear, then $\langle (\epsilon_{\times i}^s \epsilon_{\times j} \rangle \to 0$. However, in the practice this does not happen and what we can do to neglect this term is avoid correlation of galaxies in the same redshift bin. Another advantage of this estimator is that not information about the mask is required.

It is also convenient write this correlation function in terms of complex correlation in the following way:

$$\xi_+ = \langle e^* e \rangle = \big\langle (e_{\tan} - i e_\times)(e_{\tan} + i e_\times) \big\rangle \tag{3.102}$$
$$\Re(\xi_+) = \langle e_{\tan} e_{\tan} \rangle + \langle e_\times e_\times \rangle \tag{3.103}$$
$$\mathbb{I}(\xi_+) = \langle e_{\tan} e_\times \rangle - \langle e_\times e_{\tan} \rangle \tag{3.104}$$

$$\xi_- = \langle ee \rangle = \big\langle (e_{\tan} + i e_\times)(e_{\tan} + i e_\times) \big\rangle \tag{3.105}$$
$$\Re(\xi_-) = \langle e_{\tan} e_{\tan} \rangle - \langle e_\times e_\times \rangle \tag{3.106}$$
$$\mathbb{I}(\xi_-) = \langle e_{\tan} e_\times \rangle + \langle e_\times e_{\tan} \rangle \tag{3.107}$$

In applications, such as cosmic shear we in fact define a unique system of coordinates which is independent of galaxy position [6]. As a consequence ϑ in eq. (3.65) is constant and by convention we can set it to zero, previous equations now are:

$$\Re(\xi_+) = \langle e_1 e_1 \rangle + \langle e_2 e_2 \rangle \tag{3.108}$$
$$\mathbb{I}(\xi_+) = \langle e_1 e_2 \rangle - \langle e_2 e_1 \rangle \tag{3.109}$$

[6] In application such as cluster lensing we have one system of coordinates for each cluster

$$\Re(\xi_-) = \langle e_1 e_1 \rangle - \langle e_2 e_2 \rangle \tag{3.110}$$

$$\mathbb{I}(\xi_-) = \langle e_1 e_2 \rangle + \langle e_2 e_1 \rangle \tag{3.111}$$

Since eq. (3.96) supplies us a theoretical modelling of the shear 2PCF that depends on the cosmological parameters, and eq. (3.99) gives us an estimator of this function in a shear catalogue, we can use both of them to calculate cosmological parameters. In order to do this analysis we define the likelihood function

$$\mathscr{L} = |C|^{-1/2} \exp\Big(- \frac{\mathbf{d}^T \mathbf{C}^{-1} \mathbf{d}}{2} \Big), \tag{3.112}$$

where the data vector $\mathbf{d}$ is the difference between the measurements and the theoretical model of the analysed probe, $\mathbf{d} = \xi_p(\theta) - \hat{\xi}(\theta)$, and $\mathbf{C}$ is the covariance matrix. The $\xi_p(\theta)$ is the theoretical value that depends on the cosmological parameters p. Given the previous likelihood function, we will use a Monte Carlo Markov Chain (MCMC) routine to maximize it and to get the best set of cosmological parameters according to the measurements.

Chapter 4

Galaxy shapes and the Point Spread Function

Even though we have called observables the shear, the convergence, and the magnification, the truth is that in practice, we can measure none of these quantities. We have seen that all three observables are linked one with each other, in such a way that only determine either the convergence or the shear, the other two observables can also be known. But how we relate these observables with actual measurement? Well, in practice, we observe a noisy surface brightness, if we can eliminate noise and possible systematic biases, then we can get the observed shape of the galaxy, and this shape will be related to shear. To be more specific, the shape is characterized by a parameter that we will call *ellipticity*, although it refers to a parameter that can describe shapes beyond ellipsoids. Then, we will see that it is possible to define in different ways these ellipticities. However, we will be focused on those definitions that hold the *ellipticity as an estimator of the shear*, and preferably an *unbiased estimator*. Then we can study the consequences of using those estimators in the 2PCF.

Besides this discussion of how to estimate the shear and the 2PCF from ellipticities, in this chapter, we will dedicate a significant part to the foundations of the Point Spread Function (PSF) modeling. As it has already been introduced, lensed images of galaxies get blurred and smeared by different effects, one of the main ones is the dispersion by the atmosphere, then in ground-based telescopes as in the case of DES, needs to model this effect. And the PSF is a standard approach to solve for this effect. A significant part of the results of the present work will be focused on quantifying errors that can be introduced in case of a miss-estimation of PSF, therefore, we will treat the theoretical perspective in a bit more detail.

We will end this chapter briefly discussing some of the common biases we find in cosmic shear such as the shear measurement bias, intrinsic alignment, baryons modeling, and expectation bias. And we will also describe how E and B modes can help us to look for possibles systematic errors.

4.1 Galaxy shapes and estimators of weak lensing

In previous chapters, we study two types of forms, circles, and ellipses. However, shapes in the universe are much more than just circles and ellipses. In this section, we will introduce a methodology to describes more complex shapes. There are many approaches to study shape of galaxies. We can en-globe all of them in two categories, *moment-based* methods and *model-fitting* methods. In the moment-based method, based on the surface brightness profile, we define a tensor. We will see that the shape of a galaxy is characterized by the second moments of this tensor. On the other hand, the model fitting approach uses a general model for the surface brightness and perform the best fit for its parameters. This approach is intrinsically related to PSF modeling, so we let this discussion for later. In the following section, we will be concentrated only in the moment-based methods.

When we measure the ellipticity of an image, we can use different estimators. Most of them based on the second moments (also called quadrupole moments) of the surface brightness $S(\overrightarrow{x})$

$$\boxed{Q_{ij} = \frac{\int d^2\mathbf{x}(x_i - x_i^{\rm cen})(x_j - x_j^{\rm cen})S(\overrightarrow{x})}{\int d^2\mathbf{x}S(\overrightarrow{x})},} \tag{4.1}$$

where $x_i^{\rm cen}$ and $x_j^{\rm cen}$ are the brightness centre or first moments, defined as

$$\boxed{x_j^{\rm cen} = \frac{\int d^2\mathbf{x}x_i S(\overrightarrow{x})}{\int d^2\mathbf{x}S(\overrightarrow{x})}.} \tag{4.2}$$

An analogous definition common in physics is the inertia tensor which characterizes the rotations of rigid body. Similarly, the *second moment tensor of the surface brightness* Q_{ij} determine the shape of the galaxies.

When we think in to characterize the shape of an ellipse, the eccentricity and direction of a semi-major axis is probably our first guess. However, what can we do in the cases where our shape is more general than an ellipse. The next shape in complexity might be is a compressed circle that forms ellipsoids. And it is in terms of this geometrical figure that we will define our *ellipticities*. The eccentricity can also be defined for ellipsoids, however to characterizes how much the original figure was compressed and stretched, it is not than convenient. In fact, in weak lensing, we are more interested in the flattening or stretching the image suffer, rather the shape itself. As a consequence, we will use variations of what is known in mathematics as the *third flattening*. This concept becomes more relevant because we can quantify the variation of shapes beyond ellipses. Given a and b the semi-major and semi-minor axis of an ellipsoid the third flattening is defined as

$$\boxed{n = \frac{a-b}{a+b},} \tag{4.3}$$

where we can see that when n goes to zero, there was no compression at all, while if n goes to ± 1 we get the maximum possible compression. The idea now is to define a similar quantity. But instead of talking of the semi-axis, we will use the direction of the fastest change and slowest change. In that way, shapes beyond ellipsoids can be characterized too.

4.1.1 Ellipticities

In appendix H, we present an example of how these directions of fastest change and slowest change are related to the eigenvalues and eigenvector of Q_{ij}. We proved that they are related to the semi-axis of a hypothetical characteristic ellipse that we will use to determine the characteristic sizes on an orthogonal basis. We prove that the eigenvalues λ_1 and λ_2 of Q_{ij} are related to the semi-axis a and b as follows

$$a = \lambda_2^{-1/2} \qquad b = \lambda_1^{-1/2}, \tag{4.4}$$

where $\lambda_1 > \lambda_2$ and $a > b$. Respectively, the eigenvectors correspond to the direction maximum and minimum variation. Or in terms of this characteristic ellipse to its semi-axis[1]. The general eigenvectors and eigenvalues of Q_{ij} are

$$\begin{aligned} \lambda_{1,2} &= \frac{1}{2}\left(Q_{11}+Q_{22} \pm \sqrt{(Q_{11}-Q_{22})^2+4Q_{12}^2}\right) \\ \overrightarrow{v}_{1,2} &= \frac{1}{2}\left(Q_{11}-Q_{22} \pm \sqrt{(Q_{11}-Q_{22})^2+4Q_{12}^2}\right)\hat{\boldsymbol{i}} + Q_{12}\hat{\boldsymbol{j}}, \end{aligned} \tag{4.5}$$

with the exception of a tensor with $Q_{12} = 0$, in that case the normalized eigenvectors correspond to the Cartesian unitary vectors.

We can get the angle φ between $\overrightarrow{v}_1$ and the x-axis taking into account

$$\begin{aligned} \tan^2(\varphi) &= \frac{4Q_{12}^2 + \left[(Q_{11}-Q_{22})^2 - (Q_{11}-Q_{22})^2\right]}{\left(Q_{11}-Q_{22}+\sqrt{(Q_{11}-Q_{22})^2+4Q_{12}^2}\right)^2} \\ &= \frac{\sqrt{(Q_{11}-Q_{22})^2+4Q_{12}^2} - (Q_{11}-Q_{22})}{\sqrt{(Q_{11}-Q_{22})^2+4Q_{12}^2} + (Q_{11}-Q_{22})} \end{aligned} \tag{4.6}$$

It is important to remember that φ in this way is defined respect to the x axis and the semi-axis associated to $\overrightarrow{v}_1$. The idea now is to generalize the concept of third flattening given by eq. (4.3) using these eigenvalues. We will call as ellipticities to this generalization. In particular, below we will study two ellipticities of interest, the *polarization* and the *distortion*.

[1]It is important to emphasizes that we are not fitting an ellipse to the surface brightness, but instead finding the principal axis and characteristic dimensions, which are associated to an ellipse equation.

The polarization ellipticity

The *polarization* ellipticity χ corresponds to the case where we use the eigenvalues directly in eq. (4.3) instead of the values of the semi-axis. It is to say

$$\boxed{\chi = \frac{\lambda_1 - \lambda_2}{\lambda_1 + \lambda_2} e^{2i\varphi},} \tag{4.7}$$

where we have extended the definition of the third flattening introducing complex number notation contained in the factor $e^{2i\varphi}$, and the reason of the factor 2φ are the symmetrical properties of ellipsoids, that we have discussed before in chapter 3. Notice that in the case of elliptical isophotes the polarization can be determined using eq. (4.4), leading to

$$\chi^{\text{ellipse}} = \frac{a^2 - b^2}{a^2 + b^2} e^{2i\varphi} \tag{4.8}$$

We can write the polarization directly as a function of the second moments tensor, substituting eq. (4.5) in eq. (4.7) and using the identities

$$\cos 2\theta = \frac{1 - \tan^2(\theta)}{1 + \tan^2(\theta)} \qquad \sin 2\theta = \frac{2\tan\theta}{1 + \tan^2(\theta)}, \tag{4.9}$$

we get

$$\boxed{\chi = \frac{Q_{11} - Q_{22} + 2iQ_{12}}{Q_{11} + Q_{22}}} \tag{4.10}$$

The distortion ellipticity

Another way to define the ellipticity is to use the third flattening directly, i.e., we want that in the case of elliptical isophotes, this new ellipticity satisfies

$$\boldsymbol{\epsilon}^{\text{ellipse}} = \frac{a - b}{a + b} e^{2i\varphi}. \tag{4.11}$$

It results more convenient to use this definition, because as we saw in eq. (E.24), the modules of the shear are intrinsically related to the third flattening. To extend this idea to the general case where the surface profile is not elliptical, we need to call back the eigenvalues of Q_{ij}. Therefore using eq. (4.4) we define the distortion ellipticity as

$$\boxed{\boldsymbol{\epsilon} = \frac{\sqrt{\lambda_1} - \sqrt{\lambda_2}}{\sqrt{\lambda_1} + \sqrt{\lambda_2}} e^{2i\varphi}.} \tag{4.12}$$

We can link both definition of ellipticities considering

$$\boldsymbol{\epsilon} = \left(\frac{\lambda_1 - \lambda_2}{\lambda_1 + \lambda_2}\right) \frac{\lambda_1 + \lambda_2}{\lambda_1 + \lambda_2 + 2\sqrt{\lambda_1\lambda_2}} e^{2i\varphi} = \boldsymbol{\chi} \frac{\lambda_1 + \lambda_2}{\lambda_1 + \lambda_2 + 2\sqrt{\lambda_1\lambda_2}} = \frac{\boldsymbol{\chi}}{1 + \sqrt{\frac{4\lambda_1\lambda_2}{(\lambda_1+\lambda_2)^2}}}, \quad (4.13)$$

using the modulus of the definition of the polarization eq. (4.7) and the equation $4\lambda_1\lambda_2 = (\lambda_1^2 - \lambda_2^2)$ we obtain

$$\boxed{\boldsymbol{\epsilon} = \frac{\boldsymbol{\chi}}{1 + \sqrt{1 - |\boldsymbol{\chi}|^2}}.} \quad (4.14)$$

Taking the module in both sides, we get a quadratic equation, when we solve for $|\boldsymbol{\chi}|$,

$$\boxed{\boldsymbol{\chi} = \frac{2\boldsymbol{\epsilon}}{1 + |\boldsymbol{\epsilon}|^2}.} \quad (4.15)$$

It also convenient to write explicitly the distortion ellipticity in terms of the second moments. Substituting eq. (4.5) in eq. (4.13)

$$\boldsymbol{\epsilon} = \frac{Q_{11} + Q_{22}}{Q_{11} + Q_{22} + 2\sqrt{Q_{11}Q_{22} - Q_{12}^2}} \boldsymbol{\chi}, \quad (4.16)$$

$$\boxed{\boldsymbol{\epsilon} = \frac{Q_{11} - Q_{22} + 2iQ_{12}}{Q_{11} + Q_{22} + 2\sqrt{Q_{11}Q_{22} - Q_{12}^2}}.} \quad (4.17)$$

Relating with the shear

Once defined the ellipticity, we can make use of the conservation of the surface brightness and the lens equation to get an expression relating the shapes in the plane of the observer, in the plane of the source, and the shear components. In appendix G, we present the deduction of how are these expressions, for the cases of the polarization see eq. (G.11), and in the case of the distortion see eq. (G.30). Additionally, we proved why it is more convenient to work in terms of the distortion rather the polarization. Both are unbiased local estimator, however while the distortion estimate the reduced shear $\boldsymbol{g}$, the polarization estimate $\boldsymbol{\delta}$ which is defined in eq. (G.39), and it is invariant under the transformation $\boldsymbol{g} \to \frac{1}{\boldsymbol{g}}$. Consequently, from now, we will use the distortion as our estimator of the shear, each time we refer below to ellipticity we will mean the distortion, although below we will present several calculations using the polarization since it is easier to handle.

4.1.2 Ellipticity weighting

In the previous section, we described the perfect case where there is no noise in the observed image, and we can uniquely determine the right surface brightness and its el-

lipticity. However, in practice, we need to optimize the signal over the noise. This is essentially a turnover between the more area to capture more signal, and the less area to avoid include more noise. These proper selection of the area used to measure the surface brightness is include using a weighting function in the second moments tensor

$$\boxed{Q_{ij}^{\rm obs} = \int d^2\theta S^{\rm obs}(\overrightarrow{\theta})W(\overrightarrow{\theta})\theta_i\theta_j,} \tag{4.18}$$

where we have unconsidered the normalization factor because it cancels out in the definition of ellipticity, and we assume our frame of reference is located in the first moment, i.e, in the center of brightness. We are interested in to see how the inclusion of this weighting function will affect our ideal estimator of the shear. Expanding the surface brightness up to first order in Taylor series around $\overrightarrow{\beta}$ we have

$$S^{\rm obs}(\overrightarrow{\theta}) \approx S(\overrightarrow{\beta}) + \frac{\partial S}{\partial\theta_l}(\theta_l - \beta)$$

$$S^{\rm obs}(\overrightarrow{\theta}) \approx S(\overrightarrow{\beta}) + \frac{\partial S}{\partial\theta_l}(\alpha_l)$$

$$\boxed{S^{\rm obs}(\overrightarrow{\theta}) \approx S(\overrightarrow{\theta}) + \frac{\partial S}{\partial\theta_l}\Psi_{lm}\theta_m} \tag{4.19}$$

where in the second line we have used the lens equation eq. (3.4) and in the third we use the conservation of the surface brightness and we did an additional Taylor expansion of the reduced deflection angle, i.e, $\alpha_l(\overrightarrow{\theta}) \approx \text{Cte} + \frac{\partial\alpha_l}{\partial\theta_m}\theta_m$, recalling the definition of the distortion matrix eq. (3.34) and setting to zero the constant.

Without going in the details, if we substitute eq. (4.19) in eq. (4.18), and after integrating by parts neglecting terms of the order θ^3, and defining

$$W' = \frac{\partial W}{\partial\theta^2}, \tag{4.20}$$

we get

$$\boxed{Q_{ij}^{\rm obs} = Q_{ij} + \Psi_{lm}Z_{lmij},} \tag{4.21}$$

where

$$\boxed{Z_{lmij} = \int d^2\theta S(\overrightarrow{\theta})\left(W(\overrightarrow{\theta})\left[\delta_{il}\theta_j\theta_m + \delta_{lm}\theta_j\theta_i + \delta_{jl}\theta_i\theta_m\right] + 2W'\theta_i\theta_j\theta_l\theta_m\right).} \tag{4.22}$$

For the purpose of this discussion, we now write the change in the polarization ellipticity in terms of this function Z; from eq. (4.21) we know $\delta Q_{ij} = \Psi_{lm}Z_{lmij}$. It is also convenient to write the trace of Q as a new variable, let's call it $T = Q_{11} + Q_{22}$. Using this expression

it is easy to see that the change of polarization is

$$\delta\boldsymbol{\chi} = \frac{\Psi_{lm}}{T}\left[Z_{lm11} - Z_{lm22} - \chi_1(Z_{lm11} + Z_{lm22}) + i\left[2Z_{lm12} + \chi_2(Z_{lm11} + Z_{lm22})\right]\right] \quad (4.23)$$

Given that we are expanding up to first order in Taylor series, then we can define a tensor of transformation connecting the weak lensing observables and the change on the ellipticity. Moreover, this linear transformation is weakly dependent on the convergence, then we define the *shear polarizability* tensor P as

$$\boxed{\delta\boldsymbol{\chi} = P_{1i}\gamma_i + iP_{2i}\gamma_i.} \quad (4.24)$$

The origin of this name comes actually from analogy to the polarization in electrodynamics. When an electrical field is applied to a distribution of charges, it can create dipole moments. If the distribution is isotropic, there is a linear response. By analogy, the shear field can create shear polarizability, i.e., changes in the ellipticity of galaxies. In the first order, we can assume this as a linear response too.

By direct comparison with eq. (4.23), we can expect the shear polarizability to be decomposed in two components, one proportional to $\boldsymbol{\chi}$ and another independent of it. Therefore, it is convenient to use

$$P_{ij} = X_{ij} - \boldsymbol{\chi}^{\gamma}_{j}\boldsymbol{\chi}_i, \quad (4.25)$$

where $\boldsymbol{\chi}^{\gamma}_{j}$ is a term that couples the shear and the ellipticities and can be seen as a diagonal matrix. And X_{ij} is the tensor having in general out of diagonal terms. Comparing term by term eq. (4.23) with eq. (4.24), and using eq. (4.25) we get

$$\begin{cases} X_{11} = \frac{1}{T}\left(Z_{1111} - Z_{1122} - Z_{2211} + Z_{2222}\right) \\ X_{12} = \frac{1}{T}\left(Z_{2111} - Z_{2122} + Z_{1211} - Z_{1222}\right) \\ X_{22} = \frac{2}{T}\left(Z_{2112} + Z_{1212}\right) \\ \boldsymbol{\chi}^{\gamma}_{1} = \frac{1}{T}\left(Z_{1111} + Z_{1122} - Z_{2211} - Z_{2222}\right) \\ \boldsymbol{\chi}^{\gamma}_{2} = \frac{1}{T}\left(Z_{2111} + Z_{2122} + Z_{1211} + Z_{1222}\right) \end{cases} \quad (4.26)$$

Finally, we calculate all the Z using eq. (4.22) and given the definition of the polarization ellipticities, we have the following component of the shear polarizability

$$X_{ij} = \begin{bmatrix} 2 & 0 \\ 0 & 2 \end{bmatrix} + \frac{2}{T}\int d^2\theta S(\overrightarrow{\theta})W'(\theta)\left(\begin{bmatrix} (\theta_1^2 - \theta_2^2)^2 & 2\theta_2\theta_1(\theta_1^2 - \theta_2^2) \\ 2\theta_2\theta_1(\theta_1^2 - \theta_2^2) & 2\theta_1^2\theta_2^2 \end{bmatrix}\right) \quad (4.27)$$

$$\boldsymbol{\chi}_j^{\gamma}\boldsymbol{\chi}_i = 2\begin{bmatrix}\boldsymbol{\chi}_1^2 & \boldsymbol{\chi}_1\boldsymbol{\chi}_2\\ \boldsymbol{\chi}_1\boldsymbol{\chi}_2 & \boldsymbol{\chi}_2^2\end{bmatrix} + \frac{2}{T}\int d^2\theta S(\overrightarrow{\theta})W'(\theta)\theta^2\begin{bmatrix}(\theta_1^2-\theta_2^2)\boldsymbol{\chi}_1 & \theta_1\theta_2\boldsymbol{\chi}_1\\ (\theta_1^2-\theta_2^2)\boldsymbol{\chi}_2 & \theta_1\theta_2\boldsymbol{\chi}_2\end{bmatrix} \tag{4.28}$$

And the total shear polarizability can be written as

$$\boxed{\begin{aligned} P = {} & 2\begin{bmatrix}1-\boldsymbol{\chi}_1^2 & \boldsymbol{\chi}_1\boldsymbol{\chi}_2\\ \boldsymbol{\chi}_1\boldsymbol{\chi}_2 & 1-\boldsymbol{\chi}_1^2\end{bmatrix} + \\ & \frac{2}{T}\int d^2\theta S(\overrightarrow{\theta})W'(\theta)\left(\begin{bmatrix}(\theta_1^2-\theta_2^2)^2 & 2\theta_2\theta_1(\theta_1^2-\theta_2^2)\\ 2\theta_2\theta_1(\theta_1^2-\theta_2^2) & 2\theta_1^2\theta_2^2\end{bmatrix}\right. \\ & \left. - \begin{bmatrix}\boldsymbol{\chi}_1 & \boldsymbol{\chi}_2\end{bmatrix}\begin{bmatrix}(\theta_1^2-\theta_2^2) & \theta_1\theta_2\\ (\theta_1^2-\theta_2^2) & \theta_1\theta_2\end{bmatrix}\right) \end{aligned}} \tag{4.29}$$

Finally, we can write an expression for the estimator of the shear in term of this shear polarizability tensor. Other way of writing eq. (4.24) is

$$\boldsymbol{\chi}_i^{\text{obs}} = \boldsymbol{\chi}_i^s + P_{ij}\gamma_j \tag{4.30}$$

where $\boldsymbol{\chi}_i$ is the polarization ellipticity, $\boldsymbol{\chi}_i^s$ is an assumed intrinsic ellipticity, γ_i represents the shear field and P_{ij} is the polarizability. Inverting the previous equation and taking into account that the mean of the intrinsic ellipticity vanish, we obtain a estimator for the shear

$$\boxed{\hat{\gamma}_i = P_{ij}^{-1}\boldsymbol{\chi}_j^{\text{obs}}.} \tag{4.31}$$

In the practice, using the whole inverse of eq. (4.29) is a noisy process, however is has been observed that using only a characteristic proportionality factor is equivalent an more accurate, this factor is know as the *responsivity* $\boldsymbol{R}$ and $\hat{\gamma}_i = \frac{\boldsymbol{\chi}_i^{\text{obs}}}{\boldsymbol{R}}$. If we approximate the shear polarizability tensor to the first order term, $\langle\boldsymbol{\chi}_1^2\rangle = \langle\boldsymbol{\chi}_2^2\rangle = \boldsymbol{\chi}_{\text{RMS}}^2$ and $\langle\boldsymbol{\chi}_1\boldsymbol{\chi}_2\rangle = 0$, $\boldsymbol{R} = 2(1-\boldsymbol{\chi}_{\text{RMS}}^2)$.

4.2 Point Spread function

Images of galaxies are blurred and smeared because the presence of the atmosphere, the electronics of the telescope, and several other distortions that are present in optical systems, such as aberrations and difraction. To measure properly the shape and size of a galaxy, we need to model those optical aberrations. On ground based acquisition systems, and particularly those that uses CCD cameras, we model those effects as a function that

convolves the actual surface brightness in to the observed surface brightness i.e.,

$$\boxed{S^{\text{obs}}(\overrightarrow{\theta}) = \int d^2\theta' S(\overrightarrow{\theta} - \overrightarrow{\theta'})P(\overrightarrow{\theta'}),} \tag{4.32}$$

where $S^{obs}(\overrightarrow{\theta})$ is the observed surface brightness, $S(\overrightarrow{\theta})$ is the actual surface brightness before the aberration take place, and $P(\overrightarrow{\theta'})$ is the point spread function (PSF). We now need to define a strategy to determine this function. One of those strategies that has become standard in astronomy, is to use stars as the point sources and extrapolate for extended sources like galaxies. In other words, stars satisfies

$$\boxed{P_{\text{stars}}(\overrightarrow{\theta'}) = \overrightarrow{\delta}_D(\overrightarrow{\theta'}).} \tag{4.33}$$

Therefore, we can use all the stars in the neighbourhood of a galaxy as points for the fitting of the PSF in that region.

This is the general idea of PSF modeling. However, there are some subtleties and details to consider. Let us do a brief review of some of the most important considerations and approaches used.

First, this extrapolation process is not performed for each galaxy. Instead, full regions of the sky have their PSF, and even more, each exposure has one defined PSF because it might be we are using a different filter or sky conditions change during the observation.

Second, there are local distortions due to the dependency on the position of the galaxy. To solve this and other inconveniences, different modeling has been proposed, Kaiser method [27], the elliptical Gaussian weighting method proposed by Bernstein and Jarvis[28] are probably the most famous methods before principal component analysis PCA. PCA is a method proposed in [29] and consist of modeling the PSF for each image, and then create a global model for all the images. Leading to a spatially and temporally variable PSF, this is known as *multiepoch method*.

Third, it has been observed that the PSF is highly dependent on the brightness of the nearest stars. Those stars typically are not too bright to induced undesired overcharge in the chip and are not too faint are too noisy to induce bias errors. So an appropriate, magnitude range selection needs to be done before the modeling.

Fourth, to choose the proper weight function, a wide variety of orthogonal basis have been implemented. Today, gaussian weighted Hermite polynomials or "Shapelets" in [30] are the state of the art.

4.2.1 Moments of the PSF

We are now interested in to correct the shape of the galaxies for the PSF, assuming we have already determined it. We start by expanding the surface brightness in Taylor series

around $\overrightarrow{\theta}$,

$$S^{\rm obs}(\overrightarrow{\theta}) \approx S'(\overrightarrow{\theta}) + \frac{1}{2}\frac{\partial^2 S'}{\partial\theta_l \partial\theta_m}\bigg|_{\overrightarrow{\theta}} \int d^2\theta' P(\overrightarrow{\theta}')\theta'_l\theta'_m, \tag{4.34}$$

where $S'(\overrightarrow{\theta})$ represents the surface brightness before our local optical distortions appear. We have assumed the PSF is normalized, and we choose a system of coordinate where the first order term of the expansion is null in the center of brightness of the PSF profile. The integral part of the last expression is the second moment tensor of the PSF, $Q^{\rm PSF}$. then

$$S^{\rm obs}(\overrightarrow{\theta}) \approx S'(\overrightarrow{\theta}) + \frac{1}{2}\frac{\partial^2 S}{\partial\theta_l \partial\theta_m} Q^{\rm PSF}_{lm}. \tag{4.35}$$

It follows a similar process to the previous section. we introduce eq. (4.35) in eq. (4.18), after we integrate by parts twice we get

$$Q^{\rm obs}_{ij} = Q'_{ij} + Y_{lmij} Q^{\rm PSF}_{lm}, \tag{4.36}$$

with

$$Y_{lmij} = \frac{1}{2}\int d^2\theta S(\overrightarrow{\theta})\frac{\partial^2}{\partial\theta_l\partial\theta_m}\left[W(\overrightarrow{\theta})\theta_i\theta_j\right]. \tag{4.37}$$

In the same way, how we define the shear polarizability tensor to get an estimate of the shear, we now define the *smear polarizability* P^s_{ij} to correct for the PSF. But this time instead of the shear be the responsible of the change in the ellipticity the moments of the PSF are. It is convenient to define the smear polarizability in terms of linear combinations of the second moment of the PSF, in particular we define

$$\begin{cases} q^{\rm PSF}_1 = Q^{\rm PSF}_{11} - Q^{\rm PSF}_{22} \\ q^{\rm PSF}_2 = 2Q^{\rm PSF}_{12}, \end{cases} \tag{4.38}$$

and

$$\boxed{\delta\boldsymbol{\chi}_i = P^s_{ij} q_j.} \tag{4.39}$$

We can have an estimate for the smear polarizability. If we compare eq. (4.21) with eq. (4.36) we see they are the same structure. Then we can use eq. (4.23) but instead of Z_{lmij} we use Y_{lmij}, and instead Ψ_{lm} we use Q_{lm}. Introducing this new expression and eq. (4.38) in eq. (4.39) we get and expression similar to eq. (4.29) but instead $\boldsymbol{\chi}$ we use $\boldsymbol{\chi}^{\rm PSF}$ and the second term have a complete different structure, but in general it depends also on the weighting function and polarization ellipticities of the PSF.

4.2.2 Forward Modeling

Until now, we have presented the historical progress of how to measure the shapes and PSF. Initially, shapes and PSF correction were calculated using second moments of the

surface brightness and PSF profiles. However, there is a more practical and accurate way to address both problems, the *forward modeling*. The idea of this method is simple; basically, it is proposed two suitable models, one for the surface brightness before the local optical distortion, and another for the PSF profile, then we calculate the best fit with the observed surface brightness, finally from this best fit we obtain the shape. This is advantageous in comparison to second moments in cases where there is lacking information in certain pixels. It is important to bear in mind that we get the parameters of the PSF profile using stars since they are considered *point sources*, then we convolve with our model of the surface brightness and solve the fitting problem to get the parameters of the surface.

Chapter 5

Errors and cosmic shear biases

Proper modeling and estimation of error and biases is a key issue in cosmic shear. In this section, we will present the main errors that are present and how they are typically faced. We want to have control of the systematic uncertainties in our summary statistics. In the case of the shear 2PCF, we can classify them in four major groups: redshift, number density, multiplicative shear, and additive shear. For the purpose of the present work, we will study this last two type of uncertainties; we also refer to them as shear measurement biases, but we separate in multiplicative and additive contributions since it is has been demonstrated that the first-order expansion is good enough approximation [31],

$$\gamma_i^m = (1 + m_i)\gamma_i^t + c_i, \tag{5.1}$$

where γ_i^m is the measured or observed shear, γ_i^t is the true shear, m_i characterizes the multiplicative bias and c_i the additive bias. It was also assumed there is not cross-talk among different shear component, otherwise the previous equation should be written in matricidal way. In fact, it is a good approximation to take the arithmetic mean since $m \approx m_1 \approx m_2$.

Both additive and multiplicative bias have different contributions. PSF modeling, blending, galaxy characterization, detector effects, selection of stars, and galaxy characterization are some examples. In the present work, we will focus only with the characterization of PSF errors.

5.1 Theoretical uncertainties

One of the major theoretical uncertainties in weak lensing is *intrinsic alignments*. It is to say, coherent alignments of galaxy shapes produced by physics beyond lensing. Usually associated with the local environment of the galaxies. As a consequence of this intrinsic alignment, our shear 2PCF will be biased by galaxy-intrinsic correlation, and intrinsic-intrinsic correlations, also called GI and II correlation.

Among other theoretical uncertainties are the Limber's approximation, the Born's approximation, baryonic physics affect mainly small scales of the power spectrum, magnification bias. However, for the current surveys, their significant effects are in particular scales that can be cut out to mitigate the impact.

It worth to mention also what is known as the *expectation bias* or experimenter bias. This type of error can appear because there is potential in the analysis methodology to include parameters or interpretation dependent on a particular experimenter. To face this type of problem, it was suggested to *blind the analysis*. The idea of this is to make a specific contamination to original data. This contamination is done keeping cosmological information hide for observers until all the analysis tools are ready. In this way, a particular analysis that tends to favor an expected result for the observer can be under control.

5.2 Statistical errors

The principal statistical error for weak lensing measurements is the *shape noise*. This is the standard deviation of the intrinsic ellipticity of galaxies and it is noted as $\sigma_{\rm shape}$. The standard deviation of the ellipticities due to a shear field depends on the shape noise as

$$\sigma_{\rm shear} = \frac{\sigma_{\rm shape}}{\sqrt{N}}. \tag{5.2}$$

As a consequence, the more galaxies measured, the more accurate will be the shear estimation. This type error propagates also in the two point correlation function, in appendix J we present the details.

The second type of statistical error in weak lensing is *sample variance*. These errors basically come from the fact that the universe is a particular realization of a random process, then measurements in other realizations should be different. Besides, we could also observe different regions of the same realization. In this case, we see a *cosmic variance* that can be even larger than the sample variance. In general, it is common to find in the literature no distinction between how to call the variance due to we are observing a different region or a different realization, and both names are used indistinctly.

If we assume our observable follows a Gaussian distribution, it can be proved that the variance of the estimator for the variance is $\frac{2\sigma^4}{N}$. In the case of the power spectra of the convergence, we then can approximate the uncertainty due to these two statistical errors as

$$\Delta C_l^{\kappa\kappa} = \sqrt{\frac{2}{N_l}}\left(C_l^{\kappa\kappa} + \frac{\sigma_{sh}^2}{N}\right), \tag{5.3}$$

where the last term in the r.h.s correspond to the shape noise, the first to sample variance, N is the number of galaxies, and N_l is the number of modes used. It can be proved, that

the number of modes is $2f_{\rm sky}l$ where f is the fraction of the sky covered by the survey. Then

$$\Delta C_l^{\kappa\kappa} = \sqrt{\frac{1}{f_{\rm sky}l}}\left(C_l^{\kappa\kappa} + \frac{\sigma_{sh}^2}{N}\right), \tag{5.4}$$

and from a particular l, shape noise becomes dominant over cosmic variance. Or in terms of the real space, there is a turn over scale where below of that shape noise is dominant and for larger scales cosmic variance is dominant.

5.3 Systematic errors

There are a wide variety of systematic errors that can affect weak lensing analysis. See fig. 5.1 to see a summary of some of them. First, we have the *detector systematic*, these types of errors can not be treated as a convolution, and therefore the PSF can not solve it. One of these types of errors is the *brighter-fatter* effect. Where a nonlinear response of the detector can make look fatter objects that are brighter, then if we estimate the PSF in the region of a bright star and interpolate to the position a close by a faint galaxy, our estimate will be wrong. Other types of detector errors are *tree-rings* and *edge-distortion*, which are concentric rings and stripes near edges of the focal plane. Surprisingly, we can include the solution of this problem in our astrometric and photometric solution (see section 6.1).

Secondary systematic but more treatable are the low signal to noise regime (*noise bias*) and complex galaxies morphologies (*model bias*). Which can be studied through multiplicative factor obtained from calibration with simulations [1]. To account for noise bias, it also used a different method that assumes Bayesian prior information given by the distribution of intrinsic galaxy shapes[2].

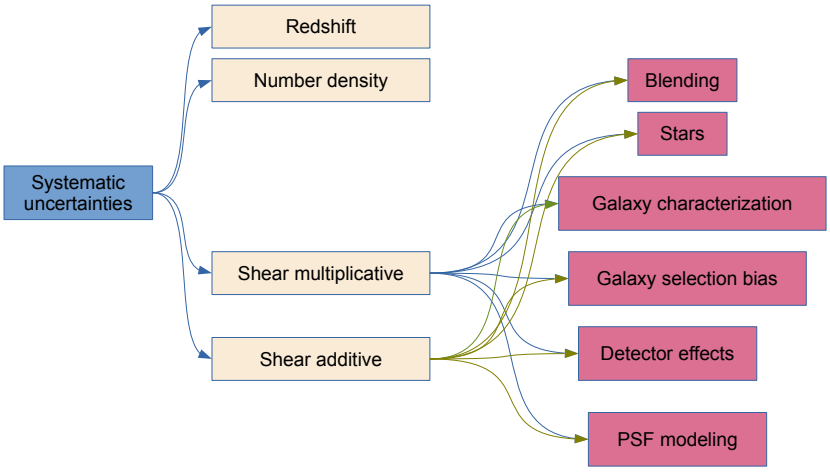

Figure 5.1: Some of the systematic uncertainties affecting summary statistics of cosmic shear.

[1] Implemented in IM3SHAPE
[2] Implemented in NGMIX

5.4 PSF errors and rho-statistics

The PSF accounts for all the systematics that can be modeled as a convolution of the surface brightness. It includes the atmospheric, optical and chromatic PSF, charge diffusion, pixel response, among other effects. A misestimation of the PSF size and shape can induce *multiplicative* and *additive* biases, respectively. Usually, PSF modeling is done for each chip independently because of differences of heights can appear. The use of stars to get the PSF and interpolate at the position of galaxies has some caveats. First, it is assumed that stars and galaxies have the same spectral energy distribution within a photometric band, which is not necessarily true. Second individual galaxy color gradients violate the assumption of a single PSF for each galaxy[4]. These two assumptions and wavelength-dependent PSF have gained a high interest in recent years[32].

One important null test of our PSF modeling is to compare the size and the shape of the PSF at the position of stars that were not used to model the PSF. Moreover, we can define a set of diagnostics statics based on the residual and determine how weak lensing observables will be affected by PSF modeling errors.

Every measurement in weak lensing demands an accurate estimation of the PSF, and to have that estimate, we need an appropriated stars catalog, from which we will extrapolate the PSF at the position of galaxies. Rho-stats [33, 34] are a set of statistical correlation functions among ellipticities and sizes of stars that somehow can help us to trace-back possible source of systematic, and to quantify the minimum requirements to have a specific precision measure.

Systematic errors in the shear correlation function are directly related with systematic errors in the measurement of galaxy ellipticity and those errors are dependent of the following statistics:

$$\rho_1(\theta) = \langle \delta e^*_{\rm PSF}(\mathbf{x}) \delta e_{\rm PSF}(\mathbf{x}+\theta) \rangle \tag{5.5}$$

$$\rho_2(\theta) = \langle e^*_{\rm PSF}(\mathbf{x}) \delta e_{\rm PSF}(\mathbf{x}+\theta) \rangle \tag{5.6}$$

$$\rho_3(\theta) = \left\langle \left(e^*_{\rm PSF} \frac{\delta T_{\rm PSF}}{T_{\rm PSF}} \right)(\mathbf{x}) \left(e_{\rm PSF} \frac{\delta T_{\rm PSF}}{T_{\rm PSF}} \right)(\mathbf{x}+\theta) \right\rangle \tag{5.7}$$

$$\rho_4(\theta) = \left\langle \delta e^*_{\rm PSF}(\mathbf{x}) \left(e_{\rm PSF} \frac{\delta T_{\rm PSF}}{T_{\rm PSF}} \right)(\mathbf{x}+\theta) \right\rangle \tag{5.8}$$

$$\rho_5(\theta) = \left\langle e^*_{\rm PSF}(\mathbf{x}) \left(e_{\rm PSF} \frac{\delta T_{\rm PSF}}{T_{\rm PSF}} \right)(\mathbf{x}+\theta) \right\rangle \tag{5.9}$$

Where $\delta e_{\rm PSF}$ is the difference between the measurements in the ellipticities, with and without taking into account the PSF model. In [34] is demonstrated how these rho-stats

for a particular PSF model propagates in the shear correlation function, they proved

$$\begin{aligned}\delta\xi_+(\theta) = 2\left\langle\frac{\delta T_{\rm PSF}}{T_{\rm gal}}\right\rangle\xi_+(\theta) + \left\langle\frac{T_{\rm PSF}}{T_{\rm gal}}\right\rangle^2\rho_1(\theta) - \alpha\left\langle\frac{T_{\rm PSF}}{T_{\rm gal}}\right\rangle\rho_2(\theta) \\ + \left\langle\frac{T_{\rm PSF}}{T_{\rm gal}}\right\rangle^2\rho_3(\theta) + \left\langle\frac{T_{\rm PSF}}{T_{\rm gal}}\right\rangle^2\rho_4(\theta) - \alpha\left\langle\frac{T_{\rm PSF}}{T_{\rm gal}}\right\rangle\rho_5(\theta)\end{aligned} \tag{5.10}$$

where α is the leakage and usually is very small. For the interest of that analyses was found that the most important contribution come from ρ_1 and ρ_2. We can give to the rho-stats easily a physical meaning. By definition the closer to zero the less correlated they are. Hence, we do not expect that the residuals in two different point to be correlate (ρ_1), neither the ellipticity in one point and the the residual in other point (ρ_2). A question here that matters to analyze is how so close to zero means no correlation, or even better how close to zero this rho-stats should be to be able to say that our PSF modeling is good enough for our cosmological interest. Of course, we want it as close to zero as possible. While it is two or three orders of magnitude lower than average ellipticity, it will be the minimum required to get good precision cosmology.

Chapter 6

Foundations behind PSF catalogs

Until now, we have only discussed which are the weak lensing observables and how can we study cosmology from them. In this chapter, we discuss some of the foundations behind catalog construction.

6.1 How we create PSF catalogs

Part of the present work was to test different stages in the process of the creation of PSF catalogs looking for improvement in diagnostic function. In fig. 6.1 is presented the general chart-flow for the process of creation of PSF catalogs. We will discuss some generalities about each step.

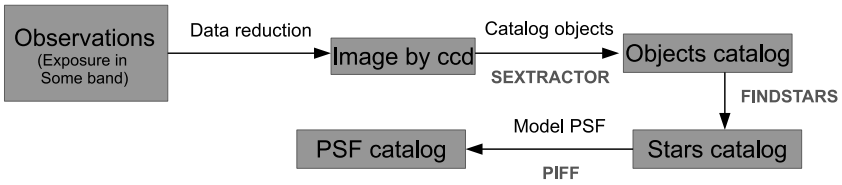

Figure 6.1: Flowchart depicting the process of creation a PSF catalogue

Data reduction

After the measurements, many data reduction steps are performed. Below follow a list of the most relevant:

1. Background subtraction

2. Deblending

Initial reduced image by ccd

Our initial reduced image contents in the header all the physical information like the band, the date of the exposure, the time it lasts, the observatory position, the target position, physical quantities describing atmospheric conditions (Humidity, Pressure, Airmass, Wind...), location of the Charge coupled device (CCD) on the focal plane, and so on. But most importantly, we need to Mask the regions in the image where there are bright stars or saturation, satellite trials, cosmic rays, tape bumps. In fig. 6.2, we observe the Header Data Unit (HDU)s associated with our initial reduced image.

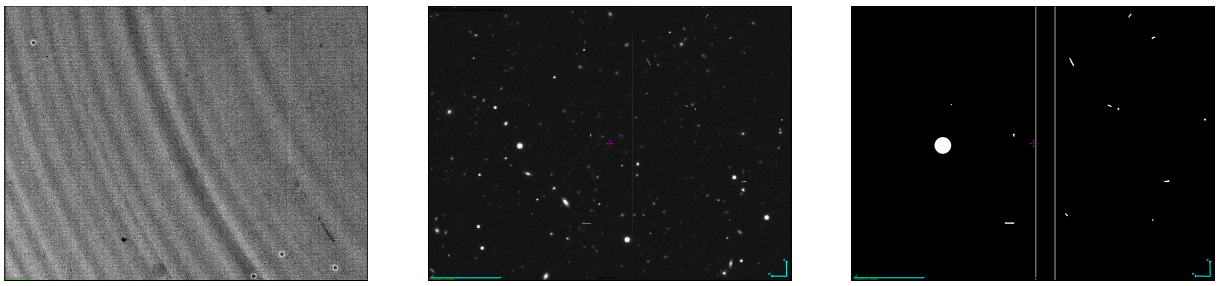

(a) Weight **(b)** Reduced image **(c)** Masked region

Figure 6.2: Example of the content of the reduced images. Basically, each image have its mask and a Weight map associated.

All objects catalog

To create the objects catalog we used `SEXTRACTOR`[35], it is one of the codes widely used to build catalogs, it is gifted with several functionalities. For our interest, besides creating the catalogs we get from it the following physical quantities

1. MAG-AUTO: To determine the magnitude of a star
2. sigma0: Initial size of the star. (Gaussian fitting)

Star-galaxy Separation

One key step before estimating PSF is to identify in the catalog of objects, which one corresponds to stars and which one to galaxies. When we compare stars and galaxies, stars images are essentially point sources before blurring by the PSF. Therefore, we use star images to fit a model for the PSF. There are different methods to separate galaxies from stars. Most of them are based on an initial separation using color filters and later a morphological analysis, although spectroscopy features some times are included to improve results. If we make a plot of size against magnitude of all objects, stars will be located on a horizontal line known as the Stellar locus. Most of the objects in the stellar locus are

stars. However, other objects could be in this region, especially faint galaxies with high redshift.

Not all stars are useful to model PSF over a region, some are too faint and are including noise to the model, and others are too bright that brighter-fatter effect appears. Hence, besides the separation, additional selection must be made. If we define limits in the magnitude, and we neglect some objects in between such as binary stars, or blended objects. We are doing what is known as modest classification.

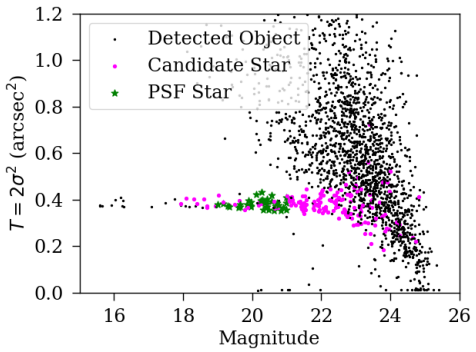

Figure 6.3: Size-magnitude plot for star galaxy separation

In fig. 6.3 is presented a particular size-magnitude plot for a particular exposure and CCD of DECAM. All black points correspond to detected objects, mostly corresponding to galaxies. Close to size 0.4, there is a horizontal line associated with the stellar locus. Around a magnitude of 22, we can distinguish an overlapping between the stellar locus and where the most of galaxies are, we want to avoid including galaxies in the star catalogs then we let this overlapping region as a candidate objects. On the other side, objects around magnitude 16 are too bright and probably will bias our PSF because of the brighter-fatter effect. So we will use the objects in the stellar locus between eighteen and twenty-one for the PSF modeling, and we reserve twenty percent of those stars for testing purposes.

Astrometry

All the analysis of shapes and PSF model is done in celestial coordinates. However, measurements comes in pixel coordinates, so that, the transformation from pixel(x,y) to sky coordinates(θ , ϕ) is a key step, and highly affects the systematic of the measurements. This transformation must be let invariant the shape of the same object, independently of the exposure, since each fitting of a galaxy uses all the exposures where that galaxy was detected. (which is know as multi-epoch fitting). In the elaboration of the catalogs used in the present work, was used the package `PIXMAPPY` [36], to perform this transformation.

Shape and sizes

Once we have the stars catalog, we determine the shape and sizes of those stars. There are two highly used ways to measure galaxy shapes. The first one involves measuring second and higher-order moments of the galaxy and the PSF (KSB, Gaussian weighting, and Hirata adaptative moments [37]). The second is a model-fitting method of a PSF-convolved galaxy model to the data, also known as forward modeling. For the porpoise of building PSF catalogs, it was used forward modeling and in particular, the package `NGMIX` [38]. This code uses a first estimate of the size and then iterate using an exponential disk model for the shape of the galaxies, and calculates the N-dimensional posterior associated with the fitting problem. This first estimate of the shape is based on Gaussian fitting of the brightness profile of stars. This process is done by `Sextractor`, which will return σ_0. We then calculate an initial guess for the size as $T = 2\sigma_0^2$.

PSF

To model the PSF, we use the code PIFF (PSFs in the Full Field of view) [39] The structure of this software is divided into four classes. Two classes to control inputs and outputs and two additional core classes. As expected, we need two input files, the image catalog, and the stars catalog [1]. The two core classes are, the class *model* that defines the type of model to be used, and fit the parameters to that model for each star. And the class *interp* that defines how to interpolate the coefficients of the model in all the image. For instance, we can define a *PixelGrid* type of model, whose parameters are determined by Gaussian in the grid points in (u,v) pixel coordinates. And a *BasisPolinomial* of order three to interpolate the PSF in the different targets (galaxies)[2].

[1] Other important parameters are the maximal and minimal Signal to Noise ratio (SNR), typically the accepted range is between 20-100. A minimum SNR of 20 seems too big, but we must remember that those are stars, and they are brightter than galaxies.

[2] Usually the convergence criteria is the Newton algorithm

Chapter 7

Results

The main objective of the present work is to see how it will be the influence of PSF modeling in cosmological estimates. For this problem, we proposed an extension of the work done in [40], where it is suggested a parametrization based on unweighted second moments (see eq. (4.1)). We found this extension to be more convenient given that it considers the effects of misestimation of the sizes, and not only the shapes. This was not considered before because it is an order of magnitude lower impact in comparison to the shape residuals. The present work is in the context of the Y3 measurements of the Dark Energy Survey (DES).

7.1 Effects of PSF modeling in cosmological estimates

We have already discussed in chapter 5 that we can catalog the shear measurements bias in additive and multiplicative. The PSF modeling errors make a significant contribution to the additive bias. To see how additive systematic errors due to PSF misestimation propagate, and derive how such biases affect measurements of cosmic shear, we extend the work done in the appendix A in Troxel et al. 2017 [40] including three parameters α, β and η; one for each term in the error propagation proposed by Paulin-Henrikson et al. 2008 [41].

The observed shape of a galaxy is not the true cosmic signal and additive systematic errors and noise are present. We can write this statement in the following way

$$e^{\mathrm{gal}} = \gamma + \delta e^{\mathrm{sys}} + \delta e^{\mathrm{noise}}, \tag{7.1}$$

where e^{gal} is the observed shape, γ the true cosmic signal, δe^{sys} are additive systematic errors and $\delta e^{\mathrm{noise}}$ the noise. In practice, we expect $\langle \delta e^{\mathrm{noise}} \rangle = 0$ and δe^{sys} not to be null due to several contributions. A possible error in the estimation of the PSF is one of those contributions, although many other systematic uncertainties can contribute.

We will focus our attention only on those errors that come from PSF modeling. Some

examples of possible sources of PSF miss-estimations are model bias, interpolation scheme, deconvolution, and errors in the processing of the set of stars used for the modeling.

The model bias comes from the selection of a particular base for the PSF profile. We are not able to predict what is the right PSF theoretically. Then we use the more general base of functions to describe it. However, not necessarily that base will be able to describe the actual PSF.

The interpolation scheme can be particularly dependent on the number of stars and effects in the borders can emerge, for instance, it is common to use polynomial interpolation to get the PSF at the position of the galaxies, however polynomials are not good distinguishing abrupt changes and in general we can not assume the PSF to be a smooth and analytical function. Different interpolation schemes have been implemented [42–44] that face these difficulties, however unavoidable they have the potential to induce systematic errors.

Once we have determined the PSF at the position of the galaxy, we need to deconvolve the surface brightness to get the shape of the galaxy. However, the resolution of detectors is not perfect, and the PSF deconvolution can carry some effects. For instance, if the PSF is asymmetric, we would break background galaxies isotropy. On the other hand, if our PSF is symmetric, we will *dilute* the lensing distortions [28].

To determine $\delta e^{\rm sys}_{\rm PSF}$ we propose the parametrization

$$\boxed{\delta e^{\rm sys}_{\rm PSF} = \alpha e^{\rm p} + \beta \left(e^{*} - e^{p} \right) + \eta \left(e^{*} \frac{T^{*} - T^{p}}{T^{*}} \right),} \tag{7.2}$$

where α, β and η are the coefficients we must solve for, $e^{\rm p}$ is the modeled PSF ellipticity that is in general interpolated at arbitrary sky positions, e^{*} is the true PSF ellipticity measured directly from stars, $T^{\rm p}$ is the modeled PSF size and T^{*} is the actual PSF size. To have a mathematical perspective of the origin of this parametrization, see appendix I. It worth to mention that in previous work was used independent α_i and β_i for each component of the fields. However, this decreases degrees of freedom and fitting quality, and in practice, values are almost the same. Thus, it is more convenient to use only one parameter for the whole spin two fields.

The first term in eq. (7.2) represents a bias that is proportional to the PSF ellipticity. It originates from its erroneous deconvolution, usually referred to as PSF "leakage" and expected to be null ($\alpha = 0$) [45]. The second term represents incorrect modeling of the PSF, which to first order leads to a systematic error that adds linearly, so we expect $\beta \sim 1$. The last term describes the errors in the size of the PSF modeling, and in this first-order approximation should also lead to a linear additive error such that we expect $\eta \sim 1$ (see appendix I for details of this expected values).

To illustrate why this parametrization can reproduce the misestimation correctly, see

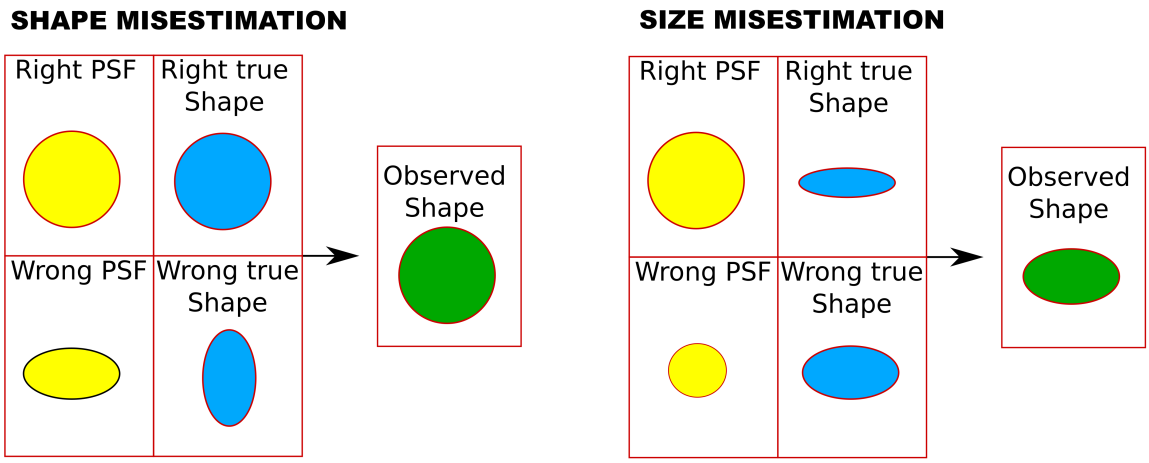

Figure 7.1: Diagram illustrating possible consequences of missestimation of the PSF

fig. 7.1, where we show possible consequences of error in the PSF modeling. In the l.h.s, we present the case when instead of an actual round PSF, we estimate an elliptical one. If we observe a round shape, then our true shape after PSF correction would be in the opposite direction, trying to compensate. Then we need to correct subtracting to the true shape the estimated one, which corresponds to the second term of eq. (7.2). Similarly, if we determined a smaller round PSF, and we observe an elliptical shape, then our estimated true shape will be less elliptical that actually should be. Then, we need to correct subtracting to the real observed shape the estimated, which corresponds to the third term of eq. (7.2).

Notice that e^* and T^* can only be obtained at the stars, and therefore $e^{\rm p} - e^*$ and $T^{\rm p} - T^*$ must be obtained at a set of "reserved" stars which are not used in the modeling algorithm. For simplicity, we can rename the terms on eq. (7.2) as $q \equiv e^* - e^{\rm p}$ and $w \equiv e^* \left(T^* - T^{\rm p}\right)/T^*$, then

$$\delta e^{\rm sys}_{\rm PSF} = \alpha e^{\rm p} + \beta q + \eta w. \tag{7.3}$$

In order to solve for the 3 unknown coefficients, we correlate the observed shear of galaxies eq. (7.1) with each of the e^p, q, w terms. Assuming that the true cosmic signal γ does not correlate with any of them, we can write the following equations

$$\left\langle e^{\rm gal} e^{\rm p} \right\rangle = \left\langle \delta e^{\rm sys}_{\rm PSF} e^p \right\rangle + \left\langle \gamma \right\rangle \left\langle e^p \right\rangle \tag{7.4}$$

$$\left\langle e^{\rm gal} q \right\rangle = \left\langle \delta e^{\rm sys}_{\rm PSF} q \right\rangle + \left\langle \gamma \right\rangle \left\langle q \right\rangle \tag{7.5}$$

$$\left\langle e^{\rm gal} w \right\rangle = \left\langle \delta e^{\rm sys}_{\rm PSF} w \right\rangle + \left\langle \gamma \right\rangle \left\langle w \right\rangle . \tag{7.6}$$

Although we expect $\langle\gamma\rangle = 0$ in the whole sky, it is preferred to avoid dealing with this term, this can be done if we instead correlate mean subtracted quantities, i.e , any field x will be transformed to

$$\boxed{x' = x - \langle x\rangle\,,} \tag{7.7}$$

note that by definition all those modified fields satisfies $\langle x'\rangle = 0$. Considering this transformation and introducing eq. (7.3) in eqs. (7.4) to (7.6) we now have

$$\left\langle e^{\mathrm{gal}'} e^{\mathrm{p}'}\right\rangle = \alpha\left\langle e^{p'} e^{p'}\right\rangle + \beta\left\langle q' e^{p'}\right\rangle + \eta\left\langle w' e^{p'}\right\rangle \tag{7.8}$$

$$\left\langle e^{\mathrm{gal}'} q'\right\rangle = \alpha\left\langle e^{p'} q'\right\rangle + \beta\left\langle q' q'\right\rangle + \eta\left\langle w' q'\right\rangle \tag{7.9}$$

$$\left\langle e^{\mathrm{gal}'} w'\right\rangle = \alpha\left\langle e^{p'} w'\right\rangle + \beta\left\langle q' w'\right\rangle + \eta\left\langle w' w'\right\rangle \tag{7.10}$$

We can write the resulting correlations in terms of the mean-subtracted version of the rho-statistics

$$\boxed{\begin{aligned} \rho'_0 &= \left\langle e^{p'} e^{p'}\right\rangle \quad , \quad \rho'_1 = \left\langle q' q'\right\rangle \quad , \quad \rho'_2 = \left\langle q' e^{p'}\right\rangle, \\ \rho'_3 &= \left\langle w' w'\right\rangle \quad , \quad \rho'_4 = \left\langle q' w'\right\rangle \quad , \quad \rho'_5 = \left\langle e^{p'} w'\right\rangle, \end{aligned}} \tag{7.11}$$

where a extra rho-stat ρ'_0 was included to the set of definitions [34], the primed notation in the rho -stats was used to distinguish labels but the only fields being mean subtracted are the shapes and residuals, not the full correlations. To make notation even more compact we define tau-stats as

$$\boxed{\tau'_0 = \left\langle e^{\mathrm{gal}'} e^{p'}\right\rangle \quad , \quad \tau'_2 = \left\langle e^{\mathrm{gal}'} q'\right\rangle \quad , \quad \tau'_5 = \left\langle e^{\mathrm{gal}'} w'\right\rangle} \tag{7.12}$$

then eqs. (7.8) to (7.10) becomes

$$\tau'_0 = \alpha\rho'_0 + \beta\rho'_2 + \eta\rho'_5 \tag{7.13}$$

$$\tau'_2 = \alpha\rho'_2 + \beta\rho'_1 + \eta\rho'_4 \tag{7.14}$$

$$\tau'_5 = \alpha\rho'_5 + \beta\rho'_4 + \eta\rho'_3. \tag{7.15}$$

Basically, the r.h.s of eqs. (7.13) to (7.15) is obtained directly from the reserved stars, while the l.h.s involves correlating the observed galaxy shapes e^{obs} with PSF fields. The l.h.s. taus are computed using `MetaCalibration` shape catalog, so we divide those statistics by the total shear and selection response R [46] .

It is important to recall that the idea here is not to solve the system of equations in each scale, but instead use all of the equation to solve a fitting problem, i.e. to find the best parameters α, β and η that match our model with the measurements up to the scales where errors in the correlations are trustworthy. Given the definition of the model and data vector in eqs. (7.13) to (7.15), we define our fitting problem as the maximization of

the likelihood function

$$\mathscr{L} = |C|^{-1/2} \exp\left(-\frac{\mathbf{d}^T \mathbf{C}^{-1} \mathbf{d}}{2}\right), \tag{7.16}$$

where

$$\begin{aligned}\xi_p = \big[&\alpha(\rho'_{0+} + \rho'_{2+} + \rho'_{5+}), \alpha(\rho'_{0-} + \rho'_{2-} + \rho'_{5-}),\\ &\beta(\rho'_{1+} + \rho'_{2+} + \rho'_{4+}), \beta(\rho'_{1-} + \rho'_{2-} + \rho'_{4-}),\\ &\eta(\rho'_{3+} + \rho'_{4+} + \rho'_{5+}), \eta(\rho'_{3-} + \rho'_{4-} + \rho'_{5-})\big],\end{aligned} \tag{7.17}$$

$$\hat{\xi} = [\tau_{0+}, \tau_{0-}, \tau_{2+}, \tau_{2-}, \tau_{5+}, \tau_{5-}] \tag{7.18}$$

and $\mathbf{C}$ is the covariance matrix of the data vector $\hat{\xi}$. Note that in the definition of the model and data vectors, we include both positive and negative correlation (see section 3.9), although positive correlations are larger, we want to include also negative ones because we want to carry as much information as possible. Bear in mind that we are using a compact notation, and the full model vectors and data vector are the concatenation of all the summary stats.

The expected contamination to the true cosmic shear signal $\xi_+^{ij} \equiv \left\langle \gamma^i \gamma^j \right\rangle_+$ is then

$$\xi_+^{ij'(\mathrm{obs})} = \left\langle e^{i'}_{\mathrm{obs}} e^{j'}_{\mathrm{obs}} \right\rangle = \left\langle (\gamma^{i'} + \delta e^{i'}_{\mathrm{sys}})(\gamma^{j'} + \delta e^{j'}_{\mathrm{sys}}) \right\rangle \tag{7.19}$$

$$\xi_+^{ij'(\mathrm{obs})} = \xi_+^{'(t)} + \left\langle \delta e^{i'}_{\mathrm{sys}} \delta e^{j'}_{\mathrm{sys}} \right\rangle, \tag{7.20}$$

where cross terms does not appear because the true cosmic signal does not correlate with $\delta e^{i'}_{\mathrm{sys}}$ and we are also using mean subtracted quantities. Introducing eq. (7.3) in eq. (7.20) we get

$$\xi^{ij'}_{+\mathrm{obs}} = \xi^{ij'}_{+t} + \left\langle (\alpha^i e^{p'} + \beta^i q' + \eta^i w')(\alpha^j e^{p'} + \beta^j q' + \eta^j w') \right\rangle \tag{7.21}$$

$$\boxed{\begin{aligned}\xi^{ij'}_{\mathrm{obs}} = \xi^{ij'}_{+t} + \alpha^i \alpha^j \rho'_0 + \beta^i \beta^j \rho'_1 + \eta^i \eta^j \rho'_3 + \left(\beta^i \alpha^j + \beta^j \alpha^i\right) \rho'_2 +\\ \left(\alpha^i \eta^j + \alpha^j \eta^i\right) \rho'_5 + \left(\beta^i \eta^j + \beta^j \eta^i\right) \rho'_4,\end{aligned}} \tag{7.22}$$

where we have assumed that α, β and η are uncorrelated between different redshift bins.

In the deduction of eq. (7.22), we have used tomography notation. This is essentially performing the analysis independently for galaxies in a particular redshift bin (or equivalently studying the samples from different periods of the universe). In our case, we are working with four tomographic bins. Then this corresponds to solve eq. (7.16) four times, i.e., we want to obtain twelve independent parameters. Tomography results advantageously in the estimation of cosmological parameters because it might help to break degeneracies between parameters.

7.2 Results of $\alpha\beta\eta$ test

In the previous section, we condensed the problem of studying additive PSF bias to the measurements of some summary statistics. In one hand, the modified version of rho-stats eq. (7.11), and on the other correlations galaxy-reserved-stars that we called tau-stats eq. (7.12). The bias of the shear two-point correlation function will be determined by the rho-stats and a set of twelve parameters, α, β, and η, one per each redshift bin. This set of parameters will determine how much each rho-stat will contribute to the final PSF bias. And we use tau-stats to solve the fitting problem and find them.

Our first step is then to perform accurate measurements of these summary statistics. For this porpoise, we used the stars PSF catalog obtained using some of the steps described in section 6.1, and the galaxy catalog Y3 `MetaCalibration`[47], which is the galaxy catalog used to do cosmic shear for the year three analysis of DES. All the rho-stats and tau-stats were obtained using the package `TreeCorr` [48], which in our particular case calculates error bars using shape noise propagation (see the propagation of shape noise error in appendix J).

In fig. 7.2, it is shown the mean subtracted rhos-stats. In general, what we expect is these correlations to be as close to zero as possible. In weak lensing, typically, galaxies are distorted their shape by 1%; consequently, we might expect that the shear 2PCF has values smaller than 10^{-4}. Then, as close to zero as possible means several orders of magnitude smaller than 10^{-4}. We can observe that this statement is true for all the rhos-stats except for ρ_0. However, its contribution to the contamination of the shear two-point function will be suppressed by the leakage parameter α as we will present later. From the definition ρ_- (section 3.9) these correlations are smaller than ρ_+.

In order to measure taus, we need initial information of the redshift distribution of galaxies, since we need it to perform the tomographic analysis. In fig. 7.3 is presented the preliminary population of the sources for Y3 weak lensing analysis. DES is not a spectroscopic survey redshift of galaxies are estimated using multi-band photometry, i.e., the redshift of the sources is not determined as direct measurement, instead, we can estimate its PDF. Once known the PDF, we can assign a photometric redshift using the mean and from all the sources estimate the full PDF associated with the occupation probability, which is what is depicted in fig. 7.3. Notice that although the occupation probabilities can overlap, this does not mean we are not able to assign a redshift bin for each galaxy. In fact, the inverse process is done. First, we determine the photometric redshift edges, and from them, we assign galaxies, then using each PDF, the final PDF of all the sources is obtained.

In fig. 7.4 are the measures of taus for the Y3 preliminary redshift binning. We observe that in general, these statistics are larger than rhos, which is expected given one of the fields in the 2PCF corresponds to galaxies. On the other hand, $\tau_-(\theta)$ are around one order

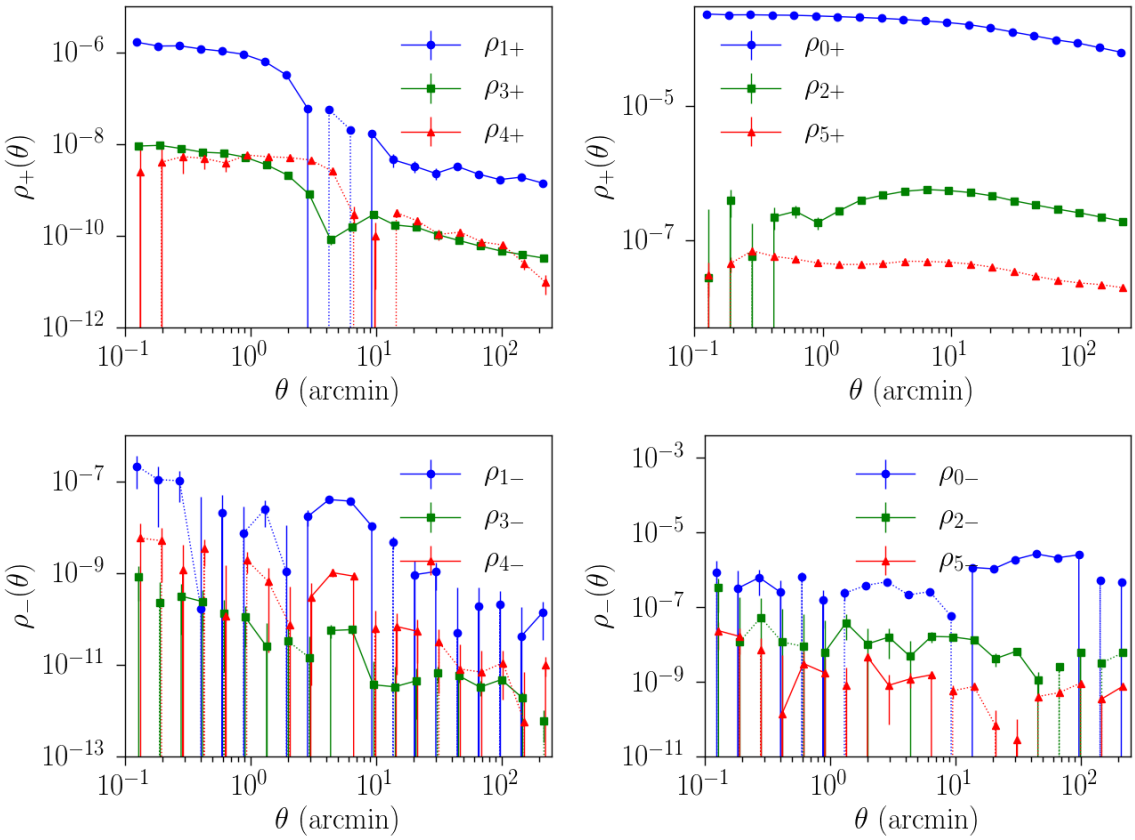

Figure 7.2: Summary statistics of PSF residual using reserved stars (mean subtracted rho-stats). In top are the ξ_+ correlation which is the addition of the two point function of the tangential and cross components. In bottom are ξ_- correlations which correspond to the subtraction of cross and tangential two point functions. Given that those correlations can have positive and negative values and we are using a log-log plot we have defined the convention of trace a dashed line joining point with negative values.

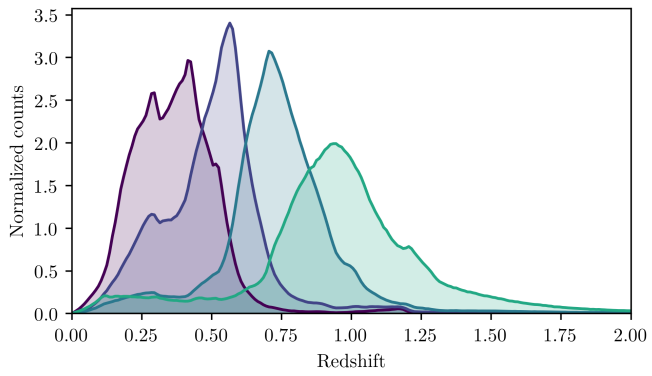

Figure 7.3: Preliminary redshift distribution for galaxies for Y3 analysis of DES

of magnitude smaller in comparison to their $\tau_+(\theta)$ associated, as in the case of rho-stats this is also expected given their definitions. Also notice that in general $|\tau_{0+}| > |\tau_{2+}| > |\tau_{5+}|$ this is a consequence of the different PSF fields involved, in general we have that PSF shapes > PSF shape residuals > PSF size residuals. Finally, when comparing the behavior of the taus stats for different redshift bins, it can be observed similar decreasing behavior when going to large scales, and normal fluctuations in some scales associated with sample variance. The similarity of the 2PCF is expected given that we are using the same PSF local field, and the statistical properties of the shear field do not change significantly for our redshift binning. The decreasing effect is produced because angular bins in log scale, large scales have more pairs, indeed, this behavior should also be observed in the rho-stats. However, there are some few rho-stats with not decreasing behaviour, and it is a topic for further research.

The next step in our analysis is to test how good are the statistical errors of our summary stats. First, note that the model we are using is involving measurements. Therefore they have an associated error. Strictly speaking, the covariance matrix in eq. (7.16) must consider both rho-stats and tau-stat errors, and this is a more complex problem. However, as it is depicted in fig. 7.5, the rho-stats errors are sub-dominant in comparison to tau-stats errors. This is true for each equation in eqs. (7.8) to (7.10). As a result, we will be able to assume the covariance matrix in eq. (7.16) is the same as the taus covariance matrix. Second, given that we are using only one realization of the galaxy catalog, important error contributions such as sample variance are not being considered (see section 5.2). We need to bear in mind that at large scales, shape noise gets subdued loads, and these other noise contributions become important. In fig. 7.5, we have used only shape noise error, therefore when considering sample variance, full errors of tau-stats are even greater than rho-stats errors, making our assumption about the tau errors to be dominant stronger. Rho-stats do not have sample variance because we are studying a unique PSF field for our Survey, and the PSF field is independent of the realization observed.

Once we measure all the diagnostics and summary statistics, we found α, β, and η parameters using three different approaches. First, we only use a convenient scale range where shape noise errors are dominant. Second, we include sample variance errors performing a Jackknife sampling, and we solve the fitting problem using the full range of scales. And third, we use FLASK[49] simulations.

7.2.1 Initial guess using only shape noise and an appropriate scale range

To get an initial guess of the $\alpha\beta\eta$, we will assume that exist a characteristic maximum scale up to which shape noise will be dominant over cosmic variance (see section 5.2). If

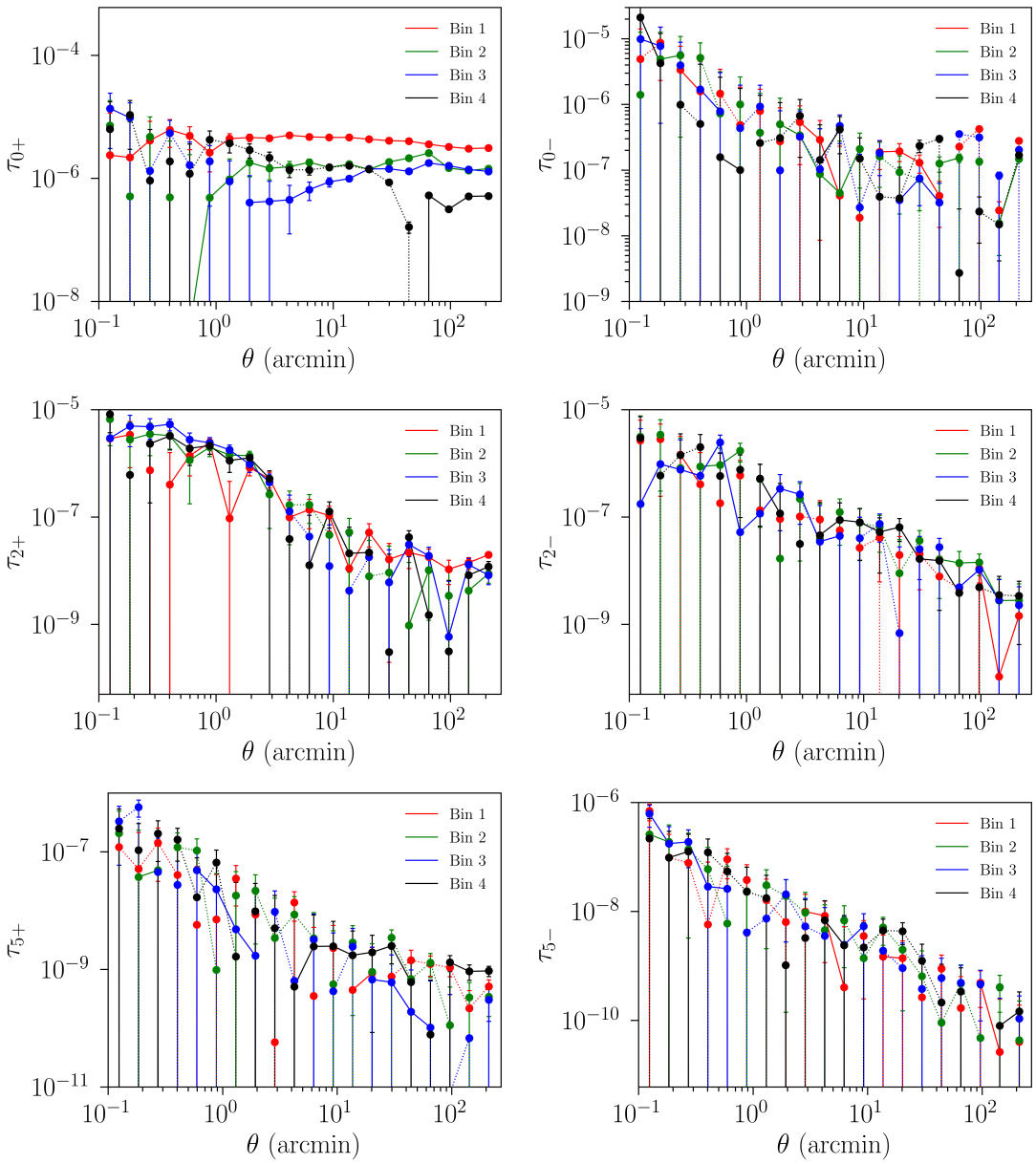

Figure 7.4: Summary statisc of PSF residual of reserved stars and galaxies (mean subtracted taus)

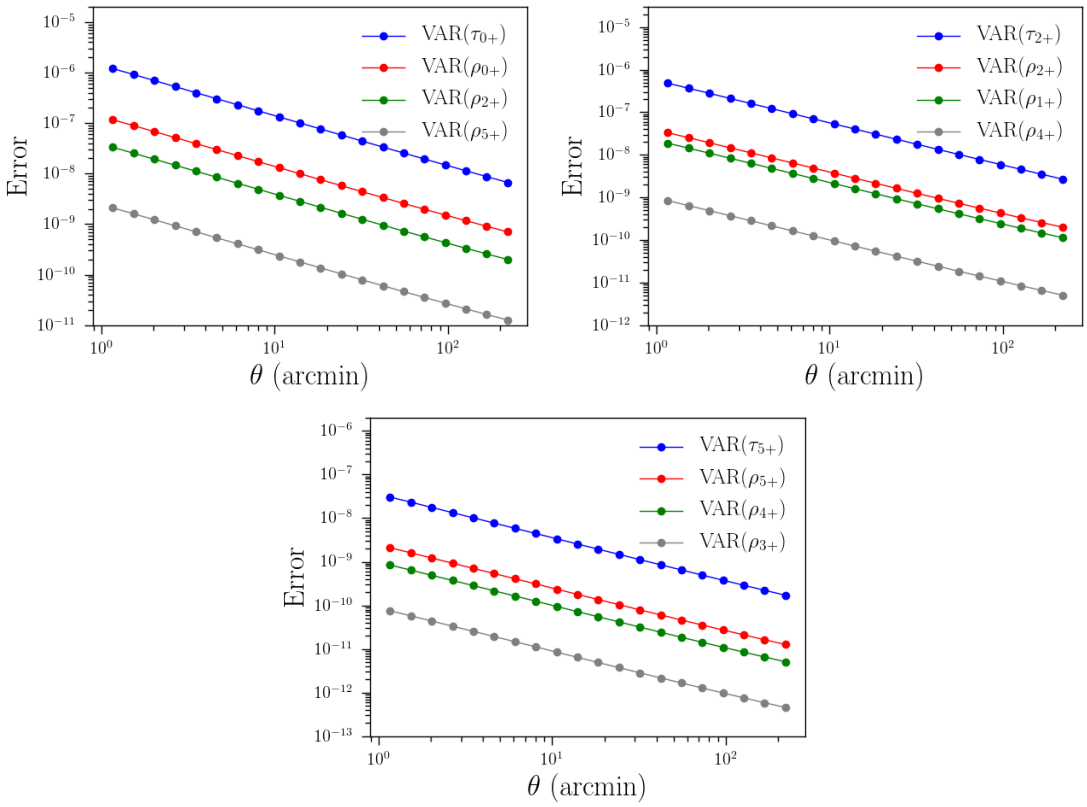

Figure 7.5: Shape noise errors as a function of the scale for rho-stats and tau-stats.

this is true, we can assume a diagonal covariance without sample variance contribution. This assumption eases the analysis. However, we will see that reducing the analysis to a smaller range of scales first makes our fitting less informative (mainly because $\alpha\beta\eta$ are scale independent), and second we are not confident of the effects that sample variance can have. Nevertheless, it worth to do this first analysis as a starting point to check that further analysis using a full range of scales and sample variance errors do not go so far from this initial result. It is more convenient to think in this initial guess as a prove that cosmic variance errors are essential in tau-stats, rather than the final estimates.

The selection of the lowest scale will be based on the variation of rho-stats in small scales. Rho-stats not only are diagnostic functions of our PSF field, but they also are the constituents of our model of the PSF bias. We will see in detail later that the number of bin pairs increases as a power law when our angular binning is uniform in log-scale. As a consequence, when we go down to small scales, our summary stats are noisier. Thus, we need to select the limit in low scales used for fitting carefully. A signal that we probably are exceeding the smallest scale would be an abrupt change in any of the rho-stats in comparison with the overall behavior of the full function. If that happens, it means that our PSF bias model will be affected because, at those scales, we did not have enough statistics to have an accurate estimate of the rho-stats, making noise dominates over the signal.

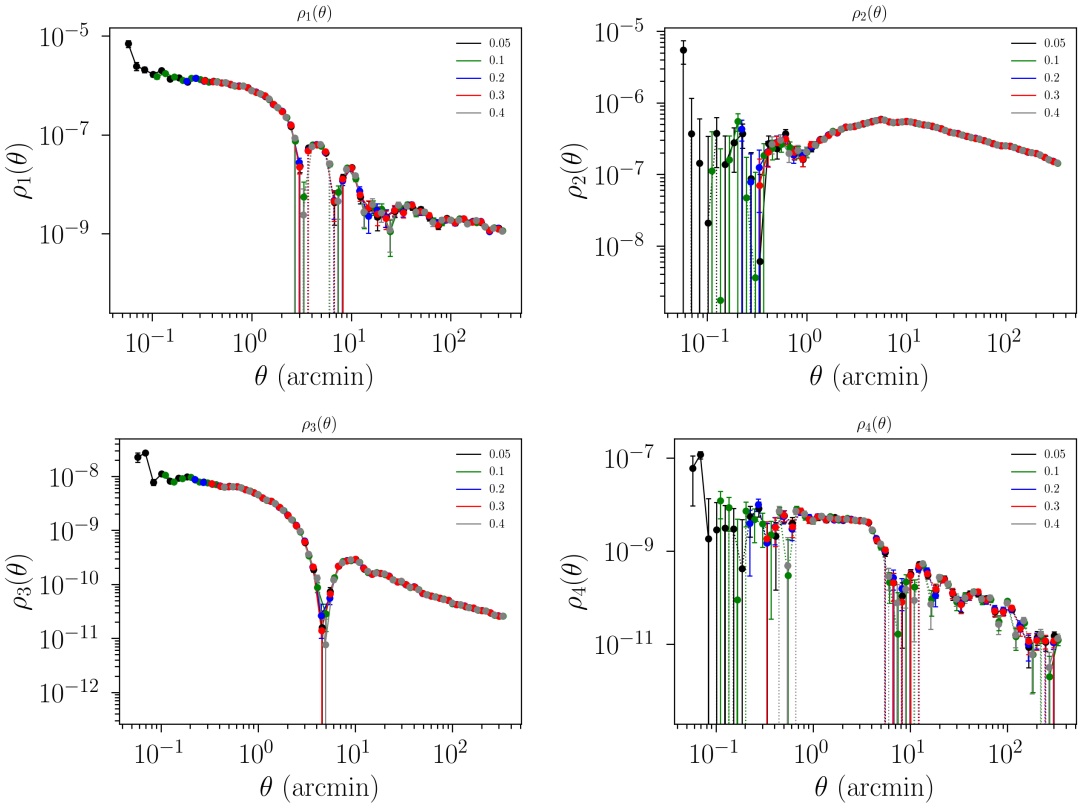

Figure 7.6: $\rho_+(\theta)$ varying the smallest scale from 0.05 to 0.4 arcmin.

In fig. 7.6 and fig. 7.7 we observe the results of the measurements of $\rho_+(\theta)$ for different low scale limits, where we have used the same bin-size in log scale to make stats comparable. First, notice that for scales larger than 0.4 arcmins, all rho-stats are almost the same as expected. There are some small fluctuations associated with the accuracy of the bin-size, which is not let fixed to compute correlations faster[1]. Second, we are interested in abrupt changes of any of the rho-stat in the scales between 0.05 and 0.4 arcmins. In fig. 7.7, we observe this effect when the low scale limit was 0.05 arcmin, meaning that we have exceeded the noise of the rho-stats. Consequently, we have decided to use 0.1 arcmin as our low limit in angular scales for estimating $\alpha\beta\eta$.

On the other hand, to define a superior limit of the angular scales, we need to have proper error estimation at large scales. Moreover, it is still not well understood why rho-stats do not continue decreasing at large scales. For our analysis, we will be conservative, and we will select the maximum scale limit used in Y1 analysis. In the next two sections, we return to this sample variance discussion. By the moment, let's define the maximum scale analyzing the inverse problem, i.e., finding $\alpha\beta\eta$ parameters varying the maximum scale, and figure it out the point where estimated parameters start to diverge. This demands to be able to estimate $\alpha\beta\eta$ and their errors more than once, but we have only measured one realization of the sky. What we are going to do is to split the Y3 DES

[1]The bin_slop parameter in Treecorr defines this. These fluctuations are so small that we are confident they would not affect science

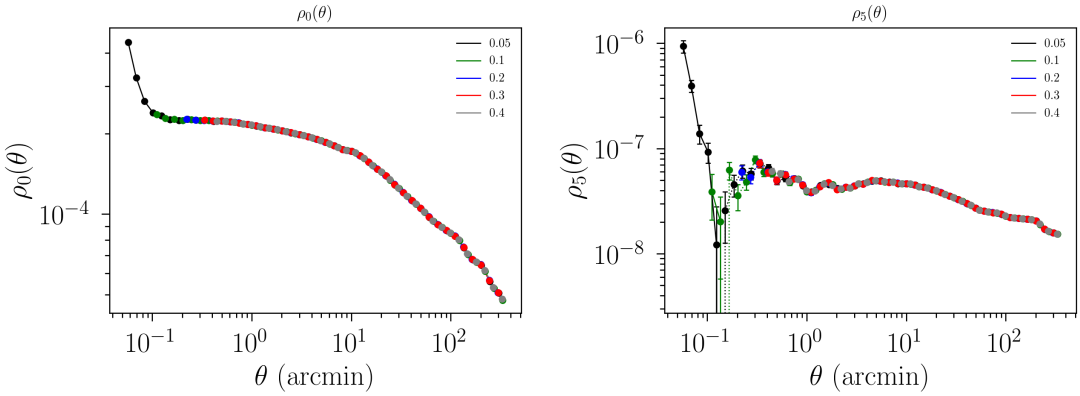

Figure 7.7: $\rho_{0+}(\theta)$ and $\rho_{5+}(\theta)$ varying the smallest scale from 0.05 to 0.4 arcmin. From this two rho-stats can be better appreciated that a smallest scale of 0.05 arcmin would introduce more noise than signal. Then we define the low limit scale as 0.1 arcmin

footprint into four patches and assume that each one is an adequate sub-sample of the full footprint. Thus the solutions corresponding to different patches should not diverge significantly.

In fig. 7.8 are depicted the four regions used to solve our problem. In fig. 7.9 are the variations in the estimation of $\alpha\beta\eta$ varying the maximum scale, and fixing the minimum scale to 1 arcmin. Error bars are one sigma confidence interval of the marginalized posterior distributions.

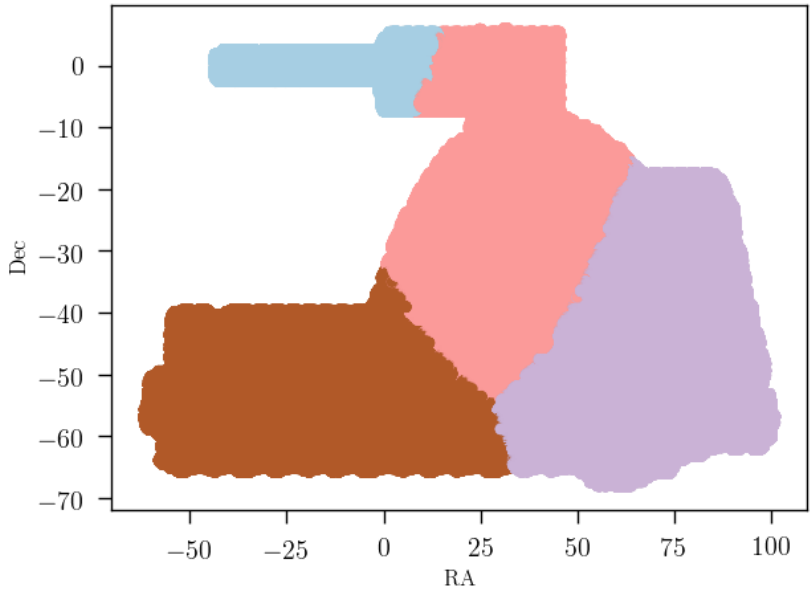

Figure 7.8: Regions of the footprint to test the validity of the maximum scale for the analysis. They have approximately same area and the indexes of the objects in each region were obtained using the software `kmean_radec`

First notice that the error bars for low scales are extremely large, this is just a consequence of the lack of data points. Despite this huge error bars mean values and errors

match for the three parameters in those scales. However, while going to large scales, error bars become more restrictive, and the overlap between error bars does not hold anymore. Where mean values of the parameters and their error bars do not match for any of the three parameters will be our maximum scale for the fitting . If you observe the behavior of the three parameters in fig. 7.9, you will see that a scale of around 15 arcmins is a profitable choice. We could have been more restrictive performing with tomography.

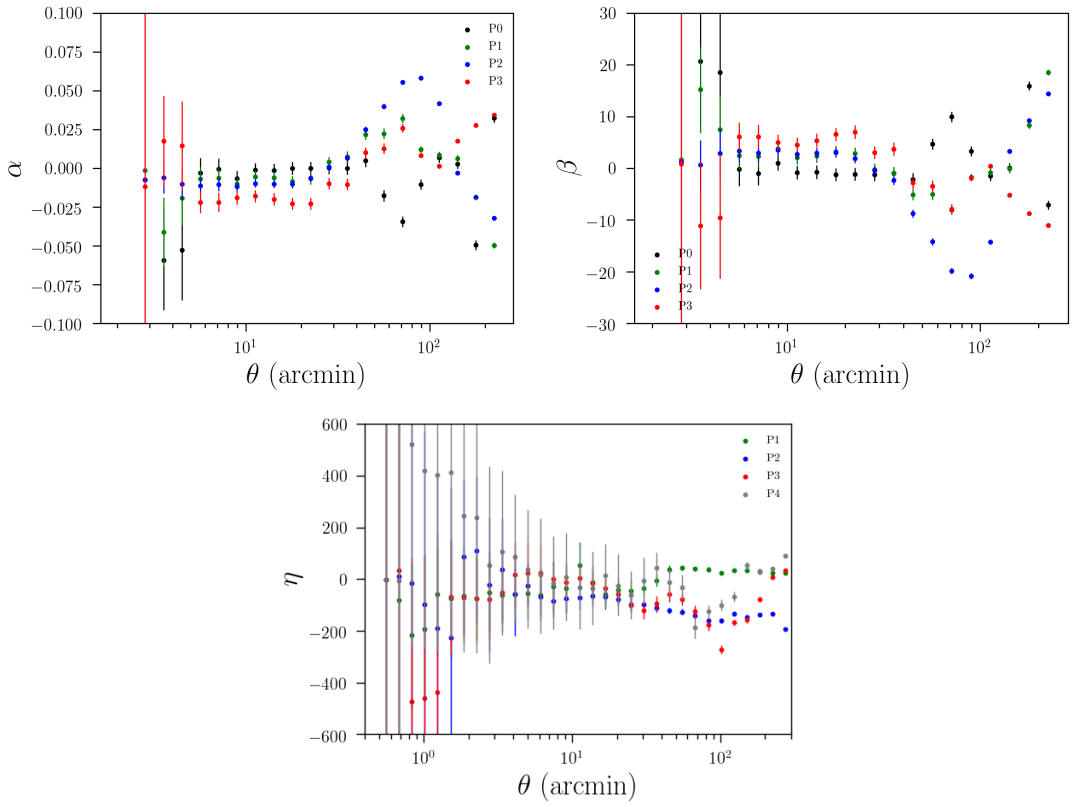

Figure 7.9: Solution of the fitting problem for four independent patches. It was used a min scale of 1 arcmin, and the maximum scale corresponds to the point where the parameter is calculated

However, this is an initial guess, and we will assumethe variance in the estimation of $\alpha\beta\eta$ between different tomographic bins is negligible.

Once defined the angular limits for the fitting, we perform a MCMC sampling of the posterior distribution eq. (7.16). From the marginalization of the posterior, we obtain the best fits. In our case, given the symmetry of the distribution, the best fits parameters would be the mean of the marginalization, and from here, the confidence intervals are defined. For the MCMC sampling, we used the code *emcee* [50], and after confirming the convergence of the MCMC chains, we found the set of parameters and their 1σ confidence interval, which are presented in table 7.1. In fig. 7.10 are the sampled posterior, correlations among parameters and 1σ, and 2σ contours plots for the second tomographic bin. A similar process and results are obtained for the other bins. Note there is a positive cross-correlation between α and η, a negative cross-correlation between α and β, and a small

	Bin1	Bin2	Bin3	Bin4
α	$0.023^{+0.001}_{-0.001}$	$0.002^{+0.001}_{-0.001}$	$-0.003^{+0.001}_{-0.001}$	$-0.016^{+0.001}_{-0.001}$
β	$1.538^{+0.271}_{-0.270}$	$2.260^{+0.319}_{-0.327}$	$2.857^{+0.295}_{-0.312}$	$2.317^{+0.329}_{-0.331}$
η	$0.239^{+2.813}_{-2.710}$	$-2.732^{+3.472}_{-3.386}$	$1.960^{+3.180}_{-3.286}$	$0.396^{+3.420}_{-3.574}$
χ_ν	1.245	0.922	1.071	0.844

Table 7.1: $\alpha\beta\eta$ estimated values and 1σ confidence intervals using shape noise errors and a limit in large scales of 15 arcmin. Ndf = 117.

positive cross-correlation between β and η. These cross-correlations among parameters could have a significant contribution to the estimation of the errors of the bias eq. (7.22).

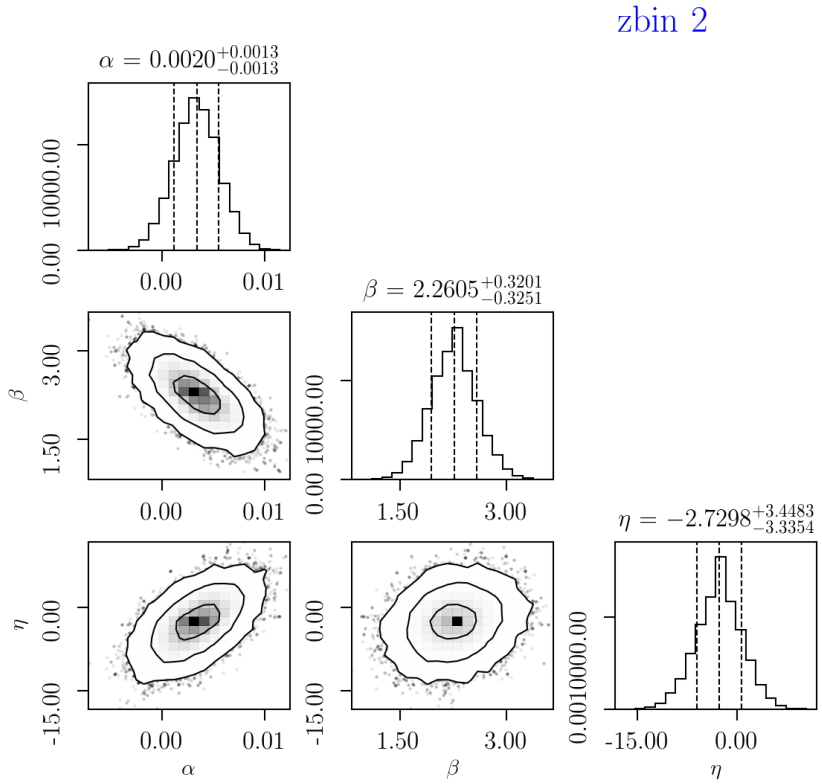

Figure 7.10: Solution of the fitting problem for the whole footprint up to 15 arcmins for the redshift bin 2.

We conclude that despite all the approximations, fittings are almost consistent with expected values using unweighted moments. β, in particular, get away the expected value of one. However, this is not a warning signal, but only an indicator that our measurements are far from unweighted moments, which is expected. The important fact is that we are not extremely far from it, which would be an indicator of significant systematic errors. Particular attention must be given to the η extra parameter, which is more uncertain.

The resulting χ_ν values in table 7.1 are an indicator that the proposed model reproduces observations, and we can be confident that the estimation is adequate from 0.1

arcmins to 15 arcmins. However, the right full problem should also match large scales. In fig. 7.11 is presented the comparison of the different data measures (taus) and the model best fit. In overall we see that all the best fits are inside the regions of data scatter considering error bars, looking for each redshift bin there are few points out of the best fits, given there is not a clear pattern of a region where these points are, we can see the fitting describes well all the implemented scales.

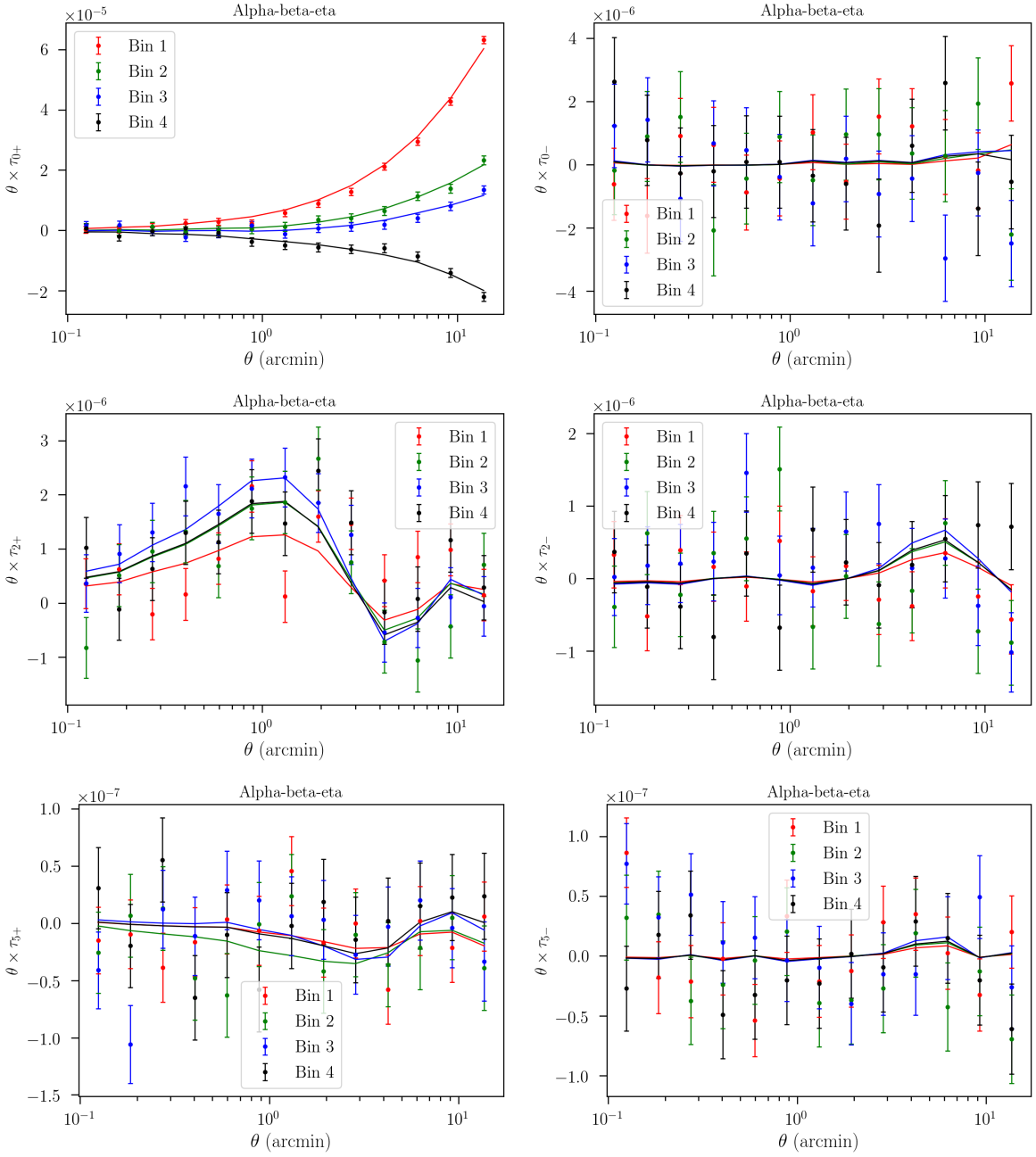

Figure 7.11: Best fits obtained, as data points are taus correlations, and as continuous curve the product of estimated mean values of $\alpha\beta\eta$ and rho-stat model vector as defined in eqs. (7.13) to (7.15)

Using this initial set of parameters, we can contaminate fiducial cosmology to study consequences in final estimates. However, we will let this process to the end, where we

will compare the three different approaches for error modeling.

7.2.2 Getting $\alpha\beta\eta$ using Jackknife sampling

The next step to improve our preliminary result for the fitting of the parameters is to consider proper modeling for the taus covariance matrix, including not only shape noise as we did before but also sample variance. Sampling modeling will allow going to larger scales than 15 arcmins. To do this more consistent estimation, we implement a Jackknife sampling. Statistically speaking Jackknife method tries to measure the bias of an estimation. In most of the statistical analyses, we do not measure the full population, but instead, we get access to a sample. However, the selection of a particular sample can introduce a bias in the estimates, and we are interested in to determine this bias, or equivalently perform an unbiased estimation considering the selection effect. Those are the problems Jackniffe tries to solve. And the way how this is done is by aggregating n observations of n-1 sized subsamples.

Let's translate this to our particular case. In general terms, we are interested in considering variations of our tau-stat as a consequence of observing a specific sample. In our case, this particle sample means two things. First, we see a particular region of the sky, and second, we are observing a specific realization of the universe. Of course, we are not able to change the realization of the universe, nevertheless as mentioned in chapter 5 the sampling variance related to the observation of a particular region is more relevant. This is the cosmic variance in eq. (5.4), and Jackknife can help us to include this effect in our estimate of taus.

Our first concern is how to do the subsampling of taus. Tau measures are based on pairs star-galaxy, so we initially can think in our population as all the set of possible pairs star-galaxy. However, regardless of the particular binning the number of pairs is in the order of the number of galaxies times the number of stars, this for one of our specific redshift bin corresponds to 10^{14} pairs approximately, so it is excessive expensive calculate taus by subsampling each pair. The conventional approach for the sampling is then to divide the footprint in patches of approximately the same area. In fact, we did this in the previous subsection initial estimate. The difference now is that we are going to divide the footprint into 1000 patches, and each taus subsample will correspond to a measure removing stars and galaxies of the ith patch, leading to a subsample of 1000 taus.

The selection of how many regions are convenient for the subsampling depends on contrasting two effects. On the one hand, the more regions, the more samples, and as a consequence, our covariance matrix can overcome the noise. An appropriate number of samples is determined by the number of data points involved in the fitting. In general, we want the number of samples to be significantly larger than the number of data points. On the other hand, too many regions imply that the area of each patch will be smaller,

and given that the calculation of taus depends on the angular distance between pairs, we can not be confident of errors in angular scales greater than the characteristic size of the patch. In other words, there is a trade-off between requiring large enough patches and requiring a sufficient number of patches.

We can make a justification for the selection of one thousand regions as adequate, considering the following. The DES footprint has an area of approximately 5000 degs^2. If we convert this to arcmins, it corresponds to 18 million arcmins^2, dividing by one thousand we have that each patch would have an area of 18 thousand arcmin^2. Finally, approximating each patch to a square, we get that the characteristic size would be around 134 arcmins. Therefore measures involving scales larger than this should be avoided at least if the errors come from Jackknife subsampling. Additionally, our data vector is the concatenation of six tau correlation functions, each with 20 data points, i.e., we have a total of 120 data points. Comparing with the number of samples, there is one order of magnitude difference between both, which is reasonable.

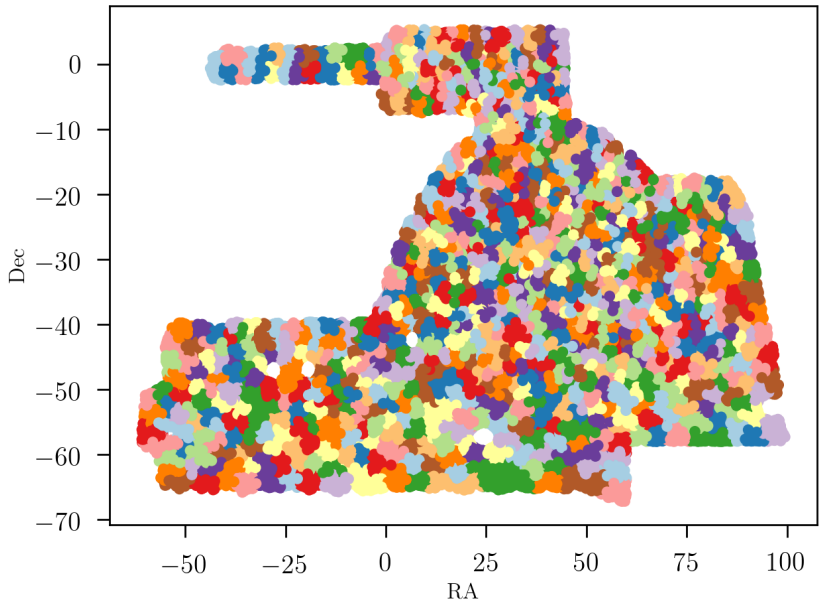

Figure 7.12: 1000 Jackknife patches used to estimate covariance matrix of taus

In fig. 7.12 can be observed the 1000 thousand patches used for the subsampling of taus, for the measure was selected the same small scale limit of 0.1 arcmins. However, to compare with Full-sky Lognormal Astro-fields Simulation Kit (FLASK) errors, which will be presented in the next section, we decided to go beyond this save region of 130 arcmins and define a large scale limit of 250 arcmins. Notice, that here we are not being so unaware, recall that we are using log scale binning, and for these limits, the number of data points exceeds 130 arcmins is only two of the twenty as can be observed in fig. 7.4.

Using one thousand realizations of the DES Y3 footprint obtained from Jackknife subsampling, we can build the taus covariance matrix, where each random variable cor-

responding to the values of one of the six different taus in one of the 20 angular bins, i.e., we have a total of 120 random variables. For analysis porpoises, it is more convenient to plot the correlation matrix. This is the normalization of the covariance matrix by the product of standard deviation of two random variables involved, i.e., $\rho = \frac{\mathrm{COV}(x,y)}{\sigma_x \sigma_y}$.

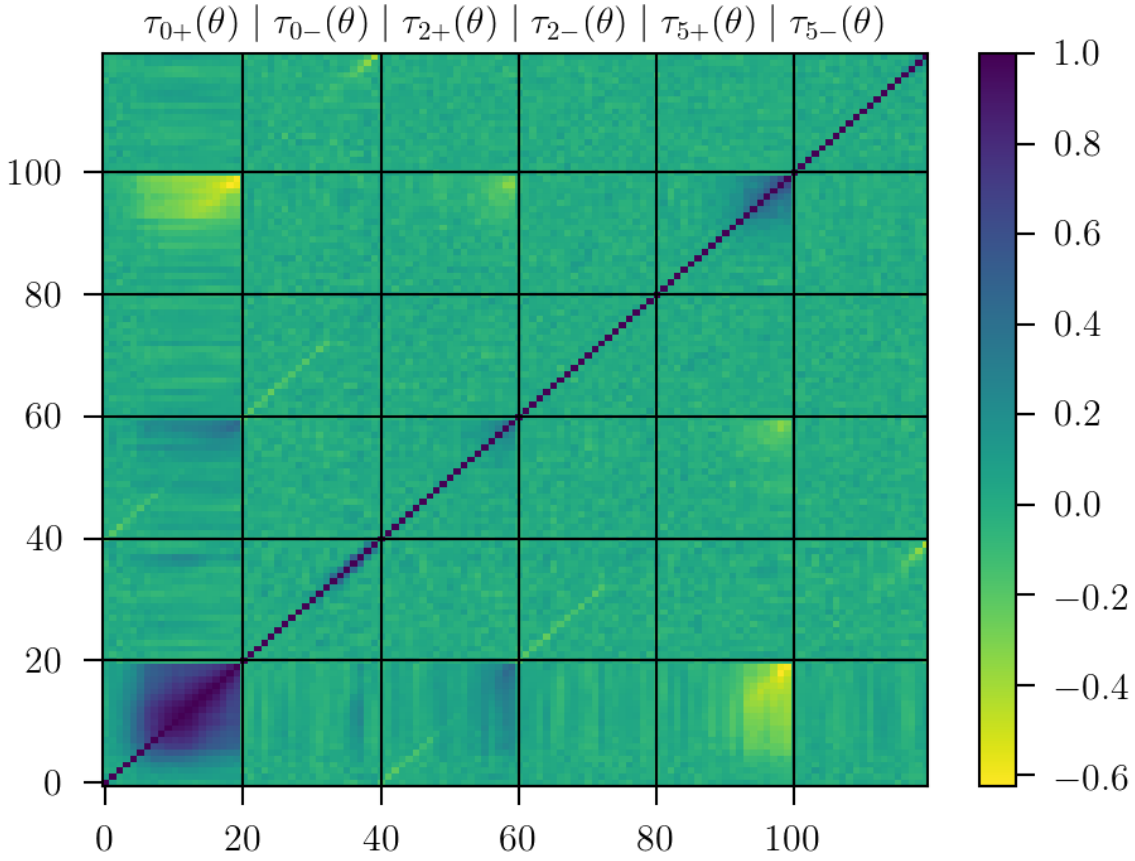

Figure 7.13: Correlation matrix of taus for tomobin 1, were used 1000 Jackknife samples, each tau-stat have 20 data points going from 0.1 arcmin to 250 arcmin in logarithmic uniform binning

In fig. 7.13 is the correlation matrix of taus for galaxies in the first redshift bin. A correlation matrix can take values from -1 to 1, where close to zero values mean there are not correlations, i.e., the occurrence of that random variable in the ith position is independent of the presence of a random variable in the jth place. There are particular regions where we can appreciate correlation among variables. In the main diagonal are the variances (self-correlations). In the correlation matrix they represent a total correlation equal to the unity. However notice that there some other diagonals that correspond to same angular bins of two different τ_+ or two different τ_-, particularly τ_0 anti-correlates with τ_2 and τ_5, and τ_2 correlates with τ_5. The last is not surprising given the definition of w and q both are proportional to e^* (see lines above eq. (7.3) and definition of taus), the former is due to the sign difference of e^p in taus, although in τ_5 there is not an explicit dependence with e^p the term $-T^p$ carries somehow the sign. Another important observation is that τ_0 is highly correlated among cross angular bins in comparison to the

other stats. The reason for this is a consequence of being correlating the same field but different types of objects. From this result can be thought that our galaxy catalog might content stars or the opposite. However, this high correlation is more related to the fact that we measure stars and galaxies shapes in the same way rather than an issue in the star-galaxy separation.

Before solving eq. (7.16), we will select the maximum scale more conservatively. We already said that in our case, 130 arcmins is the characteristic size of patches used for Jackknifing. However, we should go below that scale to be safe. Indeed, now our errors are correct, and we can go further our initial guess of 15 arcmins. To define this new maximum scale limit, we will present in advance errors obtained using simulations, which are advantageous given they do not show these scale limits, and we will talk in detail in the following section.

In fig. 7.14 is depicted the comparison of errors of taus as a function of the angular scale, for three different approaches: using only shape noise propagation, from the diagonal of the covariance matrices using Jackknife sampling and Flask simulations. We can appreciate that all tau-stats that involves residual have errors almost dominant by shape noise as can be recognized in the case of $\tau_{2\pm}$, τ_5 is not entirely dominated by shape noise and sample variance effects appear in large scales. However, size residuals are suppressing the contribution of the e^* in star fields. This suppression does not happen for $\tau_{0\pm}$, and we observe that actually sample variance is starting to influence considerably error from 1 arcmin. The reason why this did not affect our preliminary fit was that this divergence was around only about ten of 85 data points used for the fitting. If we wanted to be extremely conservative, our initial limit should have been one arcmin.

If we look at the perceptual differences in fig. 7.15 we can distinguish another particular scale where errors diverge, particularly this effect is only appreciated clearly for τ_{0+} since for the other stats either shape noise suppresses the standard deviation or this divergence would happen out of the large scale limit of 250 arcmins, this second divergence we could say starts around 40 arcmins, and in fact correspond to the region where the selection of patch size in Jackknife start to produce an underestimation of errors.

Consequently, for $\alpha\beta\eta$ estimation, we will be conservative, and we decide to use a limit on large scales of 40 arcmins. Defined the scale limits for the fitting, we perform an analogous procedure than before. We found the best fit described in table 7.2 and fig. 7.16

Comparing with our initial guess, we now are not only going to larger scales in the process of fitting but also our best fit improved, based on the χ^2_ν criterion.

7.2.3 Getting $\alpha\beta\eta$ using FLASK simulations

Another way to consider the sample variance effect of our measures is by sampling using simulations. For the porpoise of the present work, it was used the code FLASK[49] to

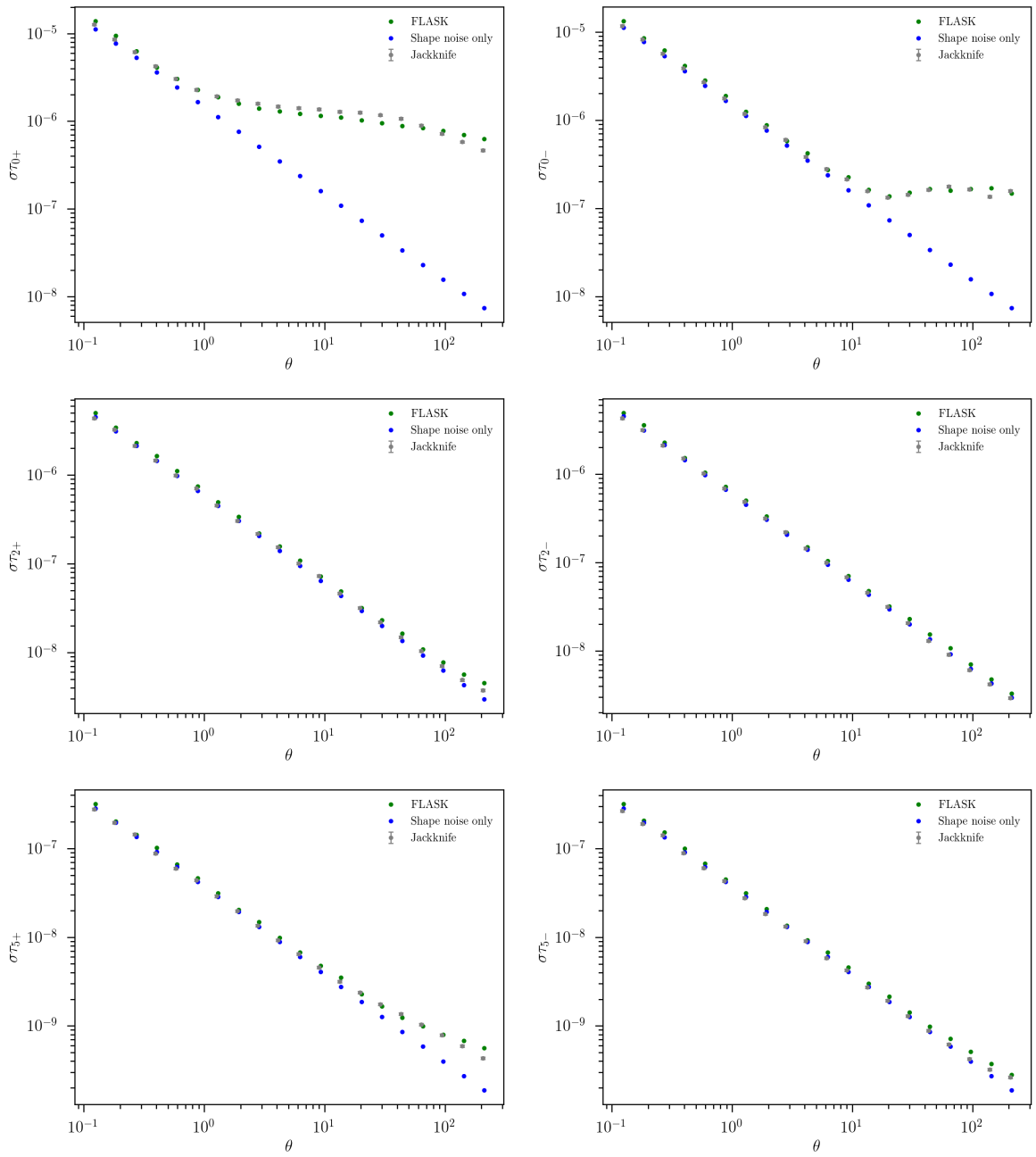

Figure 7.14: Comparison of Jackknife standard deviation against standard deviation using Flask simulations and only shape noise.

perform the simulations. In general terms, a simulation of a shear catalog of galaxies is based on the previous knowledge of the shear distribution function. To give an example, let's analyze the one-dimensional case. If we suppose the distribution of this scalar quantity is a Gaussian, and somehow we know the properties of this particular Gaussian, i.e., its standard deviation. We can produce samples of this scalar that follows the same distribution, where each sample would be a realization of the scalar field. In one dimension, there are several methods for doing this sampling, for instance, Monte Carlo based on the cumulative distribution. However, when we go to higher dimension distributions,

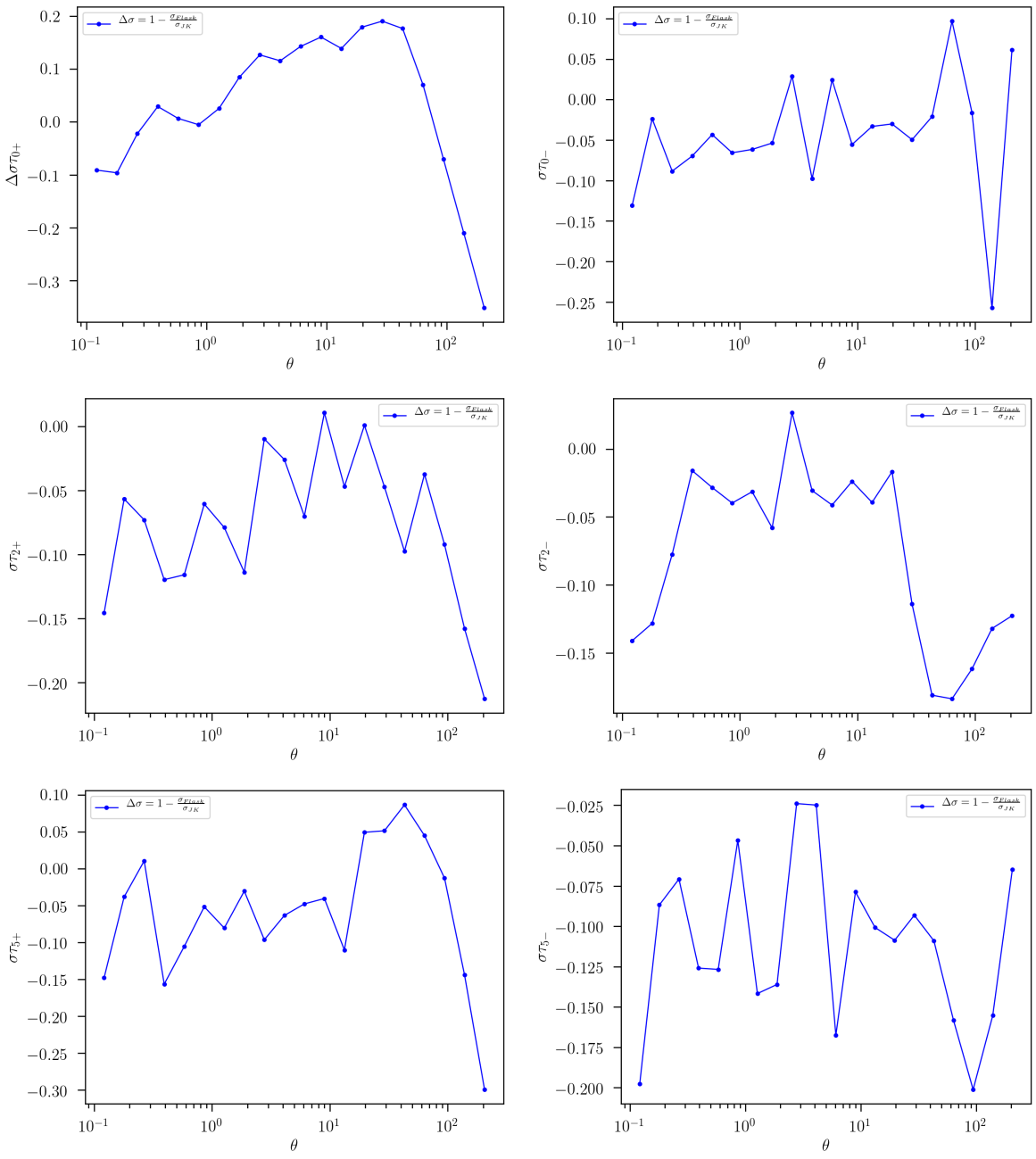

Figure 7.15: Percents difference of errors using Jackknife and Flask simulations

the problem is more challenging, and this idea of using the cumulative distribution is not uniquely determined, and a more complex method has to be implemented, as MCMC to mention one.

In our problem, we are interested in obtaining samples of the shear field. The characteristic property of this two-dimensional distribution would be the shear 2PCF, or even higher moments can be included to study non-Gaussianities. The question now is how can we obtain a realization of shear 2PCF. It is advantageous to think in terms of the Shear Power spectra, i.e., its Fourier transform. In Fourier space, we take advantage of the equality of the shear power spectra and convergence power spectra (eq. (3.92)), and

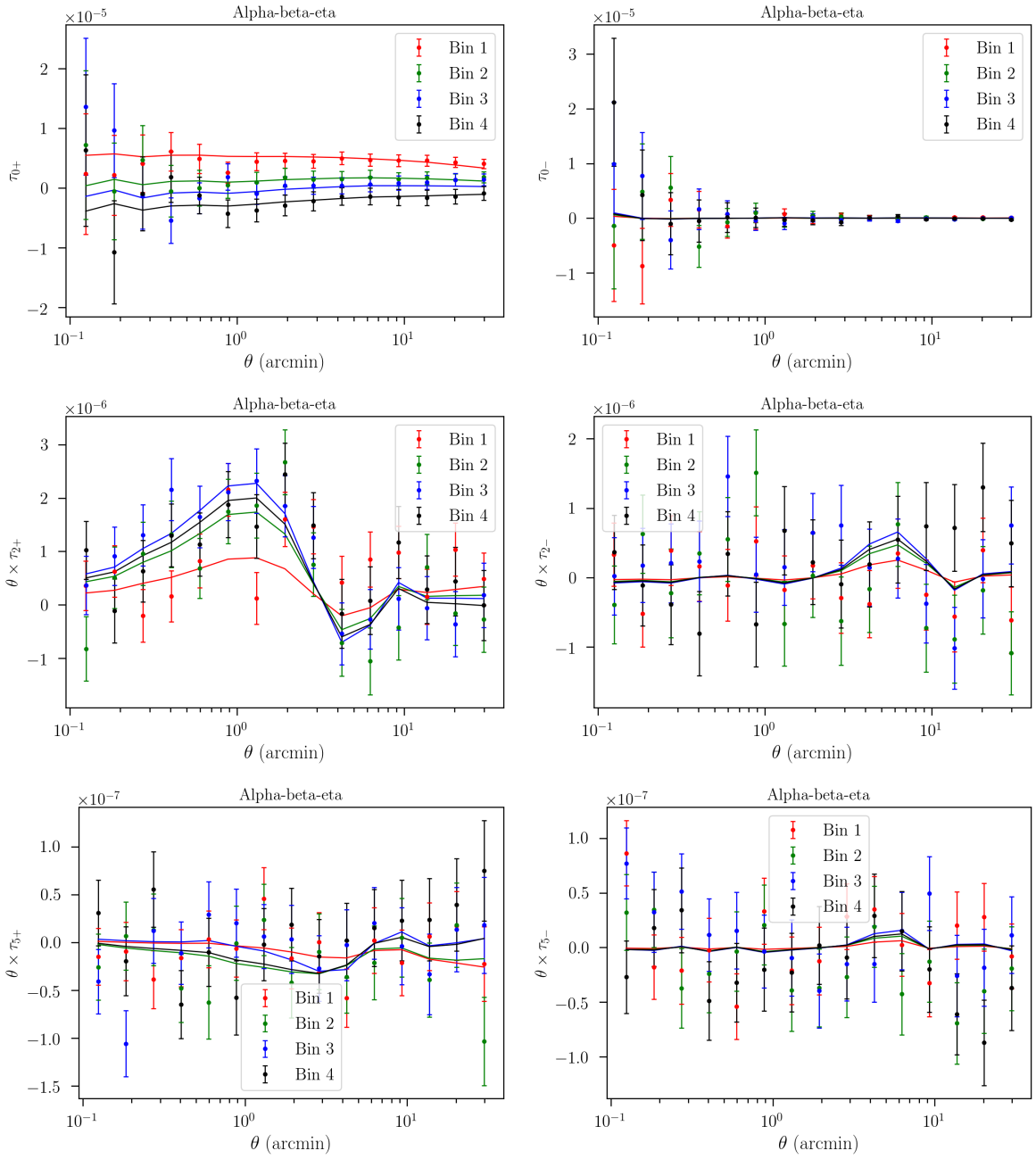

Figure 7.16: Best fits obtained using the covariance errors obtained from sampling with Jackknife. Data points correspond to taus correlations. And continuous curve the product of estimated mean values of $\alpha\beta\eta$ and rho-stat as defined in eqs. (7.13) to (7.15)

given that the convergence power spectra is the Limber's projection of the matter Power spectra (eq. (3.76) and eq. (3.96)) we can have a fiducial distribution of the shear field using the matter power spectra and a fiducial cosmology. And from this fiducial shear field produce several samples or simulations.

The selection of a particular cosmology for the building of the Covariance matrix and its effects in estimates is a topic of continuous research. Some research has been done proving that in the first approximation, cosmological dependent covariance matrix does not affect estimates. Nevertheless, in our case of study, we are using a fiducial cosmology

	Bin1	Bin2	Bin3	Bin4
α	$0.024^{+0.005}_{-0.005}$	$0.002^{+0.006}_{-0.006}$	$-0.006^{+0.006}_{-0.006}$	$-0.016^{+0.007}_{-0.007}$
β	$1.080^{+0.289}_{-0.282}$	$2.112^{+0.331}_{-0.328}$	$2.818^{+0.314}_{-0.311}$	$2.460^{+0.344}_{-0.335}$
η	$0.623^{+2.815}_{-2.891}$	$-2.509^{+3.329}_{-3.387}$	$2.190^{+3.352}_{-3.309}$	$-1.457^{+3.348}_{-3.315}$
χ_ν	1.156	1.047	1.049	1.015

Table 7.2: $\alpha\beta\eta$ estimated values and 1σ confidence intervals using Jackknife sampling to construct taus-stats covariance matrix. Was used a limit in large scales of 40 arcmin. Ndf = 117.

to create a different covariance matrix that the one used for the estimation of cosmological parameters. In other words, PSF is cosmology independent, and the estimates $\alpha\beta\eta$ should be too.

Once we have selected the fiducial cosmology and the lensing efficiency eq. (3.74) (which depend on the redshift distribution p(z) given by fig. 7.3), we obtain pure shear components γ_1 and γ_2 for each galaxy. However, our simulation does not contain any statistical error. And the main contribution of the statistical errors is shape noise (section 5.2). To include shape noise in our simulations, we need to consider the full distribution of ellipticities in our real catalog. Recalling that shear signal is around 1% of the shapes, we expect that our shape distribution to be significantly broader than the distribution of the shear. If our shape distribution from data is perfectly round and Gaussian, the inclusion of shape noise is simple. We just need to resample each component of the shear field using the one dimensional Gaussian associated.

In fig. 7.17 is presented the comparison between shape distribution and shear distribution, for a particular tomographic bin. The standard deviation difference between both shows clearly why weak lensing analysis is so challenging. Statistical errors are hiding a very small signal, which we can see in this plot because we are performing a simulation of the shear field.

We are interested in to include shape noise in the simulations, given that in first-approximation, our experimental shear field is round (see fig. 7.17). We can resample each component individually. The right way of comparing these shears and shapes distributions, is using the total variance, given that $E(\mathbf{e}) = 0$, $\mathrm{VAR}(\mathbf{e}) = E(\mathbf{e}^2) = E(e_1^2 + e_2^2)$. In the plots below, we include this quantity for comparison purposes. As can be observed in fig. 7.17, the shear distribution is essentially a Dirac delta when comparing with shape distribution.

After the addition of the shape noise in the simulations, final shapes distribution comparison is presented in fig. 7.18, where we see that variance are almost identical. However, in the marginalized distributions we see that actually there is a small change in the shapes of the distribution, this is due to the non-gausianities of real data we did not consider.

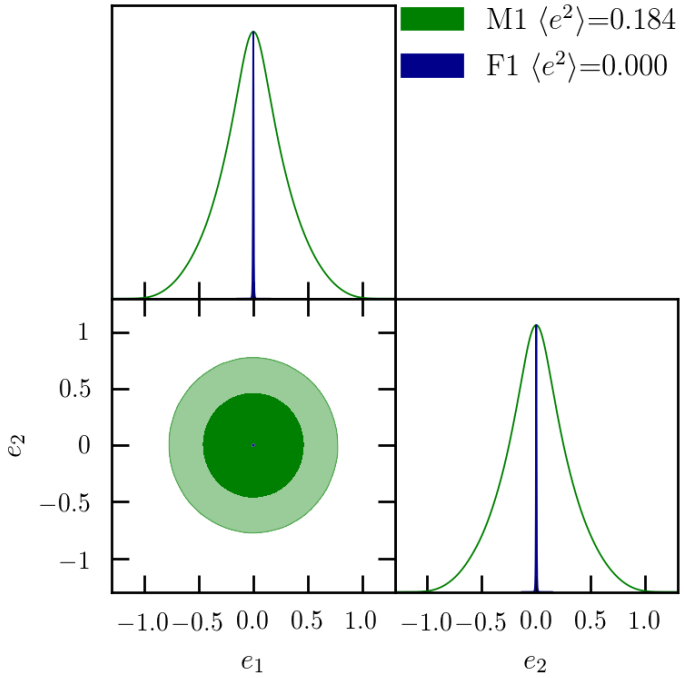

Figure 7.17: Shape distribution from Metacal (green) comparison with shear distribution using flask(blue)

The number of galaxies in each tomographic bin has to be the same in simulations and data. Otherwise, simulations can add or remove pairs star-galaxy, and shape noise scales in inverse proportion with the number of pairs. However, might be data can have regions with overpopulations, and simulations are not taking this into account. The way how we can test this is by calculating the population's pairs in each of the scale bins we are observing. If, for any particular reason, at some scale, there is a significant difference in the number of pairs, this means our simulations are not reproducing the densities population of data, and as a consequence, shape noise in those particular scales would be under or overestimated, affecting our calculation.

In fig. 7.19 is presented the ratio of the number of pairs star-galaxy using simulation and Metacal. Without separating the analysis in angular bins, we know there is around 7 % difference between Metacal and simulations of galaxy catalogs. These differences are also reproduced for most of the scales, in particular, the few first angular bins are underpopulated in the simulations. Bear in mind the y-axis scale variations are only a few percents, then as a whole, we can say our simulations are not favoring particular scales. But we must be concerned that our shape noise from simulations might be suffering a small underestimation.

When we measure the shape of a galaxy, we need to define a system of coordinates, to be able to define what is a cross and tangential component of the shear. However, in simulations is very common to find another convention for the system of reference. The most common difference between conventions is whether the right ascension will be

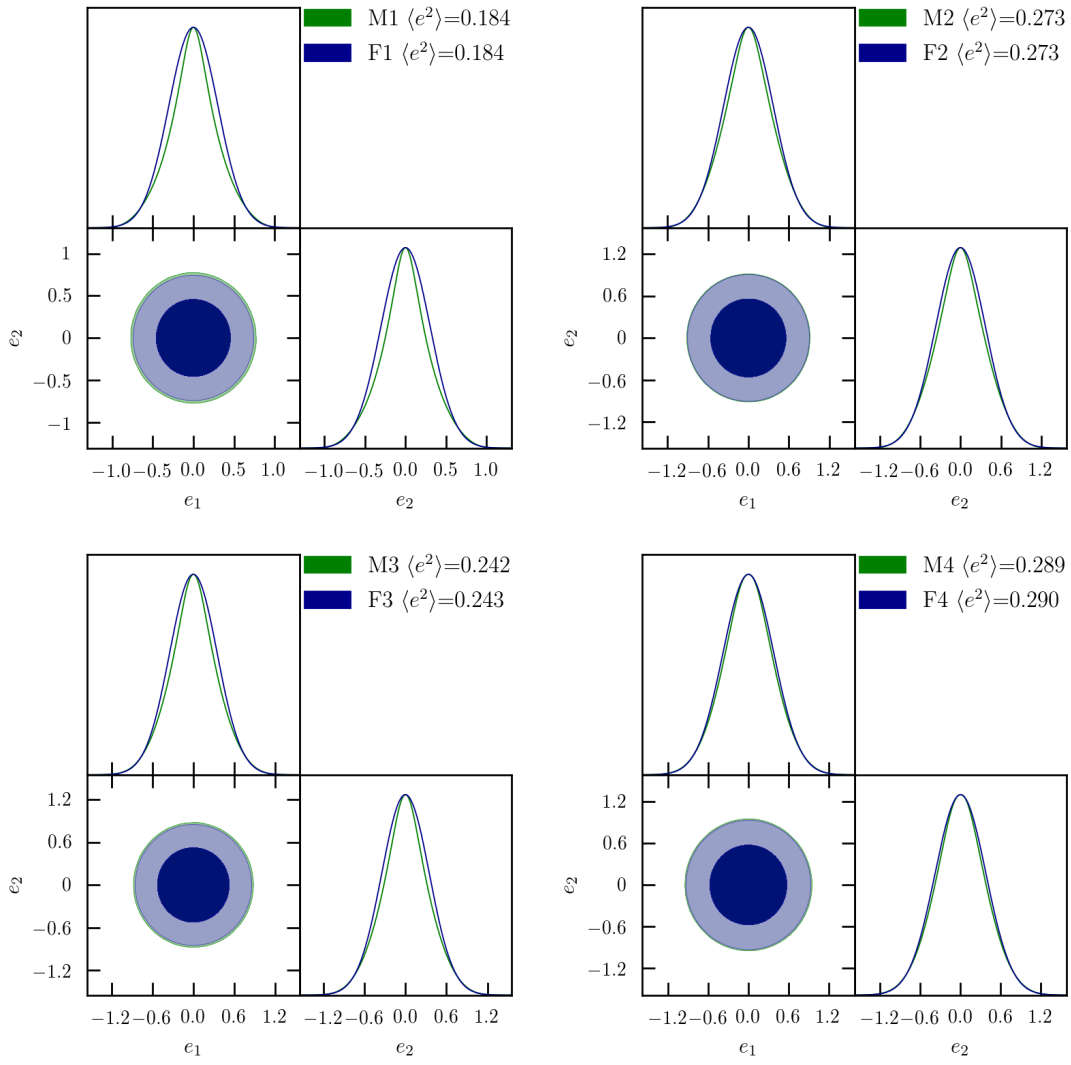

Figure 7.18: Shape distribution from Metacal (green) comparison with shape distribution using flask(blue), for each of the tomographic bins of Y3 analysis of DES

positive to the right or to the left. In astronomy, it is common to follow the rotation of Earth as a reference. In this case, the convention is that RA is positive in the direction of rotation (assuming rotation Poles are very close to Celestial Poles). However, theorists commonly to adopt the opposite convention, and this can lead to wrong estimations. Given the symmetries of the shear field discussed in chapter 3 and illustrated in fig. 3.9, the flip in the right ascension is equivalent to flip the second component of the shear, i.e., invert the sign of g_2.

To distinguish if the simulation has the right conventions, we just need to calculate the shear two-point function, since flipping g_2 will keep ξ_+ the same, but ξ_- must cancel out. In fig. 7.20 is presented the results of the mean measures for the whole set of Flask simulations considering both possible conventions. In the l.h.s are the ξ_+ correlation, which are the same as expected. On the r.h.s, we observe that when we apply a flip in the second component of the shear field, ξ_- is consistent with noise, meaning that our

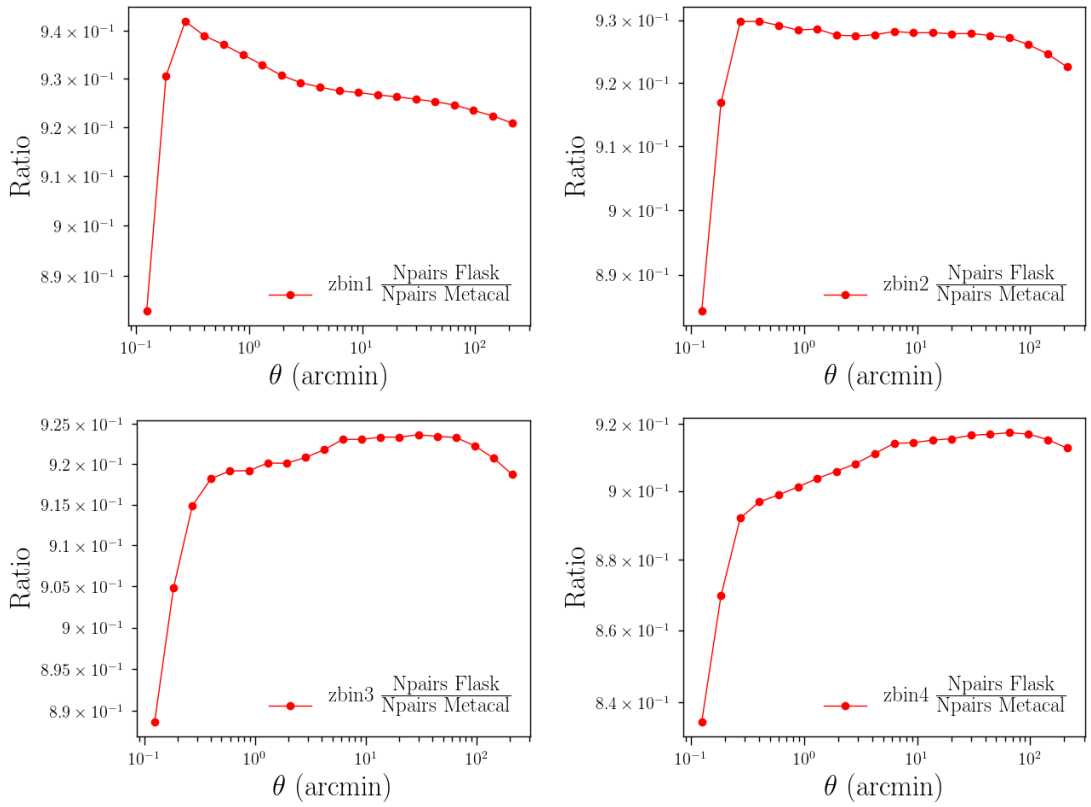

Figure 7.19: Ratio between the number of pairs

simulations have the right convention.

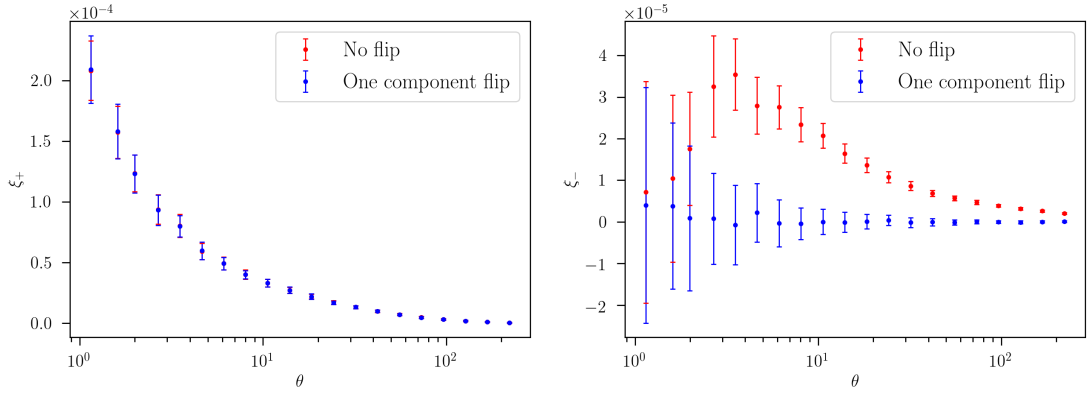

Figure 7.20: ξ_+ and ξ_- shear two point correlation function for two different system of coordinates conventions: without flipping the second component of shear and flipping it.

Anytime before performing the fitting using taus covariance from Flask, we need to do these three null tests. We have presented it in the inverse order. First, we need to be sure that simulations have the right convention for the right ascension. Second, the populations of galaxies should be almost the same for simulation and data for all the scales. And third, the shape noise must be consistent among redshift bins. All of these three null tests are fundamental for getting an adequate fitting.

Once passed all null tests, we are confident of our covariance matrix of taus and will be

ready to find $\alpha\beta\eta$. We obtained one covariance matrix for each tomographic bin using 600 flask realizations. Given the large number of simulations Harlap correction factors[51] were not used. In fig. 7.21 we show the obtained taus correlations matrix. It is very similar to fig. 7.13, most of the already discussed patterns are observed here too, with few differences in large scale cross-correlation between τ_{2+} and τ_{5+}, while in Jackknife covariance there are an anti-correlations, in Flask covariance we observe a positive correlations. Again, by the definitions of the stars residual involved, we expect positive correlations since both tau-stats have positive e^* and negative e^p and τ^p. Another indicator that our Flask covariance seems to be reproducing errors more conveniently is that among different angular bins, correlations vary more smoothly, meaning that we are overcoming statistical noise despite be using a different number of realizations.

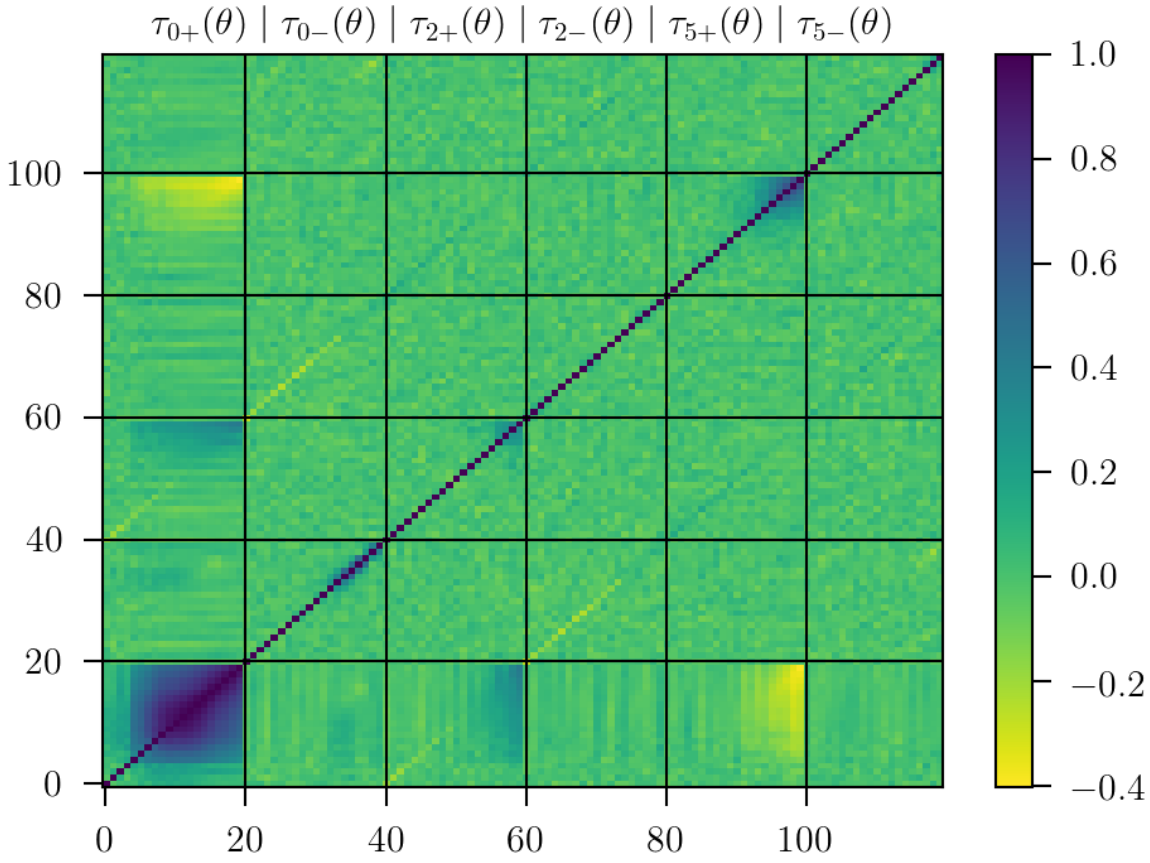

Figure 7.21: Correlation matrix of taus for tomobin 1, were used 600 Flask simulations samples, each tau-stat have 20 data points going from 0.1 arcmin to 250 arcmin in logarithmic uniform binning

Using this covariance matrix, we solved eq. (7.3) and obtained the set of $\alpha\beta\eta$ parameters presented in table 7.3. In fig. 7.22 are these best fits and their comparison with tau-stats. In general terms, we can say that our fittings are en good agreement with data points in all the scales.

If comparing with the previous fitting, we observe that χ^2_ν values in table 7.3 are

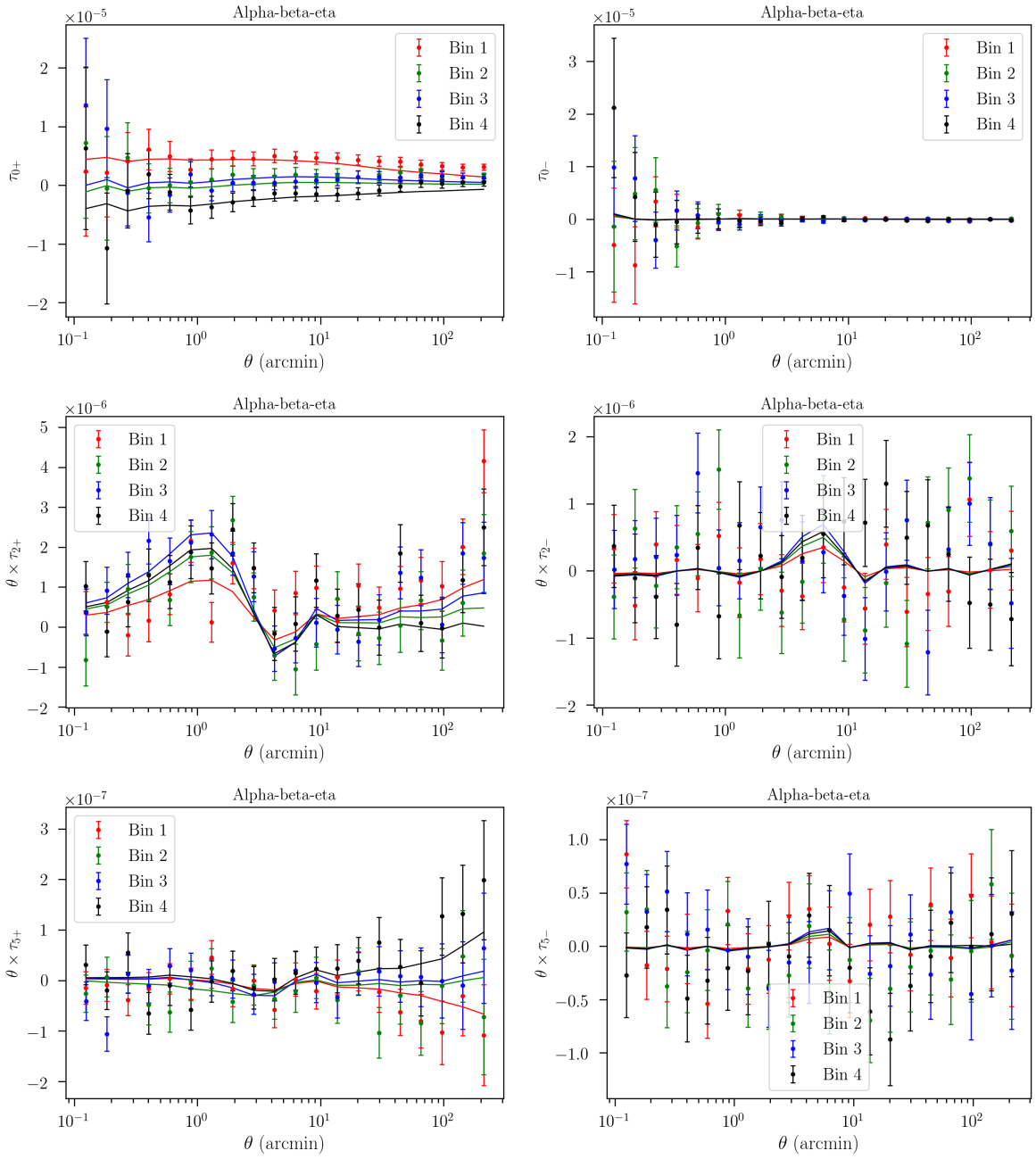

Figure 7.22: Best fits obtained using the covariance errors obtained from Flask simulations. Data points correspond to taus correlations. And continuous curve the product of estimated mean values of $\alpha\beta\eta$ and rho-stat as defined in eqs. (7.13) to (7.15)

not getting better. However, we need to remember that in previous cases, the whole set of scales is not used. When we performed the three approaches using the entire set of angular scales, the inverse is observed. Best fits come from Flask modeling errors, followed by Jackknife errors, and the fitting using only shape noise was the worst. In the last, eta can go up to values of a few hundreds and χ^2_ν of several tens.

It worth to mention why it is essential to perform this fitting in several ways. It is not only the fact that we expect similar results, but there is also a computing time request for each analysis. Although errors obtained from simulations are more convenient, performing

	Bin1	Bin2	Bin3	Bin4
α	$0.019^{+0.010}_{-0.010}$	$-0.005^{+0.012}_{-0.012}$	$-0.000^{+0.011}_{-0.011}$	$-0.017^{+0.012}_{-0.012}$
β	$1.450^{+0.547}_{-0.541}$	$2.201^{+0.656}_{-0.658}$	$2.925^{+0.611}_{-0.619}$	$2.459^{+0.686}_{-0.684}$
η	$2.143^{+5.623}_{-5.647}$	$-1.171^{+6.679}_{-6.645}$	$3.452^{+6.299}_{-6.338}$	$4.164^{+7.707}_{-7.436}$
χ_ν	1.290	1.127	1.075	1.026

Table 7.3: $\alpha\beta\eta$ estimated values and 1σ confidence intervals using Flask simulation to construct taus-stats covariance matrix. The whole range of scales defined for measures,i.e from 0.1 to 250 arcmin. Ndf = 117.

thousands of simulations of hundreds of objects is time-consuming. If, for any reason, there are changes in the analysis parameters, we need to run the whole set of simulations again. For instance, the final redshift bins limits are one of those parameters that are frequently changed for test analysis. In those cases, then it is faster and more convenient to use Jackknife covariances. Keeping in mind that for our final test, we should perform the two cases to be completely confident in some source of error divergences. For the porpoise of this work, we will use the table of values in table 7.3 as our final estimates of $\alpha\beta\eta$.

7.2.4 Propagation to cosmology

Once we have determined $\alpha\beta\eta$ we are interested in to propagate until the end, and see what would it be the effect of PSF modeling systematic errors in cosmological parameters. Since we are working with blinded data, we will present a forecast for this analysis, i.e., our data vector will correspond to a theoretical fiducial cosmology rather than the true catalog. Forecasts are common to test the pipeline, in the sense that the final estimates should correspond to the fiducial cosmology implemented. We can perform a forecast for our problem of interest too. The difference now is that we will use as our data vector fiducial cosmology "contaminated" with PSF systematics, i.e., our fiducial shear correlation function will add the bias determined by eq. (7.22). The deviation of the estimated values from the fiducial cosmology will be a consequence exclusively of the introduced contamination. Significant change will indicate a warning before performing the final estimate with unblinded data.

To be more confident of the possible effect of PSF errors in cosmology, we will contaminate fiducial shear 2PCF with the $\pm$ 2σ values of the bias. Recalling that in the calculation of errors, it is important to consider covariances among all parameters, even if they are associated with different redshift bins. This can be done by building a covariance matrix from the samples of each parameter. In fig. 7.23 is presented the covariance matrix of $\alpha\beta\eta$ for the first redshift bin, we observe that α and β are anti-correlated, α and η are not correlated, and β and η are correlated. This is essentially a consequence of correlations between different tau-stats that parameters are acting on, as we already

discussed before.

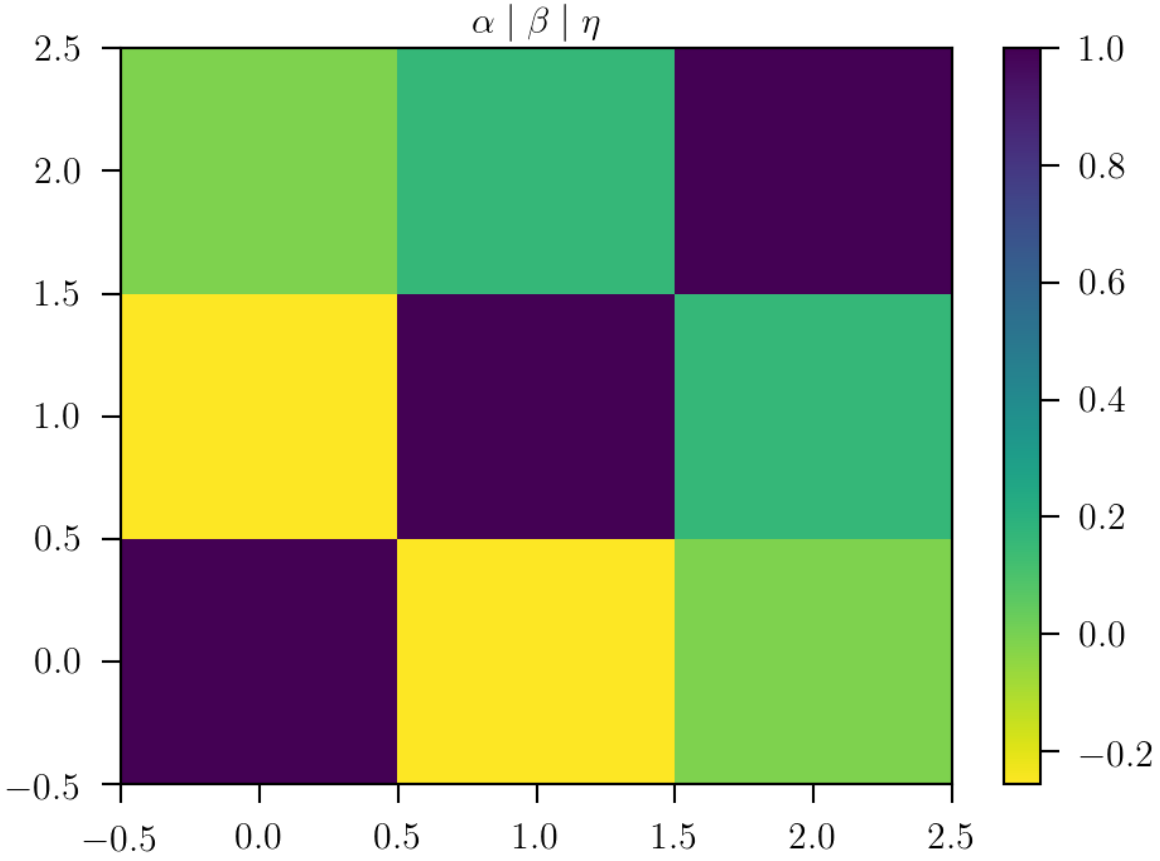

Figure 7.23: Correlation matrix of $\alpha\beta\eta$ for the first redshift bin

Using table 7.3, and propagating errors in eq. (7.22) we obtained the PSF contamination. In fig. 7.24 and fig. 7.25 are shown the total PSF bias (or contaminant factor to be included) and fiducial shear correlations functions. In general terms, we can say that the PSF contamination is one or two order of magnitude smaller than the signal, so in advance we expect this error would not affect final cosmological estimates. However, we will perform the full analysis to the end to be completely sure.

Using these contaminated data vectors, we estimate cosmological parameters and compare them with those without the contamination. In fig. 7.26 are presented the obtained marginalizations and contour levels of the posterior distributions for a set of six cosmological parameters. We use limits of $\pm 2\sigma$ contamination of the total PSF bias, to produce the comparison with the forecast without contamination at all.

From the comparison of the marginalized posteriors, we observe tiny fluctuations among the different distributions, those are not only due to the PSF contamination, but also they are associated to the precision of the sampling implement to construct the posterior distribution. Although we are using the same pipeline and input parameters and files, the implemented pipeline uses random sampling. In order to avoid these fluctuations,

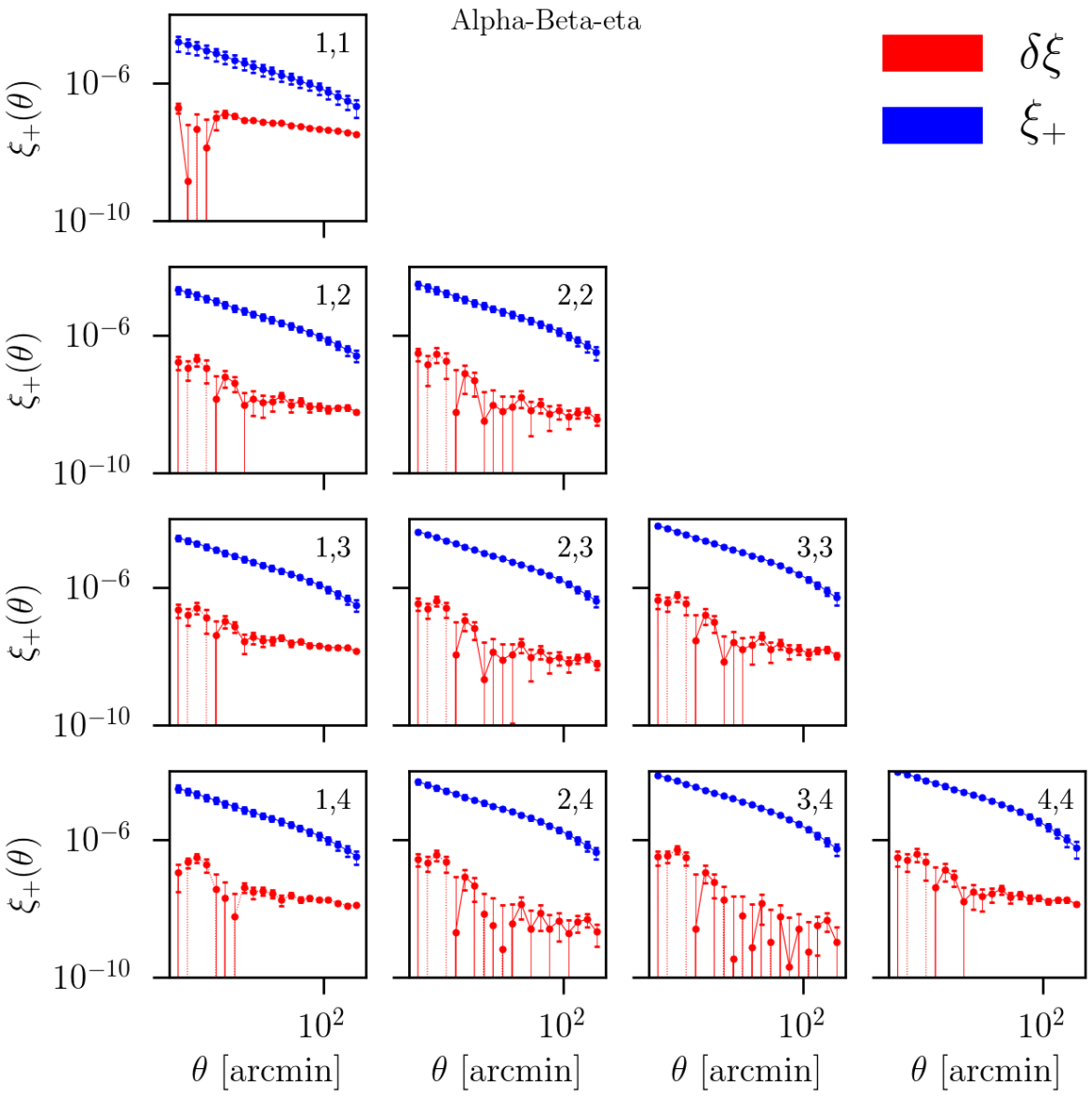

Figure 7.24: PSF error bias in the fiducial shear plus 2PCF ξ_+. Error bars correspond to 2σ confidence levels.

we need to use a large number of samples. In particular, we have performed almost on million evaluations and used around forty thousand samples, this is usually considered a large sampling, for the estimation of cosmological parameters using standard background cosmology. To have an idea of the order of magnitude of these sampling fluctuations in the estimation and contour plots, we performed several runs of the forecast without contamination. In fig. 7.27, we show the comparison of two of those runs, in general, we conclude that sampling fluctuation oscillates up to a maximum of 1% for the mean and almost 4% for the standard deviation. So if in our forecast using PSF contamination there are fluctuations larger than this, it means it was a consequence of the PSF modeling.

In table 7.4, we present the comparison of the estimated cosmological parameter for

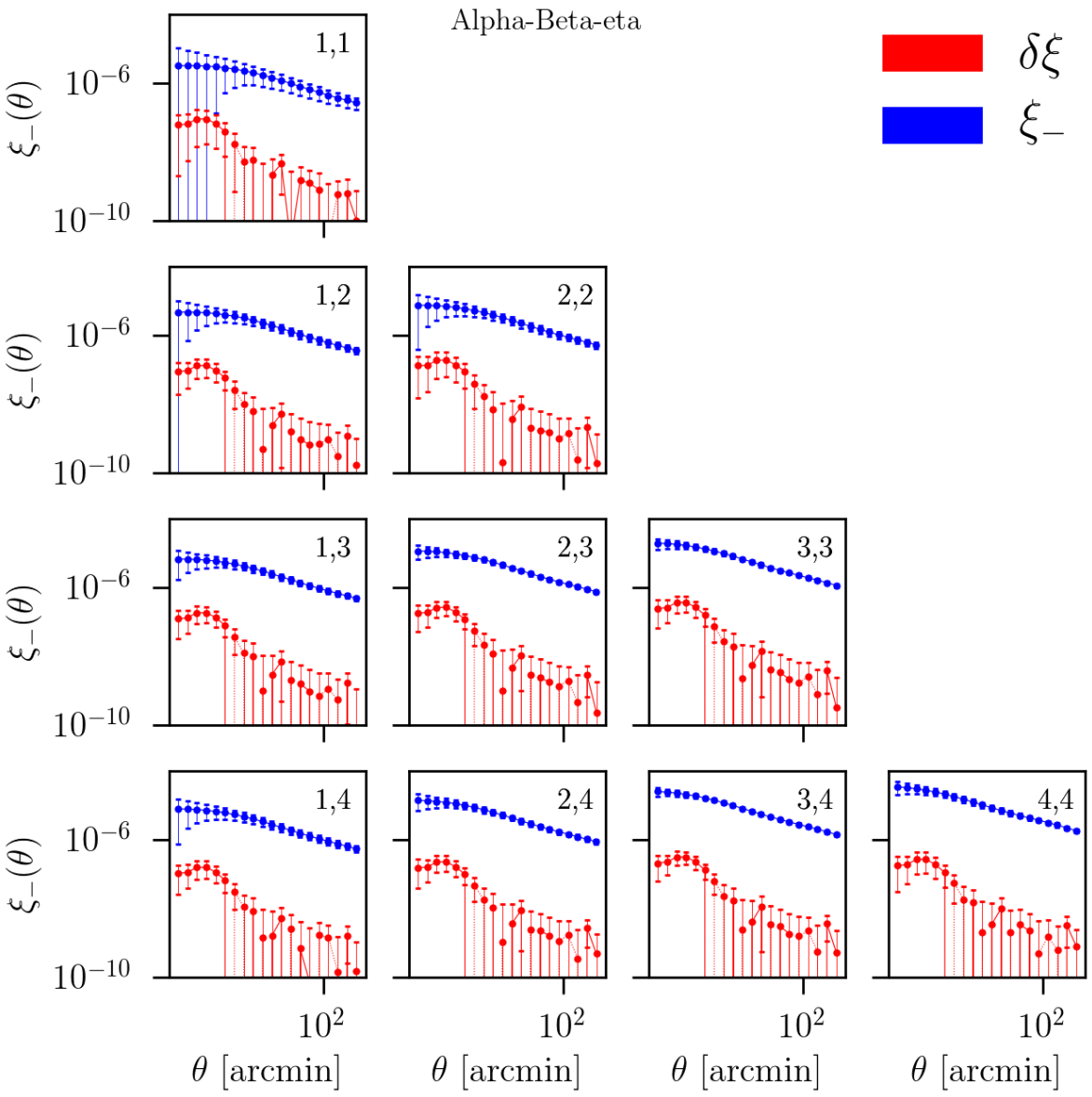

Figure 7.25: PSF error bias in the fiducial shear minus 2PCF ξ_-. Error bars correspond to 2σ confidence levels

the different forecasts. The first important thing to notice is that all our forecasts are consistent with the fiducial cosmology, i.e., fiducial values are inside the 1σ confidence intervals, which means that the pipeline is working properly. Second, when we compare the forecast using the maximum PSF contamination and minimum PSF contamination, the oscillation in central values and 1σ confidence interval are in the same order as the sampling fluctuation. This in fact is appreciated, when comparing fig. 7.26 and fig. 7.27.

Consequently, we can say that the PSF modeling essentially is not introducing additive systematic errors in the shear 2PCF. However, this analysis corresponds to only one of the main tests of several that are used to have control over PSF systematics. For instance, this analysis can be done in Fourier space and using focal plane coordinates instead of

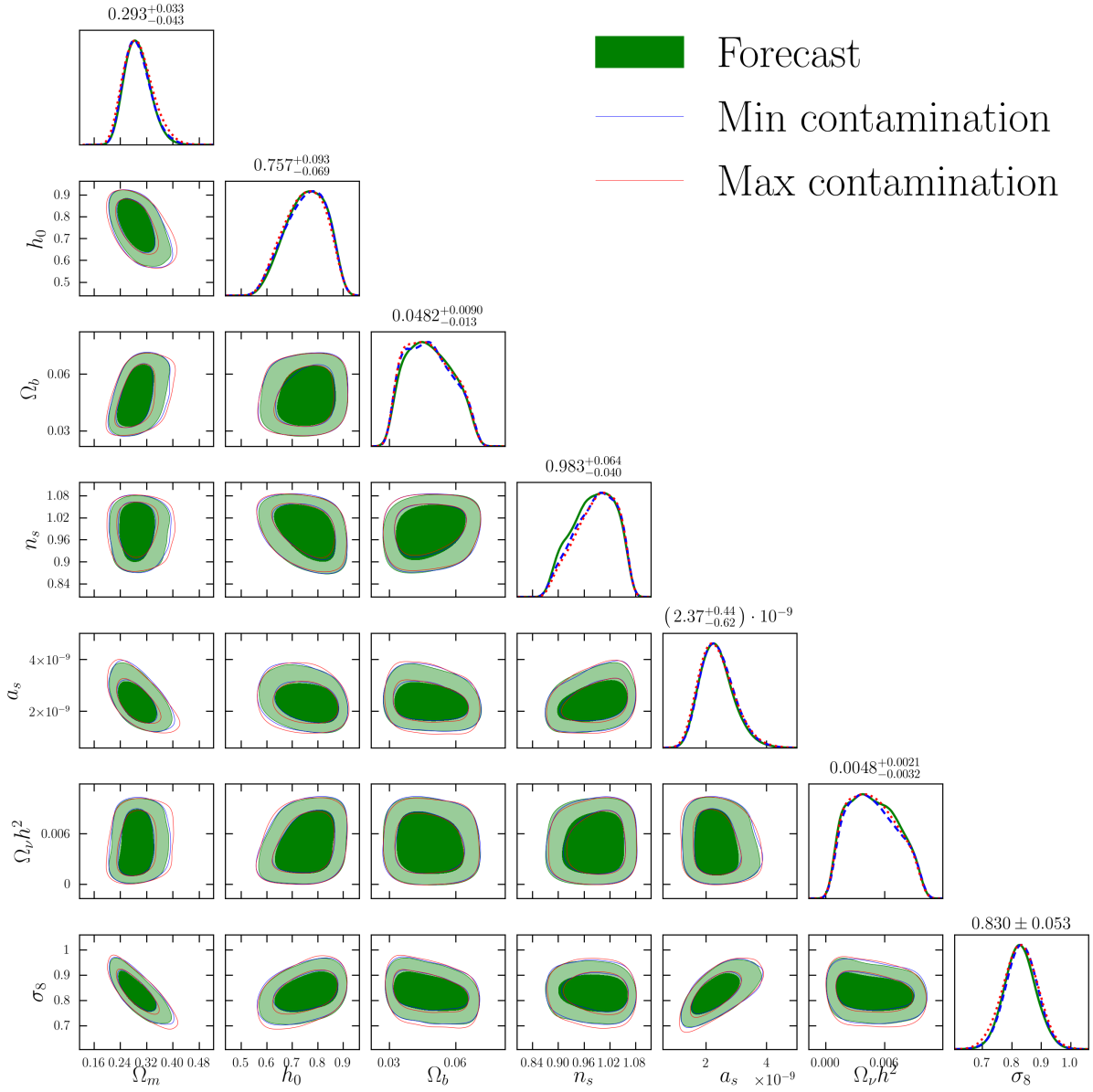

Figure 7.26: Three cosmology forecast. One where we use as data vector a fiducial cosmology, and two where we used extremes $\pm 2\sigma$ contamination of the total PSF bias.

celestial coordinates, to mention some of the options.

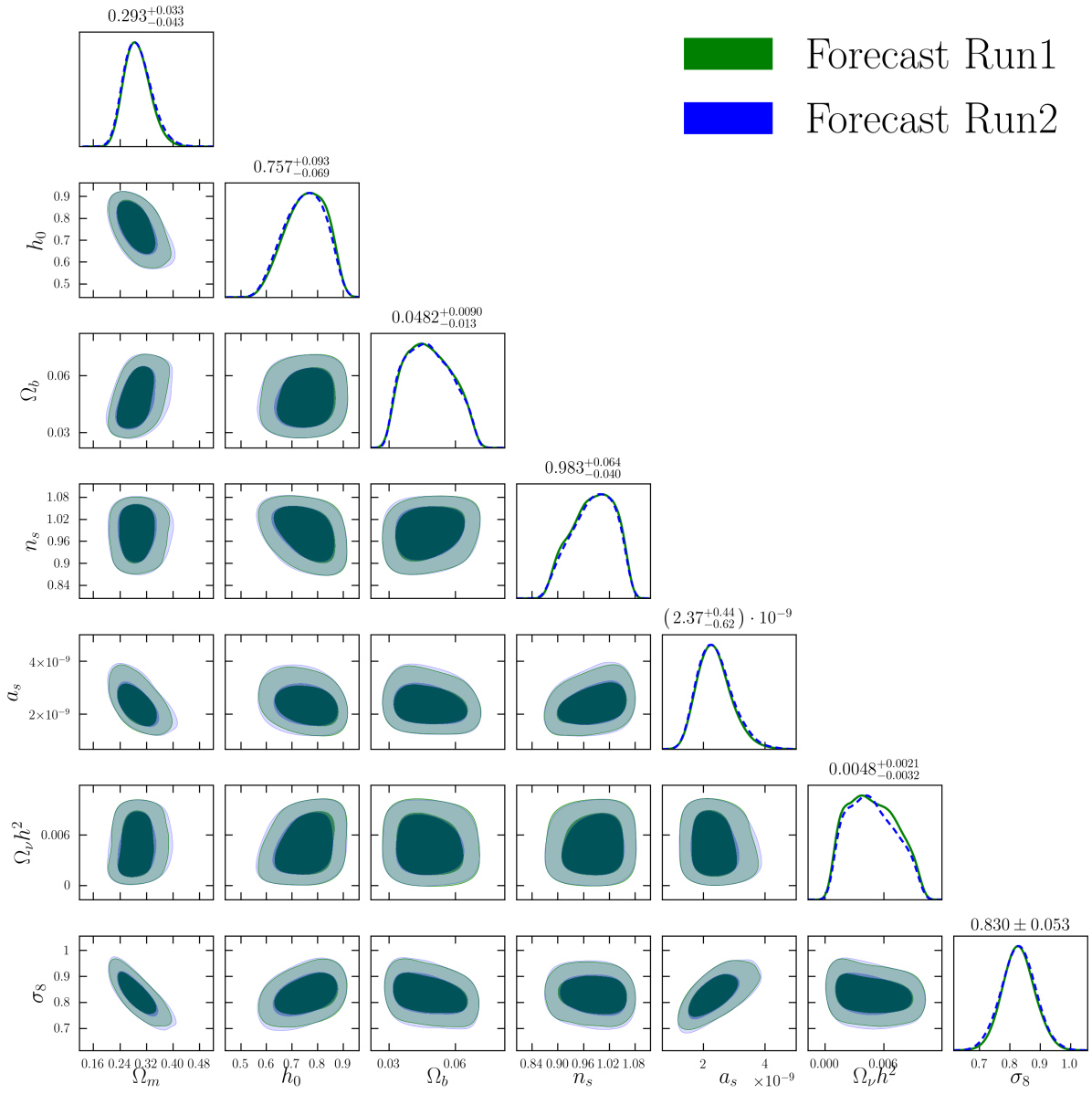

Figure 7.27: Sampling fluctuations for the same fiducial cosmology.

Parameter	Fiducial	Forecast	Max contamination	Min contamination
$\boldsymbol{\Omega_m}$	0.295	$0.293^{+0.078}_{-0.072}$	$0.295^{+0.090}_{-0.081}$	$0.293^{+0.082}_{-0.074}$
$\boldsymbol{h_0}$	0.6681	$0.76^{+0.14}_{-0.15}$	$0.75^{+0.14}_{-0.15}$	$0.75^{+0.14}_{-0.15}$
$\boldsymbol{\Omega_b}$	0.0468	$0.048^{+0.019}_{-0.017}$	$0.048^{+0.019}_{-0.017}$	$0.048^{+0.019}_{-0.017}$
$\boldsymbol{n_s}$	0.9676	$0.983^{+0.082}_{-0.092}$	$0.989^{+0.079}_{-0.092}$	$0.987^{+0.081}_{-0.093}$
$\boldsymbol{A_s}$	$2.26 \cdot 10^{-9}$	$\left(2.4^{+1.1}_{-1.0}\right) \cdot 10^{-9}$	$\left(2.4^{+1.2}_{-1.1}\right) \cdot 10^{-9}$	$\left(2.4^{+1.1}_{-1.0}\right) \cdot 10^{-9}$
$\boldsymbol{\Omega_\nu h^2}$	0.0006155	$0.0048^{+0.0044}_{-0.0041}$	$0.0048^{+0.0044}_{-0.0040}$	$0.0048^{+0.0045}_{-0.0040}$
$\boldsymbol{\sigma_8}$	Not defined	$0.83^{+0.11}_{-0.10}$	$0.83^{+0.11}_{-0.12}$	$0.83^{+0.11}_{-0.10}$

Table 7.4: Comparison of cosmological parameters estimation for and different forecast.

Chapter 8

Conclusions and perspectives

In the present work was given an introduction to cosmic shear focusing mainly on the use of diagnostic functions to control PSF systematic. Given the current progress in precision cosmology and the small-signal to be processed with this technique, the main problems cosmic shear need to face are the modeling and control of all sources of statistical and systematic errors.

We showed an introduction to the process of creation of shear catalogs, the fundamental type of errors involved, the way how shapes are measured, and the linking between those measures and cosmology.

In particular, we focus primary attention on an important test to quantify the effects of additive systematic errors of PSF modeling in cosmology. We wrote a pipeline performing this task. The idea was to use 2PCF of stars not used in the PSF modeling as diagnostic functions, and building blocks of the total PSF bias in the shear 2PCF. These diagnostic functions are weighted with a set of three parameters, each associated with a degree of freedom, leakage, shape residual, and size residuals. We found those parameters correlating with the Metacal Y3 galaxy catalog and modeling errors using Flask simulations and Jackknife sampling.

The total PSF biases obtained respect to fiducial cosmology was in the worst case, one order of magnitude smaller than the shear signal. But in most of the scales and tomographic bins, there was around two orders of magnitude difference. We confirmed that when propagating to final cosmological estimates, changes in the final marginalized posteriors and contours are in the same order than fluctuation resulting from the random sampling of the posterior, even when we use a large number of evaluations. Of course, this is a good signal that our PSF modeling of the Y3 analysis is not inducing systematic errors in estimates, and this is something desired. However, we tested cases when large values of the parameters were indicating ”wrong” PSF modeling.

For future works, we want to mention a few open questions that emerged as a result of this work. First, it is still unclear why rho-stat does not decrease when going to large

scales. Given the logarithmic binning, in large scales, the number of pairs should include domain over rho signals, but it is not the case. Second, we are interested in to apply this methodology to other PSF modelling approaches, particularly to those involving matching learning training, since they usually do not have control of uncertanties. Our methodology can help to control them in case of systematic error being introduced. Third, errors in the PSF bias can also be estimated using Fisher formalism, it might be worth comparing both methodologies.

Bibliography

[1] The Lsst. "The LSST Science Book". In: *Science* November (2009), p. 596. arXiv: 0912.0201. URL: http://arxiv.org/abs/0912.0201.

[2] DES Collaboration et al. "Dark Energy Survey Year 1 Results: Cosmological Constraints from Galaxy Clustering and Weak Lensing". In: (2017), pp. 1–31. arXiv: 1708.01530. URL: http://arxiv.org/abs/1708.01530.

[3] C. Chang et al. "Dark Energy Survey Year 1 Results: Curved-Sky Weak Lensing Mass Map". In: 000.August (2017). arXiv: 1708.01535. URL: http://arxiv.org/abs/1708.01535.

[4] Rachel Mandelbaum. "Weak lensing for precision cosmology". In: (2017), pp. 1–45. DOI: 10.1146/((please. arXiv: 1710.03235. URL: http://arxiv.org/abs/1710.03235.

[5] Matthias Bartelmann and Peter Schneider. "Weak Gravitational Lensing". In: July 2006 (1999). ISSN: 03701573. DOI: 10.1016/S0370-1573(00)00082-X. arXiv: 9912508 [astro-ph]. URL: http://arxiv.org/abs/astro-ph/9912508%7B%5C%%7D0Ahttp://dx.doi.org/10.1016/S0370-1573(00)00082-X.

[6] F. Zwicky. "On the Masses of Nebulae and of Clusters of Nebulae". In: *ApJ* 86 (Oct. 1937), p. 217. ISSN: 0004-637X. DOI: 10.1086/143864.

[7] Horace W. Babcock. "The rotation of the Andromeda Nebula". In: *LicOB* 498 (1939), pp. 41–51. ISSN: 0075-9317. DOI: 10.5479/ADS/bib/1939LicOB.19.41B.

[8] V. C. Rubin, W. K. Ford Jr., and N. Thonnard. "Extended rotation curves of high-luminosity spiral galaxies. IV. Systematic dynamical properties, Sa -> Sc." In: *ApJL* 225 (Nov. 1978), pp. L107–L111. ISSN: 0004-637X. DOI: 10.1086/182804.

[9] M. S. Roberts and R. N. Whitehurst. "The rotation curve and geometry of M31 at large galactocentric distances." In: *ApJ* 201 (Oct. 1975), pp. 327–346. ISSN: 0004-637X. DOI: 10.1086/153889.

[10] J. P. Ostriker, P. J. E. Peebles, and A. Yahil. "The Size and Mass of Galaxies, and the Mass of the Universe". In: *ApJL* 193 (Oct. 1974), p. L1. ISSN: 0004-637X. DOI: 10.1086/181617.

[11] J. K. Adelman-McCarthy et Al. "The Fourth Data Release of the Sloan Digital Sky Survey". In: *arXiv* (July 2005). DOI: 10.1086/497917. eprint: astro-ph/0507711.

[12] Ulrich G. Briel and J. Patrick Henry. "An X-ray Temperature Map of Coma". In: *arXiv* (Nov. 1997). eprint: astro-ph/9711237. URL: https://arxiv.org/abs/astro-ph/9711237.

[13] *Catching a bullet: direct evidence for the existence of dark matter*. [Online; accessed 20. Jan. 2020]. Nov. 2007. DOI: 10.1016/j.nuclphysbps.2007.08.150. eprint: arXiv:astro-ph/0611496.

[14] Sidney van den Bergh. "The Early History of Dark Matter". In: *Publ. Astron. Soc. Pac.* 111.760 (June 1999), pp. 657–660. ISSN: 0004-6280. DOI: 10.1086/316369.

[15] Katherine Freese. "Review of Observational Evidence for Dark Matter in the Universe and in upcoming searches for Dark Stars". In: *arXiv* (Dec. 2008). DOI: 10.1051/eas/0936016. eprint: 0812.4005.

[16] S. Perlmutter et al. "Measurements of Ω and Λ from 42 High-Redshift Supernovae". In: *ApJ* 517.2 (June 1999), pp. 565–586. ISSN: 0004-637X. DOI: 10.1086/307221. eprint: arXiv:astro-ph/9812133.

[17] Adam G. Riess et al. "The Rise Time of Nearby Type Ia Supernovae". In: *AJ* 118.6 (Dec. 1999), pp. 2675–2688. ISSN: 0004-6256. DOI: 10.1086/301143.

[18] Steven Weinberg. "The cosmological constant problem". In: *Rev. Mod. Phys.* 61.1 (Jan. 1989), pp. 1–23. ISSN: 1539-0756. DOI: 10.1103/RevModPhys.61.1.

[19] Barbara Ryden. *Introduction to COSMOLOGY*. 2017.

[20] J.-P. Luminet et al. "Dodecahedral space topology as an explanation for weak wide-angle temperature correlations in the cosmic microwave background". In: *arXiv* (Oct. 2003). DOI: 10.1038/nature01944. eprint: astro-ph/0310253.

[21] Boudewijn F. Roukema et al. "The optimal phase of the generalised Poincare dodecahedral space hypothesis implied by the spatial cross-correlation function of the WMAP sky maps". In: *arXiv* (Jan. 2008). DOI: 10.1051/0004-6361:20079339. eprint: 0801.0006.

[22] N. G. Sánchez and Y. N. Parijskij. *The Early Universe and the Cosmic Microwave Background: Theory and Observations*. Springer Netherlands, 2003. ISBN: 978-140201800-8. URL: https://books.google.com.br/books?id=KhTJZG-U3ssC&pg=PA161&redir_esc=y#v=onepage&q&f=false.

[23] Peter Schneider. *Extragalactic Astronomy and Cosmology*. 2006.

[24] Peter Schneider et al. "A new measure for cosmic shear". In: *Monthly Notices of the Royal Astronomical Society* 296.4 (1998), pp. 873–892. ISSN: 0035-8711. DOI: 10.1046/j.1365-8711.1998.01422.x. arXiv: 9708143 [astro-ph]. URL: https://academic.oup.com/mnras/article-lookup/doi/10.1046/j.1365-8711.1998.01422.x.

[25] Peter Schneider. "Weak Gravitational Lensing". In: (2005). DOI: 10.1007/978-3-540-30310-7_3. arXiv: 0509252 [astro-ph]. URL: http://arxiv.org/abs/astro-ph/0509252%7B%5C%%7D0Ahttp://dx.doi.org/10.1007/978-3-540-30310-7%7B%5C_%7D3.

[26] Simon Samuroff. *Systematic Biases in Weak Lensing Cosmology with the Dark Energy Survey*. [Online; accessed 19. Jun. 2019]. 2017. DOI: 10.5281/zenodo.1162395.

[27] Nick Kaiser, Gordon Squires, and Tom Broadhurst. "A Method for Weak Lensing Observations". In: *The Astrophysical Journal* 449 (1995), p. 460. ISSN: 0004-637X. DOI: 10.1086/176071. arXiv: 9411005 [astro-ph]. URL: http://adsabs.harvard.edu/doi/10.1086/176071.

[28] G. M. Bernstein and M. Jarvis. "Shapes and Shears, Stars and Smears: Optimal Measurements for Weak Lensing". In: *The Astronomical Journal* 123.2 (2002), pp. 583–618. ISSN: 00046256. DOI: 10.1086/338085. arXiv: 0107431 [astro-ph]. URL: http://stacks.iop.org/1538-3881/123/i=2/a=583.

[29] Mike Jarvis and Bhuvnesh Jain. "Principal Component Analysis of PSF Variation in Weak Lensing Surveys". In: (2004). arXiv: 0412234 [astro-ph]. URL: http://arxiv.org/abs/astro-ph/0412234.

[30] Alexandre Refregier. "Shapelets: I. A Method for Image Analysis". In: 47 (2001), pp. 35–47. ISSN: 0035-8711. DOI: 10.1046/j.1365-8711.2003.05901.x. arXiv: 0105178 [astro-ph]. URL: http://arxiv.org/abs/astro-ph/0105178%7B%5C%%7D0Ahttp://dx.doi.org/10.1046/j.1365-8711.2003.05901.x.

[31] Sarah Bridle et al. "Results of the GREAT08 Challenge*: an image analysis competition for cosmological lensing". In: *Monthly Notices of the Royal Astronomical Society* 405.3 (June 2010), pp. 2044–2061. ISSN: 0035-8711. DOI: 10.1111/j.1365-2966.2010.16598.x. eprint: http://oup.prod.sis.lan/mnras/article-pdf/405/3/2044/2901357/mnras0405-2044.pdf. URL: https://doi.org/10.1111/j.1365-2966.2010.16598.x.

[32] E. S. Cypriano et al. "Cosmic shear requirements on the wavelength dependence of telescope point spread functions". In: *Mon. Not. R. Astron. Soc.* 405.1 (June 2010), pp. 494–502. ISSN: 0035-8711. DOI: 10.1111/j.1365-2966.2010.16461.x.

[33] Barnaby Rowe. "Improving PSF modelling for weak gravitational lensing using new methods in model selection". In: *arXiv* (Apr. 2009). DOI: 10.1111/j.1365-2966.2010.16277.x. eprint: 0904.3056.

[34] M. Jarvis et al. "The DES Science Verification Weak Lensing Shear Catalogues". In: *arXiv* (July 2015). DOI: 10.1093/mnras/stw990. eprint: 1507.05603.

[35] E. Bertin and S. Arnouts. "SExtractor: Software for source extraction". In: *Astron. Astrophys. Suppl. Ser.* 117.2 (June 1996), pp. 393–404. ISSN: 0365-0138. DOI: 10.1051/aas:1996164.

[36] *gbernstein/pixmappy*. [Online; accessed 2. Aug. 2019]. Aug. 2019. URL: https://github.com/gbernstein/pixmappy.

[37] Christopher Hirata and Uroš Seljak. "Shear calibration biases in weak-lensing surveys". In: *Monthly Notices of the Royal Astronomical Society* 343.2 (2003), pp. 459–480. ISSN: 00358711. DOI: 10.1046/j.1365-8711.2003.06683.x. arXiv: 0301054 [astro-ph].

[38] Erin S. Sheldon. "An implementation of Bayesian lensing shear measurement". In: *Monthly Notices of the Royal Astronomical Society: Letters* 444.1 (July 2014), pp. L25–L29. ISSN: 1745-3925. DOI: 10.1093/mnrasl/slu104. eprint: http://oup.prod.sis.lan/mnrasl/article-pdf/444/1/L25/9420049/slu104.pdf. URL: https://doi.org/10.1093/mnrasl/slu104.

[39] *rmjarvis/Piff*. [Online; accessed 2. Aug. 2019]. Aug. 2019. URL: https://github.com/rmjarvis/Piff.

[40] M. A. Troxel et al. "Dark Energy Survey Year 1 Results: Cosmological Constraints from Cosmic Shear". In: *arXiv* (Aug. 2017). DOI: 10.1103/PhysRevD.98.043528. eprint: 1708.01538.

[41] S. Paulin-Henriksson et al. "PSF calibration requirements for dark energy from cosmic shear". In: *arXiv* (Nov. 2007). DOI: 10.1051/0004-6361:20079150. eprint: 0711.4886.

[42] Joel Bergé et al. "On point spread function modelling: towards optimal interpolation". In: *MNRAS* 419 (Jan. 2012), pp. 2356–2368. ISSN: 0035-8711. DOI: 10.1111/j.1365-2966.2011.19888.x. eprint: 1110.2517.

[43] Tianhuan Lu et al. "Testing PSF Interpolation in Weak Lensing with Real Data". In: *AJ* 153.4 (Apr. 2017), p. 197. ISSN: 1538-3881. DOI: 10.3847/1538-3881/aa661e.

[44] T. Schrabback et al. "Evidence of the accelerated expansion of the Universe from weak lensing tomography with COSMOS". In: *A&A* 516 (June 2010), A63. ISSN: 0004-6361. DOI: 10.1051/0004-6361/200913577.

[45] J. Zuntz et al. “Dark Energy Survey Year 1 Results: Weak Lensing Shape Catalogues”. In: *arXiv* (Aug. 2017). DOI: 10.1093/mnras/sty2219. eprint: 1708.01533.

[46] Eric Huff and Rachel Mandelbaum. “Metacalibration: Direct Self-Calibration of Biases in Shear Measurement”. In: *arXiv* (Feb. 2017). eprint: 1702.02600. URL: https://arxiv.org/abs/1702.02600.

[47] Erin S. Sheldon and Eric M. Huff. “Practical Weak Lensing Shear Measurement with Metacalibration”. In: *arXiv* (Feb. 2017). DOI: 10.3847/1538-4357/aa704b. eprint: 1702.02601.

[48] M. Jarvis, G. Bernstein, and B. Jain. “The skewness of the aperture mass statistic”. In: *MNRAS* 352 (July 2004), pp. 338–352. ISSN: 0035-8711. DOI: 10.1111/j.1365-2966.2004.07926.x. eprint: astro-ph/0307393.

[49] Henrique S. Xavier, Filipe B. Abdalla, and Benjamin Joachimi. “Improving lognormal models for cosmological fields”. In: *arXiv* (Feb. 2016). DOI: 10.1093/mnras/stw874. eprint: 1602.08503.

[50] Daniel Foreman-Mackey et al. “emcee: The MCMC Hammer”. In: *arXiv* (Feb. 2012). DOI: 10.1086/670067. eprint: 1202.3665.

[51] J. Hartlap, P. Simon, and P. Schneider. “Why your model parameter confidences might be too optimistic. Unbiased estimation of the inverse covariance matrix”. In: *A&A* 464.1 (Mar. 2007), pp. 399–404. ISSN: 0004-6361. DOI: 10.1051/0004-6361:20066170. eprint: arXiv:astro-ph/0608064.

[52] Andres Plazas. *Weak Gravitational Lensing Systematic Errors In The Dark Energy Survey*. 2012.

[53] Peter Schneider and Carolin Seitz. “Steps towards Nonlinear Cluster Inversion Through Gravitational Distortions. I. Basic Considerations and Circular Clusters”. In: *arXiv* (July 1994). eprint: astro-ph/9407032. URL: https://arxiv.org/abs/astro-ph/9407032.

Appendices

Appendix A

Deduction of Friedman equations

To find the known Friedman equations the starting point is to define the metric. In our case we are going to use the Friedmann-Robertson-Walker metric. Because this define the metric for a homogeneous and uniform expanding universe. In reduced-circumference coordinates it is:

$$ds^2 = dt^2 - a^2(t)\big[\frac{1}{1-kr^2}dr^2 + r^2 d\theta^2 + r^2 \sin^2\theta d\phi^2\big] \tag{A.1}$$

where r is the comoving distance, θ and ϕ are usual spherical coordinates. [1] In the covariant representation it is

$$\boxed{g_{\mu\nu} = \begin{pmatrix} 1 & 0 & 0 & 0 \\ 0 & -\frac{a^2(t)}{1-kr^2} & 0 & 0 \\ 0 & 0 & -a^2(t)r^2 & 0 \\ 0 & 0 & 0 & -a^2(t)r^2\sin^2\theta \end{pmatrix}} \tag{A.2}$$

A.1 Christoffel symbols calculation

Then we calculate the non-null Christoffel symbols in this metric. To do so we use a useful equation that comes from the Geodesic equation:

$$\boxed{\Gamma^{\mu}_{\alpha\beta} = \frac{g^{\mu\nu}}{2}\big[\partial_\beta g_{\alpha\nu} + \partial_\alpha g_{\beta\nu} - \partial_\nu g_{\alpha\beta}\big]} \tag{A.3}$$

[1] Notice that this way of FRW metric is the same that 2.18, however r here is not the radial coordinate, instead it is the comoving distance. However, in this appendix we will use this notation. So keep in mind that $r = \chi$ so this it is time independent.

Cases $\mu = 0$

Let's start setting $\mu = 0$ in this case:

$$\Gamma^0_{\alpha\beta} = \frac{g^{0\nu}}{2}\left[\partial_\beta g_{\alpha\nu} + \partial_\alpha g_{\beta\nu} - \partial_\nu g_{\alpha\beta}\right] \tag{A.4}$$

if $\nu \neq 0$ $g^{0\nu} = 0$ therefore the non-null terms have $\nu = 0$

$$\Gamma^0_{\alpha\beta} = \frac{g^{00}}{2}\left[\partial_\beta g_{\alpha 0} + \partial_\alpha g_{\beta 0} - \partial_0 g_{\alpha\beta}\right] \tag{A.5}$$

The terms $g_{\alpha 0}$ and $g_{\beta 0}$ are not null when $\alpha = 0$ and $\beta = 0$ respectively. However $g_{00} = -1$ therefore his derivative vanish. Remaining only the last term:

$$\Gamma^0_{\alpha\beta} = -\frac{1}{2}\partial_0 g_{\alpha\beta} \tag{A.6}$$

Because all terms out of the diagonal are 0, the only non-null terms are:

$$\Gamma^0_{11} = \frac{1}{2}\partial_0\left(\frac{a^2(t)}{1-kr^2}\right) = \frac{a\dot{a}}{1-kr^2} \tag{A.7}$$

$$\Gamma^0_{22} = \frac{1}{2}\partial_0\left(a^2(t)r^2\right) = a\dot{a}r^2 \tag{A.8}$$

$$\Gamma^0_{33} = \frac{1}{2}\partial_0\left(a^2(t)r^2\sin^2\theta\right) = a\dot{a}r^2\sin^2\theta \tag{A.9}$$

Notice that the three previous equation can be written in terms of the metric as:

$$\boxed{\Gamma^0_{ii} = -\frac{\dot{a}}{a}g_{ii}} \tag{A.10}$$

Cases $\mu = i$

Now we do a similar process for the spatial components. Setting $\mu = i$

$$\Gamma^i_{\alpha\beta} = \frac{g^{i\nu}}{2}\left[\partial_\beta g_{\alpha\nu} + \partial_\alpha g_{\beta\nu} - \partial_\nu g_{\alpha\beta}\right] \tag{A.11}$$

if $\nu \neq i$ then $g^{i\nu} = 0$ therefore the non-null terms have $\nu = i$, abusing of the notation writing , we have

$$\Gamma^i_{\alpha\beta} = \frac{g^{ii}}{2}\left[\partial_\beta g_{\alpha i} + \partial_\alpha g_{\beta i} - \partial_i g_{\alpha\beta}\right], \tag{A.12}$$

where g^{ii} represents the i-th terms of the diagonal of the contravariant metric [2]. Lets now study the different cases: first we check when indexes β and α are equal to 0. In that case $\Gamma^i_{00} = g^{ii}\partial_0 g_{0i} = 0$.

Cases $\mu = i$ and $\alpha = 0$

We follow the calculation setting $\alpha = 0$

$$\Gamma^i_{0j} = \frac{g^{ii}}{2}\left[\partial_j g_{0i} + \partial_0 g_{ji} - \partial_i g_{0j}\right] = \frac{g^{ii}}{2}\partial_0 g_{ji} \tag{A.13}$$

Now, we check the term in the right hand side, notice that g_{ji} can be written as $g_{ji} = f_{ij}a^2$ where f_{ij} is time independent, then

$$\frac{g^{ii}}{2}\partial_0 g_{ji} = \frac{g^{ii}}{2} f_{ji} 2a\dot{a}\left(\frac{a}{a}\right) = g^{ii} g_{ji}\frac{\dot{a}}{a} = \delta^i_j \frac{\dot{a}}{a} \tag{A.14}$$

$$\boxed{\Gamma^i_{0j} = \Gamma^i_{j0} = \delta^i_j \frac{\dot{a}}{a}} \tag{A.15}$$

Cases $\mu = i$, $\alpha = j$ and $\beta = k$

The remaining Christoffel symbols must be calculated case by case, our starting point will be the definition of the symbols in terms of the metric, which is diagonal and its terms depends as $g_{11}(t,r)$, $g_{22}(t,r)$ and $g_{33}(t,r,\theta)$.

$$\Gamma^i_{jk} = \frac{g^{ii}}{2}\left[\partial_k g_{ji} + \partial_j g_{ki} - \partial_i g_{jk}\right] \tag{A.16}$$

lets set **i=1** and **j=1**

$$\Gamma^1_{1k} = \frac{g^{11}}{2}\left[\partial_k g_{11} + \partial_1 g_{k1} - \partial_1 g_{1k}\right] = \frac{g^{11}}{2}\partial_k g_{11} \tag{A.17}$$

in this case the only not null term is when k=1, then

$$\Gamma^1_{1k} = \Gamma^1_{11}\delta^1_k = \frac{g^{11}}{2}\partial_1 g_{11}\delta^1_k = \left(\frac{1-kr^2}{-2a^2}\right)\frac{-2a^2 kr}{(1-kr^2)^2}\delta^1_k \tag{A.18}$$

$$\boxed{\Gamma^1_{1k} = \frac{kr}{1-kr^2}\delta^1_k} \tag{A.19}$$

lets set **i=1** and **j=2**

$$\Gamma^1_{2k} = \frac{g^{11}}{2}\left[\partial_2 g_{k1} - \partial_1 g_{2k}\right] = -\frac{g^{11}}{2}\partial_1 g_{2k} \tag{A.20}$$

[2] there is not sum over these three repeated indexes

$$\Gamma^1_{2k} = \Gamma^1_{22}\delta^2_k = -\frac{g^{11}}{2}\partial_1 g_{22}\delta^2_k = -\left(\frac{1-kr^2}{-2a^2}\right)(-2a^2 r)\delta^2_k \tag{A.21}$$

$$\boxed{\Gamma^1_{2k} = -r(1-kr^2)\delta^2_k} \tag{A.22}$$

lets set **i=1** and **j=3**

$$\Gamma^1_{3k} = \frac{g^{11}}{2}\left[\partial_3 g_{k1} - \partial_1 g_{3k}\right] = -\frac{g^{11}}{2}\partial_1 g_{3k} \tag{A.23}$$

$$\Gamma^1_{3k} = \Gamma^1_{33}\delta^3_k = -\frac{g^{11}}{2}\partial_1 g_{33}\delta^3_k = -\left(\frac{1-kr^2}{-2a^2}\right)(-2a^2 r\sin^2\theta)\delta^2_k \tag{A.24}$$

$$\boxed{\Gamma^1_{3k} = -r(1-kr^2)\sin^2\theta\delta^3_k} \tag{A.25}$$

lets set **i=2** and **j=1**

$$\Gamma^2_{1k} = \frac{g^{22}}{2}\left[\partial_k g_{12} + \partial_1 g_{k2} - \partial_2 g_{1k}\right] = \frac{g^{22}}{2}\partial_1 g_{k2} \tag{A.26}$$

$$\Gamma^2_{1k} = \Gamma^2_{1k}\delta^2_k = \frac{1}{-2a^2r^2}(-2a^2 r)\delta^2_k \tag{A.27}$$

$$\boxed{\Gamma^2_{1k} = \frac{1}{r}\delta^2_k} \tag{A.28}$$

lets set **i=2** and **j=2**

$$\Gamma^2_{2k} = \frac{g^{22}}{2}\left[\partial_k g_{22} + \partial_2 g_{k2} - \partial_2 g_{2k}\right] = \frac{g^{22}}{2}\partial_k g_{22} \tag{A.29}$$

$$\Gamma^2_{2k} = \Gamma^2_{21}\delta^1_k = \frac{1}{-2a^2r^2}(-2ra^2) \tag{A.30}$$

$$\boxed{\Gamma^2_{2k} = \frac{1}{r}\delta^1_k} \tag{A.31}$$

lets set **i=2** and **j=3**

$$\Gamma^2_{3k} = \frac{g^{22}}{2}\left[\partial_k g_{32} + \partial_3 g_{k2} - \partial_2 g_{3k}\right] = -\frac{g^{22}}{2}\partial_2 g_{3k} \tag{A.32}$$

$$\Gamma^2_{3k} = \Gamma^2_{33}\delta^3_k = -\frac{1}{-2a^2r^2}(-2a^2r^2\sin\theta\cos\theta)\delta^3_k \tag{A.33}$$

$$\boxed{\Gamma^2_{3k} = \sin\cos\theta\delta^3_k} \tag{A.34}$$

lets set **i=3** and **j=1**

$$\Gamma^3_{1k} = \frac{g^{33}}{2}\left[\partial_k g_{13} + \partial_1 g_{k3} - \partial_3 g_{1k}\right] = \frac{g^{33}}{2}\partial_1 g_{k3} \tag{A.35}$$

$$\Gamma^3_{1k} = \Gamma^3_{13}\delta^3_k = \frac{1}{-2a^2r^2\sin^2\theta}(-2a^2 r\sin^2\theta)\delta^3_k \tag{A.36}$$

$$\boxed{\Gamma^3_{1k} = \frac{1}{r}\delta^3_k} \tag{A.37}$$

lets set **i=3** and **j=2**

$$\Gamma^3_{2k} = \frac{g^{33}}{2}\left[\partial_k g_{23} + \partial_2 g_{k3} - \partial_3 g_{2k}\right] = \frac{g^{33}}{2}\partial_2 g_{k3} \tag{A.38}$$

$$\Gamma^3_{2k} = \Gamma^3_{23}\delta^3_k = \frac{1}{-2a^2r^2\sin^2\theta}(-2a^2r^2\sin\theta\cos\theta)\delta^3_k \tag{A.39}$$

$$\boxed{\Gamma^3_{2k} = \cot\theta\delta^3_k} \tag{A.40}$$

And the only remaining symbol Γ^3_{2k} is null.

A.2 Ricci Tensor and scalar

Now we obtain the Ricci tensor and the Ricci scalar. First write the Ricci tensor in terms of the Christoffel symbols.

$$\boxed{R_{\mu\nu} = \partial_\alpha\Gamma^\alpha_{\mu\nu} - \partial_\nu\Gamma^\alpha_{\mu\alpha} + \Gamma^\alpha_{\beta\alpha}\Gamma^\beta_{\mu\nu} - \Gamma^\alpha_{\beta\nu}\Gamma^\beta_{\mu\alpha}} \tag{A.41}$$

Suppose that $\mu \neq \nu$, bearing in mind the Christoffel symbols obtained before. We see that the first term $\partial_\alpha\Gamma^\alpha_{\mu\nu}$ disappear, since those symbols with different subscript are independent of α. The second term $\partial_\alpha\Gamma^\alpha_{\mu\nu}$ is also null, since symbols with repeated super and sub script are only dependent on the remaining index. The same will be true for the last two terms, let see the algebra. Separating time and spatial indexes, last term can be written as:

$$\Gamma^\alpha_{\beta\alpha}\Gamma^\beta_{\mu\nu} = \Gamma^\alpha_{0\alpha}\cancel{\Gamma^0_{\mu\nu}} + \Gamma^\alpha_{i\alpha}\Gamma^i_{\mu\nu} = \cancel{\Gamma^0_{i0}}\Gamma^i_{\mu\nu} + \Gamma^j_{ij}\Gamma^i_{\mu\nu} = \Gamma^j_{ij}\Gamma^i_{\mu\nu} \tag{A.42}$$

$$-\Gamma^\alpha_{\beta\nu}\Gamma^\beta_{\mu\alpha} = -\cancel{\Gamma^0_{\beta\nu}\Gamma^\beta_{\mu0}} - \cancel{\Gamma^i_{0\nu}\Gamma^0_{\mu i}} - \Gamma^i_{j\nu}\Gamma^j_{\mu i} \tag{A.43}$$

where we have cancelled terms wit scripts 0, since all non-null symbols must have the other two indexes equal. Thus the last term can be written as

$$\Gamma^{\alpha}_{\beta\alpha}\Gamma^{\beta}_{\mu\nu} - \Gamma^{\alpha}_{\beta\nu}\Gamma^{\beta}_{\mu\alpha} = \Gamma^{j}_{ij}\Gamma^{i}_{\mu\nu} - \Gamma^{i}_{j\nu}\Gamma^{j}_{\mu i} \tag{A.44}$$

If you consider one Christoffel symbols with $i \neq j$ in the last term of eq. (A.44), and you invert latin scripts, then the resulting symbol will only be non-null if $\mu = \nu$, other wise it will vanish:

$$\Gamma^{\alpha}_{\beta\alpha}\Gamma^{\beta}_{\mu\nu} - \Gamma^{\alpha}_{\beta\nu}\Gamma^{\beta}_{\mu\alpha} = \Gamma^{j}_{ji}\Gamma^{i}_{\mu\nu} - \Gamma^{i}_{i\nu}\Gamma^{i}_{\mu i} \tag{A.45}$$

now it follows direct examination of all the remaining cases.

$$\Gamma^{\alpha}_{\beta\alpha}\Gamma^{\beta}_{\mu\nu} - \Gamma^{\alpha}_{\beta\nu}\Gamma^{\beta}_{\mu\alpha} = \Gamma^{1}_{1i}\Gamma^{i}_{\mu\nu} + \Gamma^{2}_{2i}\Gamma^{i}_{\mu\nu} + \Gamma^{3}_{3i}\Gamma^{i}_{\mu\nu} - \Gamma^{1}_{1\nu}\Gamma^{1}_{\mu 1} - \Gamma^{2}_{2\nu}\Gamma^{2}_{\mu 2} - \Gamma^{3}_{3\nu}\Gamma^{3}_{\mu i} \tag{A.46}$$

$$A_{\mu\nu} = \Gamma^{1}_{11}\Gamma^{1}_{\mu\nu} + \frac{2}{r}\Gamma^{1}_{\mu\nu} + \Gamma^{3}_{32}\Gamma^{2}_{\mu\nu} - \Gamma^{1}_{1\nu}\Gamma^{1}_{\mu 1} - \Gamma^{2}_{2\nu}\Gamma^{2}_{\mu 2} - \Gamma^{3}_{3\nu}\Gamma^{3}_{\mu 3} \tag{A.47}$$

where we have defined an auxiliary symbol $A_{\mu\nu} = \Gamma^{\alpha}_{\beta\alpha}\Gamma^{\beta}_{\mu\nu} - \Gamma^{\alpha}_{\beta\nu}\Gamma^{\beta}_{\mu\alpha}$ to compact notation, notice that $A_{\mu\nu}$ is symmetric in the subscripts thanks to eq. (A.47), and we can proceed calculating the six combination of pairs of different subscripts.

$$A_{01} = \Gamma^{1}_{11}\Gamma^{1}_{01} + \frac{2}{r}\Gamma^{1}_{01} - \Gamma^{1}_{11}\Gamma^{1}_{10} - \Gamma^{2}_{20}\Gamma^{2}_{12} - \Gamma^{3}_{31}\Gamma^{3}_{03} = 0 \tag{A.48a}$$

$$A_{02} = \Gamma^{3}_{32}\Gamma^{2}_{02} - \Gamma^{3}_{32}\Gamma^{3}_{03} = 0 \tag{A.48b}$$

$$A_{03} = 0 \tag{A.48c}$$

$$A_{12} = \Gamma^{3}_{32}\Gamma^{2}_{12} - \Gamma^{3}_{31}\Gamma^{3}_{23} = 0 \tag{A.48d}$$

$$A_{13} = 0 \tag{A.48e}$$

$$A_{23} = 0 \tag{A.48f}$$

We have demonstrated that only those **components of the Ricci tensor with $\mu = \nu$ are not null**. Thus we calculate these components in the case $\mu = \nu = 0$

$$R_{00} = \partial_{\alpha}\Gamma^{\alpha}_{00} - \partial_{0}\Gamma^{\alpha}_{0\alpha} + \Gamma^{\alpha}_{\beta\alpha}\Gamma^{\beta}_{00} - \Gamma^{\alpha}_{\beta 0}\Gamma^{\beta}_{0\alpha} \tag{A.49}$$

$$R_{00} = -\partial_{0}\Gamma^{\alpha}_{0\alpha} - \Gamma^{\alpha}_{\beta 0}\Gamma^{\beta}_{0\alpha} \tag{A.50}$$

$$R_{00} = -\partial_{0}\Gamma^{i}_{0i} - \Gamma^{i}_{j0}\Gamma^{j}_{0i} \tag{A.51}$$

From the obtained Christofel symbols we can show that:

$$R_{00} = -\delta_{ii}\partial_0\frac{\dot{a}}{a} - (\frac{\dot{a}}{a})^2\delta_{ij}\delta_{ij} \tag{A.52}$$

$$R_{00} = -3[\frac{\ddot{a}}{a} - \frac{\dot{a}^2}{a^2}] - 3(\frac{\dot{a}}{a})^2 \tag{A.53}$$

$$\boxed{R_{00} = -3\frac{\ddot{a}}{a}} \tag{A.54}$$

Now see the case $\mu = \nu = i$ [3]

$$R_{ii} = \partial_\alpha\Gamma^\alpha_{ii} - \partial_i\Gamma^\alpha_{i\alpha} + \Gamma^\alpha_{\beta\alpha}\Gamma^\beta_{ii} - \Gamma^\alpha_{\beta i}\Gamma^\beta_{i\alpha} \tag{A.55}$$

Lets calculate term by term,

$$\partial_\alpha\Gamma^\alpha_{ii} = \partial_0\Gamma^0_{ii} + \partial_1\Gamma^1_{ii} + \partial_2\Gamma^2_{ii} + \cancel{\partial_3\Gamma^3_{ii}} \tag{A.56}$$

$$-\partial_i\Gamma^\alpha_{i\alpha} = -\cancel{\partial_i\Gamma^0_{i0}} - \partial_i\Gamma^1_{i1} - \partial_i\Gamma^2_{i2} - \partial_i\Gamma^3_{i3} \tag{A.57}$$

$$A_{ii} = \Gamma^\alpha_{\beta\alpha}\Gamma^\beta_{ii} - \Gamma^\alpha_{\beta i}\Gamma^\beta_{i\alpha} \tag{A.58}$$

Now, it is easier to continue analysing the three particular cases of interest. Before, going to the analysis using equations above, it worth to notice that the term $\partial_0\Gamma^0_{ii}$ is not null for all three cases, and in particular we can use eq. (A.12) and the property of the metric $\partial_0 g_{ii} = 2Hg_{ii}$ to prove:

$$\partial_0\Gamma^0_{ii} = -g_{ii}\left(\frac{\ddot{a}}{a} + H^2\right) \tag{A.59}$$

It follows

$$\begin{aligned}
R_{11} &= \partial_0\Gamma^0_{11} - 2\partial_1\Gamma^2_{12} + \Gamma^\alpha_{\alpha\beta}\Gamma^\beta_{11} - \Gamma^\alpha_{\beta 1}\Gamma^\beta_{1\alpha} \\
&= \partial_0\Gamma^0_{11} + \frac{2}{r^2} + \Gamma^\alpha_{\alpha 0}\Gamma^0_{11} + \Gamma^\alpha_{\alpha 1}\Gamma^1_{11} - 2\Gamma^0_{11}\Gamma^1_{10} - \Gamma^1_{11}\Gamma^1_{11} - \Gamma^2_{21}\Gamma^2_{12} - \Gamma^3_{31}\Gamma^3_{13} \\
&= \partial_0\Gamma^0_{11} + \Gamma^\alpha_{\alpha 0}\Gamma^0_{11} + \Gamma^\alpha_{\alpha 1}\Gamma^1_{11} - 2\Gamma^0_{11}\Gamma^1_{10} - \Gamma^1_{11}\Gamma^1_{11} \\
&= \partial_0\Gamma^0_{11} + \mathrm{H}\Gamma^0_{11} + \frac{2}{r}\Gamma^1_{11} \\
&= -g_{11}\left(\frac{\ddot{a}}{a} + 2H^2 + 2\frac{k}{a^2}\right)
\end{aligned}$$

[3] We will repeat index i but there is not sum over it

$$
\begin{aligned}
R_{22} &= \partial_0\Gamma^0_{22} + \partial_1\Gamma^1_{22} - \partial_2\Gamma^3_{23} + \Gamma^\alpha_{\beta\alpha}\Gamma^\beta_{22} - \Gamma^\alpha_{\beta 2}\Gamma^\beta_{2\alpha} \\
&= \partial_0\Gamma^0_{22} + \partial_1\Gamma^1_{22} - \partial_2\Gamma^3_{23} + 3\Gamma^2_{20}\Gamma^0_{22} + (\Gamma^1_{11} + 2\Gamma^2_{21})\Gamma^1_{22} \\
&\quad -\Gamma^0_{22}\Gamma^2_{20} - \Gamma^1_{22}\Gamma^2_{21} - \Gamma^2_{20}\Gamma^0_{22} - \Gamma^2_{21}\Gamma^1_{22} - \Gamma^3_{23}\Gamma^3_{23} \\
&= \partial_0\Gamma^0_{22} + \partial_1\Gamma^1_{22} - \partial_2\Gamma^3_{23} + \Gamma^2_{20}\Gamma^0_{22} + \Gamma^1_{11}\Gamma^1_{22} - (\Gamma^3_{23})^2 \\
&= \partial_0\Gamma^0_{22} + 3kr^2 - 1 + \csc^2\theta + \dot{a}^2r^2 - kr^2 - \cot^2\theta \\
&= \partial_0\Gamma^0_{22} + \dot{a}^2r^2 + 2kr^2 \\
&= -g_{22}\left(\frac{\ddot{a}}{a} + 2H^2 + 2\frac{k}{a^2}\right)
\end{aligned}
$$

$$
\begin{aligned}
R_{33} &= \partial_0\Gamma^0_{33} + \partial_1\Gamma^1_{33} + \partial_2\Gamma^2_{33} + \Gamma^\alpha_{\beta\alpha}\Gamma^\beta_{33} - \Gamma^\alpha_{\beta 3}\Gamma^\beta_{3\alpha} \\
&= \partial_0\Gamma^0_{33} + \partial_1\Gamma^1_{33} + \partial_2\Gamma^2_{33} + 3\Gamma^3_{03}\Gamma^0_{33} + (\Gamma^1_{11} + 2\Gamma^3_{31})\Gamma^1_{33} + \Gamma^3_{23}\Gamma^2_{33} \\
&\quad -\Gamma^0_{33}\Gamma^3_{30} - \Gamma^1_{33}\Gamma^3_{31} - \Gamma^2_{33}\Gamma^3_{32} - \Gamma^3_{03}\Gamma^0_{33} - \Gamma^3_{13}\Gamma^1_{33} - \Gamma^3_{23}\Gamma^2_{33} \\
&= \partial_0\Gamma^0_{33} + \partial_1\Gamma^1_{33} + \partial_2\Gamma^2_{33} + \Gamma^3_{03}\Gamma^0_{33} + \Gamma^1_{11}\Gamma^1_{33} - \Gamma^3_{23}\Gamma^2_{33} \\
&= \partial_0\Gamma^0_{33} + (3kr^2 - 1)\sin^2\theta + (\sin^2\theta - \cos^2\theta) + \dot{a}^2r^2\sin^2\theta - kr^2\sin^2\theta + \cos^2\theta \\
&= \partial_0\Gamma^0_{33} + 2kr^2\sin^2\theta + \dot{a}^2r^2\sin^2\theta \\
&= -g_{33}\left(\frac{\ddot{a}}{a} + 2H^2 + 2\frac{k}{a^2}\right)
\end{aligned}
$$

After expanding all the calculations we have found that the not null Ricci coefficients can be written in a compacted way as:

$$\boxed{R_{ii} = -\frac{g_{ii}}{a^2}(a\ddot{a} + 2\dot{a}^2 + 2k)} \tag{A.60}$$

Now we can calculate the Ricci scalar

$$R = g^{\mu\nu}R_{\mu\nu} \tag{A.61}$$

$$R = R_{00} + g^{ii}R_{ii} \tag{A.62}$$

$$R = R_{00} - g^{ii}\frac{g_{ii}}{a^2}(a\ddot{a} + 2\dot{a}^2 + 2k) \tag{A.63}$$

$$R = R_{00} - \frac{\delta_{ii}}{a^2}(a\ddot{a} + 2\dot{a}^2 + 2k) \tag{A.64}$$

$$R = -3\frac{\ddot{a}}{a} - \frac{3}{a^2}(a\ddot{a} + 2\dot{a}^2 + 2k) \tag{A.65}$$

$$R = -3\frac{\ddot{a}}{a} - 3\left(\frac{\ddot{a}}{a} + 2(\frac{\dot{a}}{a})^2 + 2\frac{k}{a^2}\right) \tag{A.66}$$

$$\boxed{R = -6\frac{\ddot{a}}{a} - 6(\frac{\dot{a}}{a})^2 - 6\frac{k}{a^2}} \tag{A.67}$$

A.3 Friedman equation

Once we have defined the geometry of the universe, we can study its dynamic if we consider a model for its energy density and Einsteins equations,

$$G_{\mu\nu} = R_{\mu\nu} - \frac{1}{2}g_{\mu\nu}R \tag{A.68}$$

$$G_{\mu\nu} + \Lambda g_{\mu\nu} = 8\pi G T_{\mu\nu}, \tag{A.69}$$

where $G_{\mu\nu}$ is the Einstein's Tensor and $T_{\mu\nu}$ is the energy-momentum tensor. Notice that we have included the cosmological constant Λ in the equation in the ;.h.s of the equation, although it can also be introduced as a constituent of the universe in the moment-energy tensor. In order to find the Friedman equation, besides defining the geometry (homogeneous and isotropic metric in the expansion), we need to define the constituents of the universe. Let's assume that our universe can be described as a perfect fluid. In this case, the energy-momentum tensor components can be written as:

$$T_{\mu\nu} = (p + \rho)u_\mu u_\nu - p g_{\mu\nu} \tag{A.70}$$

where ρ is the density, p is the pressure measured by the comoving observer, and $u_\mu = (1, 0, 0, 0)$ is the 4-velocity, where we do not have spatial components since we are assuming isotropy and therefore there are no privileged direction. In matricidal representation the energy-momentum tensor can be written as:

$$T^\mu_\nu = \begin{pmatrix} \rho & 0 & 0 & 0 \\ 0 & -p & 0 & 0 \\ 0 & 0 & -p & 0 \\ 0 & 0 & 0 & -p \end{pmatrix} \tag{A.71}$$

Applying Einstein equation when $\mu = \nu = 0$, we have

$$G_{00} = R_{00} - \frac{1}{2}g_{00}R \tag{A.72}$$

$$G_{00} = -3\frac{\ddot{a}}{a} + 3\frac{\ddot{a}}{a} + 3\left(\frac{\dot{a}}{a}\right)^2 + 3\frac{k}{a^2} \tag{A.73}$$

$$G_{00} = 3\left(\frac{\dot{a}}{a}\right)^2 + 3\frac{k}{a^2} \tag{A.74}$$

So the time part of the Einstein's equations lead to:

$$3\left(\frac{\dot{a}}{a}\right)^2 + 3\frac{k}{a^2} + \Lambda = 8\pi G T_{00} \tag{A.75}$$

$$\boxed{\left(\frac{\dot{a}}{a}\right)^2 + \frac{k}{a^2} + \frac{\Lambda}{3} = \frac{8}{3}\pi G\rho} \tag{A.76}$$

Applying Einstein's equation when $\mu = \nu = i$:

$$G_{ii} = R_{ii} - \frac{1}{2}g_{ii}R \tag{A.77}$$

$$G_{ii} = -\frac{g_{ii}}{a^2}(a\ddot{a} + 2\dot{a}^2 + 2k) - \frac{1}{2}g_{ii}\left(-6\frac{\ddot{a}}{a} - 6(\frac{\dot{a}}{a})^2 - 6\frac{k}{a^2}\right) \tag{A.78}$$

$$G_{ii} = -g_{ii}\left(\frac{\ddot{a}}{a} + 2\left(\frac{\dot{a}}{a}\right)^2 + 2\frac{k}{a^2}\right) + 3g_{ii}\left(\frac{\ddot{a}}{a} + \left(\frac{\dot{a}}{a}\right)^2 + \frac{k}{a^2}\right) \tag{A.79}$$

$$G_{ii} = g_{ii}\left(2\frac{\ddot{a}}{a} + \left(\frac{\dot{a}}{a}\right)^2 + \frac{k}{a^2}\right) \tag{A.80}$$

So spatial part of Einstein's equation lead to:

$$g_{ii}\left(2\frac{\ddot{a}}{a} + \left(\frac{\dot{a}}{a}\right)^2 + \frac{k}{a^2}\right) + \Lambda g_{ii} = 8\pi G T_{ii} = 8\pi G g_{ii}(-p) \tag{A.81}$$

$$\boxed{2\frac{\ddot{a}}{a} + \left(\frac{\dot{a}}{a}\right)^2 + \frac{k}{a^2} + \Lambda = -8\pi G p} \tag{A.82}$$

eq. (A.82) is known as the *acceleration equation* and have the important property of being independent of the curvature.

Friedman equations are usually found in literature in terms of energy density $\epsilon = \rho c^2$, the Hubble parameter $H = \frac{\dot{a}}{a}$, and the Gaussian curvature k is written in terms of the

present curvature radius R_0 and κ (-1, 0,1) [4], $k = \frac{\kappa}{R_0^2}$ as:

$$\boxed{H(t)^2 = \frac{8\pi G}{3c^2}\epsilon(t) - \frac{\kappa c^2}{R_0^2 a^2} - \frac{\Lambda c^2}{3}} \tag{A.83}$$

$$\boxed{2\frac{\ddot{a}}{a} + H^2 + \frac{\kappa}{R_0^2 a^2} + \Lambda = -8\pi G p} \tag{A.84}$$

[4]the sign of k or κ tells the curvature of the universe $\kappa = 0$ means a flat universe, $\kappa = 1$ a universe positively curved and $\kappa = -1$ negatively curved. Usually positively curved is referred to us as a closed universe and negatively to a open universe

Appendix B

Deduction of fluid equation

Energy conservation

In general relativity, the conservation of the energy tensor is written as

$$T^{\mu\nu}{}_{;\mu} = 0 \tag{B.1}$$

If our smooth universe is modelled as a perfect fluid, the moment-energy tensor is

$$T^{\mu\nu} = (\rho + p)u^{\nu}u^{\mu} - pg^{\mu\nu} \tag{B.2}$$

where ρ is the density of the fluid, p the pressure and $u_{\mu} = (1, 0, 0, 0)$ is the 4-velocity, where we do not have spatial components since we are assuming isotropy and therefore there are not privileged direction. From the Leibniz rule of tensors, we have that the covariant derivative of 2-rank tensor in terms of the components is

$$T^{\mu\nu}{}_{;\alpha} = T^{\mu\nu}{}_{,\alpha} + \Gamma^{\nu}_{\lambda\alpha}T^{\lambda\mu} + \Gamma^{\mu}_{\lambda\alpha}T^{\lambda\nu}. \tag{B.3}$$

From equation eq. (B.1) and eq. (B.3) we have

$$T^{\mu\nu}{}_{,\mu} + \Gamma^{\nu}_{\lambda\mu}T^{\lambda\mu} + \Gamma^{\mu}_{\lambda\mu}T^{\lambda\nu} = 0. \tag{B.4}$$

Lets now set $\nu = 0$ and examine each term:

$$T^{\mu 0}{}_{,\mu} = T^{00}{}_{,0} = \partial_t \rho \tag{B.5}$$

$$\Gamma^{0}_{\lambda\mu}T^{\lambda\mu} = \Gamma^{0}_{00}T^{00} + \Gamma^{0}_{ij}T^{ij} = \Gamma^{0}_{ij}T^{ij} = 3Hp \tag{B.6}$$

$$\Gamma^{\mu}_{\lambda\mu} T^{\lambda 0} = \Gamma^{\mu}_{0\mu} T^{00} = \Gamma^{i}_{0i} T^{00} = 3H\rho \tag{B.7}$$

where we have used eq. (A.10) and eq. (A.13) to calculate the second and the third terms respectively. Finally, the temporal part of the conservation of the moment-Energy tensor lead to:

$$\boxed{\partial_t \rho + 3H(p + \rho) = 0} \tag{B.8}$$

Appendix C

Perturbation theory

Evolution of density fluctuations

The idea of this appendix is to find a dependency for the evolution of the density fluctuations with the cosmological constant. To do so, it will be assumed that the universe is a fluid, before presenting the fluid equations it is important to keep in mind, that we will use the Euler description, i.e we will treat the fluid as a field of velocities, i.e , we will see the fluid passing through different fixed space elements characterized by a velocity vector, instead of travelling with the flow of one differential element (Lagrangian perspective). The first of this equation is the *continuity equation* which is basically relating the rate of change of the mass inside the space element and the flux of matter through its surfaces.

$$\boxed{\frac{\partial \rho}{\partial t} + \nabla \cdot (\rho \overrightarrow{v}) = 0} \tag{C.1}$$

Second, we have the *Euler equation* which can be interpreted as a law of moment conservation. In an analogous, way how we define the field of velocities we can define an acceleration field in the fluid. In terms of the material derivative and using the newtons second law, we have

$$\boxed{\frac{d\overrightarrow{v}}{dt} = \frac{\partial \overrightarrow{v}}{\partial t} + (\overrightarrow{v} \cdot \nabla)\overrightarrow{v} = -\frac{\nabla p}{\rho} - \nabla \Phi} \tag{C.2}$$

And finally the gravitation field inside the space element will be described by the Poisson's equation

$$\boxed{\nabla^2 \Phi = 4\pi G \rho.} \tag{C.3}$$

we can think in eq. (C.2) how a response of the matter to the gravitational field (and the pressure of the fluid), and eq. (C.3) how the production of a gravitation field because the presence of a matter distribution inside the fluid. The idea now is to include a small

perturbation to the fields and see how this perturbation evolves.

$$\rho(\mathbf{r},t) = \bar{\rho} + \delta\rho(\mathbf{r},t) \tag{C.4a}$$
$$\overrightarrow{v}(\mathbf{r},t) = \overrightarrow{\bar{v}}(\mathbf{r},t) + \overrightarrow{\delta v}(\mathbf{r},t) \tag{C.4b}$$
$$\phi(\mathbf{r},t) = \bar{\phi} + \delta\phi(\mathbf{r},t) \tag{C.4c}$$
$$p(\mathbf{r},t) = \bar{p} + \delta p(\mathbf{r},t) \tag{C.4d}$$
$$\tag{C.4e}$$

It is convenient to write the perturbation of the pressure as a function of a perturbation in the density, thus we will suppose that the pressure is a state function with two degrees of freedom, and we will select the density and the entropy as our thermodynamic variables, with this assumption the perturbation in the pressure is

$$\delta p = \left(\frac{\partial p}{\partial \rho}\right)_S \delta\rho + \left(\frac{\partial p}{\partial S}\right)_\rho \delta S = c_s^2 \delta\rho + \sigma\delta S \tag{C.5}$$

where in the right we introduce the sound speed c_s definition and the constant σ. Replacing eq. (C.4a) and eq. (C.4b) in eq. (C.1) using zero order continuity equation and neglecting second order terms we get

$$\frac{\partial \delta\rho}{\partial t} + \bar{\rho}\nabla\cdot\delta\overrightarrow{v} + \nabla\cdot(\overrightarrow{\bar{v}}\,\delta\rho) = 0 \tag{C.6}$$

$$\frac{\partial \delta\rho}{\partial t} + \bar{\rho}\nabla\cdot\delta\overrightarrow{v} + \delta\rho\nabla\cdot\overrightarrow{\bar{v}} + \left(\overrightarrow{\bar{v}}\cdot\nabla\right)\delta\rho = 0. \tag{C.7}$$

Now, replacing eq. (C.4b), eq. (C.4d) and eq. (C.5) in eq. (C.2) , using zero order Euler's equation, and neglecting higher order terms,

$$\frac{\partial\overrightarrow{\bar{v}}}{\partial t} + \frac{\partial\overrightarrow{\delta v}}{\partial t} + (\overrightarrow{\bar{v}}\cdot\nabla + \overrightarrow{\delta v}\cdot\nabla)(\overrightarrow{\bar{v}} + \overrightarrow{\delta v}) = -\frac{\nabla\bar{p}}{\rho} - c_s^2\frac{\nabla\delta\rho}{\rho} - \sigma\frac{\nabla\delta S}{\rho} - \nabla\Phi \tag{C.8}$$

$$\frac{\partial\overrightarrow{\delta v}}{\partial t} + (\overrightarrow{\delta v}\cdot\nabla)\overrightarrow{\bar{v}} + (\overrightarrow{\bar{v}}\cdot\nabla + \overrightarrow{\delta v}\cdot\nabla)\overrightarrow{\delta v} = -c_s^2\frac{\nabla\delta\rho}{\rho} - \sigma\frac{\nabla\delta S}{\rho} - \nabla\delta\Phi \tag{C.9}$$

$$\frac{\partial\overrightarrow{\delta v}}{\partial t} + (\overrightarrow{\delta v}\cdot\nabla)\overrightarrow{\bar{v}} + (\overrightarrow{\bar{v}}\cdot\nabla)\overrightarrow{\delta v} = -c_s^2\frac{\nabla\delta\rho}{\rho} - \sigma\frac{\nabla\delta S}{\rho} - \nabla\delta\Phi \tag{C.10}$$

Previous equations are known as continuity, Euler, and Poisson equations. To simply our deduction, we will neglect an external pressure exerted by the radiation.

Appendix D

Deduction of the angle of deflection

In this appendix we follow closely the deduction done by [52]. The general idea of the procedure is to add a perturbation to the FLRW metric for a flat universe. And solve the null geodesic equation that describes the path of the photon.

D.1 The Schwarzschild metric

In Cartesian coordinates and using natural units, the space-time interval for a FLRW universe with a perturbation given by a spherically distributed mass is:

$$ds^2 = -[1 + 2\Phi(\overrightarrow{r}, t)]dt^2 + a^2(t)[1 - 2\Phi(\overrightarrow{r}, t)](dx^2 + dy^2 + dz^2) \tag{D.1}$$

where $\overrightarrow{r}$ and t are the coordinates seen by a observer located infinitely far from de mass, $\Phi(\overrightarrow{r}, t)$ is its Newtonian potential and $a(t)$ the scalar factor. In terms of the first order perturbation theory, where

$$g_{\mu\nu} = g^{(0)}_{\mu\nu} + h_{\mu\nu}, \tag{D.2}$$

the components of the metric can be written as

$$g^{(0)}_{\mu\nu} = \begin{cases} g^{(0)}_{00} = -1 \\ g^{(0)}_{ij} = a^2\delta_{ij} \end{cases} \quad , \quad h_{\mu\nu} = \begin{cases} h_{00} = -2\Phi \\ h_{ij} = -2\Phi a^2\delta_{ij} \end{cases} \tag{D.3}$$

where the condition of the perturbation to be small $h_{\mu\nu} << g^{(0)}_{\mu\nu}$ in terms of the potential is $\Phi << 1$.

D.2 Geodesic equation

If the photons are interacting with the mass only gravitationally and there are not other forces, its path is defined by the geodesic equation

$$\frac{d^2x^\mu}{d\lambda^2} + \Gamma^\mu_{\alpha\beta}\frac{dx^\alpha}{d\lambda}\frac{dx^\beta}{d\lambda} = 0, \tag{D.4}$$

where $\Gamma^\mu_{\alpha\beta}$ are the Christoffel symbols and λ is the affine parameter, which is basically a parametrization parameter along the path of the photon. In terms of this parameter the space-time interval for photons satisfies

$$ds = g_{\mu\nu}\frac{dx^\mu}{d\lambda}\frac{dx^\nu}{d\lambda} = 0. \tag{D.5}$$

The idea now is to look how equations D.4 and D.5 change when we include the perturbation. The standard procedure in perturbation theory is the assumption that the solution of the problem goes until first order as well as the metric, this is

$$x^\mu = x^{(0)\mu} + x^{(1)\mu}. \tag{D.6}$$

Then, replacing equation D.6 and D.2 in D.5 we get

$$\begin{aligned} g^{(0)}_{\mu\nu}[\ \underbrace{x^{(0)\mu}_{,\lambda}x^{(0)\nu}_{,\lambda}}_{\text{zero order solution}} + x^{(0)\mu}_{,\lambda}x^{(1)\nu}_{,\lambda} + x^{(1)\mu}_{,\lambda}x^{(0)\nu}_{,\lambda} + \underbrace{x^{(1)\mu}_{,\lambda}x^{(1)\nu}_{,\lambda}}_{\text{second order term}}\ ] + \\ h_{\mu\nu}[x^{(0)\mu}_{,\lambda}x^{(0)\nu}_{,\lambda} + \underbrace{x^{(0)\mu}_{,\lambda}x^{(1)\nu}_{,\lambda} + x^{(1)\mu}_{,\lambda}x^{(0)\nu}_{,\lambda}}_{\text{second order term}} + \underbrace{x^{(1)\mu}_{,\lambda}x^{(1)\nu}_{,\lambda}}_{\text{third order term}}\ ] = 0. \end{aligned} \tag{D.7}$$

As equation D.5 is valid in order zero, and neglecting higher order terms, previous equation turns:

$$\boxed{2g^{(0)}_{\mu\nu}\frac{dx^{(1)\mu}}{d\lambda}\frac{dx^{(0)\nu}}{d\lambda} + h_{\mu\nu}\frac{dx^{(0)\mu}}{d\lambda}\frac{dx^{(0)\nu}}{d\lambda} = 0}. \tag{D.8}$$

Before looking how the whole geodesic equation changes, lets first see the Christoffel symbols. In terms of the metric Christoffel symbols satisfy

$$\Gamma^\mu_{\alpha\beta} = \frac{g^{\mu\nu}}{2}\left[\partial_\beta g_{\alpha\nu} + \partial_\alpha g_{\beta\nu} - \partial_\nu g_{\alpha\beta}\right], \tag{D.9}$$

insterting equation D.2 it becomes

$$\begin{aligned} \Gamma^\mu_{\alpha\beta} = \frac{g^{(0)\mu\nu}}{2}\left[\partial_\beta g^{(0)}_{\alpha\nu} + \partial_\alpha g^{(0)}_{\beta\nu} - \partial_\nu g^{(0)}_{\alpha\beta} + \partial_\beta h_{\alpha\nu} + \partial_\alpha h_{\beta\nu} - \partial_\nu h_{\alpha\beta}\right] + \\ \frac{h^{\mu\nu}}{2}\left[\partial_\beta g^{(0)}_{\alpha\nu} + \partial_\alpha g^{(0)}_{\beta\nu} - \partial_\nu g^{(0)}_{\alpha\beta} + \partial_\beta h_{\alpha\nu} + \partial_\alpha h_{\beta\nu} - \partial_\nu h_{\alpha\beta}\right], \end{aligned} \tag{D.10}$$

grouping terms of the same order and neglecting higher order terms, we can split the indices as

$$\Gamma^{\mu}_{\alpha\beta} = \Gamma^{(0)\mu}_{\alpha\beta} + \Gamma^{(1)\mu}_{\alpha\beta}, \tag{D.11a}$$

with

$$\Gamma^{(0)\mu}_{\alpha\beta} = \frac{g^{(0)\mu\nu}}{2}\left[\partial_\beta g^{(0)}_{\alpha\nu} + \partial_\alpha g^{(0)}_{\beta\nu} - \partial_\nu g^{(0)}_{\alpha\beta}\right] \tag{D.11b}$$

$$\Gamma^{(1)\mu}_{\alpha\beta} = \frac{g^{(0)\mu\nu}}{2}\left[\partial_\beta h_{\alpha\nu} + \partial_\alpha h_{\beta\nu} - \partial_\nu h_{\alpha\beta}\right] + \frac{h^{\mu\nu}}{2}\left[\partial_\beta g^{(0)}_{\alpha\nu} + \partial_\alpha g^{(0)}_{\beta\nu} - \partial_\nu g^{(0)}_{\alpha\beta}\right] \tag{D.11c}$$

Now, we see the geodesic equation including the perturbation. Replacing equations D.6 and D.2 in D.4 we get

$$\begin{aligned}\underbrace{\frac{d^2x^{(0)\mu}}{d\lambda^2} + \Gamma^{(0)\mu}_{\alpha\beta}\frac{dx^{(0)\alpha}}{d\lambda}\frac{dx^{(0)\beta}}{d\lambda}}_{\text{zero order geodesic equation}} + \frac{d^2x^{(1)\mu}}{d\lambda^2} + \Gamma^{(1)\mu}_{\alpha\beta}\frac{dx^{(0)\alpha}}{d\lambda}\frac{dx^{(0)\beta}}{d\lambda} + 2\Gamma^{(0)\mu}_{\alpha\beta}\frac{dx^{(1)\alpha}}{d\lambda}\frac{dx^{(0)\beta}}{d\lambda} \\ + \underbrace{\Gamma^{(1)\mu}_{\alpha\beta}\frac{dx^{(0)\alpha}}{d\lambda}\frac{dx^{(1)\beta}}{d\lambda} + 2\Gamma^{(0)\mu}_{\alpha\beta}\frac{dx^{(1)\alpha}}{d\lambda}\frac{dx^{(1)\beta}}{d\lambda}}_{\text{second order terms}} + \underbrace{\Gamma^{(1)\mu}_{\alpha\beta}\frac{dx^{(1)\alpha}}{d\lambda}\frac{dx^{(1)\beta}}{d\lambda}}_{\text{third order term}} = 0,\end{aligned} \tag{D.12}$$

the geodesic equation is also satisfied in the zero order and neglecting higher order terms we get

$$\boxed{\frac{d^2x^{(1)\mu}}{d\lambda^2} + \Gamma^{(1)\mu}_{\alpha\beta}\frac{dx^{(0)\alpha}}{d\lambda}\frac{dx^{(0)\beta}}{d\lambda} + 2\Gamma^{(0)\mu}_{\alpha\beta}\frac{dx^{(1)\alpha}}{d\lambda}\frac{dx^{(0)\beta}}{d\lambda} = 0}. \tag{D.13}$$

D.3 Christoffel symbols

In order to solve the perturbed geodesic equation , we need to calculate the non-zero Christoffel symbols, so we basically will replace equation D.3 in equation D.11, to handle this easily we divide the symbols according to is time and spatial dependencies, i.e

$$\Gamma^{\mu}_{\alpha\beta}A^\alpha B^\beta = \Gamma^{\mu}_{0\beta}A^0B^\beta + \Gamma^{\mu}_{i\beta}A^iB^\beta = \Gamma^{\mu}_{00}A^0B^0 + \Gamma^{\mu}_{0j}A^0B^j + \Gamma^{\mu}_{i0}A^iB^0 + \Gamma^{\mu}_{ik}A^iB^k \tag{D.14}$$

since the metric does not have terms outside the diagonal, Christoffel symbols are symmetric this is

$$\Gamma^{\mu}_{\alpha\beta} = \Gamma^{\mu}_{\beta\alpha}, \tag{D.15}$$

therefore, we can reduce the calculation to the following six symbols: Γ^0_{00}, Γ^i_{00}, Γ^0_{0j}, Γ^i_{0j}, Γ^0_{ik} and Γ^j_{ik}. Additionally, we will approximate the potential as time-independent ($\dot{\Phi} = 0$), which is valid in the neighborhood of the mass, where the path of the photon is deflected the most and its distance to the mass remains almost constant. In other words, we approximate the deflection of the path as the arc of a circle. In table D.1 is summarized the set of Christoffel symbols after doing the calculations, taking into account

Christoffel symbol	zero order	first order
Γ^0_{00}	0	0
Γ^0_{0j}	0	$\partial_j\Phi$
Γ^0_{ik}	$a\dot{a}\delta_{ik}$	$-\partial_i\Phi\dot{a}a$
Γ^i_{00}	0	$a^{-2}\partial_i\Phi$
Γ^i_{j0}	$\mathrm{H}\delta_{ij}$	0
Γ^j_{ik}	0	$-\partial_k\Phi\delta_{ij}-\partial_i\Phi\delta_{kj}+\partial_j\Phi\delta_{ik}$

Table D.1: Table with the Christoffel symbols of a perturbed geodesic by a espherically symmetric potential

the previous assumption.

D.4 Solving the perturbed geodesic equation

In order to handle easily labels lets rename the following quantities"

$$l=\frac{dx^{(1)}}{d\lambda} \qquad , \qquad k=\frac{dx^{(0)}}{d\lambda}. \tag{D.16}$$

using this new variables, the perturbed geodesic equation becomes:

$$\frac{dl^\mu}{d\lambda}=-\Gamma^{(1)\mu}_{\alpha\beta}k^\alpha k^\beta-2\Gamma^{(0)\mu}_{\alpha\beta}k^\alpha l^\beta \tag{D.17}$$

Lets see how is this equation for only one spatial component , for instance $\mu=1$. Using D.14 and the Christoffel symbols calculated in the previous section, in each component of the right hand of equation D.17 .

First component:

$$\begin{aligned}
\Gamma^{(1)1}_{\alpha\beta}k^\alpha k^\beta &= \Gamma^{(1)1}_{00}k^0k^0+\Gamma^{(1)1}_{0j}k^0k^j+\Gamma^{(1)1}_{i0}k^ik^0+\Gamma^{(1)1}_{ik}k^ik^k\\
&= k^0k^0\Gamma^{(1)1}_{00}+2k^0k^j\cancel{\Gamma^{(1)1}_{0j}}+\Gamma^{(1)1}_{ik}k^ik^k\\
&= k^0k^0a^{-2}\partial_1\Phi+k^ik^k(-\partial_k\Phi\delta_{i1}-\partial_i\Phi\delta_{k1}+\partial_1\Phi\delta_{ik})\\
&= k^0k^0a^{-2}\partial_1\Phi-k^1k^k\partial_k\Phi-k^1k^i\partial_i\Phi+\partial_1\Phi(k^1k^1+k^2k^2+k^3k^3)\\
&= k^0k^0a^{-2}\partial_1\Phi-2k^1k^i\partial_i\Phi+\partial_1\Phi(k^1k^1+k^2k^2+k^3k^3)\\
&= k^0k^0a^{-2}\partial_1\Phi-2k^1(\nabla\Phi\cdot\overrightarrow{k})+\partial_1\Phi\left|\overrightarrow{k}\right|^2
\end{aligned} \tag{D.18}$$

Second component:

$$\begin{aligned}
\Gamma^{(0)\mu}_{\alpha\beta}k^\alpha l^\beta &= \cancel{\Gamma^{(0)1}_{00}}k^0l^0+\cancel{\Gamma^{(0)1}_{0j}}k^0l^j+\Gamma^{(0)1}_{i0}k^il^0+\Gamma^{(1)1}_{ik}k^il^k\\
&= H\delta_{1j}k^0l^j+H\delta_{i1}k^il^0\\
&= Hk^0l^1+Hk^1l^0
\end{aligned} \tag{D.19}$$

Replacing in D.17, D.18 and D.19

$$\begin{aligned}\frac{dl^1}{d\lambda} &= -\big(\frac{k^0}{a}\big)^2\partial_1\Phi + 2k^1(\nabla\Phi\cdot\overrightarrow{k}) - \partial_1\Phi\Big|\overrightarrow{k}\Big|^2 - 2H(k^0l^1+k^1l^0)\\ &= -\big(\frac{k^0}{a}\big)^2\partial_1\Phi + 2k^1(\nabla\Phi\cdot\overrightarrow{k}) + \partial_1\Phi\Big|\overrightarrow{k}\Big|^2 - 2\partial_1\Phi\Big|\overrightarrow{k}\Big|^2 - 2H(k^0l^1+k^1l^0)\\ &= 2\Big(k^1(\nabla\Phi\cdot\overrightarrow{k}) - \partial_1\Phi\Big|\overrightarrow{k}\Big|^2\Big) + \partial_1\Phi\Big(\Big|\overrightarrow{k}\Big|^2 - \big(\frac{k^0}{a}\big)^2\Big) - 2H(k^0l^1+k^1l^0)\end{aligned} \tag{D.20}$$

Recalling that the affine parameter λ is define in terms of the four-moment as:

$$P^\alpha = \frac{dx^\alpha}{d\lambda} \tag{D.21}$$

we observe that the term in the middle vanish, since photons are massless particles:

$$\begin{aligned}\partial_1\Phi\Big(\Big|\overrightarrow{k}\Big|^2 - \big(\frac{k^0}{a}\big)^2\Big) &= \partial_1\Phi\frac{1}{a^2}(-k^0k^0 + a^2k^ik^i) = \partial_1\Phi\frac{1}{a^2}g_{\mu\nu}k^\mu k^\nu\\ &= \partial_1\Phi\frac{1}{a^2}(g_{\mu\nu}P^{(0)\mu}P^{(0)\nu}) = 0\end{aligned} \tag{D.22}$$

Then D.20 reduces to:

$$\frac{dl^1}{d\lambda} = 2\Big(k^1(\nabla\Phi\cdot\overrightarrow{k}) - \big(\frac{k^0}{a}\big)^2\Big) - 2H(k^0l^1+k^1l^0) \tag{D.23}$$

The previous equation can be rearranged, but before doing that, it is important to recall some concepts from multi-variable calculus. Let's suppose you have a scalar field ψ , and that you want to know its derivative along one specific direction $\hat{k}$, well this directional derivative satisfies:

$$D_{\hat{k}}\psi = (\nabla\psi\cdot\hat{k})\hat{k}. \tag{D.24}$$

Now suppose you want to calculate its gradient, but instead of using a fixed frame of reference, we will use the frame of a particle traveling along a trajectory in the field. In this frame, we are interested in how are the field changes along the trajectory and in the perpendicular direction. Hence, we want

$$\nabla\psi = \nabla_\parallel\psi + \nabla_\perp\psi. \tag{D.25}$$

Whether in the directional derivative we choose $\hat{k}$ as an unitary vector tangential to path, the parallel gradient equals the directional derivative. Consequently,

$$\nabla_\perp\psi = \nabla\psi - (\nabla\psi\cdot\hat{k})\hat{k}. \tag{D.26}$$

$$\left|\overrightarrow{k}\right|^2 \nabla_\perp \psi = \left|\overrightarrow{k}\right|^2 \nabla\psi - (\nabla\psi \cdot \overrightarrow{k})\overrightarrow{k} \tag{D.27}$$

Or in terms of the first spatial component

$$\left|\overrightarrow{k}\right|^2 \partial_{\perp 1} \psi = \left|\overrightarrow{k}\right|^2 \partial_1 \psi - k^1(\nabla\psi \cdot \overrightarrow{k}) \tag{D.28}$$

Now, it is clear that the geodesic equation can be rearranged using the perpendicular derivative, under the only condition that $\overrightarrow{k}$ to be tangential to the path. Which is true since we define $\overrightarrow{k}$ as the derivative respect to the affine parameter, and in analogy to a euclidean space where the velocity is always tangent to the trajectory, here the derivative respect a parameter that does not represent a coordinate, is always tangent to the trajectory.

Replacing equation D.28 in D.20 we let to:

$$\frac{dl^1}{d\lambda} = -2\left|\overrightarrow{k}\right|^2 \partial^1_\perp \Phi - 2H(k^0 l^1 + k^1 l^0) \tag{D.29}$$

Finally, if we consider XXX (the temporal part of the geodesic equation and other stuff)

$$\boxed{\frac{dl^i}{d\lambda} + 2Hk^0 l^i = -2\left|\overrightarrow{k}\right|^2 \partial^i_\perp \Phi} \tag{D.30}$$

Which is a differential equation of the form:

$$y' + P(x)y = q(x) \tag{D.31}$$

whose solution is given by:

$$y(x) = \exp\Big(-\int^x P(w)dw\Big)\Big[\int^x \exp\Big(\int^x P(w)dw\Big)q(u)du + c\Big] \tag{D.32}$$

Clearly, we identify that in our case

$$P(\lambda) = 2Hk^0 \qquad , \qquad q(\lambda) = -2\left|\overrightarrow{k}\right|^2 \partial^i_\perp \Phi. \tag{D.33}$$

And the integrals

$$\begin{aligned} \exp\Big(-\int^\lambda 2Hk^0 d\lambda'\Big) &= \exp\Big(-2\int^a \frac{1}{a'}\frac{da'}{dt}\frac{dt}{d\lambda'}d\lambda'\Big) \\ &= \exp\left(-2lna\right) = a^{-2} \end{aligned} \tag{D.34a}$$

$$\exp\Big(\int^\lambda 2Hk^0 d\lambda'\Big) = a^2 \tag{D.34b}$$

Using this integrals, we see that the solution to the perturbed geodesic equation D.30 take the form:

$$\begin{aligned} l^i(\lambda) &= a^{-2}\int^{\lambda} a^2(-2\left|\overrightarrow{k}\right|^2\partial_\perp^i\Phi)d\lambda + C \\ &= -2\int^{\lambda}\left|\overrightarrow{k}\right|^2\partial_\perp^i\Phi d\lambda + C \end{aligned} \tag{D.35}$$

Our contour condition is that $l^i = 0$ when $\Phi = 0$. Hence $C = 0$.

$$l^i = -2\left|\overrightarrow{k}\right|^2\int^{\lambda}\partial_\perp^i\Phi d\lambda \tag{D.36}$$

That contour condition make fully sense, since $\frac{dx^i}{d\lambda}$ is like a velocity, and because of that it will always point out in the direction of the trajectory. However l^i represents the "additional velocity" we are including due to the perturbation, or in better words, l^i represents the deviations from the unperturbed path. And in the absence of a perturbative potential, no deviation will be observed.

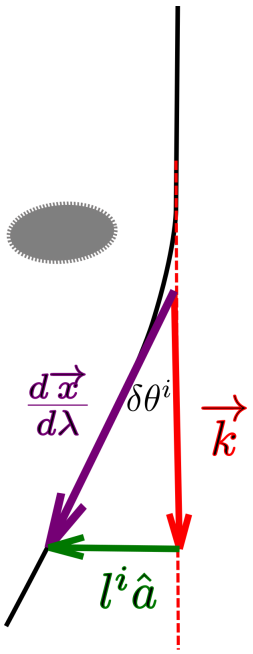

Figure D.1: *The deflection angle and its relation with the vector which define the directions of the unperturbed and perturbed paths. represents the zero order of the derivative of coordinates with respect to the affine parameter and therefore we will assume that deviation in the path is caused by*

It is in this sense that we define the deflection angle as:

$$\boxed{\delta\theta^i = -\frac{l^i}{\left|\overrightarrow{k}\right|}.} \tag{D.37}$$

In figure D.1 we present a scheme to illustrate this definition. When a photon that comes

from a background galaxy passes nearby a distribution of masses as a galaxy cluster its path is bent. Without the presence of the cluster, the photon would travel in the direction of $\overrightarrow{k} = \frac{d\vec{x}^{(0)}}{d\lambda}$, however, the perturbation modifies the trajectory to a new one that goes in the direction of $\overrightarrow{k} + \overrightarrow{l} = \frac{d\vec{x}}{d\lambda}$. The i index in the figure depicts that the deflection could happen in any direction according to the system of coordinates used by the observer.

There are two subtleties to highlight here, first that we only need two angles to characterize the new direction of the deflected path. You can think this in analogy to the Euler angles used to describe the rigid body, with the difference that in our case the order of the rotations commute, i.e., it would be the same tilt the light beam to the right and then up as tilt it first up and latter to the right. Two angles characterize these two consecutive tilts, let's call them θ_1 and θ_2. In a Cartesian frame of reference, where unperturbed photons are observed to travel in the $-\hat{z}$ direction, The deviation angles θ_1 and θ_2 are measured over the planes x-z and y-z, respectively. Probably, you can also image these two angles as being similar to the angular vectors in spherical coordinates. However, in this case ϕ is measured respect to one axis (typically $\hat{x}$) and θ respect other axis (typically $\hat{z}$). Unlike our case, where both angles θ_1 and θ_2 are defined respect to the same axis (-$\hat{z}$). It is for this reason that the minus sign is introduced in equation D.37 since the photons are observed traveling the observer inwards. The second subtlety is that the weak lensing regime has been assumed in the definition since it was used the small-angle approximation of $\tan(\theta)$.

Replacing equation D.36 in D.37

$$\delta\theta^i = 2\int^{\lambda} \partial^i_{\perp}\Phi \left|\overrightarrow{k}\right| d\lambda \tag{D.38}$$

which is basically the definition of a line integral, i.e each component of the deflection angle is the line integral of the variation of the Newtonian potential in the direction of that component, calling s the physical distance, and generalizing to other directions we have

$$\boxed{\delta\hat{\theta} = 2\int_C \nabla_{\perp}\Phi ds} \tag{D.39}$$

where C is the trajectory travelled by the photon. If we approximate the curve of integration by the background path, i.e as if we assume that the travelled distance is approximately equal to the physical distance of the unperturbed photon. We have.

$$\delta\hat{\theta} = 2\int_{s(z=0)}^{s(z_{OBS})} \nabla_{\perp}\Phi ds \tag{D.40}$$

This approximation is known as the Born's approximation.

D.5 The point mass

An illustrative example of the deduced equation for the deflection angle is to find the deflection produced when the lens is a point mass. In fig. D.2, we show the diagram for this case.

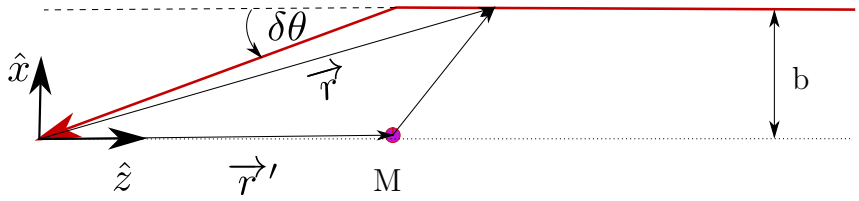

Figure D.2: *The deflection angle for a point mass using Born's approximation*

The Newtonian potential of this problem is:

$$\Phi = \frac{-GM}{\left|\vec{r} - \vec{r}\,'\right|} = \frac{-GM}{\left|x\hat{x} + (z - z')\hat{z}\right|} = \frac{-GM}{\sqrt{x^2 + (z - z')^2}} \tag{D.41}$$

In the Born approximation the path of the photon is approximately over the $\hat{z}$ direction, then the orthogonal direction to the path is approximately equal to $-\hat{x}$

$$\nabla_\perp \Phi = \partial_{-x}\Phi = \partial_u \Phi = \frac{GMu}{[u^2 + (z - z')^2]^{3/2}} = -\frac{GMx}{[x^2 + (z - z')^2]^{3/2}} \tag{D.42}$$

Then D.40 becomes

$$\delta\theta = -2\int_{\infty}^{-\infty} \frac{GMx}{[x^2 + (z - z')^2]^{3/2}} dz = -2\int_{\infty}^{-\infty} \frac{GMb}{[b^2 + v^2]^{3/2}} dv \tag{D.43}$$

where in the last step we did the substitution $v = z - z'$ and $x = b$, this last substitution is reliable because most of the deflection is produced in the proximity of the lens and this distance of maximum approach is of the order of magnitude that the impact factor. Recalling that in the weak lensing regime photon follows hyperbolas rather any other conic section. Inverting the order of integration, using the property of even integrand and doing the substitution $v = b\tan\theta$

$$\delta\theta = 4GMb\int_0^{\infty} \frac{1}{[b^2 + v^2]^{3/2}} dv = 4GMb\int_0^{\frac{\pi}{2}} \frac{\cos\theta}{b^2} d\theta = \frac{4GM}{b} \tag{D.44}$$

Finally, recovering international units, we get the famous equation that Einstein deduce to test its theory of General relativity during an eclipse.

$$\boxed{\delta\theta = \frac{4GM}{bc^2}} \tag{D.45}$$

Appendix E

Geometrical interpretation of the shear

E.1 Eccentricity, flattening and shear

In this appendix, we want to extend the preliminary analysis presented about the geometrical interpretation of the shear. Here we will treat the general case, where both components of the shear are not null. The idea is to assume that originally, we had a circular shape, and using the transformation matrix get the shape of the observed image. Before doing that. Lets first recall the general equation for the ellipse,

$$AX^2 + BXY + CY^2 + DX + EY + F = 0 \quad \text{where} \qquad B^2 - 4AC < 0, \tag{E.1}$$

to simplify our problem of interest, and without lost of generality we will choose the center to be the origin,. In that case,

$$AX^2 + BXY + CY^2 + F = 0 \quad \text{where} \qquad B^2 - 4AC < 0, \tag{E.2}$$

is the resulting equation of the ellipse. The constants A, B, and C itself have not a direct geometrical interpretation. Then what we do is to relate these constants with the semi-major axis a, the semi-minor axis b, and a rotation angle ϕ respect to the x-axis. Using the inverse rotation matrix, we have that the original coordinates relate the primed rotated coordinates via the equations

$$x = x' \cos\phi + y' \sin\phi \qquad y = -x' \sin\phi + y' \cos\phi. \tag{E.3}$$

And replacing this expression in the canonical equation of the ellipse, we have

$$\frac{x^2}{a^2} + \frac{y^2}{b^2} = 1 \tag{E.4}$$

$$b^2x^2 + a^2y^2 = a^2b^2 \tag{E.5}$$

$$b^2\left(x'\cos\phi + y'\sin\phi\right)^2 + a^2\left(-x'\sin\phi + y'\cos\phi\right)^2 = a^2b^2 \tag{E.6}$$

$$x'^2(b^2\cos^2\phi + a^2\sin^2\phi) + 2x'\cos\phi y'\sin\phi(b^2 - a^2) + y'^2(b^2\sin^2\phi + a^2\cos^2\phi) = a^2b^2 \tag{E.7}$$

Finally, comparing directly with eq. (E.2) we obtain the relations between the constants and geometrical variables

$$\begin{cases} A &= b^2\cos^2\phi + a^2\sin^2\phi \\ B &= \sin(2\phi)(b^2 - a^2) \\ C &= b^2\sin^2\phi + a^2\cos^2\phi \\ F &= -a^2b^2. \end{cases} \tag{E.8}$$

Keeping this in mind, lets write the transformation matrix eq. (3.33) for the case were both components of the shear are not null and there is absence of convergence $\kappa = 0$

$$\frac{\partial\beta_i}{\partial\theta_j} = \begin{bmatrix} 1-\gamma_1 & -\gamma_2 \\ -\gamma_2 & 1+\gamma_1 \end{bmatrix}, \tag{E.9}$$

consequently we end up with the following linear system of equations,

$$\frac{\partial\beta_1}{\partial\theta_1} = 1-\gamma_1 \quad \frac{\partial\beta_1}{\partial\theta_2} = -\gamma_2 \quad \frac{\partial\beta_2}{\partial\theta_2} = 1+\gamma_1 \quad \frac{\partial\beta_2}{\partial\theta_1} = -\gamma_2 \tag{E.10}$$

It is easy to see the solution using the Anzatz $\beta_i = A_i\theta_1 + B_i\theta_2 + C_i$, then using the contour condition $\overrightarrow{\beta}(\overrightarrow{0}) = \overrightarrow{0}$ we have the solutions

$$\beta_1 = (1-\gamma_1)\theta_1 - \gamma_2\theta_2 \quad \beta_2 = (1+\gamma_1)\theta_2 - \gamma_2\theta_1, \tag{E.11}$$

Now if we assume that originally the shape was round, we replace this equations of transformation in the circle equation $\beta_1^2 + \beta_2^2 = \beta^2$, it follows immediately the the observed shape is an ellipse, satisfying the equation

$$\beta^2 = \left[(1-\gamma_1)\theta_1 - \gamma_2\theta_2\right]^2 + \left[(1+\gamma_1)\theta_2 - \gamma_2\theta_1\right]^2, \tag{E.12}$$

writing it in the form eq. (E.2) we obtain

$$\beta^2 = \left[(1-\gamma_1)^2 + \gamma_2^2\right]\theta_1^2 - 4(1-\gamma_1)\gamma_2\theta_1\theta_2 + \left[(1+\gamma_1)^2 + \gamma_2^2\right]\theta_2^2, \tag{E.13}$$

comparing with eq. (E.8) we have

$$\begin{cases} (1-\gamma_1)^2+\gamma_2^2 & = b^2\cos^2\phi + a^2\sin^2\phi \\ -4(1-\gamma_1)\gamma_2 & = \sin(2\phi)(b^2-a^2) \\ (1+\gamma_1)^2+\gamma_2^2 & = b^2\sin^2\phi + a^2\cos^2\phi \\ \beta^2 & = a^2b^2 \end{cases} \tag{E.14}$$

Doing a bit of algebra with the first and second equations (adding and subtraction each other) we can reduced the last system to

$$\begin{cases} -4\gamma_1 & = (b^2-a^2)\cos 2\phi \\ -4(1-\gamma_1)\gamma_2 & = \sin(2\phi)(b^2-a^2) \\ 2(|\boldsymbol{\gamma}|+1) & = b^2+a^2 \\ \beta^2 & = a^2b^2 \end{cases} \tag{E.15}$$

where we have introduced the module of the shear $|\boldsymbol{\gamma}|^2 = \gamma_1^2+\gamma_2^2$. From the two first equation, we can deduce the rotation angle, if we are not in the trivial case $a=b$

$$\phi = \frac{1}{2}\arctan\left[(\gamma_1^{-1}-1)\gamma_2\right], \tag{E.16}$$

also we get the following relations for the semi-major and semi-minor axis a and b

$$a^2 = |\boldsymbol{\gamma}| + 1 + 2\sqrt{\gamma_1^2+(1-\gamma_1)^2\gamma_2^2} \tag{E.17}$$

$$b^2 = |\boldsymbol{\gamma}| + 1 - 2\sqrt{\gamma_1^2+(1-\gamma_1)^2\gamma_2^2} \tag{E.18}$$

using this two equation of the semi-axis we can recover the original radius β of the round hypothetical source. Nevertheless, we are more interested in the eccentricity,

$$\text{eccentricity} = \sqrt{1-\frac{b^2}{a^2}} = 2\sqrt{\frac{\sqrt{\gamma_1^2+(1-\gamma_1)^2\gamma_2^2}}{|\boldsymbol{\gamma}|+1+2\sqrt{\gamma_1^2+(1-\gamma_1)^2\gamma_2^2}}} \tag{E.19}$$

where we can conclude that the only way to keep unaltered the image is if both shear component are null, in which case the eccentricity is zero.

Furthermore, we can make an additional approximation, which is perfectly valid for the case of weak lensing, it is $|\gamma_1| << 1$. Under this approximation, we get a more simplified and familiar form.

$$\boxed{\phi = \frac{1}{2}\arctan\left[\frac{\gamma_2}{\gamma_1}\right],} \tag{E.20}$$

$$\boxed{a^2 = (|\boldsymbol{\gamma}| + 1)^2} \tag{E.21}$$

$$\boxed{b^2 = (|\boldsymbol{\gamma}| - 1)^2} \tag{E.22}$$

$$\boxed{\text{eccentricity} = 2\frac{\sqrt{|\boldsymbol{\gamma}|}}{|\boldsymbol{\gamma}| + 1}} \tag{E.23}$$

this is the same result we obtain when there is only one component of the shear, but this time we use have the modulus of the total shear. Notice, that eq. (E.20) result is suggesting us that we can write the shear as a complex number with modules $|\boldsymbol{\gamma}|^2 = \gamma_1^2 + \gamma_2^2$ and argument 2ϕ. This is expected since if we rotate the ellipse π radians, we will get the same ellipse, i.e., ellipses are symmetric under π rotations. Additionally, if $-1 > \gamma << 1$, the eccentricity will always be lower than one and higher than 0, guaranteeing the new shape will be always another ellipse and not another conic section.

To finish the section, we will show another measure that quantifies how much a circle was compressed or stretched, which is known as the flattening n (or ellipticity). It was introduced in chapter 4 and it is defined by eq. (4.3). It worth's to notice that in terms of the shear the third flattening is

$$n = \frac{\big||\boldsymbol{\gamma}| + 1\big| - \big||\boldsymbol{\gamma}| - 1\big|}{\big||\boldsymbol{\gamma}| + 1\big| + \big||\boldsymbol{\gamma}| - 1\big|} = |\boldsymbol{\gamma}|\,. \tag{E.24}$$

Which is very meaningful, because the modulus of the shear is the flattening. So the shear is intrinsically related with geometrical properties and we can expect to get the shear from measurement of flattening.

Appendix F

Random fields, correlation functions, and the Limber's approximation

The following appendix is based on section 2.4 in [5]. The correlation function and the Power spectrum are statistical properties of a *random field*, like the mean or the variance. Mathematically speaking, a random field is a collection of random variables indexed by elements in a topological space. For our interest, we will understand those indexes as the position in the space-time. *The two-point correlation function* $\xi(\overrightarrow{x}, \overrightarrow{y})$ of a random field $\mathbf{g}$ is defined as

$$\boxed{\xi(\overrightarrow{x}, \overrightarrow{y}) = \langle g(\overrightarrow{x}) g^*(\overrightarrow{y}) \rangle}, \tag{F.1}$$

where the brackets denote average over the whole $(\overrightarrow{x}, \overrightarrow{y})$ space, i.e., we evaluate the product of the random field in all the possible couple of points resulting of the Cartesian product of the random vectors $\overrightarrow{x}$ and $\overrightarrow{y}$, and we divide by the number of couples. *Two points in the sky are said to be correlated if it is more likely that the realization of the field in those two points have the same value.* In the case of the over-density field, for instance, this happens when the correlation function takes values greater than the unit.

We say that a random field $\mathbf{g}$ is *homogeneous* when we can not distinguish statistically $\mathbf{g(x+y)}$ from $\mathbf{g(x)}$, i.e, both have the same mean, variance, and in particular the two point correlation function satisfies

$$\xi(\overrightarrow{x}, \overrightarrow{y}) = \xi(\overrightarrow{x} - \overrightarrow{y}). \tag{F.2}$$

We say that a random field $\mathbf{g}$ is *isotropic* if $\mathbf{g(\Re x)}$ and $\mathbf{g(x)}$ share the same statistical properties, where $\Re$ is an arbitrary rotation. Including this property the correlation function of random field homogeneous and isotropic have to satisfies

$$\xi(\overrightarrow{x}, \overrightarrow{y}) = \xi(\mid \overrightarrow{x} - \overrightarrow{y} \mid) \tag{F.3}$$

We are now interested in correlating our random field $\mathbf{g}$ in the Fourier space. First,

we define the Fourier-transform pair of g as,

$$\hat{g}(\mathbf{k}) = \int_{R^n} d^n x g(\mathbf{x}) e^{i\mathbf{x}.\mathbf{k}} \qquad g(x) = \int_{R^n} \frac{d^n k}{(2\pi)^n} \hat{g}(\mathbf{k}) e^{-i\mathbf{x}.\mathbf{k}} \tag{F.4}$$

then we calculate the two point correlation function

$$\begin{aligned} \left\langle \hat{g}(\mathbf{k}) \hat{g}^*(\mathbf{k}') \right\rangle &= \int_{R^n} d^n x e^{i\mathbf{x}.\mathbf{k}} \int_{R^n} d^n x' e^{-i\mathbf{x}'.\mathbf{k}'} \left\langle g(\mathbf{x}) g^*(\mathbf{x}') \right\rangle \\ &= \int_{R^n} d^n x e^{i\mathbf{x}.\mathbf{k}} \int_{R^n} d^n x' e^{-i\mathbf{x}'.\mathbf{k}'} \xi(\mid \mathbf{x} - \mathbf{x}' \mid) \end{aligned}, \tag{F.5}$$

where in the last step we assume that the random field is isotropic and homogeneous. Changing the variable $\mathbf{x}' = \mathbf{x} + \mathbf{y}$,

$$\begin{aligned} \left\langle \hat{g}(\mathbf{k}) \hat{g}^*(\mathbf{k}') \right\rangle &= \int_{R^n} d^n x e^{i\mathbf{x}.(\mathbf{k}-\mathbf{k}')} \int_{R^n} d^n y' e^{-i\mathbf{y}.\mathbf{k}} \xi(\mid \mathbf{y} \mid) \\ &= (2\pi)^n \delta_D(\mathbf{k} - \mathbf{k}') \int_{R^n} d^n y' e^{-i\mathbf{y}.\mathbf{k}} \xi(\mid \mathbf{y} \mid) \end{aligned} \tag{F.6}$$

But the integral is the definition of what we will call the *Power spectrum*,

$$\boxed{P(\mid \mathbf{k} \mid) \int_{R^n} d^n y' e^{-i\mathbf{y}.\mathbf{k}} \xi(\mid \mathbf{y} \mid).} \tag{F.7}$$

we get

$$\boxed{\left\langle \hat{g}(\mathbf{k}) \hat{g}^*(\mathbf{k}') \right\rangle = (2\pi)^n \delta_D(\mathbf{k} - \mathbf{k}') P(\mid \mathbf{k} \mid)} \tag{F.8}$$

Therefore the power spectrum and the correlation function are representation of the same statistical property.

The idea now is to find a relation between the three-dimensional random field and its two-dimensional projection. This is known as the *Limber's approximation*. The only important assumption we will request for this field is to be homogeneous and isotropic and with expectation value zero. Given the importance of this projection, we will choose our field conveniently as δ (over-density field) and its projection in two dimensions as κ(convergence) although other labels can be selected indistinguishably.

Let's start by defining the two-dimensional projection of the over-density as

$$\kappa_i(\theta) = \int_0^{\chi_H} d\chi g(\chi) \delta(S_K(\chi)\theta, \chi) \tag{F.9}$$

where $g(\chi)$ are weight functions, i.e, the projection is the weighted integral along the whole comoving radial space. Now we calculate the two point correlation function of this

projection

$$\left\langle \kappa_i(\theta)\kappa_j^*(\theta')\right\rangle = \int_0^{\chi_H} d\chi g_i(\chi)\int_0^{\chi_H} d\chi' g_j(\chi')\left\langle \delta(S_K(\chi)\theta,\chi)\delta(S_K(\chi')\theta',\chi')\right\rangle, \tag{F.10}$$

it results convenient to write the three-dimensional random field δ in a Fourier expansion

$$\delta(\boldsymbol{\chi}) = \frac{1}{(2\pi)^3}\int d^3k\tilde{\delta}(\boldsymbol{k},\chi)e^{-i\vec{k}\cdot\boldsymbol{\chi}}, \tag{F.11}$$

writing the wave-vector as the parallel and perpendicular component to the line of sight, i.e $\vec{k} = \boldsymbol{k}_\perp + \boldsymbol{k}_\parallel$, the Fourier expansion becomes

$$\delta(S_K(\chi)\boldsymbol{\theta},\chi) = \frac{1}{(2\pi)^3}\int d^3k\tilde{\delta}(k,\chi)e^{-iS_K(\chi)\boldsymbol{k}_\perp\cdot\boldsymbol{\theta}}e^{-ik_\parallel\cdot\chi} \tag{F.12}$$

substituting in eq. (F.10) we came up with

$$\begin{aligned}\left\langle \kappa_i(\theta)\kappa_j^*(\theta')\right\rangle = \int_0^{\chi_H} d\chi g_i(\chi)\int_0^{\chi_H} d\chi' g_j(\chi')\int\frac{d^3k}{(2\pi)^3}\int\frac{d^3k'}{(2\pi)^3}\times \\ \left\langle \tilde{\delta}(k,\chi)\tilde{\delta}^*(k',\chi')\right\rangle e^{-iS_K(\chi)\boldsymbol{k}_\perp\cdot\boldsymbol{\theta}}e^{iS_K(\chi')\boldsymbol{k'}_\perp\cdot\boldsymbol{\theta'}}e^{-ik_\parallel\cdot\chi}e^{ik'_\parallel\cdot\chi'}\end{aligned} \tag{F.13}$$

using eq. (F.8) we can introduce the matter power spectra and a delta of Dirac $\delta_D(\mathbf{k}-\mathbf{k}')$

$$\begin{aligned}\left\langle \kappa_i(\theta)\kappa_j^*(\theta')\right\rangle = \int_0^{\chi_H} d\chi g_i(\chi)\int_0^{\chi_H} d\chi' g_j(\chi')\int\frac{d^3k}{(2\pi)^3}\int\frac{d^3k'}{(2\pi)^3}\times \\ (2\pi)^3\delta_D(\mathbf{k}-\mathbf{k}')P_\delta(|\mathbf{k}|,\bar{\chi})e^{-iS_K(\chi)\boldsymbol{k}_\perp\cdot\boldsymbol{\theta}}e^{iS_K(\chi')\boldsymbol{k'}_\perp\cdot\boldsymbol{\theta'}}e^{-ik_\parallel\cdot\chi}e^{ik'_\parallel\cdot\chi'},\end{aligned} \tag{F.14}$$

where in the power spectrum we use the mean distance between χ and χ', since the two point correlation function is evaluated in different spatial points, this exact value for $\bar{\chi}$ is not than important as we will see. Using the main property of the delta of Dirac we obtain

$$\begin{aligned}\left\langle \kappa_i(\theta)\kappa_j^*(\theta')\right\rangle = \int_0^{\chi_H} d\chi g_i(\chi)\int_0^{\chi_H} d\chi' g_j(\chi')\int\frac{d^3k}{(2\pi)^3}\times \\ P_\delta(|\mathbf{k}|,\bar{\chi})e^{-iS_K(\chi)\boldsymbol{k}_\perp\cdot\boldsymbol{\theta}}e^{iS_K(\chi')\boldsymbol{k}_\perp\cdot\boldsymbol{\theta'}}e^{-ik_\parallel\cdot\chi}e^{ik_\parallel\cdot\chi'},\end{aligned} \tag{F.15}$$

Now we will do the approximation $S_k(\chi') = S_k(\chi)$ and $g_i(\chi) = g_j(\chi')$ which are known as *the Limber's approximations*, it might seem a strong approximation but let us justify it. Consider a comoving distance of coherence L_{coh}, that will characterize a scale where essentially there is not power in the density fluctuations, typically some hundred Mpc. This can be considered since the power spectrum is proportional with $\mathbf{k}$ then for a sufficiently large scale $P_\delta(\boldsymbol{k}) \to 0$. The same will happen with the associated correlation function when $|\chi-\chi'| > L_{\text{coh}}$. Additionally, we can consider that during the time light travel this

distance the over-density δ remain constant. Therefore when $|\chi - \chi'| < L_{\rm coh}$ we expect the weight functions $g_i(\chi)$ do not vary appreciably, and the difference between χ and χ' becomes irrelevant and $\bar{\chi}$ is essentially χ.

It is important to mention that because of this selection of coherence scale, Limber's approximations are accurate only for small angular scales, a detailed explanation of how these inaccuracies will affect the measurements go out the scope of this work.

Under Limber's approximation eq. (F.15) becomes

$$\begin{aligned}\left\langle \kappa_i(\theta)\kappa_j^*(\theta')\right\rangle = \int_0^{\chi_H} d\chi g_i(\chi)g_j(\chi)\int \frac{d^3k}{(2\pi)^3}\times \\ P_\delta(\left|\mathbf{k}\right|,\chi)e^{iS_K(\chi)\boldsymbol{k}_\perp\cdot(\boldsymbol{\theta'}-\boldsymbol{\theta})}e^{-ik_\parallel\cdot\chi}\int_0^{\chi_H} d\chi' e^{ik_\parallel\cdot\chi'},\end{aligned} \tag{F.16}$$

where the last integral yields $2\pi\delta_D(k_\parallel)$, i.e, modes parallel to the line of sight do not contribute in the projection of the correlation function. Letting to the expression

$$\left\langle \kappa_i(\theta)\kappa_j^*(\theta')\right\rangle = \int_0^{\chi_H} d\chi g_i(\chi)g_j(\chi)\int \frac{d^3k_\perp}{(2\pi)^2}P_\delta(\left|\boldsymbol{k}_\perp\right|,\chi)e^{iS_K(\chi)\boldsymbol{k}_\perp\cdot(\boldsymbol{\theta'}-\boldsymbol{\theta})}. \tag{F.17}$$

which is essentially relating the two point correlation function of the convergence with the matter power spectrum. However it results more convenient to write this linking in the Fourier space i.e.

$$P_\kappa^{ij}(l) = \int d^2\theta \left\langle \kappa_i\kappa_j^*\right\rangle(\theta)e^{il\theta} \tag{F.18}$$

where we have used the fact of κ be homogeneous and isotropic and as a consequence his correlation function only depends on $|\theta - \theta'|$ which we labeled simply as θ. Using eq. (F.17)

$$P_\kappa^{ij}(l) = \int d^2\theta e^{i\boldsymbol{l}.\boldsymbol{\theta}}\int_0^{\chi_H} d\chi g_i(\chi)g_j(\chi)\int \frac{d^3k_\perp}{(2\pi)^2}P_\delta(\left|\boldsymbol{k}_\perp\right|,\chi)e^{-iS_K(\chi)\boldsymbol{k}_\perp.\boldsymbol{\theta}} \tag{F.19}$$

$$P_\kappa^{ij}(l) = \int_0^{\chi_H} d\chi g_i(\chi)g_j(\chi)\int \frac{d^3k_\perp}{(2\pi)^2}P_\delta(\left|\boldsymbol{k}_\perp\right|,\chi)\int d^2\theta e^{-i\boldsymbol{\theta}.\left[S_K(\chi)\boldsymbol{k}_\perp-\boldsymbol{l}\right]} \tag{F.20}$$

$$P_\kappa^{ij}(l) = \int_0^{\chi_H} d\chi g_i(\chi)g_j(\chi)\int \frac{d^3k_\perp}{(2\pi)^2}P_\delta(\left|\boldsymbol{k}_\perp\right|,\chi)(2\pi)^2\delta_D\left(S_K(\chi)\boldsymbol{k}_\perp - \boldsymbol{l}\right) \tag{F.21}$$

$$\boxed{P_\kappa^{ij}(l) = \int_0^{\chi_H} d\chi \frac{g_i(\chi)g_j(\chi)}{S_K^2(\chi)}P_\delta\left(\frac{l}{S_K(\chi)},\chi\right)} \tag{F.22}$$

where in the last term we change variable and use the definition of the delta of Dirac. eq. (F.22) is a powerful equation because it relates directly two second order statistics of a three-dimensional random field and his two-dimensional projection, and several examples in cosmology this kind of projections is very common.

Appendix G

Getting the shear from ellipticities

In the following appendix, using two particular definitions of ellipticities, the polarization, and the distortion, we get expressions to estimate the shear. We will see that for weak lensing application results more convenient to use the distortion, since it is an unbiased estimator of the shear.

G.1 Getting the shear from ellipticities

The trick to link definitions of ellipticity and the weak lensing observables is to bear in mind that we can define two different surface brightness one in the plane of the source $S^{(s)}$ and other in the plane of the observer $S^{\rm obs}$. Then we can link together both using the transformation matrix eq. (3.33). Let's start, writing the second moment of the surface brightness in the plane of the source.

$$Q_{ij}^{(s)} = \frac{\int d\beta_i d\beta_j (\beta_i - \beta_i^{\rm cen})(\beta_j - \beta_j^{\rm cen}) S^{(s)}(\overrightarrow{\beta})}{\int d\beta_i d\beta_j S^{(s)}(\overrightarrow{\beta})}, \tag{G.1}$$

we now will change from the plane of the source to the plane of the observer, taking advantage of the conservation of the surface brightness $S^{(s)}(\overrightarrow{\beta}) = S^{\rm obs}(\overrightarrow{\theta})$, we will make use of the definition of the transformation tensor in the weak lensing regime, i.e , $\beta_i = A_{ik}\theta_k$ and $d\beta_i = A_{ik}d\theta_k$. Therefore, doing this substitutions we get

$$Q_{ij}^{(s)} = \frac{A_{ik}^2 A_{jn}^2 \int d\theta_k d\theta_n (\theta_k - \theta_k^{\rm cen})(\theta_n - \theta_n^{\rm cen}) S^{\rm obs}(\overrightarrow{\theta})}{A_{ik}A_{jn}\int d\theta_k d\theta_n S^{\rm obs}(\overrightarrow{\theta})}, \tag{G.2}$$

and

$$\boxed{Q_{ij}^{(s)} = A_{ik}A_{jn}Q_{kn}^{\rm obs}.}. \tag{G.3}$$

To write the last expression in matrix notation we use $(AB)_{ij} = a_{ik}b_{kj}$, given that both A_{ij} and Q_{ij} are symmetric matrices eq. (G.3) can be written as

$$\boxed{Q^{(s)} = AQ^{\rm obs}A.} \tag{G.4}$$

Using this result, we now will write other equations linking quantities in the source plane and the observer plane, but this time in terms of the two definitions of ellipticity.

G.1.1 The polarization ellipticity

To get the shear from the polarization, let's start with the definition for the polarization in the source plane

$$\boldsymbol{\chi}^{(s)} = \frac{Q_{11}^{(s)} - Q_{22}^{(s)} + 2iQ_{12}^{(s)}}{Q_{11}^{(s)} + Q_{22}^{(s)}} = \chi_1^{(s)} + i\chi_2^{(s)}, \tag{G.5}$$

using eq. (G.3) we came up to the following set of equation for the second moments

$$\begin{aligned} Q_{11}^{(s)} &= A_{11}^2 Q_{11}^{\rm obs} + 2A_{11}A_{12}Q_{12}^{\rm obs} + A_{12}^2 Q_{22}^{\rm obs} \\ Q_{22}^{(s)} &= A_{21}^2 Q_{11}^{\rm obs} + 2A_{21}A_{22}Q_{12}^{\rm obs} + A_{22}^2 Q_{22}^{\rm obs} \\ Q_{12}^{(s)} &= A_{11}A_{21}Q_{11}^{\rm obs} + (A_{11}A_{22} + A_{12}^2)Q_{12}^{\rm obs} + A_{12}A_{22}Q_{22}^{\rm obs}, \end{aligned} \tag{G.6}$$

using this relation and from eq. (3.39) we can prove

$$\begin{aligned} Q_{11}^{(s)} + Q_{22}^{(s)} &= \left[(1-\kappa)^2 + |\boldsymbol{\gamma}|^2\right](Q_{11}^{\rm obs} + Q_{22}^{\rm obs}) \\ &\quad - 2(1-\kappa)\left[\gamma_1(Q_{11}^{\rm obs} - Q_{22}^{\rm obs}) + 2\gamma_2 Q_{12}^{\rm obs}\right] \end{aligned} \tag{G.7}$$

$$\begin{aligned} Q_{11}^{(s)} - Q_{22}^{(s)} &= \left[(1-\kappa)^2 + \gamma_1^2 - \gamma_2^2\right](Q_{11}^{\rm obs} - Q_{22}^{\rm obs}) - 2(1-\kappa)\gamma_1(Q_{11}^{\rm obs} + Q_{22}^{\rm obs}) + \\ &\quad 4\gamma_2\gamma_1 Q_{12}^{\rm obs} \end{aligned} \tag{G.8}$$

$$\begin{aligned} Q_{12}^{(s)} &= -(1-\kappa)\gamma_2(Q_{11}^{\rm obs} + Q_{22}^{\rm obs}) + \gamma_1\gamma_2(Q_{11}^{\rm obs} - Q_{22}^{\rm obs}) \\ &\quad + \left[(1-\kappa)^2 - \gamma_1^2 + \gamma_2^2\right] Q_{12}^{\rm obs} \end{aligned} \tag{G.9}$$

reorganizing terms

$$\begin{aligned} \frac{Q_{11}^{(s)} + Q_{22}^{(s)}}{Q_{11}^{\rm obs} + Q_{22}^{\rm obs}} &= (1-\kappa)^2 + |\boldsymbol{\gamma}|^2 - 2(1-\kappa)(\gamma_1\chi_1^{\rm obs} + \gamma_2\chi_2^{\rm obs}) \\ \frac{Q_{11}^{(s)} - Q_{22}^{(s)}}{Q_{11}^{\rm obs} + Q_{22}^{\rm obs}} &= \left((1-\kappa)^2 + \gamma_1^2 - \gamma_2^2\right)\chi_1^{\rm obs} - 2(1-\kappa)\gamma_1 + 2\gamma_2\gamma_1\chi_2^{\rm obs}, \\ \frac{Q_{12}^{(s)}}{Q_{11}^{\rm obs} + Q_{22}^{\rm obs}} &= -(1-\kappa)\gamma_2 + \gamma_1\gamma_2\chi_1^{\rm obs} + \left[(1-\kappa)^2 - \gamma_1^2 + \gamma_2^2\right]\frac{\chi_2^{\rm obs}}{2} \end{aligned} \tag{G.10}$$

substituting in eq. (G.5)

$$\boxed{\boldsymbol{\chi}^{(s)} = \frac{(1-\kappa)^2\boldsymbol{\chi}^{\rm obs} + \boldsymbol{\gamma}^2\bar{\boldsymbol{\chi}}^{\rm obs} - 2(1-\kappa)\boldsymbol{\gamma}}{(1-\kappa)^2 + |\boldsymbol{\gamma}|^2 - 2(1-\kappa)\Re e(\boldsymbol{\gamma}\bar{\boldsymbol{\chi}}^{\rm obs})}} \tag{G.11}$$

where $\bar{\boldsymbol{\chi}}^{\rm obs}$ is the complex conjugation of the observed polarization. Notice we are using bold symbols to emphasize the complex quantities, we do not mean vector at any time. We can write even in a more compact way eq. (G.11) using the reduced definitions of the shear eq. (3.61)

$$\boxed{\boldsymbol{\chi}^{\rm source} = \frac{\boldsymbol{\chi}^{\rm obs} + \boldsymbol{g}^2\bar{\boldsymbol{\chi}}^{\rm obs} - 2\boldsymbol{g}}{1 + |\boldsymbol{g}|^2 - 2\Re e(\boldsymbol{g}\bar{\boldsymbol{\chi}}^{\rm obs})}} \tag{G.12}$$

To see how the observed polarization is an estimator of the shear, we need to do an expansion in the Taylor series considering $g << 1$, but first, we need to find the inverse relation of eq. (G.12). From eq. (G.3) and eq. (G.4) we know

$$Q^{\rm obs} = A^{-1}Q^{(s)}A^{-1} \qquad Q^{\rm obs}_{ij} = A^{-1}_{ik}A^{-1}_{jn}Q^{(s)}_{kn}. \tag{G.13}$$

Besides, it is easy to see that the inverse of the matrix of transformation A is

$$\boxed{A^{-1} = \mu\begin{bmatrix} 1-\kappa+\gamma_1 & \gamma_2 \\ \gamma_2 & 1-\kappa-\gamma_1 \end{bmatrix},} \tag{G.14}$$

where we have used eq. (3.42) to introduce the magnification. However, this factor becomes irrelevant since our definition of polarization depends on the ration of second moments, canceling out factors μ^2 that appears in both the numerator and denominator. The only difference with the procedure we did before is the sign change of the shear, which appears as a consequence of the transformation matrix inverse. Therefore we can conclude

$$\boxed{\boldsymbol{\chi}^{\rm obs} = \frac{\boldsymbol{\chi}^{\rm source} + \boldsymbol{g}^2\bar{\boldsymbol{\chi}}^{\rm source} + 2\boldsymbol{g}}{1 + |\boldsymbol{g}|^2 + 2\Re e(\boldsymbol{g}\bar{\boldsymbol{\chi}}^{\rm source})}} \tag{G.15}$$

Now, we can proceed with the Taylor expansion. Since $\boldsymbol{g} << 1$ we will expand around the origin, up to second order this is

$$\boldsymbol{\chi}^{\rm obs}(\boldsymbol{g}) = \boldsymbol{\chi}^{\rm obs}(0) + \boldsymbol{\chi}^{\rm obs'}(0)\boldsymbol{g} + \mathcal{O}^{(2)}, \tag{G.16}$$

where each contribution,

$$\begin{aligned} \boldsymbol{\chi}^{\rm obs}(0) &= \boldsymbol{\chi}^{(\boldsymbol{s})} \\ \boldsymbol{\chi}^{\rm obs'}(0) &= 2 - 2\boldsymbol{\chi}^{(\boldsymbol{s})}\Re e(\boldsymbol{\chi}^{(\boldsymbol{s})}). \end{aligned} \tag{G.17}$$

Now we substitute eq. (G.17) in eq. (G.16), and we make use of the property $2z\Re e(z) = |z|^2 + z^2$ is hold for any complex z, then

$$\boxed{\boldsymbol{\chi}^{\rm obs} \approx \boldsymbol{\chi}^{(s)} + \left[2 - (\boldsymbol{\chi}^{(s)})^2 - \left|\boldsymbol{\chi}^{(s)}\right|^2\right] \boldsymbol{g}} \tag{G.18}$$

It is very common to find in the literature, the expression $\boldsymbol{\chi}^{\rm obs} \approx \boldsymbol{\chi}^{(s)} + 2\boldsymbol{g}$, since we are in the weak lensing regime then in principle higher order contribution can be rejected. In fact, this can be obtained without the need of any Taylor expansion, we could just neglect order two terms in eq. (G.15).

G.1.2 The distortion ellipticity

Let's see how are the relations between the distortion and the shear. As before we start writing the distortion ellipticity eq. (4.17) in the source plane,

$$\boldsymbol{\epsilon}^{(s)} = \frac{Q_{11}^{(s)} - Q_{22}^{(s)} + 2iQ_{12}^{(s)}}{Q_{11}^{(s)} + Q_{22}^{(s)} + 2\sqrt{Q_{11}^{(s)}Q_{22}^{(s)} - Q_{12}^{2(s)}}} = \epsilon_1^{(s)} + i\epsilon_2^{(s)} \tag{G.19}$$

we can take advantage of all the calculation we did before for the polarization, but now we need to consider the extra term $2\sqrt{Q_{11}^{(s)}Q_{22}^{(s)} - Q_{12}^{2(s)}}$, using eq. (G.6) we can demonstrate that it satisfies

$$2\sqrt{Q_{11}^{(s)}Q_{22}^{(s)} - Q_{12}^{2(s)}} = 2\left|A_{12}^2 - A_{11}A_{22}\right| \sqrt{Q_{11}^{(\rm obs)}Q_{22}^{(\rm obs)} - Q_{12}^{2(\rm obs)}}, \tag{G.20}$$

in terms of the shear and the convergence, i.e using eq. (3.39), last expression becomes

$$2\sqrt{Q_{11}^{(s)}Q_{22}^{(s)} - Q_{12}^{2(s)}} = 2\left|\left|\boldsymbol{\gamma}\right|^2 - (1-\kappa)^2\right| \sqrt{Q_{11}^{(\rm obs)}Q_{22}^{(\rm obs)} - Q_{12}^{2(\rm obs)}}. \tag{G.21}$$

To recover the distortion we must calculate $Q_{11}^{(s)} + Q_{22}^{(s)} + 2\sqrt{Q_{11}^{(s)}Q_{22}^{(s)} - Q_{12}^{2(s)}}$, using eq. (G.7) and eq. (G.21) we see it is

$$\begin{cases} |\boldsymbol{\gamma}|^2 \left(Q_{11}^{\rm obs}+Q_{22}^{\rm obs}+2\sqrt{Q_{11}^{\rm (obs)}Q_{22}^{\rm (obs)}-Q_{12}^{2\rm (obs)}}\right) & \\ +(1-\kappa)^2\left(Q_{11}^{\rm obs}+Q_{22}^{\rm obs}-2\sqrt{Q_{11}^{\rm (obs)}Q_{22}^{\rm (obs)}-Q_{12}^{2\rm (obs)}}\right) & |\boldsymbol{\gamma}|^2>(1-\kappa)^2 \\ \quad -2(1-\kappa)\left[\gamma_1(Q_{11}^{\rm obs}-Q_{22}^{\rm obs})+2\gamma_2 Q_{12}^{\rm obs}\right] & \\ \\ |\boldsymbol{\gamma}|^2 \left(Q_{11}^{\rm obs}+Q_{22}^{\rm obs}-2\sqrt{Q_{11}^{\rm (obs)}Q_{22}^{\rm (obs)}-Q_{12}^{2\rm (obs)}}\right) & \\ +(1-\kappa)^2\left(Q_{11}^{\rm obs}+Q_{22}^{\rm obs}+2\sqrt{Q_{11}^{\rm (obs)}Q_{22}^{\rm (obs)}-Q_{12}^{2\rm (obs)}}\right) & |\boldsymbol{\gamma}|^2<(1-\kappa)^2 \\ \quad -2(1-\kappa)\left[\gamma_1(Q_{11}^{\rm obs}-Q_{22}^{\rm obs})+2\gamma_2 Q_{12}^{\rm obs}\right], & \end{cases}$$

factorizing

$$\frac{Q_{11}^{(s)}+Q_{22}^{(s)}+2\sqrt{Q_{11}^{(s)}Q_{22}^{(s)}-Q_{12}^{2(s)}}}{Q_{11}^{(o)}+Q_{22}^{(o)}+2\sqrt{Q_{11}^{(o)}Q_{22}^{(o)}-Q_{12}^{2(o)}}}=\begin{cases} |\boldsymbol{\gamma}|^2+(1-\kappa)^2\left|\boldsymbol{\epsilon}^{\rm (o)}\right|^2 & \\ -2(1-\kappa)\left(\gamma_1\epsilon_1^{\rm (o)}+\gamma_2\epsilon_2^{\rm (o)}\right) & \left|\frac{\boldsymbol{\gamma}}{1-\kappa}\right|>1 \\ \\ |\boldsymbol{\gamma}|^2\left|\boldsymbol{\epsilon}^{\rm (o)}\right|^2+(1-\kappa)^2 & \\ -2(1-\kappa)\left(\gamma_1\epsilon_1^{\rm (o)}+\gamma_2\epsilon_2^{\rm (o)}\right) & \left|\frac{\boldsymbol{\gamma}}{1-\kappa}\right|<1 \end{cases} \tag{G.22}$$

dividing eq. (G.8) by eq. (G.22) we get the real component of the distortion

$$\epsilon_1^{(s)}=\begin{cases} \frac{\left[(1-\kappa)^2+\gamma_1^2-\gamma_2^2\right]\epsilon_1^{\rm (o)}-(1-\kappa)\gamma_1\left(1+\left|\boldsymbol{\epsilon}^{(o)}\right|^2\right)+2\gamma_2\gamma_1\epsilon_2^{\rm (o)}}{|\boldsymbol{\gamma}|^2+(1-\kappa)^2\left|\boldsymbol{\epsilon}^{\rm (o)}\right|^2-2(1-\kappa)\left(\gamma_1\epsilon_1^{\rm (o)}+\gamma_2\epsilon_2^{\rm (o)}\right)} & \text{for} \quad \left|\frac{\boldsymbol{\gamma}}{1-\kappa}\right|>1 \\ \\ \frac{\left[(1-\kappa)^2+\gamma_1^2-\gamma_2^2\right]\epsilon_1^{\rm (o)}-(1-\kappa)\gamma_1\left(1+\left|\boldsymbol{\epsilon}^{(o)}\right|^2\right)+2\gamma_2\gamma_1\epsilon_2^{\rm (o)}}{|\boldsymbol{\gamma}|^2\left|\boldsymbol{\epsilon}^{\rm (o)}\right|^2+(1-\kappa)^2-2(1-\kappa)\left(\gamma_1\epsilon_1^{\rm (o)}+\gamma_2\epsilon_2^{\rm (o)}\right)} & \text{for} \quad \left|\frac{\boldsymbol{\gamma}}{1-\kappa}\right|<1 \end{cases} \tag{G.23}$$

similarly we divide eq. (G.9) by eq. (G.22) to get the imaginary component

$$\epsilon_2^{(s)}=\begin{cases} \frac{-(1-\kappa)\gamma_2\left(1+\left|\boldsymbol{\epsilon}^{(o)}\right|^2\right)+2\gamma_1\gamma_2\epsilon_1+\left[(1-\kappa)^2-\gamma_1^2+\gamma_2^2\right]\epsilon_2}{|\boldsymbol{\gamma}|^2+(1-\kappa)^2\left|\boldsymbol{\epsilon}^{\rm (o)}\right|^2-2(1-\kappa)\left(\gamma_1\epsilon_1^{\rm (o)}+\gamma_2\epsilon_2^{\rm (o)}\right)} & \text{for} \quad \left|\frac{\boldsymbol{\gamma}}{1-\kappa}\right|>1 \\ \\ \frac{-(1-\kappa)\gamma_2\left(1+\left|\boldsymbol{\epsilon}^{(o)}\right|^2\right)+2\gamma_1\gamma_2\epsilon_1+\left[(1-\kappa)^2-\gamma_1^2+\gamma_2^2\right]\epsilon_2}{|\boldsymbol{\gamma}|^2\left|\boldsymbol{\epsilon}^{\rm (o)}\right|^2+(1-\kappa)^2-2(1-\kappa)\left(\gamma_1\epsilon_1^{\rm (o)}+\gamma_2\epsilon_2^{\rm (o)}\right)} & \text{for} \quad \left|\frac{\boldsymbol{\gamma}}{1-\kappa}\right|<1 \end{cases} \tag{G.24}$$

where we have used the identity

$$\frac{Q_{11}+Q_{22}}{Q_{11}+Q_{22}+2\sqrt{Q_{11}Q_{22}-Q_{12}^2}}=\frac{1}{2}\left(1+|\boldsymbol{\epsilon}|^2\right) \tag{G.25}$$

that can be easily demonstrated using eq. (4.16) and eq. (4.15).

To make the notation more compact less introduce again the reduced shears

$$\epsilon_1^{(s)}=\begin{cases}\dfrac{\left[1+g_1^2-g_2^2\right]\epsilon_1^{(\mathrm{o})}-g_1\left(1+\left|\boldsymbol{\epsilon}^{(\mathrm{o})}\right|^2\right)+2g_2g_1\epsilon_2^{(\mathrm{o})}}{|\boldsymbol{g}|^2+\left|\boldsymbol{\epsilon}^{(\mathrm{o})}\right|^2-2\left(g_1\epsilon_1^{(\mathrm{o})}+g_2\epsilon_2^{(\mathrm{o})}\right)} & \text{for} \quad |\boldsymbol{g}|>1 \\ \dfrac{\left[1+g_1^2-g_2^2\right]\epsilon_1^{(\mathrm{o})}-g_1\left(1+\left|\boldsymbol{\epsilon}^{(\mathrm{o})}\right|^2\right)+2g_2g_1\epsilon_2^{(\mathrm{o})}}{|\boldsymbol{g}|^2\left|\boldsymbol{\epsilon}^{(\mathrm{o})}\right|^2+1-2\left(g_1\epsilon_1^{(\mathrm{o})}+g_2\epsilon_2^{(\mathrm{o})}\right)} & \text{for} \quad |\boldsymbol{g}|<1\end{cases} \tag{G.26}$$

$$\epsilon_2^{(s)}=\begin{cases}\dfrac{-g_2\left(1+\left|\boldsymbol{\epsilon}^{(\mathrm{o})}\right|^2\right)+2g_1g_2\epsilon_1^{(\mathrm{o})}+\left[1-g_1^2+g_2^2\right]\epsilon_2^{(\mathrm{o})}}{|\boldsymbol{g}|^2+\left|\boldsymbol{\epsilon}^{(\mathrm{o})}\right|^2-2\left(g_1\epsilon_1^{(\mathrm{o})}+g_2\epsilon_2^{(\mathrm{o})}\right)} & \text{for} \quad |\boldsymbol{g}|>1 \\ \dfrac{-g_2\left(1+\left|\boldsymbol{\epsilon}^{(\mathrm{o})}\right|^2\right)+2g_1g_2\epsilon_1^{(\mathrm{o})}+\left[1-g_1^2+g_2^2\right]\epsilon_2^{(\mathrm{o})}}{|\boldsymbol{g}|^2\left|\boldsymbol{\epsilon}^{(\mathrm{o})}\right|^2+1-2\left(g_1\epsilon_1^{(\mathrm{o})}+g_2\epsilon_2^{(\mathrm{o})}\right)} & \text{for} \quad |\boldsymbol{g}|<1\end{cases} \tag{G.27}$$

Finally, putting together and using complex notation we have

$$\boldsymbol{\epsilon}^{(\mathrm{source})}=\begin{cases}\dfrac{-\boldsymbol{g}\left(1+\left|\boldsymbol{\epsilon}^{(\mathrm{obs})}\right|^2\right)+\boldsymbol{\epsilon}^{\mathrm{obs}}+\boldsymbol{g}^2\bar{\boldsymbol{\epsilon}}^{\mathrm{obs}}}{|\boldsymbol{g}|^2+\left|\boldsymbol{\epsilon}^{(\mathrm{obs})}\right|^2-2\Re e\left(\boldsymbol{g}\bar{\boldsymbol{\epsilon}}^{(\mathrm{obs})}\right)} & \text{for} \quad |\boldsymbol{g}|>1 \\ \dfrac{-\boldsymbol{g}\left(1+\left|\boldsymbol{\epsilon}^{(\mathrm{obs})}\right|^2\right)+\boldsymbol{\epsilon}^{\mathrm{obs}}+\boldsymbol{g}^2\bar{\boldsymbol{\epsilon}}^{\mathrm{obs}}}{|\boldsymbol{g}|^2\left|\boldsymbol{\epsilon}^{(\mathrm{obs})}\right|^2+1-2\Re e\left(\boldsymbol{g}\bar{\boldsymbol{\epsilon}}^{(\mathrm{obs})}\right)} & \text{for} \quad |\boldsymbol{g}|<1\end{cases} \tag{G.28}$$

rewriting to simplify terms

$$\boldsymbol{\epsilon}^{(\mathrm{source})}=\begin{cases}\dfrac{\boldsymbol{\epsilon}^{\mathrm{obs}}-\boldsymbol{g}+\boldsymbol{g}\bar{\boldsymbol{\epsilon}}^{\mathrm{obs}}(\boldsymbol{g}-\boldsymbol{\epsilon}^{\mathrm{obs}})}{(\boldsymbol{g}-\boldsymbol{\epsilon}^{\mathrm{obs}})(\boldsymbol{g}-\boldsymbol{\epsilon}^{\mathrm{obs}})^*} & \text{for} \quad |\boldsymbol{g}|>1 \\ \dfrac{\boldsymbol{\epsilon}^{\mathrm{obs}}-\boldsymbol{g}+\boldsymbol{g}\bar{\boldsymbol{\epsilon}}^{\mathrm{obs}}(\boldsymbol{g}-\boldsymbol{\epsilon}^{\mathrm{obs}})}{\left(\boldsymbol{g}\bar{\boldsymbol{\epsilon}}^{(\mathrm{obs})}-1\right)\left(\boldsymbol{g}\bar{\boldsymbol{\epsilon}}^{(\mathrm{obs})}-1\right)^*} & \text{for} \quad |\boldsymbol{g}|<1\end{cases} \tag{G.29}$$

After, an additional simplification, we finally find the relation between the distortion ellipticities and the shear we were looking for

$$\boxed{\boldsymbol{\epsilon}^{(\mathrm{source})}=\begin{cases}\dfrac{\boldsymbol{g}\bar{\boldsymbol{\epsilon}}^{(\mathrm{obs})}-1}{\bar{\boldsymbol{g}}-\bar{\boldsymbol{\epsilon}}^{(\mathrm{obs})}} & \text{for} \quad |\boldsymbol{g}|>1 \\ \dfrac{\boldsymbol{g}-\boldsymbol{\epsilon}^{(\mathrm{obs})}}{\bar{\boldsymbol{g}}\boldsymbol{\epsilon}^{(\mathrm{obs})}-1} & \text{for} \quad |\boldsymbol{g}|<1\end{cases}} \tag{G.30}$$

Using the same argument that in the case of the polarization, we have that the inverse of eq. (G.30) is obtained inverting the sign of $\boldsymbol{g}$, then

$$\boxed{\boldsymbol{\epsilon}^{(\mathrm{obs})} = \begin{cases} \frac{\boldsymbol{g}\bar{\boldsymbol{\epsilon}}^{(\mathrm{s})}+1}{\bar{\boldsymbol{g}}+\bar{\boldsymbol{\epsilon}}^{(\mathrm{s})}} & \text{for} \quad |\boldsymbol{g}| > 1 \\ \\ \frac{\boldsymbol{g}+\boldsymbol{\epsilon}^{(\mathrm{s})}}{\bar{\boldsymbol{g}}\boldsymbol{\epsilon}^{(\mathrm{s})}+1} & \text{for} \quad |\boldsymbol{g}| < 1. \end{cases}} \tag{G.31}$$

Now we will expand this definition in Taylor series we will expand around the origin. Considering only the expansion up to second order we have

$$\boldsymbol{\epsilon}^{\mathrm{obs}}(\boldsymbol{g}) = \boldsymbol{\epsilon}^{\mathrm{obs}}(0) + \boldsymbol{\epsilon}^{\mathrm{obs}'}(0)\boldsymbol{g} + \mathcal{O}^{(2)}, \tag{G.32}$$

where each contribution correspond to

$$\begin{aligned} \boldsymbol{\epsilon}^{\mathrm{obs}}(0) &= \begin{cases} \frac{1}{\bar{\boldsymbol{\epsilon}}^{(\boldsymbol{s})}} & \text{for} \quad |\boldsymbol{g}| > 1 \\ \boldsymbol{\epsilon}^{(\boldsymbol{s})} & \text{for} \quad |\boldsymbol{g}| < 1 \end{cases} \\ \boldsymbol{\epsilon}^{\mathrm{obs}'}(0) &= \begin{cases} 1 - \frac{1}{\bar{\boldsymbol{\epsilon}}^{(\boldsymbol{s})\boldsymbol{2}}} & \text{for} \quad |\boldsymbol{g}| > 1 \\ 1 - \boldsymbol{\epsilon}^{(\boldsymbol{s})\boldsymbol{2}} & \text{for} \quad |\boldsymbol{g}| < 1, \end{cases} \end{aligned} \tag{G.33}$$

substituting in the Taylor expansion we have

$$\boxed{\boldsymbol{\epsilon}^{\mathrm{obs}} \approx \begin{cases} \frac{1}{\bar{\boldsymbol{\epsilon}}^{(\boldsymbol{s})}} + \left(1 - \frac{1}{\bar{\boldsymbol{\epsilon}}^{(\boldsymbol{s})\boldsymbol{2}}}\right)\boldsymbol{g} & \text{for} \quad |\boldsymbol{g}| > 1 \\ \boldsymbol{\epsilon}^{(\boldsymbol{s})} + \left(1 - \boldsymbol{\epsilon}^{(\boldsymbol{s})\boldsymbol{2}}\right)\boldsymbol{g} & \text{for} \quad |\boldsymbol{g}| < 1, \end{cases}} \tag{G.34}$$

As with the polarization, if we neglect higher order terms in the weak lensing regime we can approximate the last expression to $\boldsymbol{\epsilon}^{\mathrm{obs}} \approx \bar{\boldsymbol{\epsilon}}^{(\boldsymbol{s})} + \boldsymbol{g}$.

G.2 Unbiased local estimator of the shear

In the previous section, we have presented how two different definitions of ellipticities are related to shear. In this section, we are interested in to show which definition can be more convenient. Where convenient for us, will mean, what definition represent and *unbiased* estimate of the shear. Recalling that the expected value of an unbiased estimator is the true value of the parameter. Under the assumption of an homogeneous and isotropic universe we expect

$$\left\langle \boldsymbol{\chi}^{(\boldsymbol{s})} \right\rangle = \left\langle \boldsymbol{\epsilon}^{(\boldsymbol{s})} \right\rangle = 0, \tag{G.35}$$

otherwise a privileged shape or orientation will be given, and the cosmological principle would not be valid. Using this fact, and the weak lensing regime up to first order we get

$$\boxed{\langle \boldsymbol{g} \rangle \approx \frac{\left\langle \boldsymbol{\chi}^{\rm obs} \right\rangle}{2} \approx \left\langle \boldsymbol{\epsilon}^{\rm obs} \right\rangle} \tag{G.36}$$

Now the question is how can we construct a definition of ellipticity with the property of being unbiased respect to the shear. Well, first we will assume we are doing a local measurement and therefore in eq. (G.36) we can replace $\langle \boldsymbol{g} \rangle \to \boldsymbol{g}$. Second, given eq. (G.35) can have multiple solution for $\boldsymbol{g}$, we have to guarantee uniqueness. Let's see this in more detail, if we consider a cluster at low redshift, our first approximation is equivalent to say the reduced shear $\boldsymbol{g}$ will be the same. The expected value of the polarization under this assumption can be written as

$$\left\langle \chi_i^{(obs)}(\boldsymbol{g}) \right\rangle = \frac{1}{N} \sum_{i=1}^{N} \chi_i^{(obs)}(\boldsymbol{g}) = 0. \tag{G.37}$$

However, this expression does not have a unique solution for $\boldsymbol{g}$. In particular note the identity

$$\boldsymbol{\chi}^{\rm obs}(\boldsymbol{g}) = \frac{\boldsymbol{g}}{\bar{\boldsymbol{g}}} \bar{\boldsymbol{\chi}}^{\rm obs}\left(\frac{1}{\bar{\boldsymbol{g}}}\right) \tag{G.38}$$

is true. Therefore, eq. (G.37) can have two different solutions, one for $\boldsymbol{g}$ and another for $\frac{1}{\bar{\boldsymbol{g}}}$. To avoid this degeneracy, with need to define a variable invariant under the transformation $\boldsymbol{g} \to \frac{1}{\bar{\boldsymbol{g}}}$, [53] uses

$$\boldsymbol{\delta} = \frac{2\boldsymbol{g}}{1 + |\boldsymbol{g}|^2} \tag{G.39}$$

as this new variable. Now, our objective is to write eq. (G.37) using this $\boldsymbol{\delta}$ instead of the reduced shear. In [53] is presented the math to express this condition only in terms of $\boldsymbol{\delta}$, thus eq. (G.37) is equivalent to

$$\sum_{i=1}^{N} \frac{\delta + \boldsymbol{\chi}_i^{\rm obs}}{1 + \Re e(\boldsymbol{\delta} \bar{\boldsymbol{\chi}}_{\boldsymbol{i}}^{\rm obs})} = 0. \tag{G.40}$$

solving for $\boldsymbol{\delta}$ we get an unbiased estimate of $\frac{2\boldsymbol{g}}{1+|\boldsymbol{g}|^2}$, However the polarization alone is not a unbiased estimator, i.e, $\left\langle \boldsymbol{\chi}^{(obs)}(\boldsymbol{g}) \right\rangle \neq \frac{2\boldsymbol{g}}{1+|\boldsymbol{g}|^2}$. On the other hand, the distortion ellipticity is an unbiased local estimator of $\boldsymbol{g}$. Given eq. (G.30), we see that in first order approximation

$$\left\langle \boldsymbol{\epsilon}^{(\rm obs)} \right\rangle = \begin{cases} \frac{1}{\bar{\boldsymbol{g}}} & \text{for} \quad |\boldsymbol{g}| > 1 \\ \\ \boldsymbol{g} & \text{for} \quad |\boldsymbol{g}| < 1. \end{cases} \tag{G.41}$$

and the expected value of the distortion

$$\left\langle \epsilon_i^{(obs)}(\boldsymbol{g}) \right\rangle = \frac{1}{N} \sum_{i=1}^{N} \epsilon_i^{(obs)}(\boldsymbol{g}) = 0, \tag{G.42}$$

has a unique solution, which is either the shear or the inverse conjugate reduced shear. And this is the main property because of the distortion ellipticity is preferred.

Appendix H

Interpretation of the eigenvector and eigenvalues of the second moments tensor

We have not explained why the eigenvalues and eigenvector of the second moments tensor of the surface brightness are associated to the semi-major and semi-minor axis of an ellipsoid. To show how it is this relationship between them, we present the case of the eigenvector and eigenvalues of an elliptical uniform surface brightness.

We start by writing the quadratic form of the second moments tensor

$$\boldsymbol{u}^T Q \boldsymbol{u} = Q_x x^2 + 2xyQ_{xy} + Q_y y^2 \tag{H.1}$$

where $\boldsymbol{u}^T = [x \quad y]$, and we used the property of Q being symmetric. Now, we will write this quadratic form in terms of the eigenvalues of Q. Since our matrix is diagonizable we have $Q = PDP^{-1}$, where D is a diagonal matrix with the eigenvalues in the diagonal and P is the matrix with the eigenvector in his columns. Moreover, P has the property of being and orthogonal matrix, thus $P^T = P^{-1}$ and $Q = PDP^T$. Therefore, the quadratic form $\boldsymbol{u}^T Q \boldsymbol{u}$ is equivalent to $\boldsymbol{u}^T PDP^T \boldsymbol{u} = (P^T \boldsymbol{u})^T D(P^T \boldsymbol{u})$, and consequently our quadratic form can be written an

$$\boldsymbol{u}^T Q \boldsymbol{u} = \lambda_1(\overrightarrow{u} \cdot \overrightarrow{v_1})^2 + \lambda_2(\overrightarrow{u} \cdot \overrightarrow{v_2})^2 \tag{H.2}$$

where $\lambda_{1,2}$ and $\overrightarrow{v}_{1,2}$ are determined by eq. (4.5). Notice that this is the equation of an ellipse with semi-axis

$$\boxed{a = (\lambda_{\min})^{-1/2} \quad b = (\lambda_{\max})^{-1/2},} \tag{H.3}$$

and a suitable change of coordinates determined by the proper vectors. This result is essentially a consequence of the *principal axis theorem* and the fact of second moment of image being positive.

Then if we can demonstrate that the bilinear form $\boldsymbol{u}^T Q \boldsymbol{u}$ corresponds to the external isophotal curve of our uniform ellipse, then eq. (4.4) is the relation between semi-axis and

eigenvalues we are looking for. We will see this is not exactly true, because eq. (H.2) is associated with different ellipse equation that the one of the external isophote. Nevertheless, we are interested in to get the third flattening, which is the ratio of linear combinations of the semi-axis, then this difference will become irrelevant.

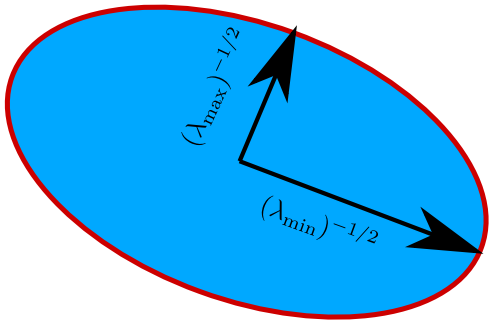

Figure H.1: *Diagram illustrating the relation between eigenvalues and the elliptical equation resulting of the quadratic form of the image second moment (This ellipse is different of the one we are observing by an scaling factor)*

Let's see this in detail with an example. We start supposing we have an uniform ellipse with their semi-axis over the Cartesian system. Given that we are assuming an uniform profile, then the second moment tensor of this ellipse corresponds to second moment of area and

$$Q = \begin{bmatrix} \frac{\pi}{4}ab^3 & 0 \\ 0 & \frac{\pi}{4}a^3b \end{bmatrix}, \tag{H.4}$$

where a and b are the semi-major and semi-minor axis of the ellipse respectively. If we replace this second moments in eq. (4.5) we get $\lambda_1 = \frac{\pi}{4}ab^3$, $\lambda_2 = \frac{\pi}{4}a^3b$ and $\overrightarrow{v}_1 = \hat{\boldsymbol{i}}$ and $\overrightarrow{v}_2 = \hat{\boldsymbol{j}}$. Finally, substituting this expression in eq. (H.2) we obtain

$$\boldsymbol{u}^T Q \boldsymbol{u} = \frac{\pi}{4}ab^3x^2 + \frac{\pi}{4}a^3by^2 = \frac{\pi}{4}a^3b^3\left[\left(\frac{x}{a}\right)^2 + \left(\frac{y}{b}\right)^2\right], \tag{H.5}$$

which is the l.h.s of the equation of another ellipse scaled by a factor of $\frac{\pi}{4}a^3b^3$. As a consequence, the bilinear form of the second moment tensor Q is different than the equation of the external isophote. Let's see that this difference in fact does not affect both definitions of ellipticity we have used. The polarization, in this particular case, it is

$$\chi = \frac{\lambda_{\max} - \lambda_{\min}}{\lambda_{\max} + \lambda_{\min}} = \frac{\frac{\pi}{4}a^3b - \frac{\pi}{4}ab^3}{\frac{\pi}{4}ab^3 + \frac{\pi}{4}a^3b} = \frac{a^2 - b^2}{b^2 + a^2}. \tag{H.6}$$

And the distortion is

$$\epsilon = \frac{\sqrt{\lambda_{\max}} - \sqrt{\lambda_{\min}}}{\sqrt{\lambda_{\max}} + \sqrt{\lambda_{\min}}} = \frac{a - b}{b + a}. \tag{H.7}$$

As a consequence, we have recovered the original definition of the third flattening in eq. (H.6) and its quadratic version in eq. (H.7). Therefore, we can work directly with the

eigenvalues obtained from the image tensor rather than try to get the exact values of the semi-axis of the external isophote. This example shows that the definitions we have used are consistent with what we expect for the case of the ellipse with their axis over Cartesian coordinates. The principal axis theorem lets us reduce the problem of a general ellipse or a more complicated shape to this example we have presented. In fact, for a tensor of dimension two, this theorem also guarantees that the eigenvectors are the directions o maximum change and minimum change of the image, that in the case of the uniform ellipse correspond to their semi-axis. Thus, somehow what we are doing in the case of a complicated shape, is finding those axis and define an ellipse over they, where the size of the axis we can assume to be the eigenvalues of the second image moment tensor (see fig. H.1), because our definition of ellipticities will keep consistent with what we expect for the particular case of the uniform ellipse. .

Appendix I

Unweighted moments and systematic errors of the PSF modeling

In the following appendix, we justify why the selected parametrization for the additive bias of the PSF is the proper choice. Our starting point is the second moment of the PSF profile. Recalling eq. (4.1) is valid in general for any profile, if instead of using the surface brightness we use the PSF profile $P(\overrightarrow{x})$ then we have

$$Q_{ij}^{PSF} = \frac{\int d^2\mathbf{x}(x_i - x_i^{\rm cen})(x_j - x_j^{\rm cen})P(\overrightarrow{x})}{\int d^2\mathbf{x}, P(\overrightarrow{x})} \tag{I.1}$$

and in analogy to the observed polarization and distortion we can define a PSF ellipticity $e^{\rm PSF}$ using now moments $Q_{ij}^{\rm PSF}$.

With these definitions in mind, we can determine for a particular galaxy its observed ellipticity experimentally measuring the surface brightness of the source. And the PSF ellipticity determining $P(\overrightarrow{x})$ using a particular model at its location. However, we are interested in the ellipticity of the galaxy before the atmosphere an other effects smear the images. So we need to find a relation between the observed ellipticity e^{obs} , the PSF ellipticity e^{PSF} and the galaxy ellipticity e^{gal}. Lets see how to do that, first at all recall that the definition of the PSF, relates all the three profiles,

$$S^{\rm obs}(\overrightarrow{x}) = \int d^2\mathbf{x}' P(\overrightarrow{x'}) S^{\rm gal}(\overrightarrow{x} - \overrightarrow{x'}) = (P \star S)(\overrightarrow{x}). \tag{I.2}$$

This definition have a particular useful property known as the Fubbini's theorem

$$\int (P \star S)(\overrightarrow{x}) d\mathbf{x} = \int P(\overrightarrow{x}) d\mathbf{x} \int S(\overrightarrow{x}) d\mathbf{x}. \tag{I.3}$$

Before trying to find relation between ellipticities we need to see how the seconds moments

relates. Lets replace the observed brightness profile in the definition of second moments

$$Q_{ij}^{\rm obs} = \frac{\int d^2\mathbf{x}(x_i - x_i^{\rm cen})(x_j - x_j^{\rm cen})(P \star S)(\overrightarrow{x})}{\int d^2\mathbf{x}(P \star S)(\overrightarrow{x})} \tag{I.4}$$

Replacing eq. (I.2) and eq. (I.3) and inverting the order of integration,

$$Q_{ij}^{\rm obs} = \frac{\int P(\overrightarrow{x'})d^2\mathbf{x}' \int d^2\mathbf{x}(x_i - x_i^{\rm cen})(x_j - x_j^{\rm cen})S(\overrightarrow{x} - \overrightarrow{x'})}{\int P(\overrightarrow{x})d^2\mathbf{x} \int S(\overrightarrow{x})d^2\mathbf{x}}. \tag{I.5}$$

Changing variable $\overrightarrow{u} = \overrightarrow{x} - \overrightarrow{x'}$, renaming $\bar{x'} = x' - x'^{\rm cen}$ and $\bar{u} = u - u^{\rm cen}$

$$Q_{ij}^{\rm obs} = \frac{\int P(\overrightarrow{x'})d^2\mathbf{x}' \int d^2\mathbf{u}(\bar{u}_i + \bar{x}'_i)(\bar{u}_j + \bar{x}'_j)S(\overrightarrow{u})}{\int P(\overrightarrow{x})d^2\mathbf{x} \int S(\overrightarrow{x})d^2\mathbf{x}} \tag{I.6}$$

$$Q_{ij}^{\rm obs} = \frac{\int P(\overrightarrow{x'})d^2\mathbf{x}'}{\int P(\overrightarrow{x})d^2\mathbf{x} \int S(\overrightarrow{u})d^2\mathbf{u}} \left(\int d^2\mathbf{u}[\bar{u}_i\bar{u}_j + \bar{u}_i\bar{x'}_j + \bar{x'}_i\bar{u}_j + \bar{x'}_j\bar{x'}_i]S(\overrightarrow{u}) \right) \tag{I.7}$$

$$Q_{ij}^{\rm obs} = \frac{\int P(\overrightarrow{x'})d^2\mathbf{x}'}{\int P(\overrightarrow{x})d^2\mathbf{x} \int S(\overrightarrow{u})d^2\mathbf{u}} \left(\int d^2\mathbf{u}\bar{u}_i\bar{u}_j S(\overrightarrow{u}) + \bar{x'}_j \int d^2\mathbf{u}\bar{u}_i S(\overrightarrow{u}) \right. \tag{I.8}$$

$$\left. + \bar{x'}_i \int d^2\mathbf{u}\bar{u}_j S(\overrightarrow{u}) + \bar{x'}_j\bar{x'}_i \int d^2\mathbf{u} S(\overrightarrow{u}) \right) \tag{I.9}$$

from the definition of second moment we see that the first term correspond to the second moments of the galaxy. A from the first moment definition the terms in the middle cancel. Leading to

$$Q_{ij}^{\rm obs} = \frac{\int P(\overrightarrow{x'})d^2\mathbf{x}' \left(Q_{ij}^{\rm gal} + x'_j x'_i \right)}{\int P(\overrightarrow{x})d^2\mathbf{x}} \tag{I.10}$$

Finally we have demonstrated that second moments are additive, i.e,

$$\boxed{Q_{ij}^{\rm obs} = Q_{ij}^{\rm PSF} + Q_{ij}^{\rm gal}.} \tag{I.11}$$

It follows immediately that this theorem also applies for the sizes $T = Q_{11} + Q_{22}$, i.e $T^{\rm obs} = T^{\rm PSF} + T^{\rm gal}$.

The field of the galaxies ellipticities can be estimated using unweighted moments through the expression

$$e_{\rm gal} = \frac{Q_{11}^{\rm gal} - Q_{22}^{\rm gal}}{T^{\rm gal}} + i\frac{2Q_{12}^{\rm gal}}{T^{\rm gal}}, \tag{I.12}$$

ordering terms to make explicit the PSF dependent terms we obtain

$$e_{\rm gal}T^{\rm gal} = Q_{11}^{\rm obs} - Q_{22}^{\rm obs} + i2Q_{12}^{\rm obs} - (Q_{11}^{\rm PSF} - Q_{22}^{\rm PSF}) - i2Q_{12}^{\rm PSF} \tag{I.13}$$

$$e_{\rm gal}(T^{\rm obs} - T^{\rm PSF}) = e^{\rm obs}T^{\rm obs} - e^{\rm PSF}T^{\rm PSF} \tag{I.14}$$

$$\boxed{\hat{e}_{\rm gal} = \frac{e^{\rm obs}T^{\rm obs} - e^{\rm PSF}T^{\rm PSF}}{(T^{\rm obs} - T^{\rm PSF})}} \tag{I.15}$$

From this expression we now make error propagation, where the deviation of the true signal due to PSF is

$$\delta e_{\rm gal} = \frac{\partial e_{\rm gal}}{\partial T^{\rm PSF}}\delta T^{\rm PSF} + \frac{\partial e_{\rm gal}}{\partial e^{\rm PSF}}\delta e^{\rm PSF} \tag{I.16}$$

$$\delta e_{\rm gal} = \frac{-e^{\rm PSF}(T^{\rm obs} - T^{\rm PSF}) + (e^{\rm obs}T^{\rm obs} - e^{\rm PSF}T^{\rm PSF})}{(T^{\rm obs} - T^{\rm PSF})^2}\delta T^{\rm PSF} + \frac{\partial e_{\rm gal}}{\partial e^{\rm PSF}}\delta e^{\rm PSF} \tag{I.17}$$

$$\delta e_{\rm gal} = \frac{-e^{\rm PSF} + e^{\rm gal}}{T^{\rm obs} - T^{\rm PSF}}\delta T^{\rm PSF} + \frac{\partial e_{\rm gal}}{\partial e^{\rm PSF}}\delta e^{\rm PSF} \tag{I.18}$$

$$\boxed{\delta e^{\rm sys}_{\rm gal} = \left(e^{\rm gal} - e^{\rm PSF}\right)\frac{\delta T^{\rm PSF}}{T^{\rm gal}} - \left(\frac{T^{\rm PSF}}{T^{\rm gal}}\right)\delta e^{\rm PSF}} \tag{I.19}$$

The previous equation is also valid for the case of stars,

$$\delta e^{\rm sys}_{*} = \left(e^{*} - e^{\rm PSF}\right)\frac{\delta T^{\rm PSF}}{T^{*}} - \left(\frac{T^{\rm PSF}}{T^{*}}\right)\delta e^{\rm PSF} \tag{I.20}$$

and we can use the stars case to quantify the bias in the shape due to PSF modelling, defining the error of the shape estimate of the PSF and size estimate as $\delta e^{\rm PSF} = e^{\rm PSF} - e^{*}$ and $\delta T^{\rm PSF} = T^{\rm PSF} - T^{*}$ we have

$$\delta e^{*}_{\rm sys} = -e^{\rm PSF}\left(\frac{T^{\rm PSF} - T^{*}}{T^{*}}\right) - \frac{T^{\rm PSF}}{T^{*}}\left(e^{\rm PSF} - e^{*}\right) + e^{*}\left(\frac{T^{\rm PSF} - T^{*}}{T^{*}}\right) \tag{I.21}$$

This result somehow justifies our choice of parametrization since we can choose either the first or the last term on the right-hand side to model the shape residual dependency. If we compare eq. (I.21) with eq. (7.2) we expect

$$\alpha \approx -\left\langle\frac{T^{\rm PSF} - T^{*}}{T^{*}}\right\rangle \to 0 \tag{I.22}$$

$$\beta \approx \left\langle\frac{T^{\rm PSF}}{T^{*}}\right\rangle \to 1 \tag{I.23}$$

$$\eta \to 1 \tag{I.24}$$

Appendix J

Shape noise error propagation

In general terms, we are want to find the variance of this estimator. To handle terms easily, lets split it the tangent and cross terms.

$$\xi^{ij}_{\pm}(\theta) = C^{ij}_{tt}(\theta) \pm C^{ij}_{xx}(\theta) \tag{J.1}$$

here the latin index i and j represent the redshift bin of the galaxy. And we will use α and β to represent sum over pairs of galaxies. Using this notation, we can write

$$C^{ij}_{tt}(\theta) = \frac{\sum_{\alpha,\beta} w^i_\alpha w^j_\beta e^i_{t,\alpha} e^j_{t,\beta} \Theta(\overrightarrow{\theta_\alpha}, \overrightarrow{\theta_\beta}) \Pi(i,j,\alpha,\beta)}{\sum_{\alpha,\beta} w^i_\alpha w^j_\beta \Theta(\overrightarrow{\theta_\alpha}, \overrightarrow{\theta_\beta}) \Pi(i,j,\alpha,\beta)} \tag{J.2}$$

where $\Theta(\overrightarrow{\theta_\alpha}, \overrightarrow{\theta_\beta})$ is a step function to count the number of pair in a particular redshift bin, i.e

$$\Theta(\overrightarrow{\theta_\alpha}, \overrightarrow{\theta_\beta}) = \begin{cases} 1 & \text{for} \quad \theta - \Delta\theta < \mid \overrightarrow{\theta_\alpha} - \overrightarrow{\theta_\beta} \mid < \theta + \Delta\theta \\ 0 & \text{otherwise,} \end{cases} \tag{J.3}$$

and $\Pi(i,j,\alpha,\beta)$ is a function to prevents double counting pairs, i.e, we do not want to see auto-correlations,

$$\Pi(i,j,\alpha,\beta) = \begin{cases} 1 & \text{for} \quad i \neq j \\ 1 & \text{for} \quad i = j, \beta < \alpha \\ 0 & \text{for} \quad i = j, \beta > \alpha \end{cases} \tag{J.4}$$

Lets consider the case where the weights are 1, i.e we do not consider large difference in the errors of the measurements of the ellipticities. Under this approximation we have

$$C^{ij}_{tt}(\theta) = \frac{1}{N_{\text{pairs}}} \sum_{\alpha,\beta} e^i_{t,\alpha} e^j_{t,\beta} \Theta(\overrightarrow{\theta_\alpha}, \overrightarrow{\theta_\beta}) \Pi(i,j,\alpha,\beta) \tag{J.5}$$

Lets calculate the variance of this tangential correlation function. Since Var $\left(\sum_i aX_i\right) =$

$a^2 \sum_i \mathrm{Var}(X_i)$, then

$$\mathrm{Var}\left(C_{tt}^{ij}(\theta)\right) = \frac{1}{N_{\mathrm{pairs}}^2} \sum_{\alpha,\beta} \mathrm{Var}(e_{t,\alpha}^i e_{t,\beta}^j) \Theta(\overrightarrow{\theta_\alpha}, \overrightarrow{\theta_\beta}) \Pi(i,j,\alpha,\beta) \tag{J.6}$$

consequently, we use the fact that we expect to have $\langle e_t \rangle = 0$ for the whole sky to use the identity $\mathrm{Var}(XY) = \mathrm{Var}(X)\mathrm{Var}(Y)$. In general, this is not true for a particular region, but it is a good approximation, because $\mathrm{Var}(XY) = \mathrm{Var}(X)\mathrm{Var}(Y) + E(X)^2\mathrm{Var}(Y) + E(Y)^2\mathrm{Var}(X)$ and the last to term are even smaller than the first. Consequently,

$$\mathrm{Var}\left(C_{tt}^{ij}(\theta)\right) = \frac{1}{N_{\mathrm{pairs}}^2} \sum_{\alpha,\beta} \mathrm{Var}(e_{t,\alpha}^i)\mathrm{Var}(e_{t,\beta}^j) \Theta(\overrightarrow{\theta_\alpha}, \overrightarrow{\theta_\beta}) \Pi(i,j,\alpha,\beta) \tag{J.7}$$

$$\mathrm{Var}\left(C_{tt}^{ij}(\theta)\right) = \frac{1}{N_{\mathrm{pairs}}^2} \sum_{\alpha,\beta} (\sigma_{e_t}^i)^2 (\sigma_{e_t}^j)^2 \Theta(\overrightarrow{\theta_\alpha}, \overrightarrow{\theta_\beta}) \Pi(i,j,\alpha,\beta) \tag{J.8}$$

$$\mathrm{Var}\left(C_{tt}^{ij}(\theta)\right) = \frac{1}{N_{\mathrm{pairs}}^2} N_{\mathrm{pairs}} (\sigma_{e_t}^i \sigma_{e_t}^j)^2 = \frac{(\sigma_{e_t}^i \sigma_{e_t}^j)^2}{N_{\mathrm{pairs}}} \tag{J.9}$$

Writing this in terms of the dispersion in total ellipticity, which satisfies $(\sigma_e^i)^2 = (\sigma_{e_t}^i)^2 + (\sigma_{e_\times}^i)^2 = 2(\sigma_{e_t}^i)^2$, we have

$$\mathrm{Var}\left(C_{tt}^{ij}(\theta)\right) = \frac{(\sigma_e^i \sigma_e^j)^2}{4N_{\mathrm{pairs}}} \tag{J.10}$$

Analogous result is obtained for the cross component, $\mathrm{Var}\left(C_{\times\times}^{ij}(\theta)\right) = \mathrm{Var}\left(C_{tt}^{ij}(\theta)\right)$ and as a consequence, we finally have a first approximation for the variance of the shear two point correlation function.

$$\mathrm{Var}(\xi_\pm^{ij}(\theta)) = \mathrm{Var}(C_{tt}^{ij}(\theta)) + \mathrm{Var}(C_{xx}^{ij}(\theta)) = \frac{(\sigma_e^i \sigma_e^j)^2}{2N_{\mathrm{pairs}}} \tag{J.11}$$

.